BERGISCHE
UNIVERSITÄT
WUPPERTAL

Chemical modification of gas-phase cluster dynamics in ion mobility spectrometry

Dissertation

zur Erlangung des akademischen Grades
Doktor der Naturwissenschaft (Dr. rer. nat.)

vorgelegt von
Florian Stappert

Bergische Universität Wuppertal
Fakultät für Mathematik und Naturwissenschaften
Physikalische und Theoretische Chemie

Wuppertal, April 2022

The PhD thesis can be quoted as follows:

urn:nbn:de:hbz:468-20220531-113045-9
[http://nbn-resolving.de/urn/resolver.pl?urn=urn%3Anbn%3Ade%3Ahbz%3A468-20220531-113045-9]

DOI: 10.25926/bnkv-qv66
[https://doi.org/10.25926/bnkv-qv66]

Erklärung

„Ich versichere, die Arbeit selbstständig verfasst zu haben, nur die in der Dissertation angegebenen Hilfsmittel benutzt und alle wörtlich und inhaltlich übernommenen Stellen als solche gekennzeichnet zu habe, und dass die Dissertation in der gegenwärtigen oder einer anderen Fassung noch keiner anderen Fakultät, keiner Gesamthochschule und keiner anderen wissenschaftlichen Hochschule vorgelegen hat."

Diese Dissertation wurde ohne Änderung ihres Aufbaus, Inhalts oder sonstiger Form, sprachlich von Scribbr B.V. (Amsterdam, Niederlande) überarbeitet.

Wuppertal, den
12. April 2022 Florian Stappert

Danksagung

Viele Menschen haben mich bei der Fertigstellung dieser Arbeit unterstützt und mich immer wieder aufgebaut.

Zunächst möchte ich mich bei Prof. Dr. Thorsten Benter bedanken. Du hast mir die Möglichkeit gegeben diese Arbeit durchzuführen und mir dabei immer die Freiheit gelassen meine eigenen Ideen zu entwickeln und auszuprobieren. Gleichzeitig hattest du immer ein offenes Ohr, wenn es Probleme gab. Während meiner Zeit in der Arbeitsgruppe konnte ich von Beginn an auf Augenhöhe mit dir diskutieren, was ich nie als selbstverständlich wahrgenommen habe.
Das Gleiche gilt für das gesamte Team der PTC. Ich bedanke mich bei euch für die offenen und teilweise hitzigen Diskussionen, nach denen man sich trotzdem immer in die Augen schauen konnte, für die vielen Stunden in Labor und Büro, in denen wir Frust und Freude geteilt haben und natürlich auch für die vielen Stunden, in denen wir die Wissenschaft auch mal vergessen konnten. Selbst wenn im Labor mal wieder nichts funktionieren wollte, wurde ich immer aufgefangen und neu motiviert.

Auch ohne die Unterstützung von externen Partnern wäre diese Arbeit so nicht möglich gewesen. Ich bedanke mich bei der Gruppe von Prof. Dr. Stefan Zimmermann (Leibniz Universität Hannover, Deutschland), dass ich in euren Laboren forschen durfte, bei der Gruppe von Prof. Dr. Scott Hopkins (Universtiy of Waterloo, Kanada), für die enge digitale Zusammenarbeit, als dies analog nicht möglich war, und bei der Firma Sciex (Concord, Kanada) für die unkomplizierte Unterstützung bei Problemen jeglicher Art. Natürlich hat mir auch der Blick von außen, der in unzähligen Gesprächen ausgetauscht wurde, erlaubt meine Ergebnisse ganzheitlich einzuordnen und zu verstehen.

Ein besonderer Dank gilt meiner Familie und meinen Freunden, die mich außerhalb der Universität aufgefangen, aufgebaut und mein Jammern ertragen haben. Ohne euch wäre ich oft an Problemen im Labor, an langwierigen Auswertungen und am Schreiben dieser Arbeit verzweifelt.

Abstract

In this work, the interactions of ions and neutral species in the gas phase are studied from selected points of view. These interactions are important in most analytical methods operating at atmospheric pressure (AP) because they affect substance-specific properties such as the *m/z* ratio or ion mobility. Therefore, understanding these processes is necessary for the interpretation of measurement results and for the optimization of an analytical system for a particular problem. In addition to, for example, fragmentation reactions due to energetic collisions (collision-induced dissociation, CID), the formation of clusters is a main interaction and is the focus of this work. Cluster dynamics with actively added gas-phase modifiers are investigated with differential mobility spectroscopy (DMS) coupled with mass spectrometry (MS) and high kinetic energy ion mobility spectrometry (HiKE-IMS).
In the first part, the impact of the ion structure on the cluster effect in DMS is investigated, and two main effects can be observed. Firstly, an increase in the absolute ion size, respectively in the collision cross section (CCS), leads to a decrease in the strength of the cluster effect, and secondly, a sterically more challenging ion at the charged position leads to effects such as charge shielding and thus impaired cluster formation. Furthermore, the ratio of ion and modifier sizes defines the behavior of a cluster. In the case of a significantly larger modifier, the behavior of the ion-modifier cluster depends mainly on the modifier. Additionally, the ion structure of a multiply charged ion, well known for ionization with electrospray ionization (ESI), influences the basic cluster formation. Depending on the distance between two charged positions, the experimental results indicate one superior cluster systems or two almost independent cluster systems.
In the second part, the cluster dynamic under constant energetic conditions in a HiKE-IMS is investigated. In addition to a permanent cluster formation with water due to a not water-free gas phase, a steady clustering and declustering process is demonstrated. Therefore, this dynamic must also be adopted for all instruments working at atmospheric pressure so that a signal in an ion mobility spectrum cannot be assigned to a specific ion. Instead, it must be assigned to a chemical system that is therefore highly susceptible to external influences such as variation in background temperature or humidity. The only exceptions to this rule are less reactive ions.
Finally, an attempt is made to achieve enantiomeric separation by stereoselective clustering due to the addition of an enantiopure modifier. Independently of the chirality of the ion or the optimized conditions, such experimental separation could not be realized with DMS.

The reason could be the formation of highly charged nanodroplets in the ESI process, which pass the DMS cell and even the ion inlet of the MS system. This demonstrates a deviation from the textbook ESI mechanism, for which there is also evidence in the literature. The ion-like behavior of these nanodroplets in DMS is shown, which is why complete separation from bare ions is almost impossible. A cluster-like effect on the nanodroplets can also be observed by the addition of a modifier. Furthermore, even numerical studies with optimized conditions have demonstrated only a weak stereoselective cluster formation.
In summary, this work provides fundamental findings on the cluster dynamic of ions and neutral species in the gas phase. A transfer to other analytical methods and other chemical systems is very likely permissible. Nevertheless, it must be mentioned that the present studies were performed on specially selected chemical systems of small ions. When real samples and bigger ions are studied, other interactions and effects are to be expected. Thus, further experimental and numerical studies are necessary, for example, in the field of HiKE-IMS or nanodroplet distribution.
Accordingly, the findings of this work fit into the overall study of cluster chemistry, but they do not claim to fully elucidate all fundamental mechanisms.

Table of Contents

1 Introduction

1.1 Ion-neutral interactions in chemical analysis

The interactions of ions with neutral species (atoms, molecules, etc.) in the gas phase are important in several analytical methods, such as *mass spectrometry* (MS) [1, 2], that are based on the behavior of charged species under defined conditions. Most of these interactions can be classified into three main categories:

- Cluster dynamics: clustering and declustering processes of ions with neutral species in the gas phase [2–7]
- Chemical reactions: formation of new chemical bonds [2, 8]
- Fragmentation reactions: breaking of covalent or intermolecular bonds as a result of increased internal energy due to collisions with neutral species (*collision-induced dissociation,* CID) [2, 9–12]

The complex chemical system is composed of these reactions, the influence of which depends on the physical and chemical conditions. While the cluster formation is preferred by the presence of polar species such as water [3, 7], a high number of collisions induce a declustering process [2]. In addition, the steric and chemical behavior of the ion and the neutral species is decisive for the cluster structure, size and strength [6, 13]. Chemical dependency is also evident for chemical reactions [8]. Furthermore, strongly accelerated ions lead to high-energy collisions, which can induce declustering and fragmentation reactions. These processes are summarized as CID [11]. Thereby, the inter- and intramolecular bonds are broken according to the binding energy. In many cases, the declustering process occurs first [2].
Each interaction influences the behavior and properties of the charged species such as the *molecular mass m* [1] or the *collision cross section* (CCS) [14, 15]. Especially in *atmospheric pressure ionization* (API), as it is widely used in mass spectrometry, a large number of collisions and, consequently, interactions occur [16]. Moreover, analytical methods

based on absolute ion mobility, such as *ion mobility spectrometry* (IMS) [17] and *high kinetic energy ion mobility spectrometry* (HiKE-IMS) [18], or on differential mobility, such as *differential mobility spectrometry* (DMS) [4], are strongly influenced by these interactions.
In addition to the unintended, mostly unavoidable effects, these interactions are used and controlled in a targeted manner to manipulate chemical systems in a desired direction. Thus, clustering via chemical modification of the drift gas is an important and common method in DMS [5, 6, 19–25] and is well known in IMS [14, 15, 26–29]. In both cases, an understanding of the chemical system is critical for the interpretation of the resulting spectra.
The comparability of the results (e.g., of different analytical methods such as MS, IMS and DMS or of one method with different settings) depends mainly on the comparability of the system parameters (e.g., background pressure and temperature). A frequently consulted value in this context is the *reduced field strength E/N*, which is defined as the ratio of the *electric field strength E* and the *gas number density N*. This parameter is a measure of the *kinetic energy* gained by a charged species between two collisions and so is particularly important for CID. The unit for *E/N* is *Townsend* (Td) [30].

$$1\ \mathrm{Td} = 10^{-21}\ \mathrm{Vm}^2 \tag{1.1}$$

The variation of a single parameter such as the temperature, the pressure, the chemical composition of the gas phase or the applied electric field, can alter the chemical dynamics in the observed system.
There are also further interactions of ions in the gas phase, for example, with other ions (e.g., recombination), with surfaces or with photons [1]. These kinds of interactions are not described or investigated in detail in this work.

1.1.1 Cluster dynamics

By using analytical methods that operate at least partially at *atmospheric pressure* (AP) or at only slightly reduced pressure (low to medium vacuum), complete avoidance of chemical contaminations of the basically inert matrix gas is nearly impossible. Even a high purity system is contaminated under non-laboratory conditions (e.g., by the sample introduction) [2]. In particular, the experimental creation of a completely water-free setup is hardly feasible, and a small number of water molecules H_2O is always present. In presence of a cation M^+ (e.g., a protonated analyte or H^+), clusters can be formed [2]. Thereby, intermolecular bonds are created between the charged species and the polar water molecules. The energy released in the process is removed by an *impact partner* IP, which can be, for example, a background gas particle [7]. A cluster grows through a sequence of these kind of reactions [7, 31].

$$\mathrm{M}^+ + m\mathrm{H_2O} + \mathrm{IP} \rightarrow [\mathrm{M} + (\mathrm{H_2O})_m]^+ + \mathrm{IP} \tag{R 1.1}$$

This process would lead to an uncontrolled cluster growth if there were no counter-reactions. In fact, there are declustering reactions. Typically, molecular cluster systems are destroyed by collisions with other IPs (CID; see Section 1.1.3) [2].

$$[\mathrm{M} + (\mathrm{H_2O})_m]^+ + \mathrm{IP} \rightarrow [\mathrm{M} + (\mathrm{H_2O})_n]^+ + (m-n)\mathrm{H_2O} + \mathrm{IP} \qquad \text{(R 1.2)}$$

The cluster strength, which depends on the binding energies in the cluster, must be exceeded to achieve a declustering process. Besides the polar clustering species, chemical characteristics (e.g., the charge distribution) or molecular geometry of the ion are important [13]. This results in preferred and less preferred cluster structures. From the equilibrium of the clustering process and CID results a mean cluster size *n*. It is important to note that only in limited cases is just one cluster size present [3, 18]. Instead, a cluster distribution can generally be observed. The shape of the distribution depends significantly on chemical and physical conditions.
Already in the 1960s, Kebarle et al. experimentally demonstrated the humidity and temperature dependence of the mean cluster size of protonated water clusters $[(H_2O)_n+H]^+$ [3]. Numerically, investigations could qualitatively confirm these dependencies [18, 32]. The clustering reaction is amplified by increasing the water mixing ratio [3, 18], while increasing the energy and/or number of impacts (e.g., by increasing the electric field, the pressure, or the temperature) amplifies the declustering process and a decreasing *n* [3, 18, 32].
Besides water, various species such as other *solvent molecules* S can be part of the chemical system. These can either be contaminations, for example, from the sprayed solution (e.g., from an upstream *liquid chromatography* (LC) system [2]) during *electrospray ionization* (ESI), or have been deliberately added to the matrix gas [5, 6, 14, 15, 19–29]. An additional cluster system is created that behaves equivalently to the water cluster system. In addition, a combined cluster system is also created.

$$\mathrm{M^+} + m\mathrm{H_2O} + aS + \mathrm{IP} \rightarrow [\mathrm{M} + (\mathrm{H_2O})_m + \mathrm{S}_a]^+ + \mathrm{IP} \qquad \text{(R 1.3)}$$

Declustering of a mixed cluster system also occurs via CID. The relative mixing ratios are decisive in addition to the parameters discussed above. Such complex cluster systems are therefore very sensitive to variations in the chemical composition of the system or of *E/N*, as shown by Erdogdu et al., for the distribution of a mixed water-acetone cluster system [33]. It should be noted that the cluster dynamics of anions are comparable; however, only positively charged species are considered in this work, and negatively charged clusters are not discussed.

1.1.2 Chemical reaction

Thermal collisions between ions and neutral species can lead to a series of chemical reactions [1, 8]. Besides reactions that are well known from the liquid phase, typical gas-phase reactions also occur. In particular, reactions that are essential in ionization such as proton or charge transfer reactions often govern the analytical result.

Most ionization methods at AP do not directly ionize an analyte. Instead, charge is generated on a reagent species and then transferred to the analyte. A typical reagent in *atmospheric pressure chemical ionization* (APCI) is nitrogen. The positively charged nitrogen species (charged, e.g., by a corona discharge) reacts with other species (e.g., water or methane) in a reaction cascade to form a protonated species (e.g., H_3O^+ or CH_5^+), which can protonate the analyte M (see *Atmospheric pressure chemical ionization*) [34–36].

$$M + H_3O^+ \rightarrow [M + H]^+ + H_2O \qquad \text{(R 1.4)}$$

This kind of protonation requires that the *proton affinity* (PA) of the analyte is higher than that of the reagent (water in reaction 1.4). Otherwise, a proton transfer is not possible [34–36]. In the next step, the protonated analyte $[M + H]^+$ can protonate other species with higher PAs (e.g., solvent clusters [37]). Therefore, a contamination with a higher PA compared to the analyte can prevent the entire analyte signal.
Multiple charged ions as a result of ESI are very typical in the field of proteomics, and charges in the mid two-digit range are not uncommon [38]. Such ions in combination with neutral species exhibit a phenomenon known as supercharging. The addition of a modifier in a mixing range of about 100 ppmV up to a few volume percentages into the gas phase leads to a charge depletion or a charge retention (depending on the chosen modifier) [37]. Numerical simulations show that this effect is related to an increased PA of large solvent clusters, which are typical for protic solvents [13].
Overall, if ions undergo chemical reactions with neutral species, this usually has major effects on the observed spectra, regardless of the analytic method. Similar to the clustering effects discussed above, those can be used or prevented by a deliberate manipulation of the chemical and physical conditions of the reaction system (e.g., addition of a modifier).

1.1.3 Fragmentation

In addition to the formation of covalent and intermolecular bonds, those can also be broken as a result of high-energy collisions (CID) of the ion with neutral species. In this process, the internal energy of an ion is increased until it becomes instable, and bonds break. The relative velocity of ions and neutral species to each other must be observed for this, and therefore the center of mass framework is typically used [9]. In this section, the focus is on the kinetic energy of accelerated ions, which is directly related to the collision energy in the center of mass framework [9].
A distinction can be made between high-energy and low-energy collisions [9, 12]. High-energy collisions of ions with a kinetic energy in a range of keV can lead to a dissociation as a result of only one collision. Thus, the ion is activated, and before the excess energy can be released (e.g., by a deactivating collision), a unimolecular dissociation results in *o* fragments F_x [9, 11].

$$M^+ + IP \rightarrow M^{+*} + IP \rightarrow {F_1}^+ + F_2 + \cdots + F_o + IP \qquad \text{(R 1.5)}$$

Without high-energy collisions, this two-step mechanism does not occur. In this case, the dissociation energy, which is needed to break bonds, can be picked up gradually by low-energy collisions. These collisions of ions with a kinetic energy in the range of a few eV up to a few hundred eV [9, 11] lead to either a stepwise dissociation or a stepwise activation followed by a fragmentation of the sufficiently activated ion [11]. As the dissociation energy is gradually achieved, weak bonds, such as intermolecular bonds from cluster formations, typically break first [2, 9]. Both kinds of CIDs cause different fragmentation patterns [12].

Decisive for the kinetic energy of an ion is the electric field strength *E* of the acceleration field and the acceleration time between two collisions. The acceleration time depends on the CCS and the gas number density *N*. There is an anti-proportional relationship between the resulting collision number and the acceleration time of the ion. In addition, there is a proportional relationship between the acceleration time and the kinetic energy [16, 39]. The already introduced *E/N* combinates both the electric acceleration of the ion and the number of collisions with neutral species. Depending on these, high-field (> 10 Td) and low-field (< 10 Td) conditions can be defined [4].

Without any added electric field, the kinetic energy of an ion depends on the *thermal temperature T*, but by increasing *E/N*, the electric acceleration increases the average kinetic energy of the ions. For moderate electric accelerations, this enables the definition of an *effective temperature* T_{eff}, which considers the additional acceleration. It is the sum of the thermal temperature and the *temperature by electric heating* T_{h} [30].

$$T_{eff} = T + T_h \tag{1.2}$$

In addition to the formation of unavoidable fragmentations, CID can be used to classify chemical bonds, which is crucial for *tandem mass spectrometry* (tandem MS or MS^n) [1, 10–12, 40, 41]. Ion species are accelerated in a low-pressure area to create high-energy collisions with an inert gas. The fragments resulting from CID are interpreted for the determination of the original ion. This is a common process in structure clarification of large analytes like proteins or other natural products [12, 40, 41] but also of smaller charged species such as clusters or complexes [12, 42]. Targeted CID is also used to determine and classify bond strengths [37, 42]. Furthermore, the CID of a clearly understood chemical system is utilized to investigate the energetic situation, for example, during ionization [43] or another analyzing step [44].

Fragmentation via CID is also influenced by other types of interactions. For example, previous results indicate large cluster structures can significantly prevent an ion from undergoing CID [45].

1.1.4 Thermodynamic versus kinetic control

The combination of all interactions results in a complex and potentially sensitive reaction system. Depending on the behavior of the individual reactions (e.g., reaction rate constant),

the retention time and the collision number, a chemical reaction system can be thermodynamically or kinetically controlled. For the interpretation of such a system and the resulting spectra, it is crucial to determine if the chemical system reached the thermodynamic equilibrium or not. The minimal resident time of ions in commercial AP ion sources is in the range of a few milliseconds [46, 47], while the exact resident times depend on the source design and the gas dynamic and can increase up to a few hundred milliseconds. If the resulting number of collisions is sufficient, then a thermodynamic equilibrium is reached under these conditions, and the thermodynamically most stable species can be observed [48]. With a shorter resident time or a significantly reduced number of collisions, slow reactions do not reach equilibrium, and the system is kinetically controlled. Caroll et al. have illustrated a dependence of the resulting spectrum on the ionization position and the resulting reaction time of the ions in APCI-MS [35], which demonstrates such kinetic control. Decreasing the pressure can also generate a kinetically controlled reaction system, as shown by Kroll et al., for a protonation reaction in a plasma-based ion source [49]. Cluster reactions also display a strong dependence on the ambient pressure with respect to thermodynamic or kinetic control [50].
In summary, investigations of the same reaction system under comparable energetic behavior with different analytical methods can provide totally different results as a consequence of the thermodynamic or kinetic control.

1.2 Mass spectrometry

The aim of mass spectrometry is the ion separation dependent on the *mass-to-charge ratio m/z*. Thereby, ions include every charged species such as charged atoms or molecules but also charged clusters [51]. Based on first explorations of the motion of ions in an electromagnetic field dependent on the *m/z* ratio (Thomson [52]), mass spectrometry has developed into one of the most important tools with applications in nearly all scientific and medical fields [51]. Typically, the process occurring in mass spectrometry can be divided into three main sections: ionization, analyzation, and detection.
Ionization methods can be classified by the background pressure presented in the ionization area. Traditional ionization methods such as *electron ionization* (EI) or *chemical ionization* (CI) operate at significantly reduced pressure compared to atmospheric conditions, which often leads to various vacuum problems (e.g., due to leaks) [9], but interactions in the gas phase can be minimized. Currently, many commercial MS systems operate with an ion source under AP conditions (see Section 1.2.1). In this case, the ions must be transferred from the AP area into the high-vacuum area of the mass analyzer. The low-pressure condition is necessary for the mass analysis as collisions would disrupt the process. In the ion transfer, the combination of a reduced pressure and a relatively high E leads to high *E/N* ($T_{\mathrm{eff}} >> T$). Therefore, in fragmentation reactions due to CID are well known in these areas [2].
There is now a wide range of different mass analyzers available for ion separation (e.g., *time-of-flight mass spectrometer* [Tof-MS] and *quadrupole ion traps* [QIT]), which can be

adapted to the respective measurement conditions [51]. For this work, a triple quadrupole mass spectrometer was used (see Section 1.2.2).
The ion detection often happens using a *secondary electron multiplier* (SEM) or a channeltron, which uses the ions to generate free electrons. These are multiplied by accelerating, hitting another surface, and releasing more electrons until an observable charge is generated. Classic and simple *Faraday cups* are also still used [51].

1.2.1 Atmospheric pressure ionization mass spectrometry

Atmospheric pressure ionization mass spectrometry (API-MS) is very susceptible to the interactions discussed in Section 1.1 in the AP area. Low-field conditions (collision-dominated situation) are usually present in the AP area of the ion source due to the high particle density and the collision frequency [39]. Through an electrical focusing with skimmer systems, ion funnels or similar devices [2, 16] and simultaneous pressure reduction (often in several pressure stages), ions can reach high kinetic energies in the ion transfer. Thinius et al. have depicted the pressure dependency through numeric investigations, which show a shift of the *kinetic energy distribution* (KED) from a partly collision-controlled situation to a pure acceleration effect in the pressure range between 1 Pa and 0.001 Pa [39]. In the transfer stage, extremely high-field conditions can be achieved. However, under high to ultra-high vacuum conditions and a resulting lack of collisions, direct interactions with other particles are insignificant. Nevertheless, in the first transfer stages, where collisions are still relevant, fragmentation and declustering reactions occur and must be considered in the interpretation of the resulting spectra [53].
Typical API methods, besides ESI and APCI, also include newer methods such as *atmospheric pressure laser ionization* (APLI) [9, 51].

Electrospray ionization

Even though ESI is one of the most-used ionization methods in modern proteomics, the underlying mechanism has not yet been completely clarified. First, the classic and commonly proposed mechanism is explained.
In the first step, ions are generated in the liquid phase of an analyte solution being pumped through a capillary [9, 16]. By applying a high voltage of a few kV on the thin capillary, a high electric field is generated at the tip. A field gradient of about 10^6 V/m [54] is typical with the MS inlet as a counter-electrode. As a result of the strong electric field, a charge separation in the liquid phase is generated. The charged species with opposite polarization compared to the inside wall shift to it, while the other charges gather at the surface, where a so-called Taylor cone is formed [9, 16, 54]. Subsequently, the tip of the cone becomes instable due to the high charge density, and small, charged parent droplets are ejected from the cone. This process can be supported by the injection of gas or liquid flows to the tip of the needle [16, 54]. A commonly accepted mechanism of the release of ions from a parent droplet is a combination of evaporation and fission. Accordingly, the solvent in the parent droplet evaporates in the AP area (auxiliary gases and elevated temperatures support this

process) until the charge density in the shrunken droplet is sufficient to make the system instable. This is the case when the *Rayleigh stability limit* is reached. By a fission of the droplet called a *Rayleigh explosion* or *Coulomb explosion*, the instable situation is resolved, and significantly smaller charged droplets are generated [9, 16, 38, 54]. A cascade of such events can occur until bare ions are released from an offspring droplet, for which two possible mechanisms have been proposed: The *ion evaporation model* (IEM) assumes that ions are evaporated as bare ions from the surface of extremely highly charged, small droplets (> 10 nm), while the *charge residue model* (CRM) assumes ion release by total evaporation of solvent from the smallest droplets in the AP area [9, 54]. A combination of both cases, depending on the analyte, is also possible. Both theories have in common that almost bare ions leave the AP area.
In recent publications, however, more results have been presented that cast doubt on the mechanisms known in literature. While the classic literature assumes parent droplets with a radius in the order of about 1 µm [9], several publications have identified significantly larger droplet radii in the range of a few µm to about 100 µm depending on the spray conditions and sprayed solution [55–58]. Additionally, there are signs of a long lifetime in the range of a few hundred milliseconds [58], which would allow the droplets to pass the AP area. Accordingly, these significantly larger droplets do not completely release the ions in the AP area and potentially reach the transfer stage of the MS. Kang et al. have reported significant contamination in the transfer stage of a commercial TripleQuad system due to the continuous operation of an ESI source [59]. The degree and speed of contamination clearly indicate the ingress of nanodroplets. Based on these results, Markert et al. have observed signs of highly charged nanodroplets from ESI processes in several API-MS systems with various inlet systems [60]. This observation does not appear to be system-specific but method-specific, and the mechanism explained above must be extended or at least adapted accordingly.
A particular ESI version is nanoESI (or nESI) with a reduced liquid flow compared to classic ESI. While a classic ESI source operates with a typical flow rate of about 5 µL/min [9] (even significantly higher flow rates are possible), a nanoESI source is characterized by a working flow rate of 1 to 1000 nL/min [16]. This could lead to much smaller parent droplets in the range of about 0.15 µm [54] and a Taylor cone that behaves rather ideally [16].

Atmospheric pressure chemical ionization

The term APCI includes all ionization methods starting from an ionized precursor species, which transfers the charge on the analyte by chemical reactions (intermediate steps are possible). In contrast to ESI, ions are generated in the gas phase [16], so charged nanodroplets should be irrelevant for this ionization method. An ^{63}Ni source or a point-to-plane corona discharge can be used to generate the primary charge [2]. Depending on the matrix gas and the source of the primary charge, the ionization mechanism can largely differ in some cases. Here, the initiation by a corona discharge in nitrogen is discussed.
A corona discharge is created at the tip of a sharp needle, to which a high electrical voltage (> 5 kV [9]) is applied, and typically a plane is used as a counter-electrode. An extraordinarily strong electric field is generated at the tip, which leads to a relatively weak discharge

(plasma) [61]. During this process, free electrons e^- are released. Through collisions with nitrogen N_2, further electrons are ejected, and the resulting nitrogen cation N_2^+ can react with another nitrogen molecule to form N_4^+ [9, 34].

$$N_2 + e^- \rightarrow {N_2}^+ + 2e^- \quad \text{(R 1.6)}$$
$${N_2}^+ + 2N_2 \rightarrow {N_4}^+ + N_2 \quad \text{(R 1.7)}$$

In the presence of water, charge transfer occurs with a subsequent protonation of water and the formation of protonated water clusters $[(H_2O)_n{+}H]^+$ (dynamic cluster equilibrium, as described in Section 1.1.1) [9, 34].

$${N_4}^+ + H_2O \rightarrow N_2 + {H_2O}^+ \quad \text{(R 1.8)}$$
$${H_2O}^+ + H_2O \rightarrow {H_3O}^+ + OH \quad \text{(R 1.9)}$$
$${H_3O}^+ + mH_2O + IP \rightarrow [(H_2O)_{m+1} + H]^+ + IP \quad \text{(R 1.10)}$$

Depending on the humidity, reaction 1.4 leads to a proton transfer on the analyte M (low humidity). Alternatively, a proton and ligand transfer from a water cluster to the analyte can occur [34, 62].

$$[(H_2O)_n + H]^+ + M \rightarrow [M + (H_2O)_b + H]^+ + (n-b)H_2O \quad \text{(R 1.11)}$$

The cluster-size-dependent PA (increasing PA with increasing mean cluster size) is important here, which is why a certain humidity limit should not be exceeded [36, 63]. Through a targeted declustering by reaching a critical *E/N*, less proton-affine cluster species can be generated. This method is known as *proton-transfer reactio*n (PTR) and operates at over 100 Td to generate bare ${H_3O}^+$ as a result of CID [63].

Atmospheric pressure laser ionization

The same as *atmospheric pressure photo ionization* (APPI), APLI is based on the interaction of molecules with electromagnetic radiation (photons). The absorption of photons by an analyte or possibly a precursor species is the basic principle of both methods.
Via positive APPI, short-wavelength, high-energy light is used to extract an electron from the analyte in the gas phase [9, 16]. Therefore, the energy of the emitted photons must be at least as high as the ionization energy of the analyte, which is in the range of about 10 eV for the most typical analytes [9, 64]. Similarly to APCI, the charge can first be generated on a precursor species and then be transferred by chemical reactions onto the analyte [64]. The photons are typically emitted by vacuum ultraviolet lamps [9, 16] and have wavelengths of about 124 nm [9].
Since, in this wavelength range, many typical matrix gases and contaminations also absorb, interfering side reactions and intensity loss can be observed [9, 65]. These problems can be solved with APLI, which uses a multi-photon approach for the ionization: the *resonance-enhanced multiphoton ionization* (REMPI) [9, 65]. In contrast to APPI, not only one photon

is needed for the ionization; instead, the analyte M is stimulated by one or more (*r*) photons in a first step [46, 65].

$$M + r\ h\nu \rightarrow M^* \qquad \text{(R 1.12)}$$

In a second step, the activated analyte is ionized with *s* photons, which release an electron [46, 65]. The combination of both steps describes the (*r*+*s*) REMPI process [65].

$$M^* + s\ h\nu \rightarrow M^{+\cdot} + e^- \qquad \text{(R 1.13)}$$

Further reactions such as deactivation, photodissociation or fragmentation occur [65] but are not discussed further at this point.
Compared to APPI, less energetic photons are needed for REMPI since the ionization energy does not have to be reached in one step. Instead, the photon density must be significantly higher to realize the ionization step before the activated species M^* is deactivated spontaneously or by collisions [9, 65]. The use of a laser system can generate the high photon density. This also results in the possibility of a spatially resolved and substance-specific selective ionization. Lorenz has proven the possibility of characterizing an API source with this method [46].

1.2.2 Triple quadrupole mass spectrometer

Quadrupoles are a widely used component in mass spectrometry. In addition to their use in ion transfer such as in the QJet ion guide from Sciex [66], they are also commonly used as a mass analyzer. Quadrupoles consist of four rod electrodes, which are positioned in a square. A *direct current* (DC) voltage and an alternating voltage with a frequency in the order of 1 MHz (→ *radio frequency* [RF] voltage) are applied to the rods, while the pairs of opposing rods are at the same potential. If an ion cloud is passed through the center of this structure, the electric field leads to a deflection of the ions, but due to an optimized tuning ratio of the DC voltage to the RF voltage, ions pass through a stable trajectory depending on the *m/z* ratio [67]. A systematic variation of the voltages ensures that only ions with specific *m/z* ratios can sequentially pass the quadrupole, which is used for mass analysis [51, 67]. By switching off the DC voltage (RF-only mode), a high-pass mass filter can be created [59, 60].
For a *triple quadrupole* (QqQ) mass spectrometer, three quadrupoles are connected in series. Traditionally, the first quadrupole (Q1) and the third quadrupole (Q3) are used as a mass analyzer, as described above, and the second quadrupole (q2) is used as a collision cell. Increased pressure of about $7 \cdot 10^{-3}$ torr [67] compared to the high vacuum in Q1 and Q3 exists here by adding a collision gas (e.g., N_2 or Ar) [51, 67]. As a result of the increased pressure, a significant number of collisions between the accelerated ions and neutral species occurs, and CID can be observed. Thus, a stepwise fragmentation and a structural investigation of the precursor ion are possible [12, 51, 66].

Therefore, the QqQ design offers several scan methods. In addition to classic MS investigations with only one quadrupole (Q1 or Q3), tandem MS can be used. Typical scan modes are the product-ion mode or the *multiple reaction monitoring* (MRM) mode [51, 66]. In the product-ion mode, the Q1 is set to one *m/z* ratio, and after a fragmentation in the q2, a full scan is performed in Q3. Thus, the fragmentation structure of a precursor ion can be detected [68, 69]. The *selective reaction monitoring* (SRM) mode is comparable, but here, too, the Q3 is set to the *m/z* ratio of a typical fragment ion, for example, to analyze a sample with high sensitivity on one specific analyte. This method can be used in proteomics to reduce the matrix signals, which allows an analysis of even trace substances [70]. An extension is the MRM mode, in which several analyte/fragment pairs are detected in a cycle to measure several analytes or one specific analyte by monitoring different typical fragmentation reactions [66, 69, 70]. Further scan modes such as precursor ion scans or neutral loss scans are also possible and are important in protein analysis [69].

1.3 Ion mobility

In addition to the *m/z* ratio, other substance-specific properties can also be used for ion separation. *Ion mobility K* is such a frequently used property, which is the proportionality factor between the *drift velocity* v_d of an ion and E applied to accelerate the ion. It can be calculated as a ratio of both [30, 71].

$$K = \frac{v_d}{E} \tag{1.3}$$

The decisive factor is the CCS. The larger the CCS, the more collisions between the ion and other species occur. Since the kinetic energy, and thus the drift velocity, depends on the number of collisions, an increased CCS leads to a decrease in ion mobility [26]. Even the background temperature *T* and the background pressure *p* have a noticeable influence on the ion mobility, so often the *reduced ion mobility* K_0 is determined. The absolute ion mobility is converted to *standard pressure* p_0 and *standard temperature* T_0, which leads to a value that is independent of both physical quantities [17, 30, 71–73].

$$K_0 = K \cdot \frac{p}{p_0} \cdot \frac{T_0}{T} \tag{1.4}$$

In the last several decades, different spectroscopic methods using the ion mobility for ion separation have been developed that differ strongly in their operating conditions (e.g., the working pressure) [4, 73, 74].

1.3.1 Ion mobility spectrometry

The classic spectrometric method using the mobility for ion separation is the traditional IMS. The basic principle is illustrated here with the ambient *drift tube IMS* (DTIMS) working under AP conditions or close to them [17, 26, 73, 75]. The same as a mass spectrometer,

an ion mobility spectrometer can be divided into three sections (see Figure 1.1): the reaction area, the drift tube, and the detector.

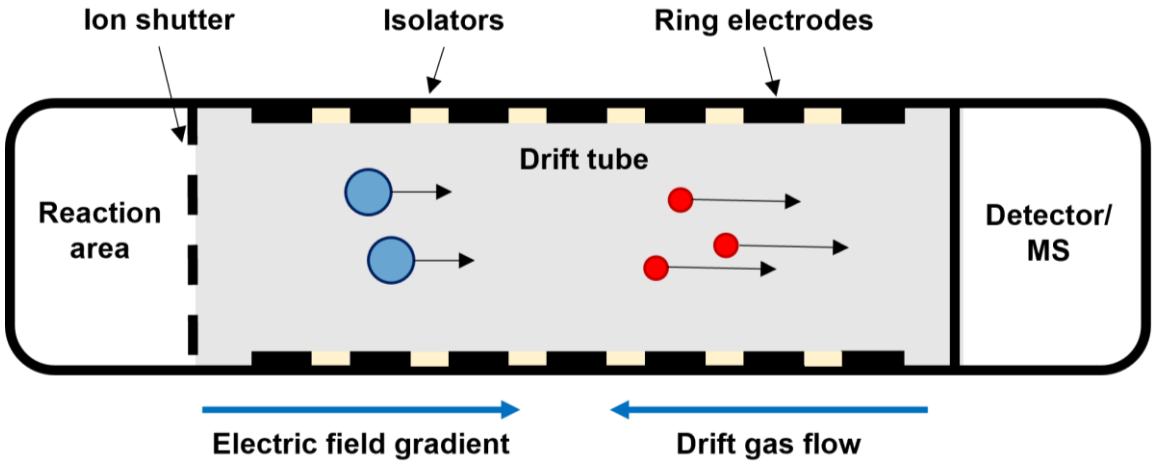

Figure 1.1: Schematic of a drift tube ion mobility spectrometer.

Ions are generated in the reaction area by an API source [71] (see Section 1.2.1). Before entering the drift tube, the ions pass an ion shutter, which "collects" a defined ion packet for the drift time measurement [71, 76]. The starting width, which depends on the drift velocity and the shutter time, is not identical for each species (a high mobility leads to a high starting width). Consequently, ions with a low mobility reach the drift tube in a lower proportion than ions with higher mobility. This leads to a kind of ion discrimination. Therefore, the shutter should be adapted to the measurement method to minimize this discrepancy [76]. Through the shutter, the ions reach the drift tube, although the shutter typically constitutes only about 1% of the time permeable for ions [71].

A uniform electric field in the drift tube moves ions through the drift tube. An ion mobility analyzer can have a different field geometry, while the linear electric field drift tube is the most common [71] and least complex method [75]. A linear electric field is generated by a series of ring electrodes, which are separated from each other by isolators (see Figure 1.1). The electric field accelerates the ions to a constant substance-specific drift velocity [14, 71]. Depending on the applied voltage gradient between the rings and the dimension of the drift tube, a linear electric field in the range of 5 to 100 V/cm [75] to several hundred V/cm is obtained [14, 26, 27, 71]. Due to the high pressure, E/N is relatively small (< 2 Td [75]), but some modern DTIMS systems operate with significantly different E/N than classic DTIMS instruments [17].

The electrical acceleration is opposed by a constant neutral gas flow (several 100 ml/min up to a few L/min [26, 27, 71]) in the direction of the ion source [71], which prevents neutral species from entering the drift tube. In addition, there are decelerating collisions depending on the CCS of the ion and the neutral species, which has a massive influence on drift velocity. A common drift gas is nitrogen [26, 27, 71].

The following ion detection is comparable to the detection in MS, but Faraday cups or plates are still much more widespread in IMS today [71]. Alternatively, a coupling with a

mass spectrometer is also a common method and provides a further dimension of ion separation with a manageable effort [74]. The drift velocity and thus the ion mobility (see Equation 1.3) can be calculated from the determined *drift time* t_d and *length of the drift tube* l_d.

$$v_d = \frac{l_d}{t_d} \tag{1.5}$$

The drift tube is typically 4 to 20 cm [71] long, but lengths up to 3 m are also used [75]. For classical IMS, the drift time is usually in the range of milliseconds [71].

Chemical modification in IMS

The chemical composition of the drift gas in IMS can influence the reduced ion mobility, just like the physical conditions. A completely water-free setting is not realizable under AP conditions using "dry" nitrogen as a drift gas [27], which means that cluster reactions cannot be totally suppressed even in IMS (see Section 1.1.1). An increased water mixing ratio in the drift gas leads to a shift to longer drift times for most ion mobility signals [14, 15, 26, 27]. Brachthäuser has clearly shown this humidity effect for the ion mobility signals of different solvent clusters [14], whereby an analyte dependence can be observed. Thus, the reduced ion mobility of the protonated acetone (ACE) monomer $[ACE+H]^+$ is already strongly dependent on variations of the humidity at a low level (low ppmV range), while that of the protonated ACE dimer $[(ACE)_2+H]^+$ is almost independent of the humidity, up to a water mixing ratio of about 80 ppmV [14]. The explanation for this observation is the clustering with water, which Izadi et al. have shown experimentally and numerically [27]. Increasing the water mixing ratio leads to an increasing mean cluster size and thus an increase in the CCS of the charged species. Since the mean cluster size also depends on the temperature, an increase in temperature leads to decreasing drift times [14, 15, 27]. Besides the typical contamination with water, other substances with a tendency to cluster formations in the gas phase can produce qualitatively identical results, as illustrated by de Gouw et al. [15]. Furthermore, a *T*-dependent cluster formation has been demonstrated by using CO_2 as a drift gas [77]. The uncontrolled clustering and the resulting influence on the reduced ion mobility are a challenge for analytical applications. While experiments under laboratory conditions can guarantee an almost constant gas composition, this is not the case for field experiments. A possible and applied solution for this challenge is a targeted chemical supersaturation (e.g., with ammonia) [78], which minimizes the influence of contaminations in the drift gas.

Chemical modification is also deliberately used in IMS to optimize ion separation [26, 28, 29]. If different species of an ion mixture have identical ion mobility within the limits of the measurement errors, then an ion separation is impossible. The addition of a chemical modifier such as 2-butanol (2-BuOH) in the gas phase and the resulting clustering can lead to a different shift of the drift time for several analytes, as depicted by Fernández-Maestre et al. [26]. In this application, 2-BuOH offers itself as a sterically challenging, polar modifier that causes large CCS differences by clustering to an ion. Based on the analyte structure

and the cluster geometries, different average cluster sizes are formed. The resulting relative change of CCS due to cluster formation is crucial for the variation of the drift time [26]. The effect of chemical modification depends on the chosen modifier and the modifier mixing ratio, as shown by Roscioli et al. [28], who reduced the ion mobility of the protonated dimethyl-phosphonate (DMMP) monomer $[DMMP+H]^+$ up to 30.5% [28]. Thus, the addition of the right modifier in the correct mixing ratio to the drift gas can achieve ion separation that is impossible with pure matrix gas [28, 29].
Evidence of enantioselective cluster formations in the gas phase at IMS can also be found in the literature. Even small mixing ratios of enantiopure 2-BuOH as a modifier (low ppm range) should allow enantioselective separation [79]. This effect is discussed in more detail in Section 1.4.

1.3.2 High kinetic energy ion mobility spectrometry

The classic DTIMS operates under low-field conditions [75, 80] since the high collision rate at AP limits the kinetic energy of the accelerated ions. Thus, the reduced ion mobility is nearly independent of E/N [4, 71, 75, 81], and T_{eff} is increased only slightly by the electric field heating ($T_h < 5$ K) [30]. The reduced ion mobility becomes dependent on the electric field when higher E/N values are reached ($E/N > 80$ Td leads to a T_{eff} of hundreds K over T [82]). The field dependence of ion mobility in an asymmetric alternating electric field is used in analytical methods such as DMS and *high-field asymmetric-waveform ion-mobility spectrometry* (FAIMS; see Section 1.3.3) [4].
High-field conditions, in which field-dependent mobilities can be observed, would need field gradients in the range of kV/cm at AP and therefore voltages in the range up to a few 100 kV [71], which are not experimentally feasible. However, Langejuergen et al. [73] have indicate that the necessary E/N ranges can also be achieved for IMS systems by significantly reducing the pressure. *High kinetic energy ion mobility spectrometry* (HiKE-IMS) operates at a pressure of about 20 mbar, which allows ions to be accelerated for much longer time between two collisions. Even with experimentally possible voltages in the range of up to a few kV, high-field conditions with over 100 Td can be achieved [73, 83]. As a result, the drift time in HiKE-IMS is often in the range of under 1 ms. Based on a short residence time of ions in the drift tube and a low number of collisions, not every chemical system is able to achieve the thermodynamic equilibrium [18].
The HiKE-IM spectrometer used in this work is very similar in its basic structure to a classical drift tube ion mobility spectrometer (compare to Figure 1.1). It allows the observation and investigation of cluster dynamics, which has been experimentally shown and numerically confirmed by Erdogdu et al. [18, 33]. Furthermore, decreasing the mean water cluster size by increasing E/N in the reaction area allows the ionization of analytes with low proton affinity, which cannot be protonated by water clusters with a larger mean cluster size (PTR) [73]. Furthermore, a HiKE-IMS-MS coupling provides the chance to investigate the chemical systems underlying the individual signals in HiKE-MS spectra. First approaches in this direction were presented by Allers et al. [83].

1.3.3 Differential mobility spectrometry

The deviation of *E/N-dependent ion mobility K*(*E/N*) from *field-free ion mobility K*(0) is defined by the *E/N*-dependent α value.

$$K\left(\frac{E}{N}\right) = K(0) \cdot \left[1 + \alpha\left(\frac{E}{N}\right)\right] \tag{1.6}$$

Under low-field conditions (*E/N* < 10 Td [84]), α is nearly 0, which means that under these conditions, *K*(*E/N*) is almost identical to *K*(0) [4, 30, 82, 84]. The differential between ion mobility at two different *E/N* conditions (at least one must be high-field condition) is a substance-specific property, which is used for ion separation in DMS. Buryakov et al. presented this application in 1991 [85].
The first section of a DMS system is an API source, from which the ions are transferred into the actual DMS cell, which is also operated under AP conditions (see Figure 1.2).

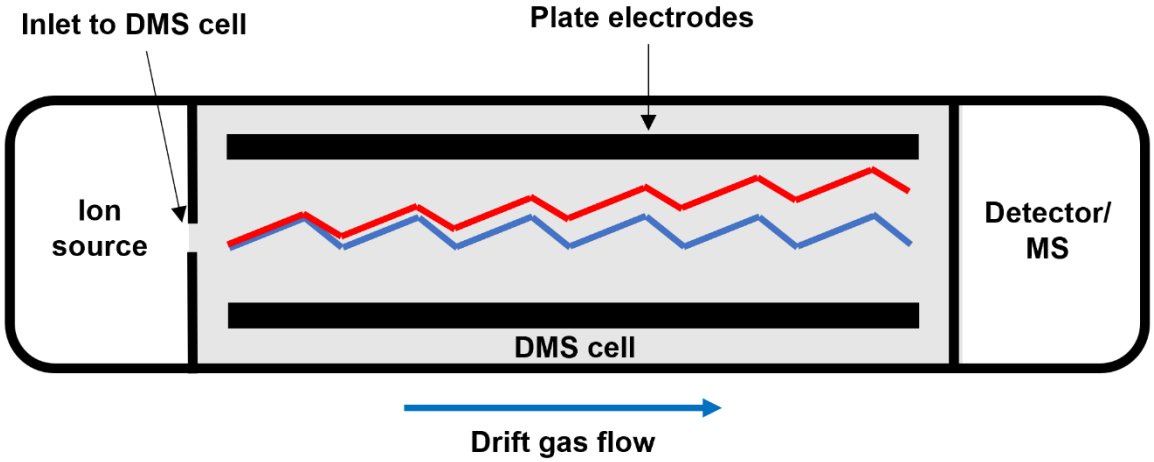

Figure 1.2: Schematic of a differential mobility spectrometer.

Since ion currents instead of ion packages are continuously separated in DMS [4], no electric ion shutter is needed. A DMS cell consists of two planar electrodes between which the ions are transported by a gas flow [4, 30, 82, 85, 86]. If no voltage is applied, all ions pass the cell, and only diffusion losses can be observed. For ion separation, an alternating electric potential called *separation voltage* (*SV*) is applied to the electrodes. *SV* is an alternating voltage, which is asymmetrical in time and in level (peak-to-peak voltage) and generates an alternating electric field with two different electric field strengths, which are separated from each other in time. The temporal section with a higher field strength is called high field, while the other one is called low field [4, 30, 86]. It should be noted that these are relative classifications, which are not indicative of the actual field strengths.
In the DMS system used in this work, the *electric field strength of the low-field* E_{low} is half of the *electric field strength of the high-field* E_{high}.

$$E_{high} = 2 \cdot E_{low} \tag{1.7}$$

The field difference is compensated for by the time the respective field is applied. Thus, the *low-field time* t_{low} is twice as long as the *high-field time* t_{high}.

$$2 \cdot t_{high} = t_{low} \tag{1.8}$$

This basic structure of the electric field is realized by superimposing two sinusoidal curves with different frequency [4], which was described by Krylov in 1997 [87].
The electric fields accelerate ions orthogonal to their direction of movement through the DMS cell. The motions toward the electrodes cancel each other if the reduced ion mobilities in high and low fields are identical ($\alpha_{high} = \alpha_{low}$). In this case, a zigzag motion results, which is, on average, parallel to the electrodes (blue trajectory in Figure 1.2). At sufficiently high *SV*, the reduced ion mobility is field-dependent (at least in the high field), and the oscillating motion becomes unbalanced. Thus, a substance-specific ion drift to one electrode can be observed (red trajectory in Figure 1.2). In addition to the *SV*, a *compensation voltage* (*CV*; alternative: *CoV*) is added to the electrodes [4, 30]. This DC voltage compensates the ion drift to enable an ionic species to pass through the DMS cell. Therefore, the *CV* is a substance-specific property. The *CV* is scanned in an actual DMS measurement, while the passed ion current is recorded to determine a differential mobility spectrum. A high reproducibility was found for this method [21]. Equivalent to IMS, the ions enter the detector after the separation. Since the basic separation mechanism is orthogonal to the mechanisms of most other commonly used separation methods, coupling with other methods such as LC and/or MS is an obvious application.
The separation principle in FAIMS is identical to that in DMS, although cylindrical electrodes are used instead of planar ones [4].

Typical behaviors of the α-function

The α value as a function of *E/N* can be calculated by the substance-specific α-function [4, 30], which can be determined by solving Equation 1.6 for $\alpha(E/N)$. Thereby, most ions have an α-function, which can be assigned to one of the three main types: type A, type B and type C (see Figure 1.3). Depending on the type of the α-function, an ionic species is found in DMS at negative (type A) or positive (type C) *CV* values, or the *CV* values are negative at low *E/N* and become positive with increasing *E/N* (type B) [4, 30, 88].
An α-function of type A describes a continuously increasing α value with increasing *E/N*, which means that the reduced ion mobility increases with increasing *E/N*. This leads to a stronger motion to the electrodes during the high-field phases compared to the low-field phases and is often explained by cluster dynamics in the DMS cell [4, 5]. In the presence of cluster-forming neutrals (e.g., water), the mean cluster size and therefore the CCS are larger under a low field since declustering reactions by CID occur more frequently under high-field conditions (decreased mean cluster size). This effect of cluster formation in the gas phase (cluster effect) is often utilized to increase ion separation by the addition of appropriate chemical modifiers to the drift gas (see *Chemical modification in DMS*) [4–6, 19–21].

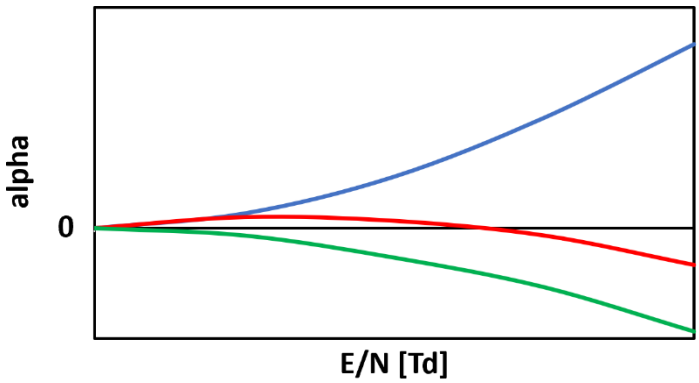

Figure 1.3: Qualitative traces of the three main types of the α-function; blue: type A, red: type B, green: type C.

Type C behavior is characterized by a continuously falling curve ($\alpha < 0$). Thus, the low-field mobility is higher than the high-field mobility, which can be explained by collisions and interactions of the ion with non-clustering background gas species. This effect is based on the higher collision energy under high-field conditions, which leads to a stronger deceleration of the ions. Here, the ions are considered as hard spheres comparable to billiard balls, which is why the effect is known as the hard-sphere effect (see *Hard-sphere effect*) [4, 30]. While the cluster effect depends on the presence of mostly polar cluster-forming species, the hard-sphere effect always occurs in DMS.
The third type (type B) can be interpreted as an intermediate stage of both other types. First, type A behavior is observed, but with increasing *E/N*, the presented curve starts falling. An explanation is a weak cluster strength, which leads to a cluster effect at low *SV* settings. As *SV* increases, the *E/N* in the low field also prevents a significant cluster growth. From this point, the cluster effect becomes weaker, while the hard-sphere effect becomes stronger and finally dominates [4]. Consequently, type A behavior corresponds to type B behavior, whereby the reversal point has not yet been reached, which has been demonstrated in previous work for Substance P as an analyte by increasing the *DMS temperature DT* [23]; additionally, Shvartsburg has come to the same conclusion [30].

Chemical modification in DMS

The addition of a chemical modifier to the drift gas and the active use of the cluster effect is a common principle in DMS. Therefore, commercial DMS systems often offer, by default, the option of adding a modifier to the drift gas [86]. Usually, modifier mixing rations up to the percentage range are used. The basic effect has been studied and described in literature many times (e.g., by Schneider et al. [19], Hopkins [5], Auerbach et al. [20] and Campbell et al. [6]) and is qualitatively identical to and independent from the investigated analyte-modifier combination: as a result of reversible cluster reactions, a signal shift to lower *CV* values can be detected. As a result, a switch of the α-function from type C to type A or at least to type B in the classically examined *SV* area can be forced [19].
The magnitude of this effect depends on physical properties such as the *DT* in the DMS cell (see *Temperature effect in DMS*) and chemical and structural properties of the ion and

modifier. Therefore, the effect of a modifier is quantitatively different for each analyte and can be different for one analyte in various protonation stages. An example for an analyte is shown in Figure 1.4. The signal of the triply protonated species of Substance P (blue) is shifted significantly stronger to a lower *CV* value than the signal of the doubly protonated species (red) by adding acetonitrile (ACN) to the gas phase of the DMS cell.

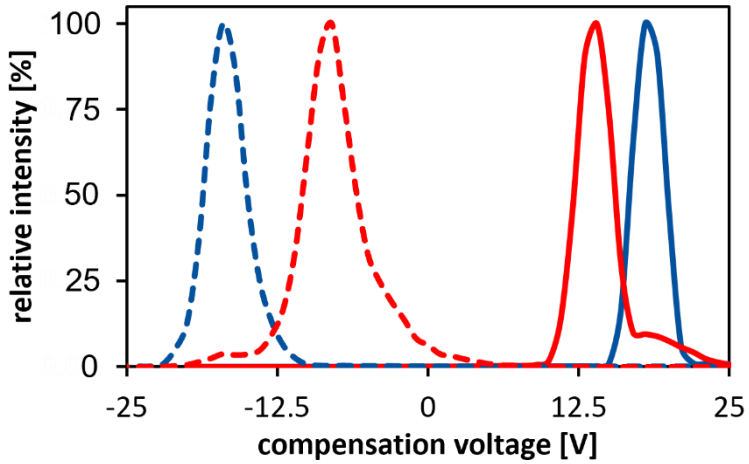

Figure 1.4: Typical effect of chemical modification in DMS on doubly (red) and triply (blue) protonated Substance P recorded with and without gas-phase modifier (3%) present in nitrogen (*SV* = 4000 V; *DT* = 150°C). Solid: pure nitrogen; dashed: ACN.

A variation of the chosen modifier indicates the expected quantitative influence [23]. By a variation of the added modifier, the cluster effect can be adjusted, and thus the ion separation can be optimized, as shown by Schneider et al. [21]. Besides the functional group and the electrical *dipole moment* μ_D of a modifier, which are necessary for the strength of intermolecular bonds to the ion (clustering), other parameters such as the cluster structure and the size of the modifier have a discernable impact on the strength of the cluster effect and thus on the differential mobility [6, 22]. Larger modifiers such as 2-propanol (IPA) can lead to a stronger effect than smaller modifiers with the same polar group, such as methanol (MeOH) [6, 20, 23, 25]. This steric dependence is systematic and therefore predictable within certain limits. Auerbach et al. [20] have predicted the *CV* values of a wide range of analytes without complex numerical simulations but with the use of comparative measurements. By using primary alcohols with a carbon chain length between 1 (MeOH) and 4 (1-Butanol) as modifiers and parameters such as the gas-phase acidity, a linearization of the results could be demonstrated. This allowed a subsequent prediction of omitted measurements with extremely high accuracy (deviation mostly about 0.5 V or less) [20]. Comparable qualitive dependencies are also evident in the analyte structure. The influence of the steric shielding of the charge on the bonding energy and therefore on the cluster formation and the cluster effect was demonstrated experimentally and numerically by Campbell et al. investigating systematic analyte systems such as R_4N^+ [6].

Kafle et al. have demonstrated an increasing cluster effect on two deoxyguanosine adducts of DNA by increasing the modifier mixing ratio for different modifiers [22]. However, the strength of the cluster effect increases more slowly with an increasing modifier mixing ratio. A possible interpretation is that the relative change of the CCS from adding a modifier molecule to a cluster becomes smaller with an increasing mean cluster size induced by high modifier mixing ratios. In addition, several saturation effects were reported, which may indicate a maximum cluster size for at least some analyte-modifier combinations [22]. Furthermore, the experimentally investigated cluster effect was confirmed numerically and qualitatively reproduced for the water-cluster system by Erdogdu et al. [24].

Hard-sphere effect

In the presence of a modifier, the hard-sphere (or hard-shell) effect is often superimposed with the cluster effect; nevertheless, it is always part of the ion separation with DMS. Compared to the chemical cluster effect, the hard-sphere effect is more a physical phenomenon that can be rationalized with the model of ions as hard spheres. Crucial for this effect are the collisions of ions with neutral species and the resulting trajectories of both, which depend on *E/N* [30]. A collision leads to a deceleration and can cause a rebound of the ion, which is enhanced by increasing the kinetic energy, for example, due to an increased acceleration field [4].
At low *E/N*, T_{eff} is close to *T* ($T_{eff} \approx T$). Thus, the velocities of the neutral species and the ions are approximately thermal. However, in high-field conditions, T_{eff} is significantly higher than *T* ($T_{eff} >> T$). In the resulting high-energy collisions, the uncharged thermal particles behave like a solid wall for the accelerated ions, which effectively bounce off [30]. As a result, the reduced ion mobility decreases with an increasing acceleration field [4]. This causes an α-function of type C and positive *CV* values in DMS spectra. In summary, the hard-sphere effect is based on the significantly higher velocity of the accelerated ions compared to the neutral collision partners so that *T* becomes irrelevant for kinetic energy of the ion, which should therefore be independent from *T* [30].
If the drift gas is polarizable, the hard-sphere effect is weakened due to countereffects. This is the case, for instance, with the commonly used nitrogen but not with helium, which is why Schneider et al. [19] could experimentally show a stronger type C behavior by adding helium as a drift gas to the otherwise pure nitrogen. The polarized nitrogen can interact with ions and leads to an effect comparable to the cluster effect. Increasing the helium concentration decreases these interactions and supports the type C behavior. A temperature effect on the interactions of ions with polarized nitrogen cannot be excluded.

Temperature effect in DMS

In addition to T_{eff}, the background temperature of the matrix gas also has an influence on the processes occurring in DMS. In IMS, an increasing temperature leads to a decreasing mean cluster size. Since the cluster effect is often relevant in DMS, an influence of the temperature in the DMS is generally expected and is also known from experiments [22–25].

In the presence of a strong modifier (type A behavior), a variation of the temperature leads to a variation of the *CV* values observed. Previous experiments have suggested that the cluster effect is usually weakened by increasing temperature, which leads to a rise in *CV* values [23]. Depending on the investigated chemical system, even change of the qualitative type of the α-function can be observed [23, 25]. The strength of the temperature effect in DMS depends on the modifier [23] and the ion [89]. Thus, Schneider et al. have demonstrated the influence of an increase in temperature on the cluster effect of IPA on different analytes. This can lead to both an increase and a decrease in *CV* values depending on the chemical system [89]. This observation is probably due to the complexities and interplay of different effects in differential mobility.
The effect of the temperature in DMS was also confirmed by numerical simulations [22, 24, 32]. Kafle et al. have illustrated the reduction of the mean cluster size through increasing temperature. These simulations prove a clear temperature dependence for weak electric fields, while this effect decreases with increasing electric fields [22].
Therefore, a reproducible temperature is crucial for DMS experiments. The temperature of the DMS system can be controlled by the matrix gas, which is heated before entering the DMS area. This heating method causes a temperature gradient across the DMS cell [4, 24], which causes different *CV* values for the same species at different positions in the cell. Accordingly, the measured *CV* values are mean *CV* over the temperature range. This is important for interpretations and simulations but not for the application since the temperature profile is reproduceable. Due to a typically circular gas inlet and a rectangular cross-section of the DMS cell, temperature gradients in both directions can also be assumed in the plane, and a complex, three-dimensional temperature profile is obtained.
Other DMS parameters such as the dimensions of the cell or the associated residence time also have an influence on the ion separation or at least on the resolution in DMS [4]. Thus, reducing the working pressure leads to a strong influence on the *CV* values and intensity fluctuations, as shown by Nazarov et al. [84]. However, these parameters remain unchanged in this work and are therefore not discussed in detail.

1.4 Enantioselective analysis

One challenge of modern analytics is the enantioselective analysis of chiral molecules. It is used in various scientific subfields such as geology and medicine [79, 90], and so it is a fundamental tool in science. Particularly in pharmaceuticals, chiral control becomes increasingly important with the growing proportion of chiral ingredients. Often, only one enantiomer acts as active species, while the other is inactive or, in the worst case, dangerous. The thalidomide crisis at the end of the 1950s clearly highlights the necessity of such controls [90].
Enantiomers are equal in most properties (e.g., mass and CCS), which makes an enantiomeric separation impossible or at least very difficult with most common analytical methods. For this purpose, standard reference substances are used, which interact differently with both enantiomers. According to the three-point rule, at least three independent interactions must occur between the analyte and the reference substance, from which at least

one is different for both enantiomers to achieve two distinguishable formations [90, 91]. A classic method for enantioselective separation is chromatography with a chiral stationary phase. Meanwhile, there is a large range of chiral stationary phases for liquid and gas chromatography, which can be adapted structurally and in terms of the intrinsic binding mechanism [92].

In addition, there are increasing efforts for achieving an enantiomeric separation using methods such as IMS or MS. Metal complexes with reference ligands are a widely used approach. The addition of an M^{II}-salt (M = Cu, Ni, etc.) and a chiral, enantiopure reference substance (usually an amino acid) to the analyte solution of an amino acid with unknown enantiomeric composition $^{L/D}$AA generates $[M^{II}(ref)_2(^{L/D}AA)\text{-}H]^+$ complexes via an ionization with ESI [42, 93–95]. The structures are different for ^{L}AA and ^{D}AA, which is due to the various diastereomeric interactions with the referent ligands, which influence the CCS. Using this method, enantiomeric separation could be demonstrated with IMS [93] and FAIMS [94]. The CID in tandem MS leads to the cleavage of a ligand, resulting in a mixture of $[M^{II}(ref)_2\text{-}H]^+$ and $[M^{II}(ref)(^{L/D}AA)\text{-}H]^+$. The mixing ratio depends on the binding energies of the ligands, which is different for each enantiomer of the analyte, and the concentrations of the different ligands. This also allows the use of tandem MS for enantioselective investigations [95]. As an alternative to an M^{II}-salt, the addition of cyclodextrins leads to the formation of complex, enantioselective structures, as demonstrated by Lee et al. [96]. The addition of methylated β-cyclodextrin to a D- or an L-alanine solution causes the formation of non-covalent complexes by ionization with ESI. The structural difference of the complexes could be detected by IRMPD spectroscopy and have been confirmed by numerical simulations [96].

As an alternative to a modification of the analyte solution, the addition of a gas-phase modifier is also possible. It has been shown by Dwivedi et al. [79] that the addition of enantiopure 2-BuOH to the drift gas of an IMS system leads to enantioselective cluster formation. Even a modifier mixing ratio in the ppm range leads to an enantiomeric separation of several chiral analytes. The effect was even strong enough to achieve a clear separation of a racemic analyte mixture without further upstream preparation steps [79].

Finally, in addition to the direct stereoselective separation methods discussed here, enantioselective derivatization can also be performed, resulting in different product species. These can be separated by conventional methods, such as chromatography with an achiral stationary phase [92]. However, due to the upstream reaction steps, this method is generally more laborious than the other methods presented.

2 Aim of this work

As discussed in Chapter 1, several orthogonal and currently important analytical methods such as MS, IMS (both DTIMS and HiKE-IMS) and DMS are susceptible to interactions of ions with neutral species in the gas phase. These interactions are necessary or at least significantly influence each method. For this reason, a deeper understanding of those effects is crucial for the interpretation of spectra. These can be strongly influenced by adapting the physical and chemical conditions, such as the composition of the matrix gas, the temperature or the pressure. Particularly, the addition of a chemical modifier to the gas phase is an emerging method and is an established practice in IMS [14, 15, 26–29] and DMS [5, 6, 19–25]. It causes a clustering process, which can lead to a more effective ion separation, but due to contaminations, this effect also occurs unintentionally. In several analytical methods, increased reduced field strength is common, which has a strong influence on the spectra and must also be considered in the interpretation. The combination of all interactions leads to a complex chemical system that should always be included and ideally completely understood if new applications or adapted methods are to become established.

Therefore, the aim of this work is the investigation and understanding of mainly cluster dynamics under high-field conditions, which occur in the previously mentioned methods. A commercially available DMS-MS coupling (SCIEX, Ontario, Canada) [66, 86] and a HiKE-IMS, which was developed and manufactured at the Leibniz University Hannover (Germany) [73], are used for this purpose. Both setups allow the variation of several parameters to experimentally determine the influence on cluster dynamics and other interactions. The already extensive and often application-oriented literature on this subject area (especially in the field of DMS, publications on the cluster effect are numerous) shows the relevance of this topic.

In a first step, the influence of the ion structure (e.g., the CCS or possible shielding of the charged position) on the ion separation in DMS is determined (Chapter 4). Therefore, a series of analytes with the same functional group (amines and diamines) is investigated in combination with common modifiers. Furthermore, the influence of multiple charging on the cluster formation and thus on the cluster effect in DMS is examined on a series of linear diamines. The combination of the ion structure, the charge level and the added modifier

should significantly influence the mean cluster size as well as the cluster structure. Therefore, a structural impact of the ion structure on the cluster effect, and thus a *CV* trend in connection with the ion size, is expected. This would allow predictions to be made about the expected *CV* values of ions by extrapolation of the *CV* values of other ions with comparable structures.

In the next step, the actual clustering and declustering process is explored using HiKE-IMS (Chapter 5). The dynamic of cluster systems dependent on the reduced field strength should be investigated on various samples. Thereby, the water cluster system interacts as a benchmark, and a selection of common solvents, which are also used as common modifiers in DMS (e.g., MeOH and ACN), are used as actively added analytes. By increasing the reduced field strength, the declustering process of large cluster species is observed, and the impact of the humidity, the background temperature and an active modification on the reduced ion mobility is studied. A thesis that should be proven relates to a dynamic cluster process even under constant energetic conditions.

Finally, the knowledge accumulated from the previous fundamentals-oriented studies is used in a more application-oriented approach for enantiomeric separation in the gas phase (Chapter 6). Enantiomeric separation using enantiopure 2-BuOH as a gas-phase modifier has been documented for IMS [79], and the possibility of transferring this principle to DMS is investigated. Special attention is paid to the optimization of the measurement conditions. Thus, the most promising analyte, the optimal DMS settings and the correct ionization method are determined in preliminary measurements.
During this research, the importance of charged nanodroplets from the ESI process in the DMS cell became clear. Subsequently, the enantiomeric separation is experimentally investigated by the addition of enantiopure 2-BuOH as a modifier, and the results are numerically validated by ab-initio calculations. This approach should be understood as basic research and proof of concept and not as an establishment of a new common application for everyday analytical practice. Therefore, an actual enantiomeric separation would be desirable but is not the prerequisite of a successful study. More decisive here is the knowledge gained with respect to the cluster effect in DMS. Furthermore, the effect of typical external influences such as background temperature on the underlying interactions is investigated based on a concrete objective.

3 Experiments and methodology

3.1 Mass spectrometer

Most of the experimental work for this study was performed on a SCIEX Triple Quad™ 6500 system with a Turbo V™ Ion Source and a coupled SCIEX SelexION® Differential Mobility Separation device. The whole system is commercially available (SCIEX, Ontario, Canada) and was only slightly adapted for the experiments. If not mentioned otherwise, the device was used as received from the manufacturer.

In this system, the ions are electrically transferred from the ion source (see Section 3.1.1) through a curtain plate into the high vacuum area of the MS by an attractive potential (*entrance potential*). The curtain plate is mounted in front of the orifice, which is part of a skimmer and nozzle system. A curtain gas (nitrogen) is used as a countercurrent flow through the curtain plate and is intended to protect the high vacuum area of the MS system from contaminations [66], and by using the DMS-MS coupling, a modifier can be directly added to the curtain gas [86]. The ions are focused in a first transfer quadrupole, which is known as a QJet ion guide. A *declustering potential DP* between the orifice and the QJet increases the kinetic energy of the ions to support the declustering process by CID. These and other voltages, combined with the reduced pressure in this area, can achieve high-field conditions, which lead to declustering and fragmentation, as discussed in Section 1.1. In this work, the *DP* was set as small as possible to detect the cluster distribution coming from the DMS cell. However, complete suppression of declustering reactions is unlikely.

After the QJet and a further focusing quadrupole element (Q0), a classic QqQ setup follows (see Section 1.2.2). The Q1 and Q3 are linear scanning quadrupoles, while the ion path of the 6500 series is bent 180° in q2. In addition, it is possible to add nitrogen as a collision gas into the collision cell (q2). After passing the Q3, the ions enter the detector [66]. By intervening in the MS electronics, it is possible to switch the Q1 into an RF-only mode, thus creating a high-pass filter.

The system has an upper *m/z* limit of 1250 in low-mass mode and 2000 in high-mass mode. The scan rate can be adjusted, with various fixed values selectable. All mass spectra presented in this work were measured with a scan rate of 200 Da/s.

Depending on the measurement method, several source parameters, voltages in the ion transfer and the separation stage, fragmentation parameters in q2 and the detector voltage can be optimized for the analyte. As a result, other mass ranges are discriminated against.

The parameter optimization can be performed automatically [97] but was done manually for each analyte. The polarity of the ion path can be switched to positive or negative mode, allowing anions and cations to be analyzed, but in this work, only cations were investigated. The MS parameters as well as the voltages and flow rates of the commercial ion sources and the DMS system are controlled with the Analyst® software version 1.6.2 (SCIEX, Ontario, Canada), which also processes and displays the gathered spectra. Furthermore, the software has a peak finding feature that can be used for evaluation of *CV* values in DMS measurements [97]. For this work, the raw data were fitted separately using the open-source software Fityk [98].
The analyte solutions were pumped into the ion source using the internal syringe pump and a suitable Hamilton syringe. The syringe pump was also controlled via Analyst® [66].

3.1.1 Ion sources

In addition to two commercially available ion sources (Turbo V™ and nanoESI), an APLI source converted from a commercial source (Turbo V™) was also employed in this work. For all ion sources, pure nitrogen was added as a nebulizer and/or heater gas.

Turbo V™ Ion Source

The default ion source is the Turbo V™ Ion Source (SCIEX, Ontario, Canada), which can be used in ESI or APCI mode. The mode can be switched by changing the probe, which is installed in the probe tower at the top of the source housing. The tower is positioned with two micrometer screws in both directions parallel to the MS front (horizontal and vertical). The housing can be fixed in front of the MS inlet without any tools, whereby the probe is orthogonally positioned to the ion optics. A front window of the housing allows for checking the ionization process optically. Two gas heaters (“turbo” heaters), which are located at both sides of the probe (45° angle from above), inject hot gas into the ion source, which is the primary heat source in the source area. In the APCI mode, a fixed corona discharge needle is used for primary ion generation. During the measuring process, the exhaust gas is vented through an exhaust at the bottom of the source [99].
The TurboIonSpray® probe (in the following: ESI probe) is composed of a rigid outer tube and an inner metal capillary (emitter), which protrudes 0.5 to 1 mm from the outer tube into the source area and ends between the turbo heater in front of the MS inlet [99]. An optimal spray is supported by using the *nebulizer gas* (*GS1*), which is injected between the emitter and the outer tube of the probe [9], and the *heater gas* (*GS2*), which comes from the turbo heaters [9, 99]. In this work, the typical solution flow rate in ESI mode, which was used unless otherwise noted, was 10 µL/min. Due to the low flow rate, the source temperature was set to 0°C (the actual temperature was minimally above room temperature). The voltage on the ESI emitter (*ion spray voltage* [*IS*]) was typically set in the range of 4 to 5.5 kV to ensure a constant signal. As result of this relatively high IS, which is typical for the setup, a glowing at the tip of the electrode tube was observed, which is clear evidence of a corona discharge. Thus, a mixture of an APCI- and an ESI-based ionization must be assumed.

The APCI probe has a very similar design to the ESI probe, but it is significantly shorter. Thus, in the installed state, the tip does not end in the source housing but in a heatable ceramic tube in the probe tower. The combination of a nebulizer gas and the heated ceramic tube realizes a voltage-free nebulization. The vaporized analyte is ionized in the source housing in a typical APCI mechanism after the primary charge is generated by the corona discharge. The corona needle can be rotated about a 360° axis, which is parallel to the MS front. It can also be rotated away when it is not used, such as in ESI mode [99]. In the APCI mode, a liquid flow rate of about 10 µL/min was also typically used. In this work, the source temperature was set as low as possible to prevent heating of the remaining setup by the ion source. All other parameters were adapted to the respective analyte in both modes.

nanoESI source

The commercial NanoSpray® III Ion Source (SCIEX, Ontario, Canada) is characterized by a design that is highly open to the lab atmosphere. Thus, the matrix gas is basically lab air. Since the ion source has no closed housing, a dedicated exhaust is not needed. The nanoESI emitter with an inner diameter (ID) of 75 µm is fixed on a slider with the tip pointing obliquely from above in the direction of the MS inlet, whereby the generated spray also points in this direction. The position of the slider can be adjusted in all three spatial dimensions. A nebulizer gas can improve the spray behavior, and in addition, the evaporation could be supported by a heatable curtain plate adjusted to the system [100]. However, this was not used in this work, such as a control camera that can help position the spray.
The *IS* is typically set between 1 and 3 kV and the liquid flow rate between 50 nL/min and about 2 µL/min [100], which are both significantly lower compared to classic ESI. Both parameters required regular adjustments due to the frequently necessary emitter changes (due to blockages). The setup was always optimized for maximum signal intensity at the lowest possible flow rate and *IS*.

APLI source

A simple APLI source was generated by modifying a Turbo V™ Ion Source. The schematic setup is presented in Figure 3.1.
First, an orifice was cut in the front window of the source to install a new window (laser window) in this position. This quartz window is transparent for UV light with a wavelength between 260 and 270 nm, which would be absorbed by the front window. A laser system (NT340 UV/VIS/IR OPO from EKSPLA [101] or FQSS 266-200 from CryLaS [102]) was positioned in the laser area (outside of the source housing) in front of the laser window, and the laser beam was directed through the laser window into the ion source, using suitable optics in the laser area if necessary. Thereby, the ion source area remained unchanged, except the corona needle, which had been removed.
The laser beam is aligned on the MS inlet and crosses the area under the probe tower. Both the ESI and the APCI probes can be used to generate an analyte cloud at this position, and the ESI probe allows for setting a low IS as a support for the spray. Therefore, the IS must be low enough to prevent the ESI process from becoming the main ionization mechanism.

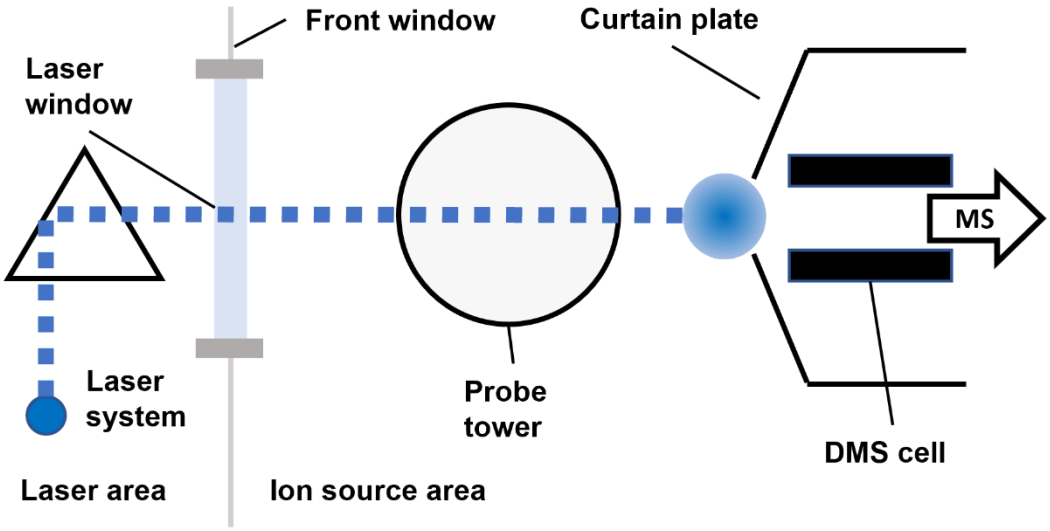

Figure 3.1: Schematic of the modified Turbo V™ Ion Source setup modified to a custom APLI source with the DMS cell installed (top view). Laser system: NT340 UV/VIS/IR OPO (EKSPLA) or FQSS 266-200 (CryLas).

Two different pulsed laser systems are available (NT340 UV/VIS/IR OPO: max. 10 Hz [101]; FQSS 266-200: max. 60 Hz [102]), which leads to discontinuous ionization. This could potentially be observable in the spectra, but a sufficient averaging of spectra should prevent this. The APLI source was operated with comparable values to the ESI and APCI settings, whereby the ionizing parameters were set to 0 or, in the case of the ESI probe (*IS*), to low values to prevent further ionization mechanisms in addition to the laser ionization.

3.2 Differential mobility spectrometer

The main element of the SCIEX SelexION® Differential Mobility Separation device (SCIEX, Ontario, Canada) is the DMS cell, which can be installed directly in front of the MS inlet. The two planar electrodes have dimensions of 10 by 30 mm and are fixed with a 1 mm gap to each other [103]. They are covered by an adapted curtain plate, which includes, in contrast to the classic curtain plate, enough space for the DMS cell. This creates a space between the ion source and the MS inlet. Nitrogen is passed through the curtain plate (curtain gas) and is released at the transition from source to DMS cell [86]. The system allows the adjustments of several parameters, which are summarized in Table 3.1.
Before entering the DMS cell, the curtain gas passes a heating area in the front part of the curtain plate. A heater, at which the DMS temperature is measured, heats a bed of ceramic balls, which emit heat to the curtain gas. Three temperatures (150°C, 225°C and 300°C) are present as default settings, but modification of the preset settings allows the reduction of the temperature to at least about 75°C. The temperature in the DMS cell is always significantly lower than the set temperature, and a temperature gradient in the DMS cell, as described before (see *Temperature effect in DMS*), must be considered. An additional gas flow from the MS side can also be introduced into the DMS cell. This throttle gas, which is set by the *DMS resolution DR* parameter, slows the ion migration through the DMS cell

and increases the residence time [86]. As a result, the DMS signals become narrower at the expense of the signal intensity, which can support the separation of species with comparable differential mobility (increase of the R_p). This value was set to 0 if not otherwise noted. An external control box (power supply) with two resonant coils generates and controls the voltages (*SV* and *CV*), and a modifier pump pumps liquid modifier into the system, where it is vaporized and mixed with the curtain gas before entering the curtain plate. The modifier flow rate to achieve the set *modifier composition MDC* (0%, 1.5% or 3.0%) is calculated from the gas flows, the molecular weight of the modifier and the modifier density [86]. In this work, the modifier pump was partly replaced with an external syringe pump and a syringe, which enables the reduction of the *MDC* and the dead volume.

Table 3.1: Main DMS parameters and their intended effect on ion separation.

	Parameter	Explanation	Effect on
SV	Separation voltage	Amplitude of high- and low-field voltage (peak to peak)	Ion separation depending on differential mobility
CV	Compensation voltage	Constant DC voltage between both electrodes	Compensation of *SV*-based drifting
DT	DMS temperature	Temperature at heater in the curtain plate	Gas temperature in DMS cell
DR	DMS resolution	Throttle gas flow (from the MS side)	Residence time in DMS cell
MDC	Modifier composition	Mixing ratio of added modifier	Cluster formation

The ion transfer from the DMS cell into the MS can be assisted by an attractive potential, which is called a *DMS offset* (*DMO*) [86]. This parameter was optimized to the analyte, but the influence on the cluster dynamics was not investigated in this work.

3.3 High kinetic energy ion mobility spectrometer

The high kinetic energy ion mobility spectrometer was developed and constructed at Leibniz University Hannover (Germany) in the Institute of Electrical Engineering and Measurement Technology. The setup is based on the design of a classic drift tube IMS with a reaction tube and a linearly coupled drift tube. Both are separated by a shutter grid [73, 104, 105]. The ionization in the reaction tube is realized by chemical ionization with primary ions generated by a corona discharge. A pump station, at the front end of the reaction tube, maintains the reduced operating pressure. The analyte is added in the area close to the shutter grid, while the drift gas is introduced at the end of the drift tube and flows through the whole system. In this work, nitrogen was used as the drift gas. The humidity of the gas is

controlled by a *dew point* (*DeP*) meter before entering the spectrometer [73]. The analytes are vaporized and mixed into the reaction area gas flow by using a diffusion through a closed plastic pipette. For this method, a closed pipette filled with an analyte is constantly heated at a temperature of 35°C in a gas-tight oven. The analyte diffused through the plastic into the gas phase and the nitrogen-analyte mixture is added into the reaction tube. With the measurement time, the density of the analyte and the exact weight loss of the pipette, the analyte mixing ratio can be calculated with the assumption of a constant diffusion rate through the pipette. In the drift gas line, pure nitrogen can be mixed with nitrogen containing a modifier from a second gas line, which allows a chemical modification in the drift tube. To generate the modifier containing gas flow, the nitrogen is also flown over a heated, closed plastic pipette filled with liquid modifier, or it is directly flown over the liquid modifier. The mixing ratio is set by the ratio of the gas flows.
The polarity of the HiKE-IMS can be switched between positive and negative mode, but similarly to the MS measurements, only the positive mode was used in this work.
For this study, a drift tube with a length of 306.5 mm was installed, which, depending on the reduced field strength in the drift tube, results in typical drift times in the range of about 0.1 ms to a few milliseconds. During the measurements, the reduced field strength in the reaction area was set constantly to 30 Td, while it was varied in the drift tube between 20 and 120 Td. The operating pressure was set at about 20.5 mbar, and the temperature was set to 318.15 K or to room temperature (about 297 K). For every spectrum, spectra were averaged until a set signal to noise ratio was achieved.

3.4 Chemicals and gases

Acetonitrile, methanol and 2-propanol used for MS experiments were purchased from Fisher Scientific (Waltham, Massachusetts, USA) and VWR International GmbH (Radnor, Pennsylvania, USA) in the highest purity (HPLC-grade), while 2-butanol (racemic as well as enantiopure) was ordered from Sigma Aldrich GmbH (Seelze, Germany) in a purity of 99.5% (racemic) and 99% (enantiopure). The MS system was operated with boiled-off nitrogen.
The amines and diamines were given to us by Prof. Dr. Kirsch's group (University of Wuppertal, Germany). These were ordered from various manufacturers in highest purity grades. Both enantiomers of chiral amino acids (serine, threonine, phenylalanine and tryptophan) as well as the Maruoka catalysts (analytes for the enantiomeric separation) were ordered by Sigma Aldrich GmbH (Seelze, Germany) in the highest purity. Pyrene was obtained from Merck KGaA (Darmstadt, Germany), and thermometer ions were synthesized based on the method described by Katritzky et al. [106] and stored in a deep freeze. The chemicals used for HiKE-IMS experiments were ordered from Sigma Aldrich GmbH (Seelze, Germany) with a purity > 99%, and the nitrogen was obtained from Linde Gas (Pullach, Germany) with a purity of 99.999% (5.0). All chemicals and gases were used without further purifications.

3.5 Numerical investigations

Numerical investigations were conducted with the Gaussian 16 (Revision A.03) program package [107], and GaussView 6.0.16 [108] was used for graphic visualization. Applying the *density functional theory* (DFT) with the B3LYP functional and the 6-31++G(d,p) basis set, geometric and thermodynamic calculations were performed. The assumed conditions were a temperature of 298.15 K at a pressure of 1 atm.
This method provides, among other variables, the *electronic energy* (E_0) and the *Gibbs free energy correction* (G_{corr}) [109]. If these values have been calculated for all reactants (rea.) and products (pro.) of a reaction (e.g., of a cluster reaction), the *Gibbs free energy of reaction* ($\Delta_{\mathrm{R}}G$) can be calculated using Equation 3.1 [109, 110].

$$\Delta_{\mathrm{R}}G = \sum(E_0 + G_{\mathrm{corr}})_{pro.} - \sum(E_0 + G_{\mathrm{corr}})_{\mathrm{rea.}} \qquad (3.1)$$

The use of the MobCal-MPI code allows the calculation of the CCS of the optimized species in nitrogen gas using the trajectory method [111]. For this purpose, the optimized geometries are used as input. In this work, the settings were chosen as proposed by Ieritano et al. [111]. The temperature and the pressure were set to the same values used for the geometry optimization.
This approach has already been successfully applied to similar problems [110] and should therefore lead to robust results.

4 Influence of steric properties on ion separation in DMS

Cluster formation in the gas phase is an important part of ion separation in DMS and is therefore often actively induced by the addition of modifiers (see *Chemical modification in DMS*). In previous works, the effect of typical gas-phase modifiers like ACN and MeOH have been demonstrated for both charge stages (double and triple protonation) of Substance P [23, 25]. The effect of clustering with a modifier (cluster effect) depends on the size of the CCS and the functional group of the modifier, which is in line with the general literature on this topic [5, 6, 19–21, 86]. Additionally, the structure of the ion (constitution and conformation) is significant for cluster dynamics and hence for the cluster effect. Thereby, the charge position in the ion should be relevant for its strength as well as the total size and the resulting CCS. The shielding of a charged position, for example in the center of a proton-bound modifier cluster, must be given special attention when the influence of the structure of the ion is studied, as indicated by the studies of R_4N^+ of Campbell et al. [6]. Furthermore, their studies of RMe_3N^+ also indicated an impact of the CCS on the strength of the cluster effect in DMS and a trend in *CV* depending on the alkyl R was demonstrated [6].

In the following, these effects of the ion structure are investigated for a series of linear primary diamines $H_2N\text{-}(CH_2)_n\text{-}NH_2$. With the length of the carbon chain ***n***, the absolute CCS as well as the distance between the amino groups are varied. Three typical modifiers (ACN, MeOH and IPA) for application in DMS are added to the gas phase to actively induce the cluster formation. The diamines also offer the possibility of double charging (protonation of both amine groups). In this case, the carbon chain length ***n*** defines the distance between the two charged positions, which allows investigation of the interactions of two centers of possible clusters and the impact of an increasing distance between them. Before the cluster effect on the diamine series is investigated, some preliminary measurements are made. For this purpose, various aliphatic amines and aromatic (di-)amines are used as analytes, and these should represent individual properties of the diamine series such as the increase in CCS.

Finally, system-independent statements about the influence of the ion structure on the effect of cluster formation in DMS are derived, and existing concepts are verified.

4.1 Analyte selection and typical MS spectra

The series of linear primary diamines H_2N-$(CH_2)_n$-NH_2 used to investigate the influence of the ion structure on the cluster effect was selected as analytes for several reasons. First, clustering at protonated amino groups is known in the literature and has often been demonstrated, for example, for protonated amino acids [112]. Additionally, other effects based on clustering processes like charge depletion and conservation (supercharging) by the addition of a gas-phase modifier have been demonstrated for this analyte series [113–116]. Furthermore, through variation of the length of the carbon chain ***n***, the ion size and thus the CCS can be varied without any obvious change in the qualitative chemical environment of the charged position such as additional shielding. Nevertheless, the distance between the two amine groups is varied, which could also influence cluster formation.
In addition to the diamine series H_2N-$(CH_2)_n$-NH_2 (1,2-diaminoethane [***n* = 2**], 1,3-diaminopropane [**3**], 1,5-diaminopentane [**5**], 1,8-diaminooctane [**8**] and 1,9-diaminononane [**9**]), aliphatic amines (butyl- and hexylamine) and aromatic (di-)amines (aniline, 1,2-phenylenediamine and 1,4-phenylenediamine) are investigated as analytes. For each analyte, a solution with a concentration of 0.1 mmol/L was prepared in ACN/water (1:1) with 0.05% formic acid, and the *DT* was set to a constant 150°C.
The mass spectra of the individual analytes show some commonalities based on the comparable ion structures, as shown in Figure 4.1 for three representative analytes. Through the addition of pure nitrogen into the DMS cell (no modifier), the main signal can be assigned to the singly protonated diamine $[M+H]^+$ (blue in Figure 4.1), and a typical fragment is observed at an *m/z* reduction of 17, whereby the relative intensity of the fragment depends on the analyte. This fragment can be explained by the loss of ammonia (NH_3), which results in a $[M+H-(NH_3)]^+$ species (blue dots in Figure 4.1). Furthermore, cluster species with ACN $[M+(ACN)_x+H]^+$ (blue arrows in Figure 4.1) are also observed without the modifier. These could be formed within the ion source and pass the ion transfer as it was set as soft as possible to enable cluster detection. Additionally, an entry of ACN into the DMS cell as part of a charged nanodroplet (see Section 6.2) and a cluster formation within the DMS cell or even the ion transfer cannot be excluded. The maximum observed cluster size was highest for 1,2-diaminoethane ($x = 2$), while no clusters were observable for 1,2-phenylenediamine. This could indicate a lower cluster stability, which prevents the clusters from passing through the ion transfer.
A second protonation of the diamines is possible, and the proportion of double protonation increases with increasing ***n***. The doubly protonated species $[M+2H]^{2+}$ (green in Figure 4.1) of 1,9-diaminononanen (see Figure 4.1**b**) and the first ACN cluster $[M+ACN+2H]^{2+}$ (green arrows in Figure 4.1) can be detected, while the observation of the doubly protonated bare species $[M+2H]^{2+}$ of 1,2-diaminoethane (see Figure 4.1**a**) seems to be impossible under these conditions; however, ACN clusters of it can be detected $[M+(ACN)_x+2H]^{2+}$ ($x = 3$ - 4, green arrows in the top panel of Figure 4.1). Observation of the doubly protonated 1,2-phenylenediamine $[M+2H]^{2+}$ (see Figure 4.1**c**) and its ACN clusters $[M+(ACN)_x+2H]^{2+}$ is not possible.

Independent of the added diamine, protonated ACN clusters $[(ACN)_x+H]^+$ are also detected (yellow in Figure 4.1). All in all, comparison of the mass spectra shows a decrease in the number of signals with increasing ***n*** for the diamine series.

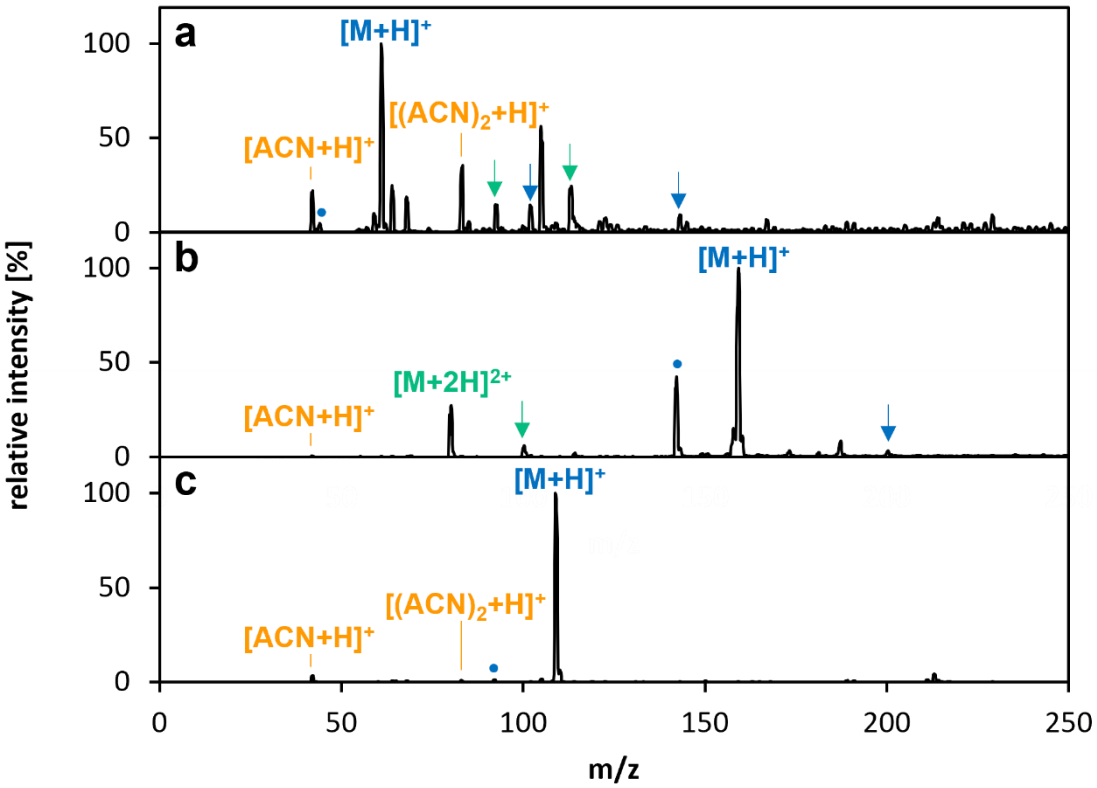

Figure 4.1: Mass spectra of 1,2-diaminoethane (**a**), 1,9-diaminononane (**b**) and 1,2-phenylenediamine (**c**) recorded in pure nitrogen. Blue: singly protonated diamine $[M+H]^+$, analyte-solvent cluster $[M+S_x+H]^+$ (arrows) and typical fragment $[M+H-NH_3]^+$ (dots). Green: doubly protonated diamine $[M+2H]^{2+}$ and analyte-solvent clusters $[M+S_x+2H]^{2+}$ (arrows). Yellow: protonated solvent clusters $[S_x+H]^+$.

The addition of ACN to the gas phase in the DMS cell (3%) leads to an increase in the mean cluster sizes $[M+(ACN)_x+H]^+$, as shown in Figure 4.2. The doubly protonated ACN cluster of the analyte $[M+(ACN)_x+2H]^{2+}$ becomes the main species of the linear diamines (x = 2 for 1,9-diaminononane and x = 5 for 1,2-diaminoethane) due to charge conservation, while a second protonation of 1,2-phenylenediamine is still prevented. It is not clear whether a second protonation of 1,2-phenylenediamine is impossible or whether this state is just very reactive. A proton transfer, for example to any contamination, might be the reason for not detecting the doubly protonated species.

The solvent cluster distribution does not follow a Gaussian distribution since the signal intensity of the third ACN cluster $[(ACN)_3+H]^+$ is significantly lower than expected for such a distribution and hardly observable (see Figure 4.2**c**). This makes it difficult to estimate the ACN mixing ratio simply from the cluster distribution, as would be helpful in measurements without actively adding modifiers in the gas phase (see Figure 4.1). The

addition of an alcohol, for example methanol, as modifier leads to corresponding solvent clusters $[S_x+H]^+$. Furthermore, charge depletion can be observed in an almost complete loss of the doubly protonated species $[M+2H]^{2+}$ (see Figure 4.8**c**/**d**). A tendency to clustering is also proven for these modifiers by the presence of clustered diamines $[M+(MeOH/IPA)_y+H]^+$, which is necessary for the cluster effect. However, the observed mean cluster size is significant lower than in the analyte-ACN clusters $[M+(ACN)_x+H]^+$.

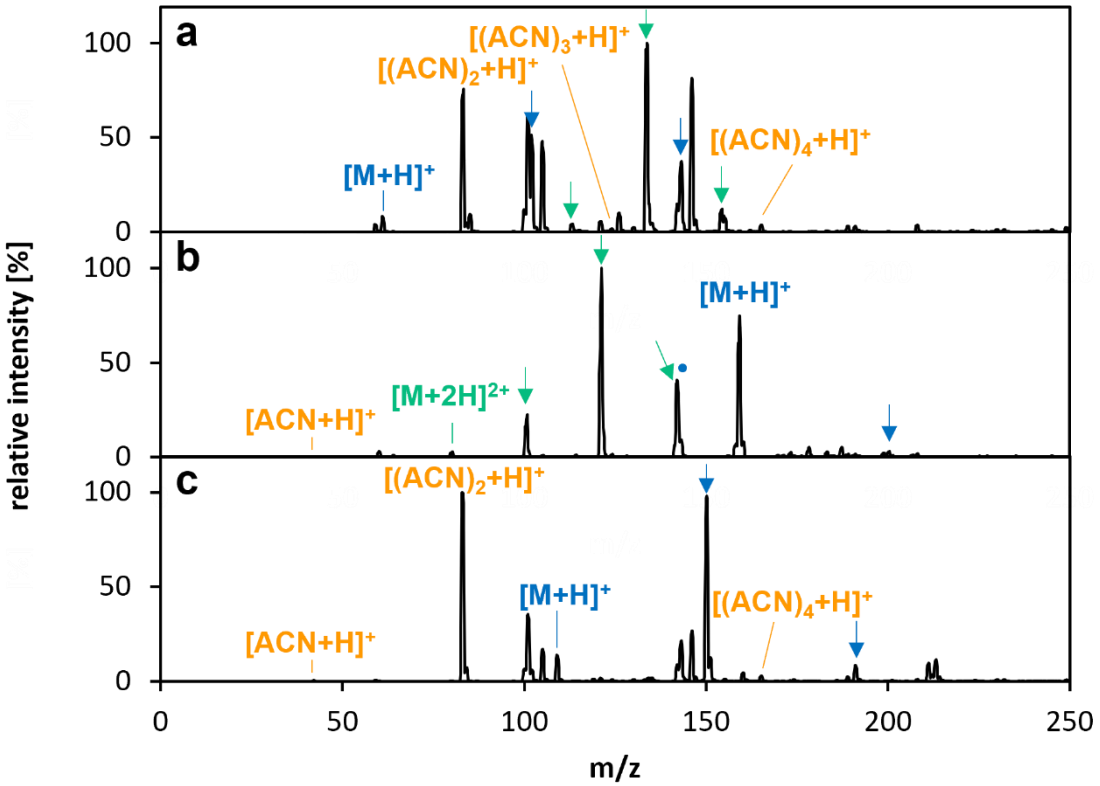

Figure 4.2: Mass spectra of 1,2-diaminoethane (**a**), 1,9-diaminononane (**b**) and 1,2-phenylenediamine (**c**) recorded with ACN (3%) added as gas-phase modifier in nitrogen. Blue: singly protonated diamine $[M+H]^+$, analyte-solvent cluster $[M+S_x+H]^+$ (arrows) and typical fragment $[M+H-NH_3]^+$ (dots). Green: doubly protonated diamine $[M+2H]^{2+}$ and analyte-solvent clusters $[M+S_x+2H]^{2+}$ (arrows). Yellow: protonated solvent clusters $[S_x+H]^+$.

4.2 Influence of the ion structure on differential mobility

As shown in Figure 4.2, the addition of ACN leads to a high number of observable species that are part of multiple cluster distributions. Therefore, grouping of species with almost identical behavior in DMS is useful. The effect of cluster formation is based on a continuous clustering/declustering process, which is why the observed cluster distributions in mass spectra are not stable over the entire ion separation in DMS. Instead of separating individual ionic species, a separation of different dynamic cluster systems with continuously varying distributions due to the varied reduced field strength *E/N* occurs. Thus, all cluster species

of the same cluster system should behave identically in DMS. Accordingly, the *CV* of a protonated molecule $[M+H]^+$ is typically identical with the *CV* of the solvent clusters of the same species $[M+S_x+H]^+$. In individual cases, the determined *CV* could be different, usually due to overlays with other cluster systems, chemical reactions after passing the DMS cell, or signal noise. However, the expected behavior, as shown in Figure 4.3, is common.

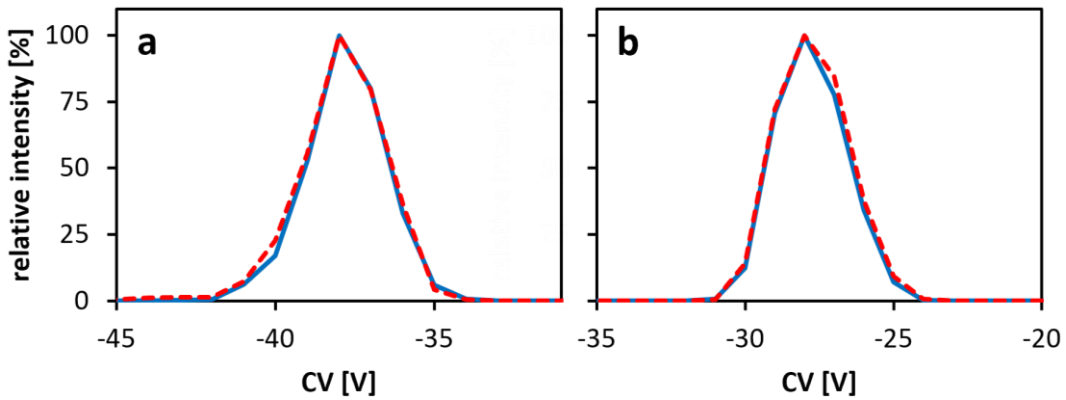

Figure 4.3: Ionograms of the protonated 1,2-diaminoethane (**a**), 1,2-phenylenediamine (**b**) and their first ACN-cluster recorded with ACN (3%) added as gas-phase modifier in nitrogen (*SV* = 4000 V). Blue: protonated analyte $[M+H]^+$. Red: corresponding first ACN cluster $[M+ACN+H]^+$.

The ionograms of the protonated analyte $[M+H]^+$ and the first ACN cluster $[M+ACN+H]^+$ are identical in the error range for 1,2-diaminoethane (see Figure 4.3**a**) and 1,2-phenylenediamine (see Figure 4.3**b**). Both analytes were measured at a constant *SV* of 4000 V, while the *CV* was ramped in 1 V increments. The identical *CV* value for each species of the same cluster distribution allows investigating only the $[M+H]^+$ species and not the entire distribution. Additionally, this permits the analysis of analyte-solvent clusters instead of the bare ion when the $[M+zH]^{z+}$ species cannot be observed. For example, $[M+(ACN)_x+2H]^{2+}$ clusters can be analyzed instead of the unobservable $[M+2H]^{2+}$ species in the case of 1,2-diaminoethane (see Figure 4.2**a**). Furthermore, chemical connections can be determined since the same *CV* values of different species indicates this connection. Thus, mass signals can be assigned to the same chemical system by DMS measurements, even when no chemical correlation is apparent on first view.

In the following, the dispersion plots are determined from ionograms. For this purpose, the raw data are plotted as a Gaussian curve, and the peak centers are given as *CV*. The mathematical error of these plots (99% confidence intervals) is defined as the error of the *CV*. It should be noted that this error should be understood as an indication of the signal quality and not as an absolute measurement error. The entire reproducibility of a DMS system was initially determined to a value of about ± 0.2 V by Schneider et al. [21, 117], but a higher reproducibility can be achieved as well [21], depending on the DMS system and the measuring conditions.

4.2.1 Introductory measurements

The influence of ion structure on the cluster effect should be investigated by some introductory measurements. Therefore, two groups of amines (aliphatic and aromatic) in combination with different modifiers are investigated here. These should reveal generally applicable relationships between the ion structure, the added modifier and the cluster effect, which can be used to interpret observations in the subsequent DMS measurements of the linear diamine series.

Aliphatic amines

The aliphatic amines (butyl- and hexylamine) differ in the carbon chain length, so the influence of the CCS of the bare ions on the cluster effect should be observable in the DMS results. In pure nitrogen, both amines exhibit type-B behavior (see Figure 4.4), whereby in the examined *SV* range (0–4500 V), the *CV* values are still in the low negative range (about -10 V to 0 V).

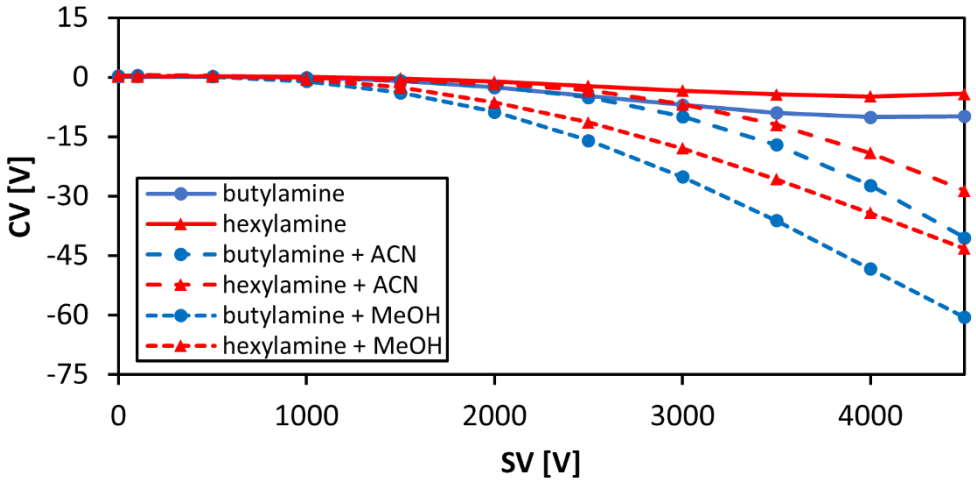

Figure 4.4: Dispersion plots of protonated aliphatic amines $[M+H]^+$ recorded with and without gas-phase modifier (3%) present in nitrogen.

Thus, ion mobility increases with increasing *E/N*, which should not be the result of the classic cluster effect since no modifier was added in these measurements. One explanation for this is a reproducible structure change, as is known regarding Substance P. Silveira et al. [118] demonstrated a temperature-dependent folding, which has significant impact on the CCS of Substance P. In the case of the amines, this kind of mechanism seems to be improbable due to the less complex structure compared to Substance P. Therefore, if no significant amount of contamination entered the DMS cell, interactions with the matrix gas (nitrogen) must be the cause of this observation. The influence of the matrix gas on ion separation in DMS is known in the literature [19]. The reduced ion mobility is higher in non-polarizable gases such as helium than in polarizable gases such as nitrogen, which is due to interactions of ions with the polarized gas (compare *Hard-sphere effect*). This causes

a weak effect that is comparable to the modifier-induced cluster effect, as shown by Schneider et al. [19]. Since nitrogen was used as a matrix gas for all measurements, these interactions became the main effect. The competing weak hard-sphere effect of the small ions is superimposed, which explains the type-B behavior.
The addition of a modifier (ACN or MeOH) induces a cluster effect, which outweighs other effects such as the hard-sphere effect. As result, a switch to type-A behavior is observed for both amines, as shown in Figure 4.4.
The addition of ACN leads to an absolute weaker cluster effect than the addition of MeOH, which is demonstrated in Figure 4.4 through less negative *CV* values. This is explainable by the different cluster structure of the modifiers. A protonated MeOH cluster $[(MeOH)_x+H]^+$ increases through interactions of a free MeOH molecule with the outer MeOH molecules of the cluster, and delocalization of the charge over the entire cluster by hydrogen bonding occurs, as Haack et al. demonstrated [13]. In contrast, ACN interacts mainly with the central charge since only one hydrogen bond can be formed (no delocalization of the charge). As result, an absolute higher cluster size can be achieved with MeOH than with ACN, which could cause a stronger cluster effect and thus a lower *CV* value. However, it is striking that with increasing *SV*, the *CV* values with both modifiers converge as the ACN curves slope more strongly at high *SV* of over 3000 V (see Figure 4.4). This can be explained by a lower cluster strength with MeOH than with ACN, which was numerically proven for protonated Me-NH_2 as the central ion [13]. As a result, the mean cluster size with MeOH $[M+(MeOH)_x+H]^+$ is in the low-field low, which reduces the strength of the cluster effect in high *SV* ranges. A possible explanation for this is the higher electrical dipole moment μ_D of ACN compared to MeOH (see Table 4.1) [6, 22], which should lead to a stronger polarization and thus promote a stronger binding of ACN.

Table 4.1: Electrical dipole moment μ_D of typical drift gas and modifiers.

Modifier	Electric dipole moment μ_D	Ref.
nitrogen	0 D	[6]
methanol	1.70 D	[119]
ethanol	1.69 D	[119]
2-propanol	1.56 D	[119]
2-butanol	1.8 D*	[119]
acetonitrile	3.92 D	[119]
acetone	2.88 D	[119]

*Measured in the liquid phase, which results in less reliable data than with gas-phase measurements [119].

The first clearly observable decrease of the *CV* value being at an *SV* of about 2000 V with ACN versus about 1000 V with MeOH (see Figure 4.4) could indicate the different binding energies of the modifiers. A lower *SV* is sufficient to cause significant declustering of MeOH clusters in the high field as compared to the corresponding ACN cluster, which

seems to be stable enough to prevent significant declustering at these *SV*s. The addition of IPA (data not shown) results in a qualitatively identical but recognizably weaker cluster effect compared to MeOH. Since the electric dipole moment μ_D of IPA is lower than that of MeOH (see Table 4.1), a higher binding energy through the addition of MeOH was expected, which could lead to a stronger clustering effect. In contrast, the addition of IPA leads to a stronger cluster effect for Substance P [23] as well as, for example, Me_4N^+ [6] compared to modification with MeOH. Accordingly, the dipole moment of the modifier cannot be used as the only criterion for the qualitative classification of the chemical modifier. Instead, the structure of the ion influences the cluster structure (e.g., by charge shielding [6]) and consequently the binding energies in the cluster and the cluster effect.
Separation of butylamine and hexylamine is achieved with a sufficiently high *SV* (see Figure 4.4), whereby hexylamine is characterized by a *CV* composition of the drift gas. The relative variation of the CCS is stronger for butylamine at the same cluster transition since the bare protonated butylamine is smaller than the bare protonated hexylamine. As a result, the effect of cluster formation on protonated butylamine is stronger. The same applies to interactions with polarized nitrogen, which leads to negative *CV* values even without the added modifier (see Figure 4.4). In general, increasing the CCS of the bare ion leads to a decreasing cluster effect in DMS (the cluster effect decreases with increasing cluster size). However, only two small analytes were investigated here, in which effects like charge shielding can almost be excluded.

Aromatic (di-)amines

In this section, 1,2-phenylenediamine and 1,4-phenylenediamine are investigated, focusing on structural similarities. Compared to the aliphatic amines, the carbon structure is not the distinguishing feature; this feature is the position of the second amino group. As a reference, aniline is also investigated, which differs from the other two analytes by the absence of a second amine group. The three protonated analytes differ in reduced ion mobility and thus in the CCS. Aniline has two reduced mobilities depending on the protonated position [120] (1.93/2.07 cm^2/Vs in air at 200 °C [121]), while the reduced mobilities of 1,2-phenylenediamine (1.96 cm^2/Vs in air at 200 °C [121]) and 1,4-phenylenediamine (1.82 cm^2/Vs in air at 200 °C [121]) are unique. Since for aniline, the less mobile species dominates [122], a similar reduced mobility to 1,2-phenylenediamine is expected and thus a similar CCS of the bare ion, while the lower ion mobility of protonated 1,4-phenylenediamine indicates a higher CCS.
As shown in Figure 4.5, type-B behavior is observed in pure nitrogen (see Figure 4.5**a**) for the singly protonated aromatic (di-)amines because of the interactions with the drift gas. Aniline and 1,4-phenylenediamine behave almost identically, while 1,2-phenylenediamine shows a deviating behavior (lower *CV* shift). It follows that the effect of the interactions with polarized nitrogen is weakened by the amino group in *ortho* position, and the amino group in *para* position has almost no effect on these measurements. Nevertheless, it must be mentioned that the absolute differences in *CV* between 1,2-phenylenediamine and the other aromatic (di-)amines are extremely small compared to other measurements (see Figure 4.**5b/c**).

The addition of ACN as a modifier (see Figure 4.5**b**) leads to type-A behavior for all (di-)amines, but 1,2-phenylenediamine again behaves quantitatively differently. The lower *CV* values indicate a stronger effect of cluster formation compared to aniline and 1,4-phenylenediamine. The difference in CCS of both diamines cannot explain this observation since the reduced ion mobility and therefore the CCS of both species of protonated aniline are closer to the values of the protonated 1,2-phenylenediamine [121]. Shielding of the charged position by the amino group in *ortho* position could lead to a different cluster structure. The optimal cluster structure seems to be blocked, leading to longer bond lengths and thus to a larger CCS and decreased bond strengths. Furthermore, a different mean cluster size due to a different shielding is possible. The mass spectra of both phenylenediamines show a higher proportion of the second ACN cluster compared to the first ACN cluster for 1,4-phenylenediamine than for 1,2-phenylenediamine. As a result, the differential mobilities differ.

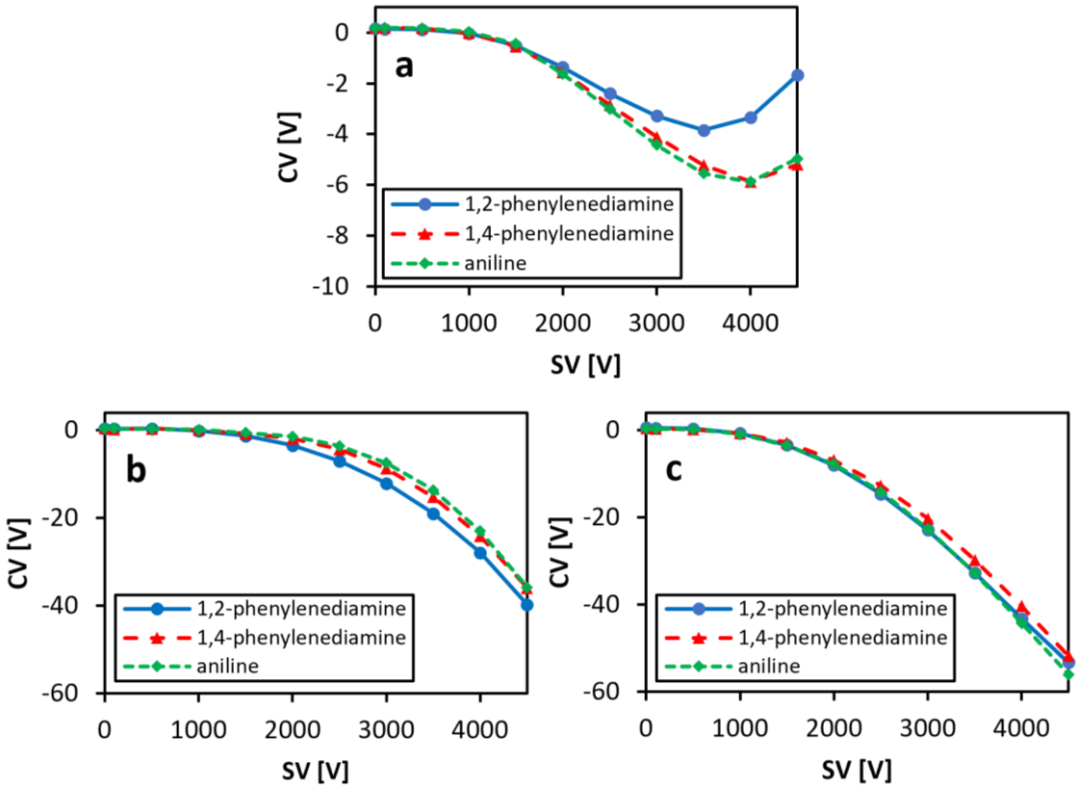

Figure 4.5: Dispersion plots of protonated aromatic amines and diamines $[M+H]^+$ recorded with and without gas-phase modifier (3%) present in nitrogen: (**a**) pure nitrogen; (**b**) ACN; (**c**) MeOH.

In contrast, the effect of MeOH (see Figure 4.5**c**) consists of a convergence of the behaviors of aniline and 1,2-phenylenediamine. An intramolecular shielding of the charged position by the amino group in *ortho* position does not seem to be significant for this cluster system, which might be explained by a delocalized charge in larger MeOH clusters. Thus, the cluster structure is more flexible to compensate for the shielding. In contrast, the CCS difference of 1,4-phenylenediamine as a result of the amino group in *para* position persists,

which leads to lower reduced ion mobility of the bare ions [121] and explains the minimum deviant behavior. It should be noted that the ion separation at this setting is very low, and the observed difference in *CV* could also be the result of measurement inaccuracies. Nevertheless, the previously determined difference in the quantitative behavior of 1,2-phenylenediamine and aniline (see Figure 4.5**b/c**) could not be determined. It should be mentioned that the intensity of the $[M+H]^+$ signal of aniline was very low, but the results were confirmed through adjustment of the $[M+MeOH+H]^+$ signal according the interrelation shown in Figure 4.3. The effect of a doubly charged ion could not be investigated since a doubly protonated species could not be detected for both diamines, which is also consistent with the literature [113].
In summary, an influence of the ion structure on the effect of cluster formation in DMS was observed for the aromatic amines. For the analytes studied, the deviations in *CV* were very low but qualitatively observable. Therefore, a modifier-dependent influence of the ion structure was demonstrated for the aliphatic and the aromatic (di-)amines. Both shielding effects and differences in the CCS of the bare ions are relevant, and the impact of the modifier used was proven. These findings should be considered in the interpretation of the results for the linear diamine series.

4.2.2 Diamine series

The series of protonated linear primary diamines $H_2N\text{-}(CH_2)_n\text{-}NH_2$ includes qualitatively many of the structural variations that were investigated in the introductory measurements. On the one hand, the enlargement of the non-polar carbon chain coincides with the structural variation of the aliphatic amines, and the effect of an increased CCS (see *Aliphatic amines*) is to be expected. On the other hand, especially for short carbon chains (***n* = 2 - 3**), the steric proximity of the second amino group could influence the cluster dynamics in a similar manner as observed with the aromatic diamines. Additionally, the large number of samples from the same chemically related series allows checking for correlations between the ion structure and the cluster effect and for trends of the *CV* with increasing carbon chain length. Such trends are already known for other chemical systems [6, 20].
In pure nitrogen, 1,2-diaminoethane exhibits type-A behavior, which is qualitatively different from that of the other diamines, as shown in Figure 4.6. This behavior can be explained by interactions with polarized nitrogen, which have the greatest influence on the differential mobility of the smallest ion, as proven also for the aliphatic amines (see Figure 4.4). Another explanation lies in the noticeable kink in the dispersion plot at *SV* = 3500 V (see blue curve in Figure 4.6), which is accompanied by substantial intensity loss. This could indicate superposition with other signals of the same *m/z* ratio (e.g., protonated IPA) or a change in the underlying mechanism. Another, albeit unlikely, explanation is the occurrence of uncharged 1,2-diaminoethane as gas-phase modifier for the protonated species, which seems to be possible at an electric dipole moment μ_D of 1.99 D [119]. Based on a vapor pressure of 1444 Pa [123] at 19 °C (real source temperature), a maximum gas-phase mixing ratio at AP of about 1.4% is possible. However, a saturated gas phase cannot be achieved by spraying the analyte solution. Therefore, the actual mixing ratio of uncharged

1,2-diaminoethane cannot reach this value. Furthermore, the signal of the dimer would be more intense (compare Figure 4.1**a**) if a modification with uncharged 1,2-diaminoethane were the reason for the type-A behavior. Thus, this observation cannot be definitively clarified. Nevertheless, the relative dispersion plots of the investigated diamines show a clear systemic trend regarding the carbon chain length.

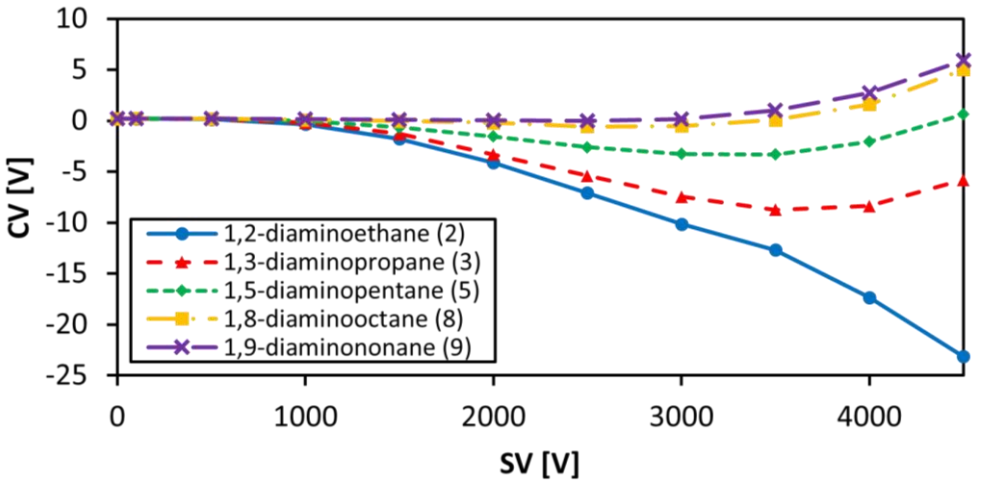

Figure 4.6: Dispersion plots of protonated linear primary diamine series $[M+H]^+$ recorded in pure nitrogen.

The diamines of medium size (**3** and **5**) are characterized by type-B behavior (see Figure 4.6), as previously demonstrated for the aliphatic amines, which can also be explained by interactions with polarized nitrogen. Furthermore, this effect is too weak to result in clearly negative *CV* values for the largest species (**8** and **9**). Although both diamines show a hint of type-B behavior, 1,9-diaminononane especially exhibits type-C behavior (see purple curve in Figure 4.6). Accordingly, an increasing ion size leads to a decreasing influence of the interactions with nitrogen and thus to less negative *CV* values. The interactions cause a decrease in reduced ion mobility in the low field, thus influencing the differential mobility. If one assumes similar absolute interactions of each singly protonated diamine due to a similar structure at the charged position, then the different relative effects on the different diamines consistent with the effects on the aliphatic amines (see *Aliphatic amines*).
Furthermore, a quantitative trend of decreased *CV* values is observed. The *CV* values do not scale linearly with the chain length, as shown in Table 4.2. The differences in *CV* (ΔCV) of singly protonated diamines $[M+H]^+$ at an *SV* of 3000 V decrease with increasing carbon chain length. Thus, $\Delta CV_{\mathbf{2\rightarrow3}}$ (ΔCV from **2** to **3**) of 2.72 ± 0.07 V is more than four times larger than $\Delta CV_{\mathbf{8\rightarrow9}}$ (0.65 ± 0.16 V), although the absolute structural variation is identical in both cases ($+CH_2$). This observation is consistent over the entire *SV* range (compare Figure 4.6). Consequently, the relative structural variation of the bare ion is more important for the effect of the interactions with nitrogen than the absolute variation, which is consistent with the explanation for the qualitative trend in Figure 4.6.

Table 4.2: Compensation voltages of the protonated diamine series $[M+H]^+$ recorded in pure nitrogen at an *SV* of 3000 V.

Analyte	*CV* [V]
1,2-diaminoethane	-10.16 ± 0.05
1,3-diaminopropane	-7.44 ± 0.05
1,5-diaminopentane	-3.18 ± 0.07
1,8-diaminooctane	-0.36 ± 0.14
1,9-diaminononane	0.29 ± 0.07

The addition of a modifier leads to the typical effect of cluster formation in DMS and results in type-A behavior for all diamines (see Figure 4.7), although with MeOH (see Figure 4.7**b**), a switch to type-B behavior is indicated for the four largest diamines (**3**, **5**, **8** and **9**) by a flatting of the dispersion plots at high *SV*s. The addition of ACN (see Figure 4.7**a**) leads to the ion-size-based sequence of the dispersion plots, which was also observed without a modifier (see Figure 4.6). However, two groups of comparable dispersion plots are formed (see Figure 4.7**a**). This grouping is size dependent, which could be due to interactions of the cluster system with the second uncharged amino group compared to the results obtained for the aromatic diamines, or it could be due to comparable cluster effects within the groups. A clear separation is observed between the first group including ***n* = 2**, **3** and **5** and the second group including ***n* = 8** and **9** ($\Delta CV_{\mathbf{5}\rightarrow\mathbf{8}}$ = 4.30 ± 0.15 V at *SV* = 3000 V). Furthermore, the proportion of doubly protonated species $[M+2H]^{2+}$ increases by adding ACN as a modifier as a result of charge retention [37]. When the carbon chain is short (**2** and **3**), the two charges appear to repel each other strongly enough to promote deprotonation under the formation of a singly protonated species even downstream of the DMS cell. This leads to a second signal in the ionograms of the $[M+H]^+$ species at the *CV* of the doubly charged species $[M+(ACN)_x+2H]^{2+}$, as is also suggested for the doubly protonated species of Substance P (with and without modifier, see red ionograms in Figure 1.4). For greater carbon chain lengths (***n* > 3**), the deprotonation was not observed, which is why it can be assumed that the grouping is due to reasons other than deprotonation.

The addition of MeOH leads to dispersion plots that are in *CV* ranges comparable with added ACN for each diamine (see Figure 4.7**b**), although a lower cluster strength can be inferred from the qualitative progression of the dispersion plots (indicated type-B behavior). The ion-size-based sequence is recognizable, but hardly the grouping although the dispersion plots of the three largest diamines (**2**, **3** and **5**) run very close to each other (see Figure 4.7**b**). With both MeOH and ACN, a significantly higher ion shift in the DMS cell can be achieved than in pure nitrogen (cluster effect), but there is a significantly different ion separation. The total ion splitting ($\Delta CV_{\mathbf{2}\rightarrow\mathbf{9}}$) at an *SV* of 3000 V without modifier (9.87 ± 0.09 V) is identical with the splitting with ACN added (9.80 ± 0.12 V) and smaller than when MeOH is added (13.38 ± 0.17 V). Accordingly, the expected ion separation due to the cluster effect is lower or absent for the modification with ACN, while it is fully

effective for added MeOH. Whether this is also related to the grouping is possible but not conclusively clarified.

The addition of IPA (see Figure 4.7**c**) leads to a totally unexpected effect. On the one hand, a grouping can be detected. On the other hand, the size-dependent order is reversed with a very weak ion splitting in the first group (**2**, **3** and **5**). One explanation is the convergence of the ion and modifier sizes. As a result, the mobilities of the clusters $[M+(IPA)_x+H]^+$ are mainly determined by the IPA cluster at the diamine. The CCS of the diamine becomes less significant; a separation with DMS becomes difficult, and grouping can be observed. Additionally, the diamines seem to act as modifier for the IPA clusters, which is why the minimum trend is reversed (see blue, red and green curves in Figure 4.7**c**). Accordingly, larger diamines cause a slightly larger shift in the DMS cell in this group. The dispersion plots with ACN also suggest the beginning of such behavior (grouping and starting positional shift of 1,2-diaminoethane, blue curve in Figure 4.7**a**).

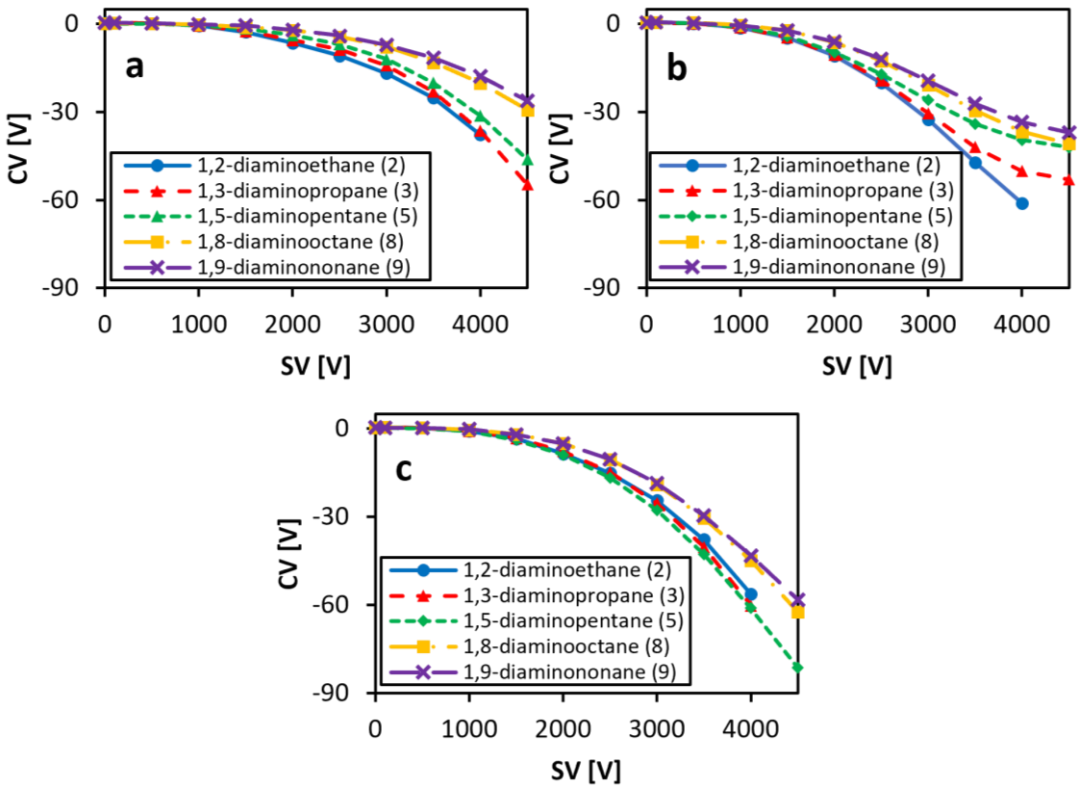

Figure 4.7: Dispersion plots of the protonated linear primary diamine series $[M+H]^+$ recorded with gas-phase modifier (3%) present in nitrogen: (**a**) ACN; (**b**) MeOH; (**c**) IPA.

The diamines of the second group (**8** and **9**) are, compared to IPA, large enough to be the crucial species for the CCS of the cluster system. These species continue to follow the original size sequence. In the case of a further increase in the CCS of the modifier, a comparable development would be expected for these diamines as well. Consequently, the CCS of an ion influences the cluster effect quantitatively and also qualitatively. Again, it must be mentioned that these are assumptions and experimentally based conjectures.

4.3 Influence of the charge level on the cluster effect

The charge retention achieved by adding ACN as a gas-phase modifier into the DMS cell favors the $[M+2H]^{2+}$ species, as shown in Figure 4.8**b**, while charge depletion through the addition of alcohols prevents detection of these species. This is shown in Figure 4.8 for 1,9-diaminononane. In pure nitrogen (see Figure 4.8**a**), the $[M+2H]^{2+}$ species is clearly observable, but it is lost upon addition of MeOH (see Figure 4.8**c**) or IPA (see Figure 4.8**d**). Therefore, the cluster effect of both modifiers cannot be investigated for the doubly protonated species $[M+2H]^{2+}$.

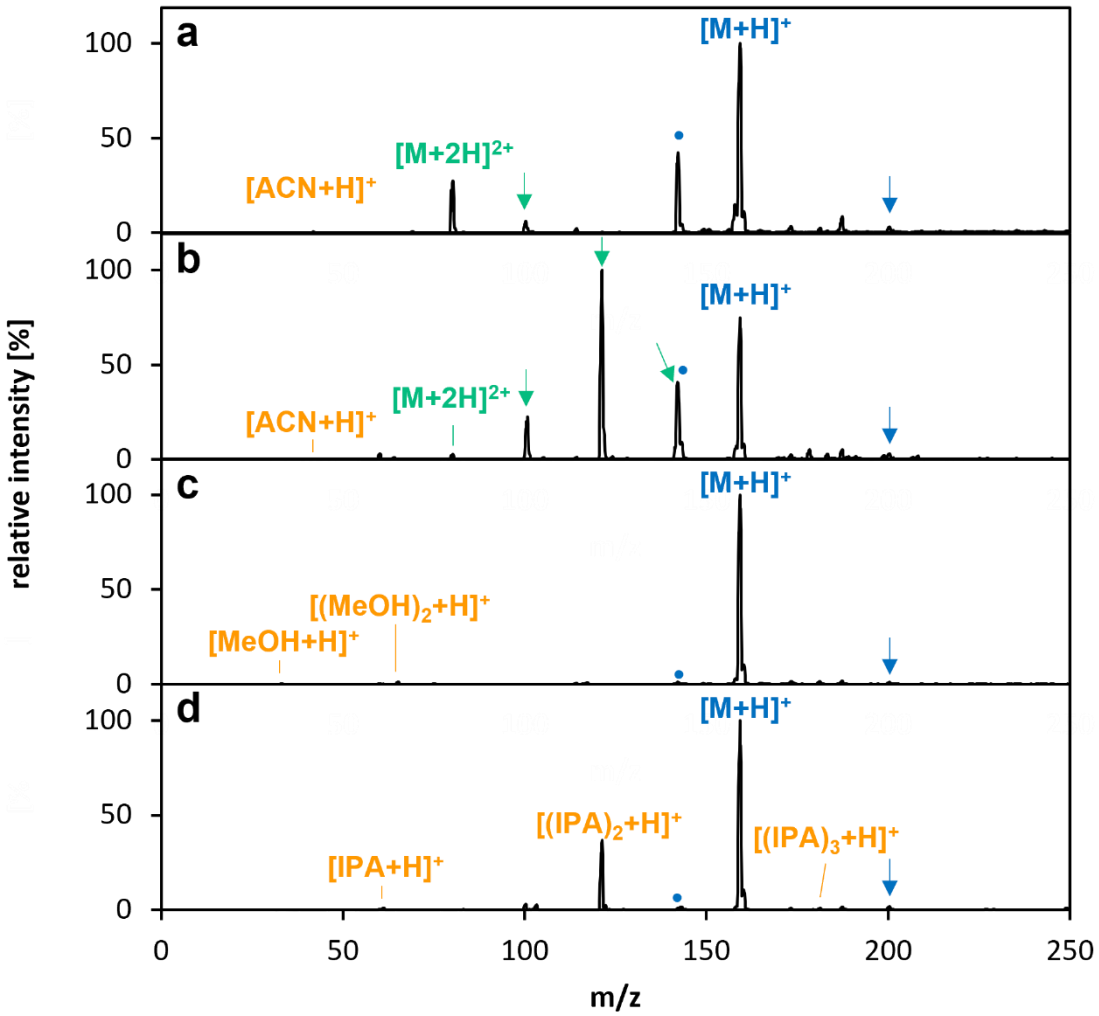

Figure 4.8: Mass spectra of protonated 1,9-diaminononane recorded with and without gas-phase modifier (3%) present in nitrogen: (**a**) pure nitrogen; (**b**) ACN; (**c**) MeOH; (**d**) IPA. Blue: singly protonated diamine $[M+H]^+$, analyte-solvent clusters $[M+S_x+H]^+$ (arrows) and typical fragment $[M+H-NH_3]^+$ (dots). Green: doubly protonated diamine $[M+2H]^{2+}$ and analyte-solvent clusters $[M+S_x+2H]^{2+}$ (arrows). Yellow: protonated solvent clusters $[S_x+H]^+$.

This behavior is also observed for the other diamines of this series and is consistent with the literature [37]. However, even with ACN, the bare doubly protonated species $[M+2H]^{2+}$ was not observed for the three smallest diamines (**2**, **3** and **5**), but the corresponding ACN clusters $[M+(ACN)_x+2H]^{2+}$ ($x \approx 3$ - 5) were detected under the given conditions (see Figure 4.2**a**). As demonstrated in Figure 4.3, these species can be analyzed as substitutes under certain circumstances; therefore, the cluster species with the most intense signals were used for the following investigations. Of course, this approach involves the risk that the results obtained could be incorrect or at least inaccurate, which must be considered in the interpretation.
The cluster effect leads to type-A behavior for each doubly protonated diamine, and a trend of the dispersion plots according to the carbon chain length is clearly visible in Figure 4.9.

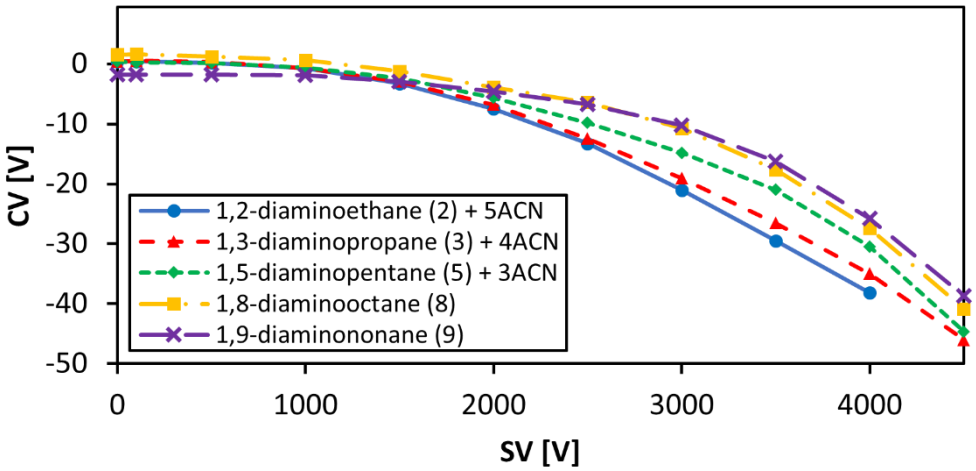

Figure 4.9: Dispersion plots of doubly protonated linear primary diamine series $[M+2H]^{2+}$ and corresponding ACN clusters $[M+(ACN)_x+2H]^{2+}$ recorded with ACN (3%) added as gas-phase modifier in nitrogen. The data point (***n* = 2**) at an SV of 4500 V could not be determined due to insufficient signal intensity.

The dispersion plot of 1,9-diaminononane starts at a significantly negative *CV* value (-1.55 ± 0.19 V, see purple curve in Figure 4.9), which does not make sense since no ion shift should occur at an *SV* of 0 V. In the *SV* range from 0 to 2000 V, the ionograms of the doubly protonated 1,9-diaminononane $[M+2H]^{2+}$ as well as of the $[M+(ACN)_x+2H]^{2+}$ species exhibited a double peak structure, which could not be detected for the $[M+H]^+$ species with the same measurements. The signal intensity in this range is relatively low even with added ACN, and thus the double peak could be the result of superposition with noise or other signals from the highly complex chemical system. Accordingly, the first part of the dispersion plot of 1,9-diaminononane ($SV \leq 2000$ V) is classified as an artifact and is not examined further in this work. In the future, a study of this observation could be helpful to understand the chemical system.
A direct comparison of the dispersion plots of the $[M+H]^+$ species (see Figure 4.7**a**) and the $[M+2H]^{2+}$ species (see Figure 4.9), which were formed from identical measurements,

reveals qualitative and quantitative differences. Grouping cannot be detected for the $[M+2H]^{2+}$ species to the same extent as for the $[M+H]^{+}$ species. The second protonation enables different cluster structures, which could prevent this observation. In addition, a significantly stronger ion shift occurs at some *SV*s due to a second protonation, as shown in Table 4.3 for an *SV* of 3000 V.

Table 4.3: Compensation voltages of singly protonated diamine series $[M+H]^{+}$ and doubly protonated species $[M+2H]^{2+}$/$[M+(ACN)_x+2H]^{2+}$ recorded with ACN (3%) added as gas-phase modifier in nitrogen at an *SV* of 3000 V.

Analyte	Single protonated *CV* [V]	Double protonated *CV* [V]	Δ*CV* [V]
1,2-diaminoethane	-16.83 ± 0.05	-21.02 ± 0.04	4.19 ± 0.06
1,3-diaminopropane	-14.26 ± 0.04	-19.10 ± 0.02	4.84 ± 0.04
1,5-diaminopentane	-12.15 ± 0.08	-14.67 ± 0.04	2.52 ± 0.09
1,8-diaminooctane	-7.85 ± 0.13	-10.23 ± 0.20	2.38 ± 0.24
1,9-diaminononane	-7.03 ± 0.11	-9.80 ± 0.19	2.77 ± 0.22

With increasing *SV*, the *CV* values of the doubly protonated ion $[M+2H]^{2+}$ approach those of the singly protonated ion $[M+H]^{+}$ for the three smallest diamines (**2**, **3** and **5**), while the *CV* values of the other diamines (**8** and **9**) are significantly higher with a second protonation at an *SV* of 4000 V (see Δ*CV* in Table 4.4).

Table 4.4: Compensation voltages of singly protonated diamine series $[M+H]^{+}$ and doubly protonated species $[M+2H]^{2+}$/$[M+(ACN)_x+2H]^{2+}$ recorded with ACN (3%) added as gas-phase modifier in nitrogen at an *SV* of 4000 V.

Analyte	Single protonated *CV* [V]	Double protonated *CV* [V]	Δ*CV* [V]
1,2-diaminoethane	-37.78 ± 0.04	-38.46 ± 0.07	0.68 ± 0.08
1,3-diaminopropane	-36.24 ± 0.05	-35.10 ± 0.07	-1.14 ± 0.09
1,5-diaminopentane	-31.31 ± 0.05	-30.53 ± 0.05	-0.78 ± 0.07
1,8-diaminooctane	-20.26 ± 0.11	-27.08 ± 0.19	6.82 ± 0.22
1,9-diaminononane	-17.67 ± 0.16	-25.57 ± 0.15	7.90 ± 0.22

A combined cluster structure for the smaller diamines (**2**, **3** and **5**) and two separated cluster structures for the larger diamines (**8** and **9**) could explain this observation: At a high *SV*, the second protonation decreases the *CV* of two diamines (**3** and **5**), and the smallest diamine (**2**) only slightly increases compared to the single protonated species (see Table 4.4). In the case of one superior cluster system, a small *SV* leads to an increased mean cluster

size compared to the $[M+H]^+$ species in the low field and thus to a significant ΔCV (see Table 4.3). With increasing *SV*, the mean cluster size decreases independently of the charge level, and at a sufficiently high *SV*, the mean sizes of the doubly protonated clusters approach those of the singly protonated cluster. This leads to the convergence of the *CV*s of both charge levels for each diamine (see Table 4.4). In contrast, the longer carbon chain of the larger diamines (**8** and **9**) ensures a sufficiently large distance between the charges so that two independent cluster systems can be formed. These cluster systems also strengthen the cluster effect at high *SV*s and at small mean cluster sizes even in the low field.
In conclusion, in the case of short carbon chains (**2**, **3** and **5**), a significant influence of a second protonation on the cluster system was detected, while long carbon chains (**8** and **9**) seem to favor the formation of a second similar and almost independent cluster system. Thus, a second functional group can sterically shield a charged position, as has been shown for the aromatic diamines (see *Aromatic (di-)amines*), but in the case of a second protonation, a combined cluster system could be formed as well, whereby the distance between both charges seems to be significant.

4.4 Summary and conclusion

The influence of ion structure on cluster formation and the resulting effect in DMS was investigated through experimental studies of a series of diamines and a set of introductory measurements. In this context, special attention was paid to the effect of different typical gas-phase modifiers for DMS applications.
The general correlation between ion structure and the CCS and ion shifting in the DMS cell was demonstrated in experiments with aliphatic amines. It was found that the relative variation in ion mobility, due for example to the cluster effect or the interactions with polarized matrix gas (nitrogen), decreases with increasing ion size. An increase in ion size leads to a decrease in *CV* value, which is consistent with the literature [6]. However, Campbell et al. studied ions with a more shielded charge position, which could also be of importance. In this work, a kind of shielding was demonstrated for aromatic (di-)amines through the modifier-dependent similarity of the behavior of aniline, 1,2-phenylenediamine and 1,4-phenylenediamine. It was found that a second amino group in *ortho* position influences the cluster effect due to ACN, while the cluster effect due to MeOH is almost independent because of a different cluster structure and a delocalized charge. References to this can also be found in the literature [13]. However, it must be mentioned that actual charge shielding in all three spatial directions (three-dimensional shielding) was not investigated. Furthermore, a redistribution of the charge in the aromatic ring cannot be excluded.
The findings of the introductory measurements were verified for a series of linear diamines. As a result of the interactions of the $[M+H]^+$ species with polarized nitrogen, ion separation according to carbon chain length was demonstrated. A notable behavior of 1,2-diaminoethane was also found as type-A behavior was observed even without an added modifier (see Figure 4.6). The addition of ACN led to grouping of the dispersion plots. This seems to be a steric effect, which is further enhanced by the addition of IPA. The sequence

of the dispersion plots reversed for **n** ≤ **5** as a consequence of the size ratio of ion to modifier. For a sufficiently large modifier, the CCS of a cluster depends mainly on the modifier rather than on the central ion. Since MeOH is significantly smaller than any measured diamine, the expected cluster effect was found.
The effect of a second protonation for the complete series could only be explored by the addition of ACN as a modifier due to the absence of doubly protonated ions with MeOH or IPA as modifiers. Depending on the carbon chain length, the *CV*s of the $[M+2H]^{2+}$ ions are shifted qualitatively and quantitatively compared to the singly protonated species, which could indicate different cluster structures. In accordance with this, a short distance between the charged positions (**n** ≤ **5**) leads to a single cluster system, whereas a longer distance (**8** and **9**) leads to two independent cluster systems, which both strengthen the cluster effect even at low mean cluster sizes.
Overall, the effect of the ion structure on the cluster effect can be attributed to two main effects that may overlap. First, the CCS of the bare ion influences the cluster effect, whereby an increase in the CCS of the bare ion leads to a decrease in the strength of the cluster effect. Second, interactions with additional functional groups can influence the cluster structure and the mean cluster size, which can strengthen or weaken the cluster effect. Further chemical interactions cannot be excluded and are even to be expected, depending on the analyte system. It can be assumed that these observations can be transferred to larger analyte systems such as oligopeptides or even proteins. However, deviations must be expected since fewer complex structures were preferred in the selection of the analyte systems studied in this work. This is not the case in the examination of real samples. With sufficiently large molecules, further effects dependent on ion structure are expected. For example, folding of the molecules can occur, as shown by Silveira et al. for Substance P [118].

5 Cluster dynamics under constant conditions

A targeted comparison of the interactions between ions and neutral species in classic IMS and in DMS/FAIMS is a quite effective procedure since the processes in IMS are more likely to be understood and are less complex. As discussed previously, the cluster dynamic is one of the main interactions of ions and neutral species and therefore has a decisive influence on both methods. However, direct comparison is not easily accomplished since the energetic conditions are significantly different. While classic DTIMS operates under low-field conditions [75, 80], in DMS and FAIMS, reduced field strengths *E/N* of over 100 Td are typical [30]. The discrepancy can be partially bridged by using HiKE-IMS. This method combines properties of both methods: a structure and measuring principle like a classic DTIMS and reduced field strengths in a range like that in DMS/FAIMS by reduced pressure. Therefore, the method provides comparative measurements in both directions. Based on a *resolving power* (R_P) up to about 140 [105] and kinetic control of some sufficiently slow reactions [18, 73], this instrument also allows an examination of cluster dynamics under high-field conditions. The maximum R_P depends on the used setup and the reduced field strength in the drift tube. Therefore, with the optimal setup, the maximum R_P is reached at maximum reduced field strength [105].
A HiKE-IMS system was used to investigate the cluster dynamic depending on the reduced field strength of several small analytes, which were partially used in Chapter 4. In addition to ACN and MeOH, the cluster dynamic of 1,3-diaminopropane is of interest. Additionally, ACE and water were examined as typical cluster-forming species. The effects of humidity and temperature were measured as well as the effect of adding a modifier to the drift gas. The modifier mixing ratios were significantly lower than in the DMS experiments as a result of using diffusion through the plastic pipette. A more direct addition that passes the nitrogen through the liquid modifier allowed setting the mixing ratio to higher and more precise values, but initial measurements showed a fast supersaturation of the system, which is why this setup was abandoned. A comparison of the experimental results with previous results and numerical investigations allowed conclusions to be reached regarding other analytical methods like DMS and classic IMS.

5.1 Cluster dynamics in HiKE-IMS

In classic DTIMS systems, the high number of collisions support the formation of a thermodynamically controlled chemical system, while the reduced pressure in HiKE-IMS (about 20.5 mbar in this work) partly prevents this. For slow reactions, the residence time in the drift tube in combination with the reduced pressure is too low to reach thermodynamic equilibrium, and even the fast reactions of the water cluster system can be almost kinetically controlled at a sufficiently low water mixing ratio, which has been proven through numerical investigations [18, 33, 104]. This fact must be considered for all interpretations of HiKE-IM spectra.
The cluster dynamics of several small analytes were analyzed. Therefore, they were added to the reaction tube in a mixing ratio set to 0 or the values listed in Table 5.1.

Table 5.1: Analytes and their mixing ratios in HiKE-IMS experiments.

Analyte	Mixing ratio [ppmV]
acetonitrile	0.9
acetone	1.3
methanol	1.6
1,3-diaminopropane	1.1

The humidity of the drift gas was varied through the mixing ratio of dry and wet nitrogen. Through ramping the *E/N* in the reaction tube from 20 to 120 Td in 5 Td steps, the impact on the cluster dynamic was investigated. The *E/N* in the reaction tube was kept constant at 30 Td during these measurements.

5.1.1 Proton bond water cluster system

The HiKE-IMS instrument cannot be kept totally water free, which is mainly due to the added nitrogen. However, even the addition of totally water-free nitrogen would not lead to water-free conditions in the instrument because micro leaks in the used setup would provide a noticeable base humidity. Accordingly, a water cluster system cannot be prevented due to the permanent presence of water, and the resulting signals are observed in every HiKE-IM spectrum unless they are chemically suppressed. Therefore, the water cluster system was first studied through analyte-free measurement (no actively added analyte) to be fixed as a benchmark. Furthermore, the water-cluster signal, which is typically known as the RIP (*reactant ion peak*), is not independent of the reaction conditions and is therefore treated as an analyte as well. The comparative measurements were carried out at a background temperature of 318.15 K and a dew point *DeP* of -90.8 °C.
At an *E/N* of 30 Td, the RIP was detected as the only signal, as shown in Figure 5.1. By increasing the *E/N* to 45 Td, the RIP shifted to a lower drift time because of the increased

drift velocity, which is also evident from Equation 1.3. Additionally, the drift time could become shorter due to increased ion mobility with increasing *E/N*, as shown in Equation 1.6. The shift in the drift time was accompanied by a significant increase in maximum signal intensity and a slightly declining peak width as result of a lower ion diffusion in the drift direction (see top-middle panel in Figure 5.1). This was confirmed through numerical simulation by Erdogdu [18, 104]. Furthermore, the peak width was determined by the experimental setup (e.g., the used amplifier). In addition to the signal shift, a further increase in the *E/N* to 55 Td led to a decrease in the maximum ion current and a visually barely noticeable peak broadening (see top-right panel in Figure 5.1). Until an *E/N* of 70 Td, the maximum intensity steadily increased. However, from 70 to 90 Td, the maximum intensity decreased again, and the peak broadening repeated much more strongly than before (see bottom-middle panel in Figure 5.1). Then, the signal increased and became narrower again, as shown for 110 Td (see bottom-right panel in Figure 5.1).

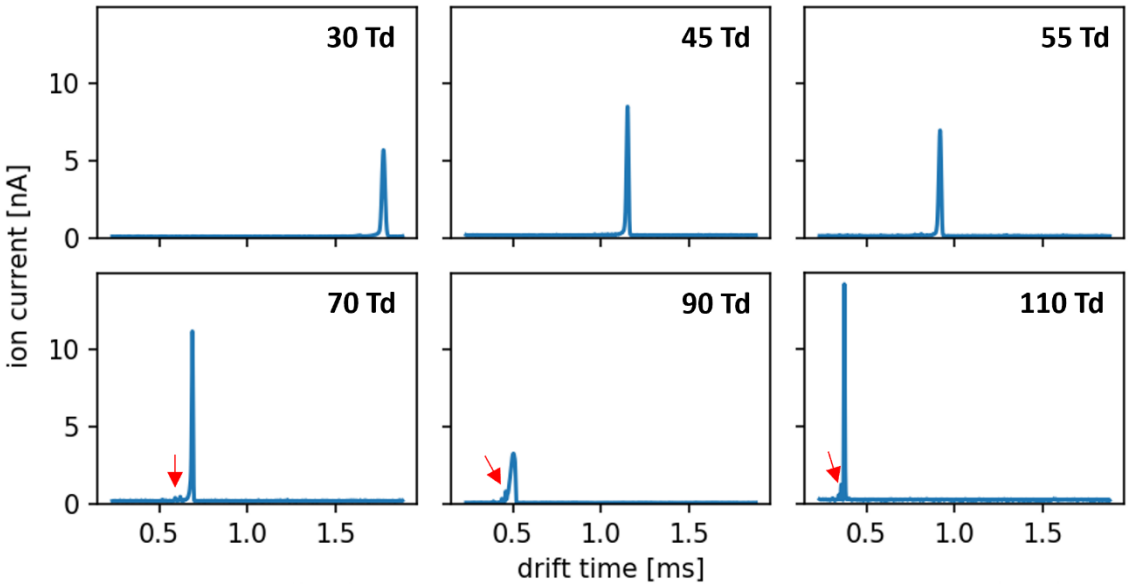

Figure 5.1: HiKE-IM spectra of background water without any analyte added depending on the reduced field strengths *E/N* (*T* = 318.15 K; *p* = 20.5 mbar; *DeP* = -90.8 °C). Red arrows: pre-RIP.

This observation can be attributed to a declustering of the water cluster system through increasing the *E/N*. The decreases in maximum intensity indicate transitions of the dominant cluster species. Erdogdu et al. [18] demonstrated that the third protonated water cluster $[(H_2O)_3+H]^+$ is the dominant species at the lowest *E/N* (see top-left panel in Figure 5.1), which is declustered stepwise to $[(H_2O)_2+H]^+$ (first drop) and $[H_3O]^+$ (second drop). It should be noted that the water cluster system is dynamic, and even at 110 Td, larger clusters are generated and dissociated. Therefore, a mean cluster size arises that depends on the *E/N*. An actual separation of the signals of different cluster species into two independent signals is not possible due to the chemistry of the water cluster system. Nevertheless, with specific settings such as low water mixing ratios and high *E/N*, it is possible to observe a signal with two maxima [18].

In addition to the RIP, a signal formation can be detected in the HiKE-IM spectra at 70 Td, 90 Td and 110 Td at lower drift times, which are marked with red arrows in Figure 5.1. The causative species are characterized by a higher reduced ion mobility, then the reduced ion mobility of the water cluster distribution. These signals, which are summarized as pre-RIP in the following, are reproducible. Allers et al. identified some of the main pre-RIP species as $[NO^+(H_2O)_m]^+$ cluster systems, which should originate in the matrix gas [83].
From Equations 1.3 and 1.4 and the ideal gas law follows that the reduced ion mobility K_0 can be calculated from the drift velocity v_d (t_d/l_d), the *E/N* and the gas number density under standard conditions N_0, as shown in Equation 5.1.

$$K_0 = K \cdot \frac{N}{N_0} = \frac{v_d}{E} \cdot \frac{N}{N_0} = \frac{v_d}{E/N \cdot N_0} \tag{5.1}$$

In Figure 5.2, the *E/N* dependence of the calculated reduced ion mobility is visualized. In the *E/N* ranges from about 45 to about 65 Td and from about 85 to about 100 Td, stepwise increases in reduced ion mobility (K_0-steps) are observable (see gray areas in Figure 5.2), whereby the second step is significantly stronger than the first. The reason for this is the declustering process demonstrated in the Figure 5.1, and it leads to an abrupt increase in the reduced ion mobility by increasing *E/N*. In addition to these individual events, a continued increase is detected over the full *E/N* range. This indicates a reduction in the mean cluster size and a shift of the cluster distribution.

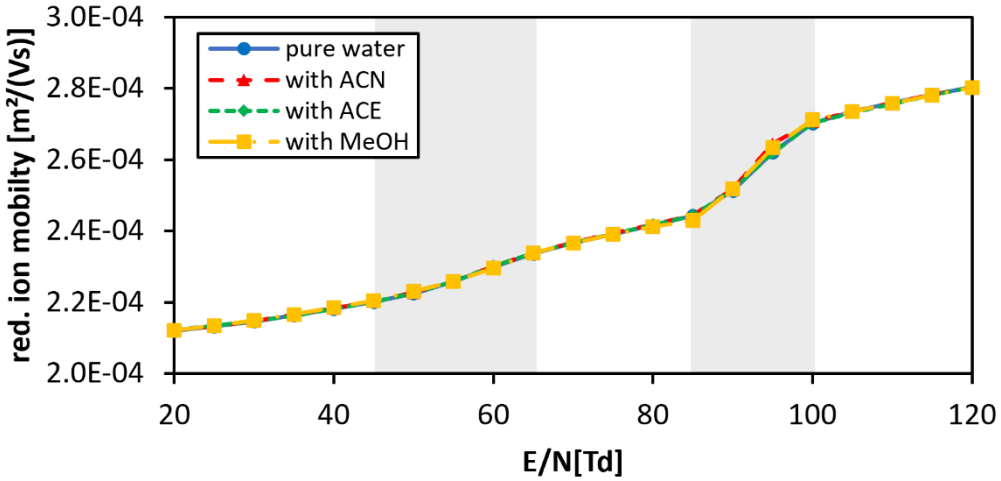

Figure 5.2: Reduced ion mobility K_0 of the water cluster system with and without added analyte depending on the reduced field strength *E/N* (T = 318.15 K; p = 20.0–20.6 mbar; *DeP* = -90.8 °C). Gray areas: stepwise increase in reduced ion mobility.

Furthermore, the lack of an effect from an added analyte in the reaction tube is shown in Figure 5.2. In the mixing ratio range of the analytes as described in Table 5.1, the RIP is totally uninfluenced by the presence of an analyte. On the one hand, this can be explained due to the addition of the analytes into the reaction tube, whereby these should be prevented

from reaching the drift tube as neutral species in a decisive mixing ratio. The cluster dynamic in the drift tube is thus determined by the composition of the matrix gas and not by the added analyte. On the other hand, even if the full analyte mixing ratio were identical in the drift and reaction tube, the influence of modification is totally unexplained and could be negligible. This approach is explored in more detail in Section 5.4. Since the presence of an analyte in the reaction tube does not significantly influence the water cluster system, the RIP is examined below using measurements with ACE added as analyte.

5.1.2 Typical HiKE-IM spectra of protonated analytes

The number of observable signals in a HiKE-IM spectrum depends on the analyte. Therefore, the addition of one analyte often caused more than one new signal, as shown in Figure 5.3. The single main signal of the RIP seems to be an exception, and typically a more complex spectrum results. A possible explanation for this is the presence of multiple chemical species. With one added species and water, there are two potential cluster-forming species present, which, in addition to the separate pure cluster systems, can form mixed cluster systems. Furthermore, potentially different clusters of the analytes can be separated by HiKE-IMS, leading to multiple signals of one solvent cluster system $[S_x+H]^+$. As not each signal is present over the full *E/N* range, and some appear while others disappear, this approach and a chemical relation between different signals seems to be very probable.
In Figure 5.3, typical HiKE-IM spectra of each analyte at varied *E/N* values are shown, and the main signals are marked (analytes: **a-d**; water: **RIP**). The internal analyte species enumeration is based on the reduced ion mobility (from high to low). Due to overlaying of some signals, it is not possible to assign every signal at every *E/N*, even if they are present in the chosen conditions. It should be noted that the unassigned signals are mostly part of the pre-RIP.

*Acetonitrile (**A**)*

The addition of ACN leads to two main signals (**a1** and **a2**), which are not both present at lower *E/N*. As shown for 20 Td (see left panel in Figure 5.3**A**), at first only **a2** is observable as a shoulder of the **RIP**, and in the following, **a2** is completely swallowed by it. At an *E/N* of 60 Td (see right panel in Figure 5.3**A**), both signals (**a1** and **a2**) are observable. The intensity of **a1** starts increasing at about 40 Td, while the intensity of **a2** decreases. Starting from a chemical connection of **a1** and **a2**, a fragmenting/declustering of **a2** to **a1** would explain this observation. Thus, with **a1/2** and the **RIP**, the signals of two different cluster systems are both present, with different typical steps in the reduced ion mobility. As a result, the sequence in which the signals occur changes constantly with increasing *E/N*.

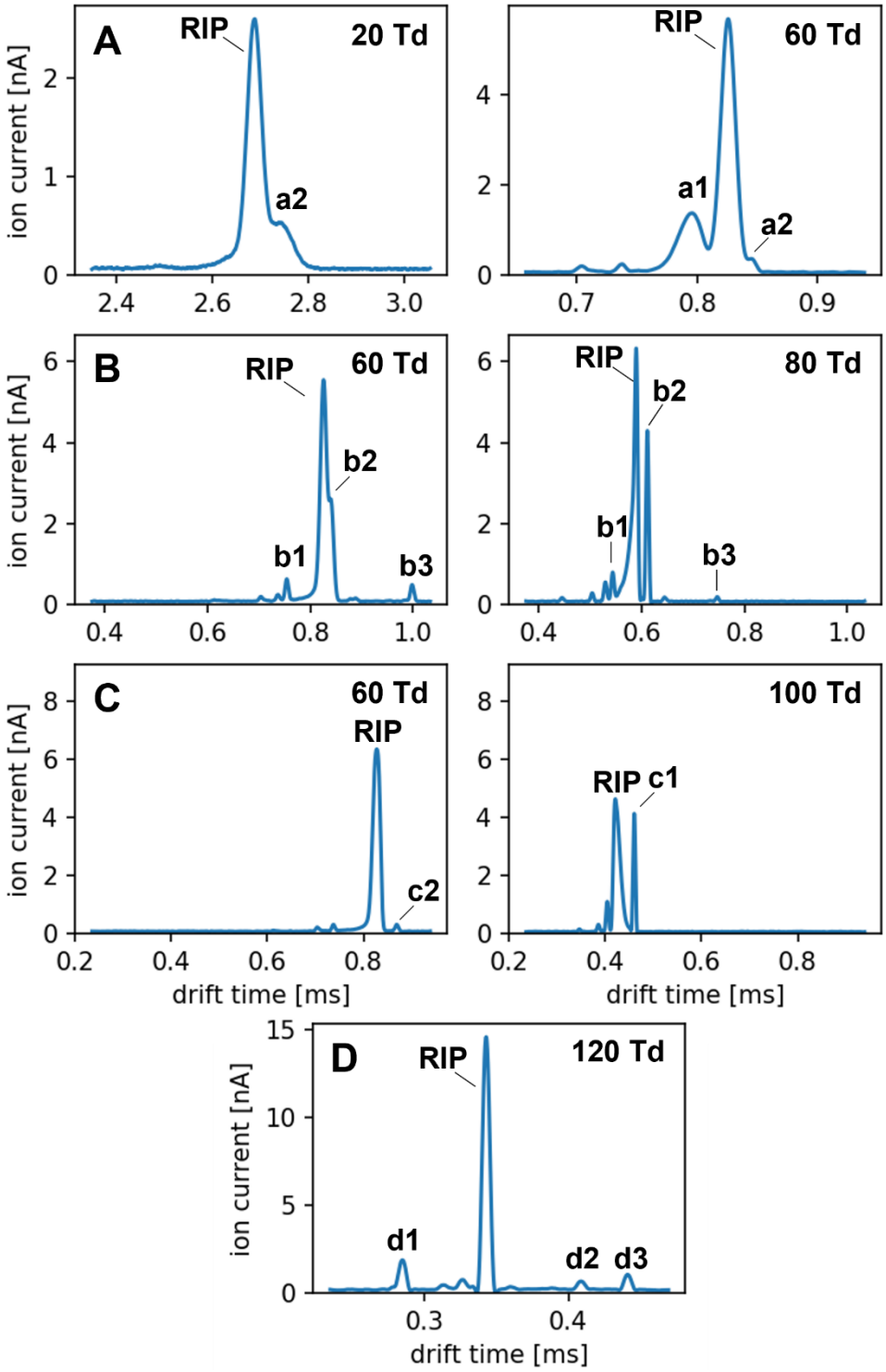

Figure 5.3: HiKE-IM spectra of ACN (**A**), ACE (**B**), MeOH (**C**) and 1,3-diaminopropane (**D**) at selected reduced field strengths *E/N* ($T_{A\text{-}C}$ = 318.15 K, $T_D \approx$ 297 K; *p* = 20.0–20.6 mbar; *DeP* = -90.8 °C).

*Acetone (**B**)*

The measurement of ACE provides three main signals: **b1, b2** and **b3**. Comparing the maximum intensity increase and decrease indicates a reaction (declustering) from **b3** to **b2** (see Figure 5.3**B**). The reduced ion mobility of **b1** is higher than that of the **RIP**. Accordingly, **b1** seems unlikely to be part of the main cluster system of protonated ACE $[(ACE)_n+H]^+$ since even the first cluster ($n = 1$) should have a lower reduced ion mobility than the $[H_3O]^+$ species, as shown by Brachthäuser using classic DTIMS [14]. Therefore, **b1** can be the result of fragmentation or another side reaction in the reaction tube. In addition to the main signals, other analyte-specific low-intensity signals can be detected (e.g., at a drift time of about 0.65 ms at 80 Td; see right panel in Figure 5.3**B**). These signals also show intensity shifts, which suggests chemical correlations. Because of the very low intensity of these signals, a detailed evaluation of them is not provided.

*Methanol (**C**)*

Two analyte-specific main signals (**c1** and **c2**) result from adding MeOH as analyte, which has – compared to the signals of the other analytes – a relatively low intensity (see Figure 5.3**C**) despite having the highest analyte mixing ratio (see Table 5.1). This could indicate a proton transfer to other species. The proton affinity of MeOH (754.3 kJ/mol at 298 K [124]) is higher than that of water (691.0 kJ/mol at 298 K [124]), which should prevent a proton transfer. Nevertheless, the cluster system of water could constitute a proton sink. Based on the low intensity of mostly **c2**, a reliable conclusion of a chemical connection between **c1** and **c2** could not be drawn, but based on the observations of the other analytes, this seems to be possible.

*1,3-Diaminopropane (**D**)*

The addition of 1,3-diaminopropane as analyte causes a high number of new signals in the HiKE-IM spectrum, whereby three main signals can be detected (**d1, d2** and **d3**; see Figure 5.3**D**). These signals do not appear to be connected in a dynamic reaction system, and dimerization or even larger cluster formations ($[(H_2N\text{-}C_3H_6\text{-}NH_2)_m+H]^+$) do not seem to occur. However, analyte-water clusters $[(H_2N\text{-}C_3H_6\text{-}NH_2)_m+(H_2O)_n+H]^+$ can also be assumed here. Possible other sources of these signals are fragmentations (especially for **d1**) or other irreversible reactions in the reaction tube. It should be noted that 1,3-diaminopropane was measured only at a background temperature T_D of about 297 K.

5.2 Humidity effect on cluster dynamic

The steady increase in the reduced ion mobility of the RIP (see Figure 5.2) proves a non-quantified mean cluster size that can assume fractional values. This is crucial for the CCS and thus for reduced ion mobility. As the cluster distribution mainly depends on the water mixing ratio, a change in humidity should show an influence on the reduced ion mobility

of each species that can be clustered by water. This postulated effect was proven by varying the *DeP* (values are listed in Table 5.2).

Table 5.2: Investigated dew points and the corresponding water mixing ratios.

Dew point [°C]	Water mixing ratio [ppmV]*
- 90.8	0.20
-56.6	29.26
- 38.7	138.07

* Calculated with the producer calculator of the dew point meter: *http://www.michell.com/calculator/*

In addition to the humidity effect on the RIP, the humidity effect on the analyte-specific signals of ACN, ACE and MeOH were also investigated.

5.2.1 Influence of humidity on the RIP

Variation in humidity has a strong influence on reduced ion mobility and the maximum intensity of the RIP, as shown in Figure 5.4. Reduced ion mobility decreases with increasing humidity, whereby the difference in reduced ion mobility ΔK_0 between a *DeP* of -90.8 °C and -56.6 °C almost disappears at 120 Td (see blue and red curves in Figure 5.4**a**). Accordingly, the mean cluster sizes are almost identical. The minimum size of the cluster $[H_3O]^+$ acts as a limit on the declustering process, and a further increase of *E/N* leads to a flattening of the curves. In contrast, at the highest humidity (*DeP* = -38.7 °C), the mean cluster size at 120 Td is still higher, and a further declustering process is possible. Consequently, the humidity has not only a quantitative effect on the reduced ion mobility but also a qualitative one.
The sharpest steps in reduced ion mobility (K_0-steps) are observed with the driest matrix gas (blue curve in the top panel of Figure 5.4**a**), but already at a middle humidity (red curve in Figure 5.4**a**), the K_0-steps are flattened. These flatter K_0-steps also start at a higher *E/N*. Due to the increased water mixing ratio, there is a shift to higher mean cluster sizes. This results in a shift of the declustering process. At a water mixing ratio of 138.07 ppmV (*DeP* = -38.7 °C), almost no K_0-steps are observed anymore (see green curve in Figure 5.4**a**). The flatting of the curves can be explained by an increased ion density. This broadens the cluster distribution and statistically smooths the steps.
The maximum signal intensities also indicate a shift of the declustering steps. As shown in Figure 5.1, there are drops in the maximum intensity during K_0-steps. These are clearly observable for each measurement in Figure 5.4**b**. Comparison of the two panels illustrates these observations, which helps to localize the position of the second K_0-step ($[(H_2O)_2+H]^+$ to $[H_3O]^+$). Why the K_0-step at 138.07 ppmV (*DeP* = -38.7 °C) can be detected in the maximum intensity but not in the K_0-curve (see Figure 5.4**a**) cannot be conclusively explained at this point.

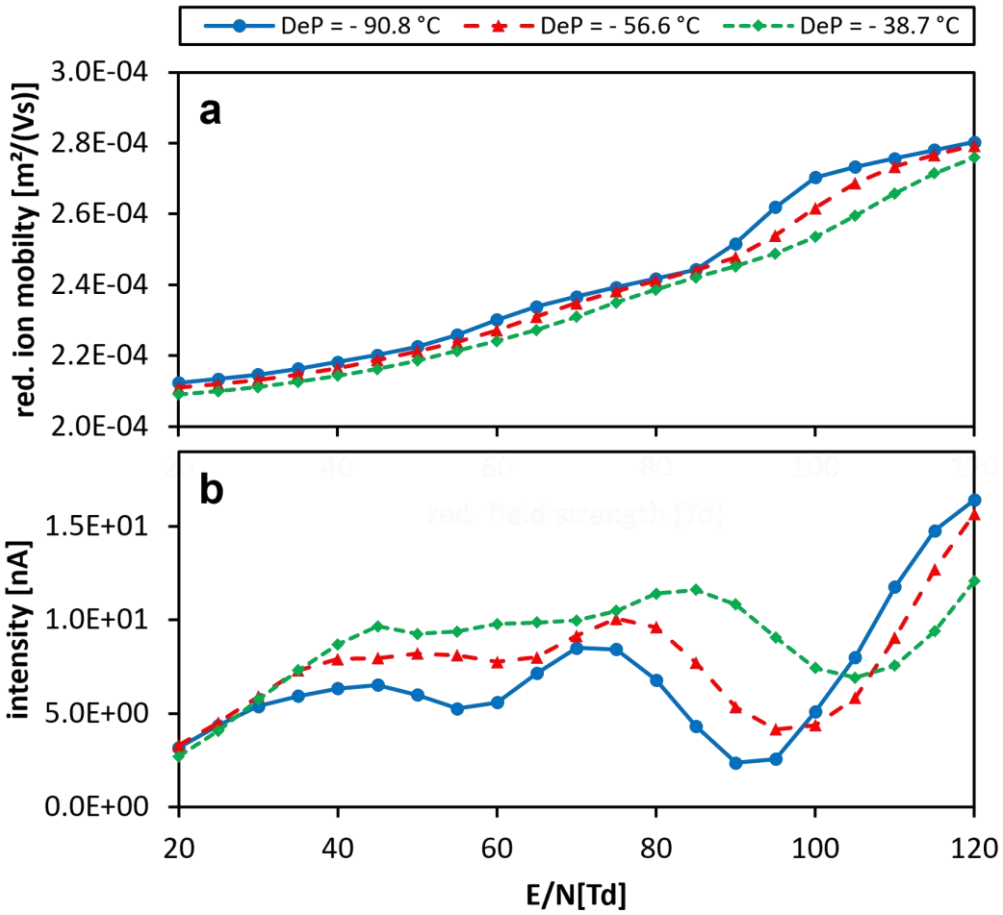

Figure 5.4: Humidity effect on reduced ion mobility K_0 (top panel) and maximum intensity (bottom panel) of the water cluster system depending on the reduced field strength *E/N* (*T* = 318.15 K, *p* = 20.5–20.6 mbar).

5.2.2 Humidity effect on solvent clusters

The effect of humidity on the RIP and therefore on the water cluster system was proven as expected. In addition to increased mean cluster sizes, a resulting greater stability of the individual cluster formations was demonstrated. A similar humidity effect is to be expected for the actively added analytes that form clusters with water.

Acetonitrile

The analyte-specific signals of ACN (**a1** and **a2**) exhibit an increasing reduced ion mobility through increasing *E/N*. The **a1** curve at a *DeP* of -90.8 °C also shows a K_0-step at an *E/N* of about 60 Td (see Figure 5.5). Both indicate the presence of a mixed ACN-water cluster system $[(ACN)_m+(H_2O)_n+H]^+$ and a declustering process at increasing *E/N*. In the literature, there is evidence of such mixed clusters $[(ACN)_m+(H_2O)_n+H]^+$ with a favored ratio of ACN and water ($m = n + 2$) [125]. A pure analyte cluster system is unlikely since a mixing ratio of uncharged ACN, which would be necessary for a similar cluster system, should not be present in the drift tube. An increase in *E/N* leads to a declustering of the water proportion *n* of the mixed cluster system. Equivalent to the observations from the RIP, the decrease in

the mean cluster size causes a steady increase in reduced ion mobility and a K_0-step (see **a1** curves in Figure 5.5). The separation of the different cluster species with regard to the water proportion is prevented, while separation depending on the ACN proportion *m* seems to be possible (declustering from **a2** and **a1)**. A rough estimation of the CCS and reduced ion mobility compared to the RIP suggests that **a2** would be the water-clustered ACN dimer $[(ACN)_2+(H_2O)_n+H]^+$, and, accordingly, **a1** would be the water-clustered ACN monomer $[ACN+(H_2O)_n+H]^+$.

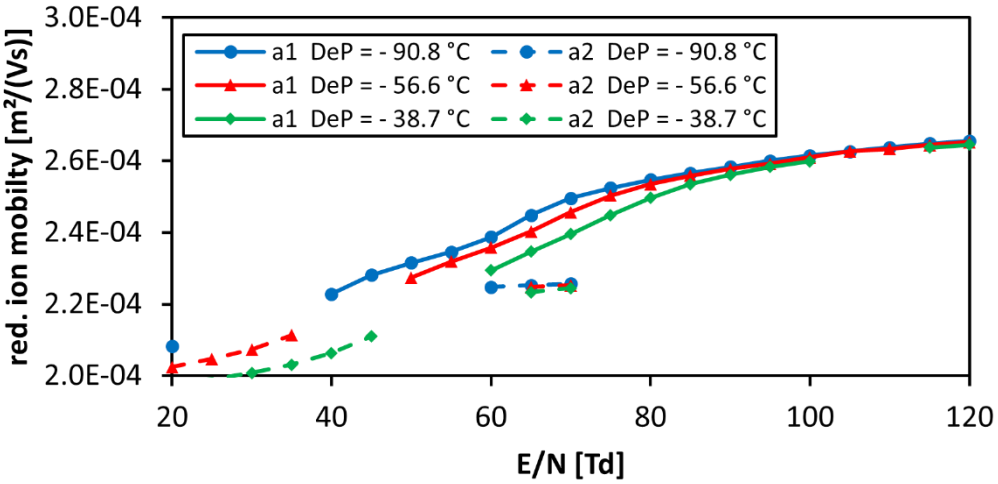

Figure 5.5: Humidity effect on the reduced ion mobility K_0 of the ACN-specific signals depending on the reduced field strength *E/N* (*T* = 318.15 K; *p* = 20.5–20.6 mbar).

The RIP overlays **a1** and **a2** in the HiKE-IM spectra over a long *E/N* range, and thus the **a2** curve could only be guessed at (assignment is possible due to an adjustment with Figure 5.11), but the data at hand also indicate an increase in reduced ion mobility in the low *E/N* range. The **a2** behavior is independent of the humidity from 60 and 70 Td. The bare ACN dimer $[(ACN)_2+H]^+$ seems to be present, and the reduced ion mobility cannot be increased by declustering reactions, with the exception of declustering to **a1**. Also, the reduced ion mobility of **a1** becomes independent of the humidity at about 100 Td, and a flattening of the curve is indicated (see Figure 5.5). At lower *E/N* values, an increase in humidity decreases the reduced ion mobility. Furthermore, a shift of the K_0-step in the curve of **a1** to higher *E/N* because of increasing humidity is observed. Both observations can be explained by an increase in the water proportion *n* of the mixed cluster distribution. Compared to the RIP, the bare protonated ACN $[ACN+H]^+$ seems to be applied at lower *E/N* than the bare $[H_3O]^+$ (compare Figure 5.4). This could indicate a lower binding energy of water to $[ACN+H]^+$ than to $[H_3O]^+$ and a complete declustering at lower *E/N*.

Acetone

The **b1** and **b2** curves are characterized by increasing reduced ion mobility with increasing *E/N* (see Figure 5.6). However, **b1** is a special feature. First, an increase in reduced ion

mobility compared to the RIP indicates that the clustering dynamic with water cannot be the reason for the increase since an absolute lower value would be expected. Furthermore, variation in the humidity has no effect on this signal if it is not overlaid by the RIP. Thus, a dynamic clustering with any species can be detected for **b1** but likely not with water. Interactions with polarized nitrogen as discussed in Chapter 4 are a possible explanation.

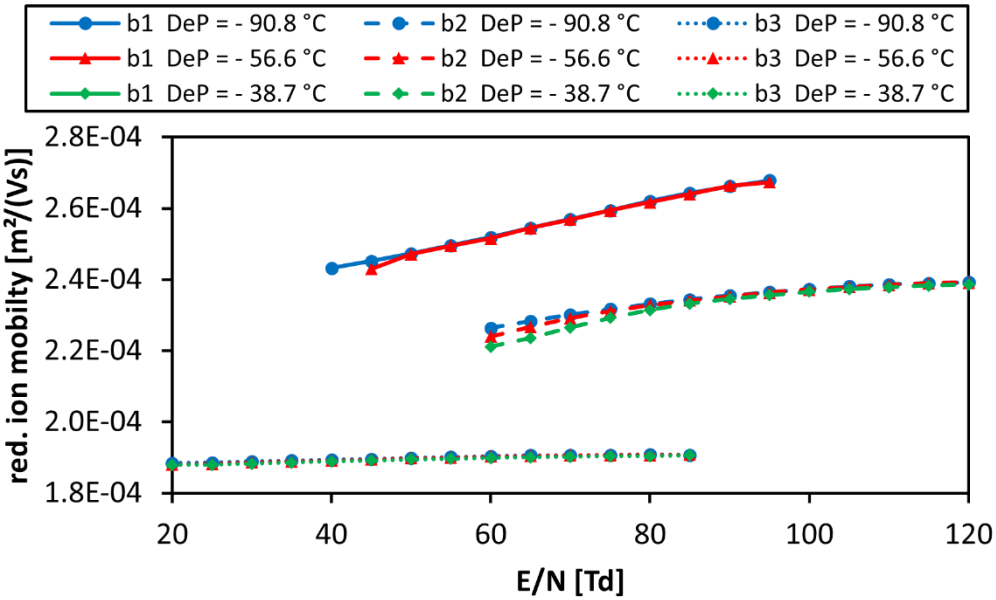

Figure 5.6: Humidity effect on the reduced ion mobility K_0 of the ACE-specific signals depending on the reduced field strength *E/N* (*T* = 318.15 K; *p* = 20.5–20.6 mbar).

On the contrary, the humidity effect on **b2** is comparable to the previous results. The reduced ion mobility is decreased at increased humidity until the *E/N* causes a too small water proportion in the mixed cluster system. Thus, all humidity plots converge between 80 and 90 Td, which is comparable with the **a1** results at about 100 Td (see Figure 5.5).
The **b3** curve is different from all the others so far. Regardless of the humidity and the *E/N*, the reduced ion mobility is almost constant at a value of about 1.9 cm²/(Vs) until the reaction to **b2** takes place, and **b3** disappears (*E/N* > 85 Td; see Figure 5.6). Only a small increase in the reduced ion mobility from 1.88 to 1.91 cm²/(Vs) is observed in Figure 5.6. The **b3** species does not appear to form mixed cluster structures with water, thus explaining the independence from humidity. From IMS-MS experiments, this behavior is known for the protonated ACE dimer $[(ACE)_2+H]^+$ under low-field conditions, and Brachthäuser determined a reduced ion mobility of 1.828 cm²/(Vs) [14]. Therefore, it is likely that the **b3** species is the protonated ACE dimer, which can be declustered to the ACE monomer $[ACE+H]^+$ (**b2**). The ACE monomer $[ACE+H]^+$ can be part of a mixed cluster system with water $[ACE+(H_2O)_n+H]^+$. This also coincides with the literature [14].

Methanol

The effect of humidity on both signals of MeOH (**c1** and **c2**) is very similar to the effect on the ACN species, but no real K_0-steps are observed. Nevertheless, a steady increase in reduced ion mobility also indicates a mixed cluster system of water and MeOH $[(MeOH)_o+(H_2O)_n+H]^+$. Due to the low intensity of the signals of **c1** and **c2**, they disappear almost completely with increasing humidity, which is why deeper interpretations become very hypothetical.

5.3 Temperature effect on cluster dynamic

The background temperature can be varied to a certain extent in the HiKE-IMS. The first measurements were performed at 318.15 K, which was close to the maximum temperature of the used setup. Therefore, the temperature was lowered to about 297 K for a second measurement. The temperature effect on the RIP and the analyte-specific signals of ACN and ACE were investigated. Since the impact of temperature on ion mobility is eliminated by using the reduced ion mobility, detected effects should be based on the interactions of ions and neutral species in the drift tube.

5.3.1 Temperature effect on the RIP

The expected correlation between temperature and cluster distribution is a decreasing mean cluster size with increasing temperature, which was proven for the protonated water cluster system with numeric examinations by Wißdorf et al. [32]. Consequently, the reduced ion mobility of the RIP should also increase, whereby especially in a strong electric field such as in DMS or HiKE-IMS, the effective temperature T_{eff} (see Equation 1.2) must be considered. The experimental investigation yielded the expected effect as shown in Figure 5.7. The decrease in temperature caused a decrease in reduced ion mobility at each *E/N*. Additionally, a shift of the K_0-step to higher *E/N* takes place. Compared to the humidity effect, increasing temperature also causes a decreased mean cluster size and thus a higher reduced ion mobility, but the K_0-steps are not smoothed as with increasing humidity (see Figure 5.4**a**). However, the experimental setup allows only a slight variation of the temperature, which could be an explanation for the leak of a flatter curve in this case (see Figure 5.7). The non-thermal proportion of T_{eff} increases with increasing *E/N*, which is why the constant thermal proportion should become relatively lower. The temperature effect becomes weaker, and an equalization of both curves is expected. Comparison of the two curves in Figure 5.7 confirms this minimally, and it can be proven by the measurement data. While at 20 Td, a ΔK_0 of $5.09 \cdot 10^{-6}$ m²/(Vs) was detected, it dropped to about 61.0% ($3.11 \cdot 10^{-6}$ m²/[Vs]) at 120 Td. However, it must be pointed out that the absolute reduction in reduced ion mobility is relatively low, and thus the decrease in the temperature effect is rather low.

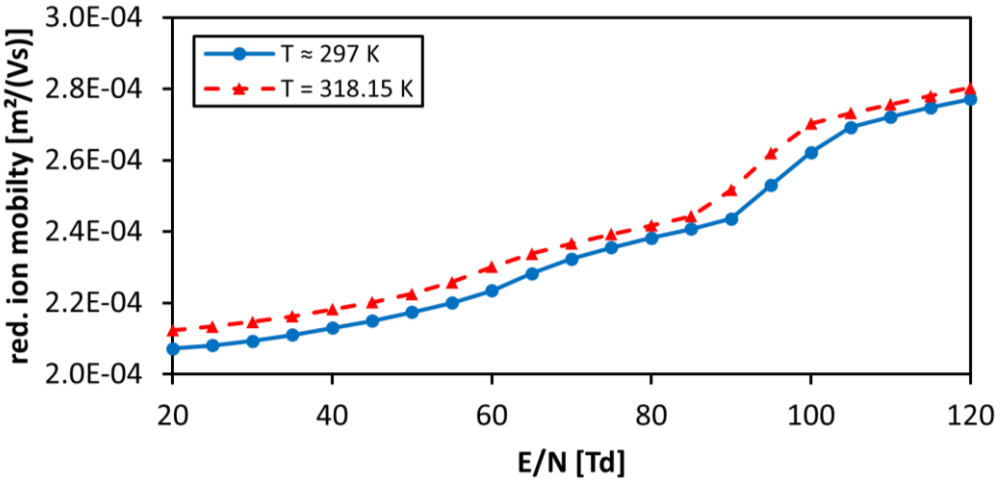

Figure 5.7: Temperature effect on reduced ion mobility K_0 of the protonated water cluster system depending on the reduced field strength *E/N* (*p* = 20.3–20.6 mbar; *DeP* = -90.8 °C).

In addition, a threshold of declustering ($[H_3O]^+$) and convergence of both curves with further increasing *E/N* can be expected. At high *E/N* with a mean cluster size close to 1 (> 110 Td), the temperature effect (see Figure 5.7) is in a similar order of magnitude as the humidity effect, which is indicated by similar differences in reduced ion mobility compared to Figure 5.4**a** (see blue and green curves). This is surprising, especially since in this *E/N* range, T_{eff} should be dominated by the non-thermal part. Nevertheless, the thermal part of T_{eff} still has a significant influence.

5.3.2 Temperature effect on analyte-specific signals

Proceeding from the parallels in behavior shown between the RIP and the analyte-specific signals for the humidity effect, similar behavior is also to be expected with the temperature effect.

Acetonitrile

As shown in Figure 5.8, the temperature effect on the ACN-specific signals is similar to the effect on the RIP. Both have a lower reduced ion mobility in the *E/N* ranges in which the cluster dynamic with water is still present. Especially, the **a1** curves show a shift to lower reduced ion mobility (see Figure 5.8), which decreases with increasing *E/N*. The K_0-step is also shifted to higher *E/N* values. Overall, the temperature effect on the water cluster-based behavior is qualitatively identical to the effect on the RIP. A smaller binding energy to water is again indicated by the decrease of the temperature effect with increasing *E/N*. Furthermore, a weak influence of temperature on the ACN proportion *m* of the mixed cluster $[(ACN)_m+(H_2O)_n+H]^+$ is also observed. The **a2** signal can be detected at higher maximum *E/N* by decreasing the temperature; at 318.15 K, it disappears after about 70 Td, while this point is shifted to about 80 Td at about 297 K. In both cases, the final reduced ion mobility of **a2** is almost identical (see Figure 5.8). The pure ACN clusters (such as

$[(ACN)_2+H]^+$) are more stable at reduced temperature, which can be explained with two theories. First, the significantly smaller reduced ion mobility at 20 Td at lower temperature indicates a higher water proportion *n*. Therefore, this part is declustered before the declustering process of the bare **a2** to **a1** takes place. Accordingly, the larger water proportion *n* of the mixed cluster $[(ACN)_m+(H_2O)_n+H]^+$ protects the bare ACN cluster (protective clustering). The other theory is a declustering process at higher *E/N* due to a decreased T_{eff} resulting from a decreased temperature. Since the thermal proportion of T_{eff} should be decreased with increasing *E/N*, this theory seems rather unlikely.

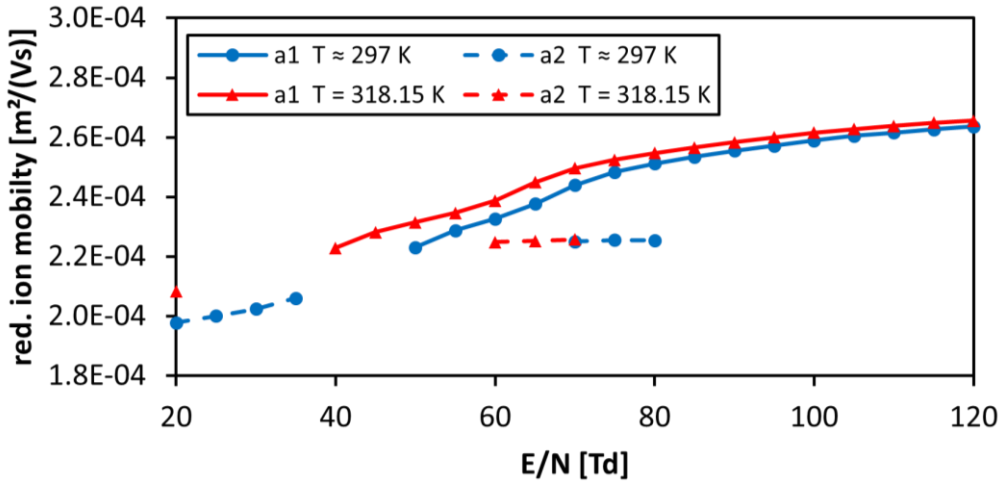

Figure 5.8: Temperature effect on the reduced ion mobility K_0 of the ACN-specific signals depending on the reduced field strength *E/N* (*p* = 20.3–20.6 mbar; *DeP* = -90.8 °C).

Acetone

The ACE-specific signals also show a temperature effect (see Figure 5.9). In particular, the **b2** curve shifts to lower reduced ion mobilities with increasing temperature, and this effect decreases with increasing *E/N*. A strong absolute temperature effect compared to the humidity effect is observed, which is reflected in a large ΔK_0 obtained by increasing the temperature (compare **b2** curves in Figures 5.6 and 5.9). Surprisingly, there is a small but still recognizable temperature effect on **b3**. The reduced ion mobility at 20 Td decreases with decreasing temperature (see Figure 5.9). This could indicate cluster formations of the ACE dimer $[(ACE)_2+H]^+$ with any species in the drift tube, albeit this is a very weak hypothesis. This observation also explains the small shift resulting from the total disappearance of the **b3** signal by 5 Td (from 85 to 90 Td). Interactions of the protonated ACE dimer $[(ACE)_2+H]^+$ with polarized nitrogen seem to be possible (compare Chapter 4), but these can be neglected at higher temperatures.
The special character of **b1** is observed here again. Based on the nearly non-existent humidity effect on **b1** and the knowledge of the other investigated species, no temperature effect would be expected. It is therefore surprising that a stronger effect compared to the

effect on other species is observed (see Figure 5.9). An almost parallel shift to lower reduced ion mobilities results from decreased temperature. This observation indicates an unknown cluster-like dynamic such as strong interactions with polarized nitrogen.

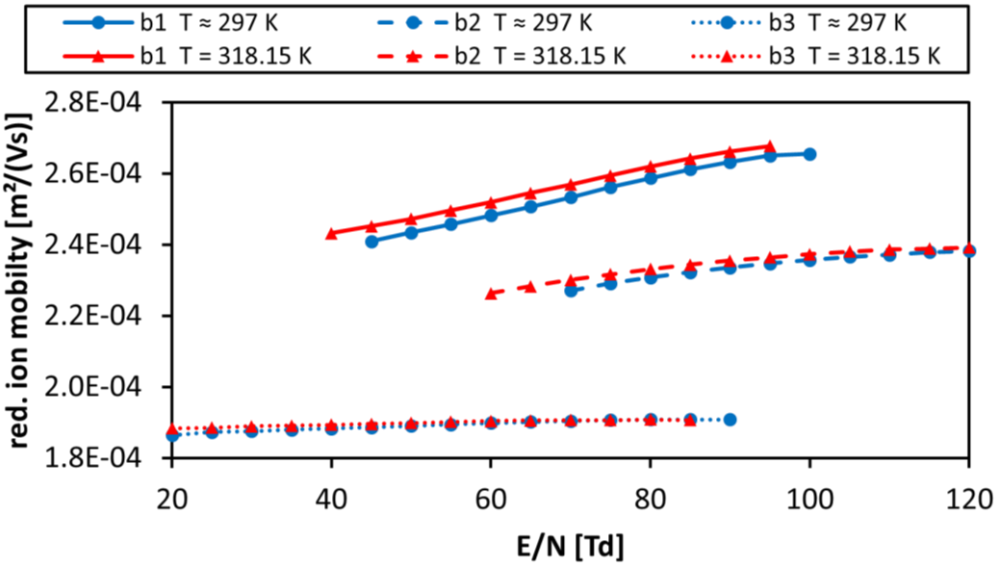

Figure 5.9: Temperature effect on the reduced ion mobility K_0 of the ACE-specific signals depending on the reduced field strength *E/N* (*p* = 20.3–20.6 mbar; *DeP* = -90.8 °C).

5.4 Chemical modification in HiKE-IMS

The unavoidable chemical modification with water and the effect on the cluster dynamic was investigated in Section 5.2. However, water is not one of the most common modifiers typically added, for example in DMS, but the observations demonstrated the effect of chemical modification in HiKE-IMS. The unintentional humidity effect is important to understanding the chemistry in those systems, but the effect of intentional modification is also of great interest. Therefore, ACN and ACE were added as modifiers to the matrix gas of the drift tube, and the effects on the cluster dynamics of ACN, ACE and 1,3-diaminopropane were examined. The modifier mixing ratios were in similar ranges as the analyte mixing ratios (ppbV to ppmV range) and significantly lower than the modifier mixing ratios in DMS (% range). The cluster effect on the RIP was measured, but the set modifier mixing ratios did not cause any deviations in reduced ion mobility, and the resulting plots were identical to the modifier-free one shown in Figure 5.2. Therefore, a more detailed consideration is omitted.

5.4.1 Acetonitrile

Modification with ACN (about 1.6 ppmV) has a massive effect on the HiKE-IM spectra of ACN, as shown in Figure 5.10. Compared to the modifier-free spectra (see Figure 5.3**A**),

the ACN-specific signals have a significantly higher maximum intensity. The whole spectrometer was pumped at the front end of the reaction tube; the modified matrix gas was also pumped through the reaction tube, and the modifier became analyte as well. This increased the mixing ration of the analyte and as a result the signal intensity.

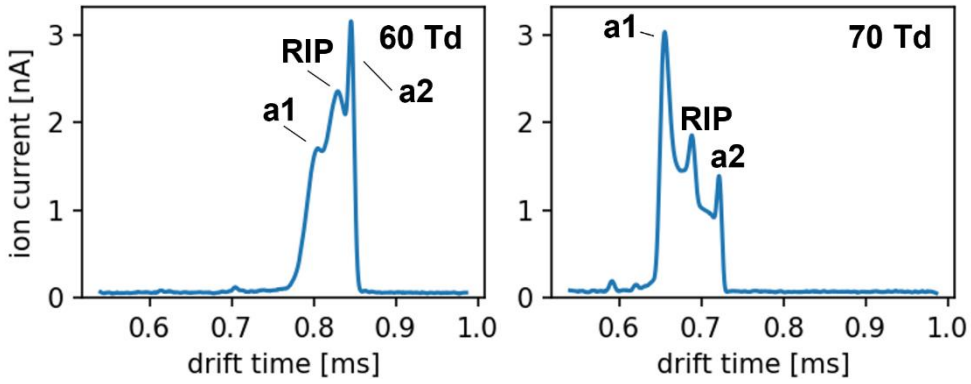

Figure 5.10: HiKE-IM spectra of ACN as analyte and as chemical modifier added to the matrix gas in the drift tube (about 1.6 ppmV) at selected reduced field strengths *E/N* (*T* = 318.15 K; *p* = 20.5 mbar; *DeP* = -90.8 °C).

In addition to the quantitative increase in the signal intensities, a qualitative effect was also obtained by modification with ACN. The chemical connection of **a1** and **a2** had so far been determined primarily by apparent coupled intensities of both signals through increasing *E/N*, but because of a sufficiently large mixing ratio of neutral ACN in the drift tube, a dynamic clustering-declustering process becomes observable in Figure 5.10. In the right panel (70 Td), a plateau between **a1** and **a2** is clearly visible. Through modification with ACN, the declustering from **a2** to **a1** becomes smoother and less quantized. Accordingly, one ionic species can have different cluster sizes due to the ACN proportion *m* of the mixed cluster $[(ACN)_m+(H_2O)_n+H]^+$ in one measurement cycle (middle reduced ion mobility). If the mixing ratio of the modifier is increased further, a stronger equalization of both defined signals would be expected through an increase in the plateau level. Thus, signal broadening as an indicator of the declustering step would be observed as is known in RIP behavior (compare Figure 5.1). This observation proves the dynamic of the clustering-declustering process even under constant conditions if a neutral modifier is present in a sufficiently high mixing ratio. This conclusion has implications that are also essential for the interpretation of other results. Therefore, it must be considered for interpretation of IM spectra and makes the chemical processes in DMS even more complex.

Modification with ACN causes only a small impact on the reduced ion mobility of **a1** in a small *E/N* range, while the reduced ion mobility of **a2** is almost independent of the added modifier (see Figure 5.11). In the *E/N* range from 45 to 55 Td, a small reduction in reduced ion mobility of **a1** is observed through the addition of ACN. A low mixing ratio of 39 ppbV is sufficient for this purpose. Overall, the effect is significantly weaker than the humidity and temperature effects (see Figure 5.11). With an *E/N* over about 80 Td, the modification seems to be insignificant for the reduced ion mobility of **a1**, while it still increases due to a

declustering of the water proportion *n* of the mixed cluster $[(ACN)_m+(H_2O)_n+H]^+$. Accordingly, the water proportion seems to still be the dominating factor that mainly determines the reduced ion mobility of **a1** and **a2**.

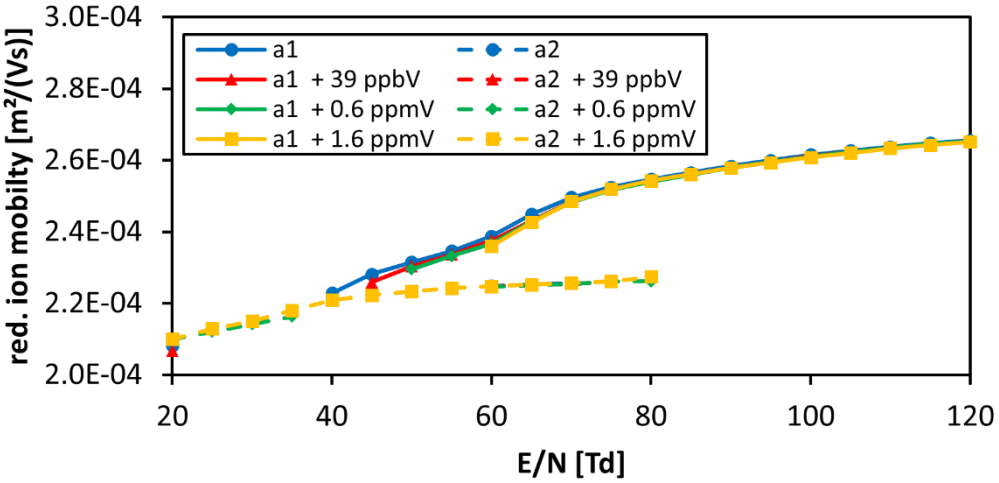

Figure 5.11: Effect of gas-phase modification with ACN on the reduced ion mobility K_0 of the ACN-specific signals depending on the reduced field strength *E/N* (*T* = 318.15 K; *p* = 20.5–20.6 mbar; *DeP* = -90.8 °C).

More assumptions regarding the ACN proportion *m* can be drawn from the occurrence of **a1** and the disappearance of **a2**. Since **a2** is the main signal in the *E/N* range from 20 to 65 Td with a modifier mixing ratio of 1.6 ppmV, the qualitative curve becomes observable, and the expected flatting of the curve as a result of the complete declustering of the bare ACN dimer $[(ACN)+H]^+$ is indicated (see Figure 5.11). In addition, the complete disappearance of **a2** is shifted to higher *E/N*, and the occurrence of **a1** is shifted in the same direction. This indicates that the cluster distribution (ACN proportion *m*) is postponed to higher mean cluster sizes by increasing the ACN mixing ratio, although no significant shifts in the curves to different reduced ion mobilities are observed in Figure 5.11. This is due to the resolution of the different cluster species. The ACN monomer and ACN dimer (potentially clustered with water) are separated in HiKE-IMS, so increasing the ACN mixing ratio leads to a relative shift in intensity to the signal of the larger cluster species (increase in mean cluster size), but the reduced ion mobilities of the individual species remain almost unchanged. If the plateau is high enough to merge the two signals, a significant effect is expected through modification with ACN on the reduced ion mobility of the overall signal.

5.4.2 Acetone

A plateau between two chemically connected signals is also observed when ACE is modified with ACE (2.2 ppmV). Equivalent to the ACN results, the declustering process from **b3** to **b2** is proven in this way (see right panel [85 Td] in Figure 5.12). Accordingly, the formation of a plateau can be classified as a common indicator for dynamic chemical connection, as in a cluster system. The signal at a drift time of about 0.8 ms at 65 Td (see left

panel in Figure 5.12) arises also without modification in Figure 5.3**B**, and thus it seems to be independent from the cluster system including **b2** and **b3**. The **b1** signal behaves qualitatively almost independent from the modification, and only a low increase in the baseline in its area is recognizable (see Figure 5.12). It should be noted that also for ACE, the intensity of the analyte-specific signals increases absolutely, especially relative to the RIP compared to the modifier-free measurement (see Figure 5.3**B**).

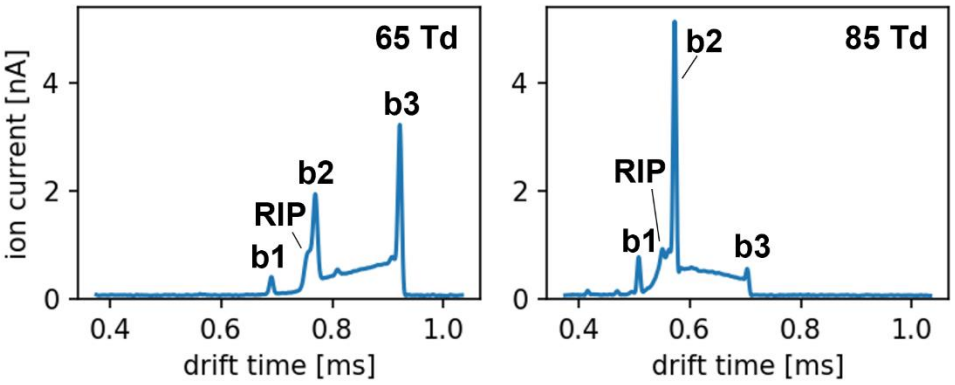

Figure 5.12: HiKE-IM spectra of ACE as analyte and as chemical modifier added to the matrix gas in the drift tube (about 2.2 ppmV) at selected reduced field strengths *E/N* (*T* = 318.15 K; *p* = 20.5 mbar; *DeP* = -90.8 °C).

A cluster effect on the reduced ion mobilities of **b1**, **b2** and **b3** is not observable in Figure 5.13. Independent from the modifier mixing ratio, the curves of reduced ion mobility are not shifted. Accordingly, clustering with water seems to be the most critical parameter for the reduced ion mobility variation of these chemical systems, except for **b3**, which is still almost independent from *E/N*. A deviation of **b3** at an *E/N* of 90 Td with 87 ppbV ACE in the matrix gas (see Figure 5.13) could be the result of extremely low signal intensity in combination with the still present plateau, which makes the accurate determination of the drift time difficult. The explanation of low signal intensity also applies to the deviation of **b1** at 45 Td and the modifier mixing ratio of 2.2 ppmV. As a result of a modifier mixing ratio of 2.2 ppmV, the **b2** signal is no longer overlaid by the RIP in the *E/N* range from 25 to 60 Td, and a small K_0-step becomes visible in Figure 5.13. This indicates the presence of mixed ACE-water clusters $[(ACE)_p+(H_2O)_n+H]^+$. The **b1** signal is also no longer overlaid by the RIP (+ 2.2 ppmV) and shows a steadily increasing reduced ion mobility with increasing *E/N* up to 120 Td. Even after reviewing all the data, it is still not possible to clarify exactly which chemical system is the source of this signal. It must be a clustering system, which in the observed range is not based on clustering with water (lack of humidity effect). Furthermore, it is not a pure ACE cluster $[(ACE)_x+H]^+$ since it has a higher reduced ion mobility than **b2,** the specific signal of the ACE monomer clustered with water $[(ACE)+(H_2O)_n+H]^+$. However, the presence of ACE in the reaction tube is necessary for the observation of **b1**. Therefore, a fragment of ACE or contamination in the liquid ACE could be the source of **b1**.

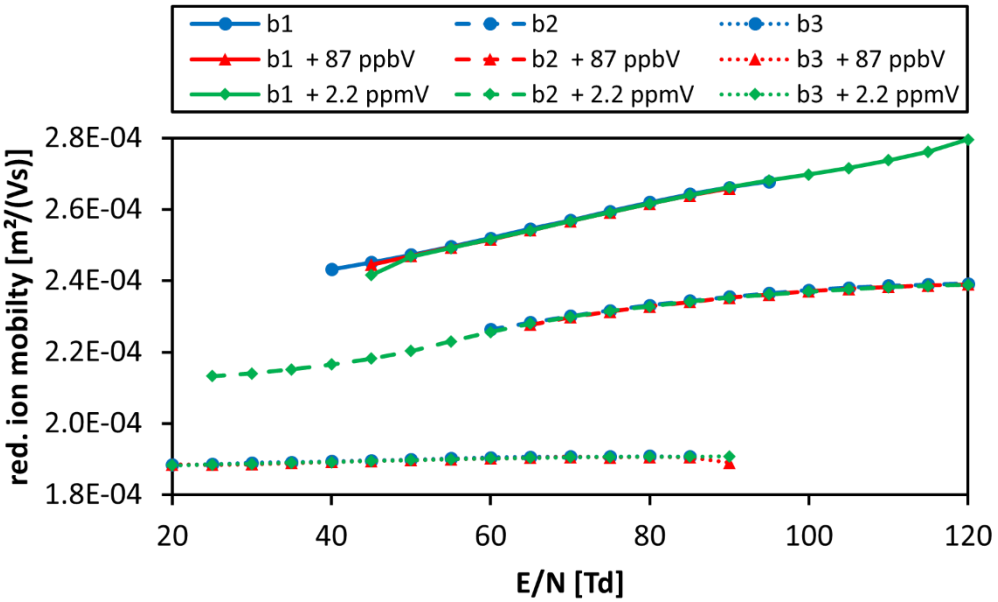

Figure 5.13: Effect of gas-phase modification with ACE on the reduced ion mobility K_0 of the ACE-specific signals depending on the reduced field strength *E/N* (*T* = 318.15 K; *p* = 20.5–20.6 mbar; *DeP* = -90.8 °C).

The modification of ACE leads to results comparable to the ACN measurements. The HiKE-IM spectra can be analyzed to detect the signals of chemically connected species, while reduced ion mobility remains almost unchanged for each species.

5.4.3 1,3-Diaminopropane

In a departure from the previous measurements, 1,3-diaminopropane was not modified with itself but with ACN and ACE. This allowed readjusting the qualitative conditions that prevailed during the DMS investigations of the diamine series (compare Chapter 4). Since the modifier in this setup always acts as an analyte, the main impact on the HiKE-IM spectra is the addition of the respective analyte spectra. While the pure 1,3-diaminopropane spectrum is characterized by an evaluable number of signals (see Figure 5.3**D**), the chemical modification leads to significantly higher complexity (e.g., mixed cluster systems of up to three different molecules). In addition, these experiments were performed at about 297 K, which led to broader signals. The analyte-specific signals **d1**, **d2** and **d3** have low maximum intensities even without a modifier (see Figure 5.3**D**), and the addition of several new signals ensures that these are often overlaid. Therefore, there is no assignable signal for a large *E/N* range, as shown in Figure 5.14. Whether this is a resolution problem or the 1,3-diaminopropane-specific signals are chemically suppressed cannot be conclusively clarified. In addition, no plateau formation can be observed between the **d1**, **d2** and **d3**. Due to the very complex spectra, it is possible that analyte-modifier clusters are generated, but accurate assignment or determination of each signal is not possible with the setup used. By separating the gas systems of the drift tube and the reaction tube, the modifier would not become an additional analyte, and the spectra should become cleaner. Additionally, a

HiKE-IMS-MS coupling could allow an accurate assignment of signals to chemical species. The hardware adaption necessary for this would be very complex and not feasible within the scope of this work.

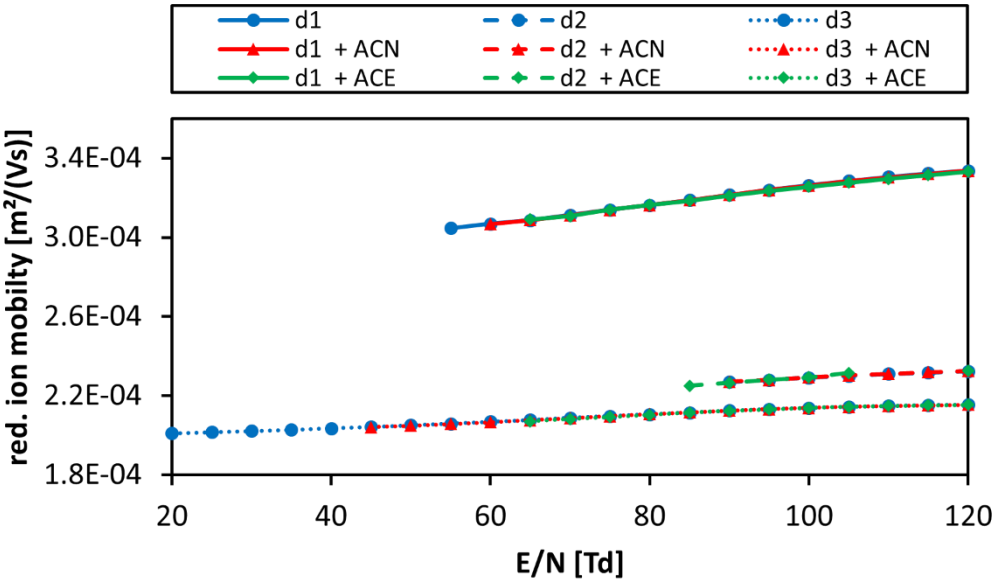

Figure 5.14: Effect of gas-phase modification with ACN (1.6 ppmV) and ACE (2.2 ppmV) on the reduced ion mobility K_0 of the 1,3-diaminopropane-specific signals depending on the reduced field strength E/N ($T \approx 297$ K; $p = 20.5–20.6$ mbar; $DeP = -90.8$ °C).

However, it can be stated that the calculated reduced ion mobility of each species is independent from the presence of a modifier. Figure 5.14 shows no effect of modification with ACN or ACE on reduced ion mobility, while clustering (e.g., with water) is proven by the steady increase in reduced ion mobility with increasing E/N. Thus, the modifier mixing ratio seems to be too low to result in a similar effect, or the analyte-modifier clusters could be separated from the analyte-specific signals **d1**, **d2** and **d3**, as mentioned previously. Compared to the DMS conditions discussed in Chapter 4, the modifier mixing ratio is several orders of magnitude lower in the HiKE-IMS experiments, which may explain the discrepancy.

5.5 Summary and conclusion

The cluster dynamics of ions and neutral species as well as dependence on the reduced field strength were demonstrated and investigated using HiKE-IMS measurements. Experiments involving variations in several reaction conditions such as humidity, background temperature and the presence of a chemical modifier in the drift gas were performed. The reduced ion mobility was used as a measurement variable, and the individual HiKE-IM spectra were analyzed and compared.

Since the water cluster system is always present, the resulting RIP is always part of the spectra and was therefore used as a benchmark. It is not possible to resolve the water cluster system; therefore, the RIP was acquired as a single signal over the entire *E/N* range and the resulting spectra allow a general study of the cluster dynamics. For the RIP, a steady increase in reduced ion mobility was proven with increasing *E/N* (see Figure 5.2). The steady curve can be explained by a decreasing fractional mean cluster size, which proves a dynamic clustering/declustering process even under constant conditions such as in HiKE-IMS as well as under an inconstant electric field (e.g., in DMS). Simultaneously, a stepwise declustering at specific *E/N* values explains the detected K_0-steps. Numerical results that confirm and almost perfectly recreate the cluster dynamic were presented by Erdogdu et al. [18]. The water cluster distribution is influenced by the humidity as well as the temperature. An increase in humidity leads to an increase in mean cluster size, while an increase in temperature decreases that mean cluster size. These cause a variation in reduced ion mobility and a shift in the K_0-steps (see Figures 5.4 and 5.7). Therefore, it is shown that the higher the humidity and the lower the temperature, the higher is the mean cluster size, and both effects decrease with increasing *E/N*. The addition of ACN or ACE as modifier had no qualitative impact on the RIP.

The addition of a solvent *S* as analyte into the reaction tube led to the formation of mixed clusters $[(S)_m+(H_2O)_n+H]^+$. Thereby, the number of signals appearing in the HiKE-IM spectra varied strongly with the analyte (see Figure 5.3). The humidity as well as the temperature effect on the most analyte-specific signals were qualitatively identical to the effects on the RIP. An increase of the mean water portion *n* can be forced by increasing the water mixing ratio. Furthermore, reversible chemical connections between **a1** and **a2** (ACN-specific signals) and **b2** and **b3** (ACE-specific signals) were proven by the formation of a plateau through adding a modifier (see Figures 5.10 and 5.12). Even the plateaus prove a dynamic cluster process in the drift tube. Variations in reduced ion mobility could not be observed due to the separation of the specific signals. Therefore, the modification leads to a shift in maximum intensity as a result of the cluster distribution to higher cluster sizes (increasing mean cluster sizes). In addition, the modifier mixing ratios were very low, especially compared to the modifier mixing ratio in DMS. However, the detected water mixing ratio of about 0.20 ppmV (*DeP* = -90.8 °C; see Table 5.2) was significantly lower than the maximum modifier mixing ratios for most measurements and produced clearly observed effects on reduced ion mobility. Accordingly, water could have a much higher tendency to cluster formation, or the measured *DeP* was significantly too low. Furthermore, separation of the different mixed clusters $[(S)_m+(H_2O)_n+H]^+$ is impossible due to the water proportion *n*. Therefore, the analyte-specific signals are generated by clusters with decreasing *n* and increasing *E/N*, which explains the variation in reduced ion mobility.

A reliable identification of species was only possible in individual cases (such as **b3** as the protonated ACE dimer). For a reliable identification of all species and, accordingly, the chemical reactions in the drift tube, a hardware modification is necessary. First steps have been made by Allers et al., who presented a HiKE-IMS-MS coupling to identify chemical species as sources of selected signals such as parts of the pre-RIP [83].

In summary, it can be stated that even under constant energetic conditions, the presence of a chemically active species (e.g., water) leads to a dynamic cluster process. Thus, the detected signals in a HiKE-IM spectrum can only in a few very special cases be assigned to one ion or charged cluster. Instead, most signals result from a dynamic chemical system and must be interpretated in that context. This chemical dynamic is also expected in other analytical methods such as DTIMS and must therefore be considered.

6 Enantiomeric separations by stereoselective clustering

In many scientific fields such as medicine (pharmacy and diagnosis), chirality is of great importance [79, 90]. Thus, reliable analytical methods for a qualitative enantioselective determination and for a quantitative determination of the enantiomeric distribution are of interest in these areas. As discussed in Section 1.4, chromatographic methods for enantiomeric separation in the gas phase are typically based on a complex sample preparation (e.g., stereoselective derivatization), or on chromatography with a chiral stationary phase [92]. Alternatively, enantiomeric separation can be realized by generating achiral complexes with defined chiral reference species [93–96]. In this way, compound-specific properties such as the CCS or the *m/z* ratio are varied enantioselectively. However, the method presented by Dwivedi et al. [79] differs significantly from all others, since it allows an enantiomeric separation without extensive sample preparation or a chiral stationary phase. Instead, the method is based on the addition of a chiral modifier (enantiopure 2-BuOH) to the drift gas of an IMS system, which leads to enantioselective cluster formation. The clusters are characterized by a different ion mobility. As a result, enantiomeric separation could be demonstrated for a wide range of chiral analytes (e.g., chiral amino acids) [79].
Based on the findings on cluster dynamics in DMS and HiKE-IMS and the work of Dwivedi et al. [79], a transmission of the underlying principle on DMS might be possible and would offer a new method for enantiomeric separation. This approach is investigated experimentally. Initially, the most promising analytes and the optimal analyte-specific conditions for a separation based on clustering with enantiopure 2-BuOH are identified. In addition to the DMS parameters, the ionization conditions and method are also in focus. Thereby, bare ions entering the DMS cell seem to have the best preconditions for successful enantiomeric separation, as these enable optimal interactions with the modifier. Therefore, the presence of charged nanodroplets as a result of electrospray ionization, which could disturb the enantiomeric separation, is investigated. These have already been documented for the measuring system used [60]. Under the optimized conditions, enantiomeric separation with enantiopure 2-BuOH is tested for two analytes (Maruoka catalyst and phenylalanine). Additionally, a numerical proof of concept is performed and compared with the experimental results.

6.1 Preliminary measurements

The most appropriate chiral analytes are selected from several candidates based on the results of preliminary measurements. Accordingly, a group of chiral amino acids (serine, threonine, phenylalanine, and tryptophan) are examined as potential analytes, since they were also successfully separated in the work of Dwivedi et al. [79]. In addition to the amino acids, the Maruoka catalyst is also considered. This catalyst, which was first developed by the group of Keiji Maruoka of Kyoto University (Japan), is used in enantioselective syntheses as a phase-transfer catalyst [126]. The amino acids and the Maruoka catalyst are chiral species; however, there are significant differences in chirality. The amino acids have stereocenters at the carbon atom bonded to the amino group, which is the charged position after protonation, while the Maruoka catalyst is axially chiral and thus has a chirality axis through the charged position. As a result, the chiral information should be stronger at the cluster center compared to the amino acids, which could favor enantioselective cluster formation and also enantiomeric separation in DMS.
Through various adjusted preliminary measurements using racemic (rac.) 2-BuOH as gas-phase modifier, possible observable stereoselective interactions of the analytes with the modifier and the optimized measurement conditions are investigated. In this way, the analytes with the highest chance of a successful enantiomeric separation are determined and selected for the later investigations.

6.1.1 Amino acids

The chiral amino acids $^{L/D}$AA were selected based on the results of Dwivedi et al. [79]. In these experiments, the amino acids were characterized by large absolute reduced ion mobility differences between both enantiomers caused by the addition of (*S*)-2-BuOH (10 ppm) into the gas phase in an IM spectrometer. This stereoselective effect was strong enough to cause an observable enantiomeric separation. In addition, α-amino acids belong to standard analytes; their behavior, therefore, is well known and their fundamental clustering process is assumed to be given. For each amino acid, two enantiopure solutions (L and D enantiomer) were assayed at a concentration of 0.1 mmol/L in a mixture of MeOH/water (1:1). Furthermore, an optimized setting designed for a maximum intensity of the signal of the protonated analyte $[^{L/D}AA+H]^+$ was established for each amino acid. The internal modifier pump was removed and replaced with an external syringe pump that allows an infinite variation of modifier mixing ratio and lower mixing ratios than the peristaltic pump used as the default.

Optimization of the modifier mixing ratio

The addition of rac. 2-BuOH as gas-phase modifier leads to a strong cluster effect. Even a low modifier mixing ratio of 0.15% leads to a significant shift in *CV* to negative values for each protonated amino acid $[^{L/D}AA+H]^+$. As a result, at an *SV* of 3500 V, *CV* values in the range from -52.35 ± 0.05 V (L-serine) to -31.86 ± 0.14 V (L-tryptophan) were detected.

The strong cluster effect should be advantageous for a stereoselective separation, since even small relative differences between the behavior of both enantiomers could lead to an observable absolute difference in the *CV*.
Even when the modification was carried out with rac. 2-BuOH, minor differences in *CV* were observed between the two enantiomers of the same amino acids. These are explainable with measurement inaccuracies and must also be considered for the addition of enantiopure modifier. An enantiomeric-independent cluster effect was expected, since rac. 2-BuOH was used as modifier. Thus, stereoselective clustering of one enantiomer of an amino acid with one enantiomer of the modifier is balanced by the mirrored analyte-modifier combination. A further reduction of the modifier mixing ratio to 0.05% leads to a significant weakening of the cluster effect. The influence of ion size—specifically the CCS of the ion on the cluster effect, which was demonstrated in Chapter 4— is also evident for these analyte systems. The strength of the cluster effect decreases with increasing relative ion size compared to the modifier.

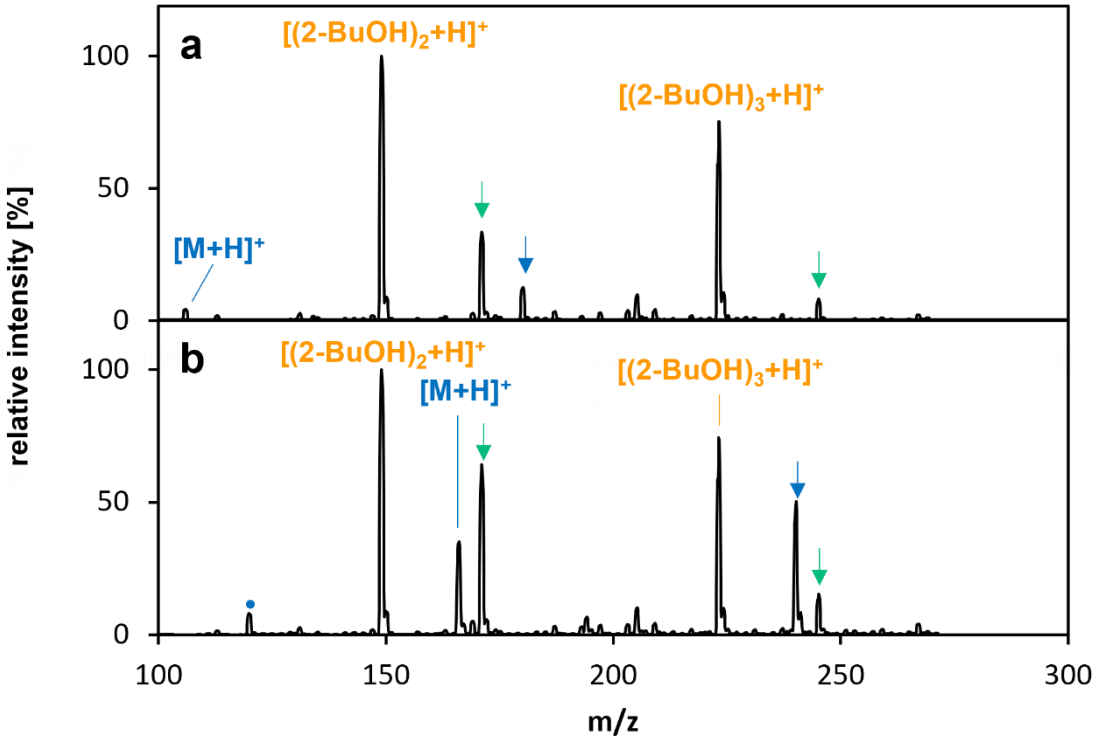

Figure 6.1: Mass spectra of D-serine (**a**) and D-phenylalanine (**b**) recorded with rac. 2-BuOH (0.15%) added as gas-phase modifier in nitrogen. Blue: protonated analyte $[M+H]^+$ and analyte-solvent cluster $[M+S_y+H]^+$ (arrows). Green arrows: protonated solvent-2-BuOH cluster $[(2\text{-BuOH})_x+S_y+H]^+$. Yellow: protonated 2-BuOH clusters $[(2\text{-BuOH})_x+H]^+$.

The chiral information and the stereoselective activity of an enantiomer should decrease with increasing distance from the stereocenter. As a result, an increasing mean cluster size leads to a decreasing chance of an enantiomeric separation. Therefore, a low modifier mixing ratio and resulting small mean cluster sizes are to be preferred to preserve the chiral

information. Consequently, a balance must be found between the strength of the cluster effect and the mean cluster size. To estimate the mean cluster sizes, the mass spectra of protonated D-serine and D-phenylalanine (modified with 0.15% rac. 2-BuOH) are represented in Figure 6.1. The protonated amino acids $[^{L/D}AA+H]^+$ and their modifier clusters $[^{L/D}AA+(2\text{-}BuOH)_x+H]^+$ are marked blue, the protonated modifier clusters $[(2\text{-}BuOH)_x+H]^+$ are marked yellow, and the protonated mixed modifier-solvent clusters $[(2\text{-}BuOH)_x+S_y+H]^+$ are marked green (see Figure 6.1). The mass spectra show qualitative parallels. Thus, the main signal is generated by the second modifier cluster $[(2\text{-}BuOH)_2+H]^+$, while the signal of the $[M+H]^+$ species is only a side signal even at a low modifier mixing ratio. As shown in Figure 6.1**a**, protonated serine is nearly completely suppressed, but larger amino acids such as phenylalanine lead to a well observable signal (see Figure 6.1**b**). This size dependence of the signal intensity has already been demonstrated for the diamine series in Chapter 4 (compare Figure 4.2). At a modifier mixing ratio of 0.15%, only the first modifier-analyte cluster $[^{L/D}AA+2\text{-}BuOH+H]^+$ is clearly observed, regardless of the amino acid selected, as demonstrated in Figure 6.1 (see blue arrows). This could be due to the ion optic, which potentially leads to a decrease in mean cluster sizes. However, due to a low 2-BuOH mixing ratio, it is also likely that only small clusters are formed. Accordingly, each amino acid is still suitable as analyte for the enantiomeric separation, whereby larger amino acids are preferred due to the higher signal intensity. Furthermore, a modifier mixing ratio of 0.15% provides robust results and an observable cluster effect.

Declustering process

A different, enantioselective CCS of the $[^{L/D}AA+2\text{-}BuOH+H]^+$ clusters as a result of different cluster structures and/or different cluster distributions as a result of different binding energies are necessary for an enantioselective separation with DMS. Consequently, the declustering step from the first protonated cluster $[^{L/D}AA+2\text{-}BuOH+H]^+$ to the bare ion $[^{L/D}AA+H]^+$ should be gradual if the modifier or the analyte is enantiopure. In this case two clusters with different binding energies are expected, which would be destroyed at different energetic levels. This approach was tested using the options of the QqQ system, which allows a uniform increase of the *collision energy CE* in q2. First, the $[^{L}AA+2\text{-}BuOH+H]^+$ clusters were formed by adding 25% rac. 2-BuOH to the analyte solutions of the L-enantiomers of each amino acid ^{L}AA. The $[^{L}AA+2\text{-}BuOH+H]^+$ clusters were isolated in Q1 and a declustering step was performed in q2 by increasing the *CE* in 0.2 V steps. In the following, the fragments were analyzed in Q3. In case of different cluster stabilities, a step-like decrease of the $[^{L}AA+2\text{-}BuOH+H]^+$ signal with simultaneous step-like increasing of the $[^{L}AA+H]^+$ signal is expected.

The $[^{L}AA+2\text{-}BuOH+H]^+$ cluster of L-threonine was not observable with this method; and since the signal intensity of the $[^{L}AA+H]^+$ species of L-serine was too low for reliable statements, Figure 6.2 shows only the results of L-tryptophan and L-phenylalanine. The signal intensity gradients of the first modifier cluster $[^{L}AA+2\text{-}BuOH+H]^+$ and the bare ion $[^{L}AA+H]^+$ of L-tryptophan (see Figure 6.2**a**) correspond to the intensity gradients of a following reaction. The *total ion chromatogram* (TIC) remains constant over the *CE* range

shown after a signal increase in a low *CE* range, and the cluster signal initially increases in parallel. From a *CE* of about 5 V, the maximum intensity of the $[^{L}AA+2\text{-}BuOH+H]^{+}$ signal decreases and the $[^{L}AA+H]^{+}$ signal increases until an intensity maximum is reached at about 11 V and the signal also decreases again. This observation can be explained by the expected declustering process, but no abrupt drops in intensity occur (see Figure 6.2**a**).

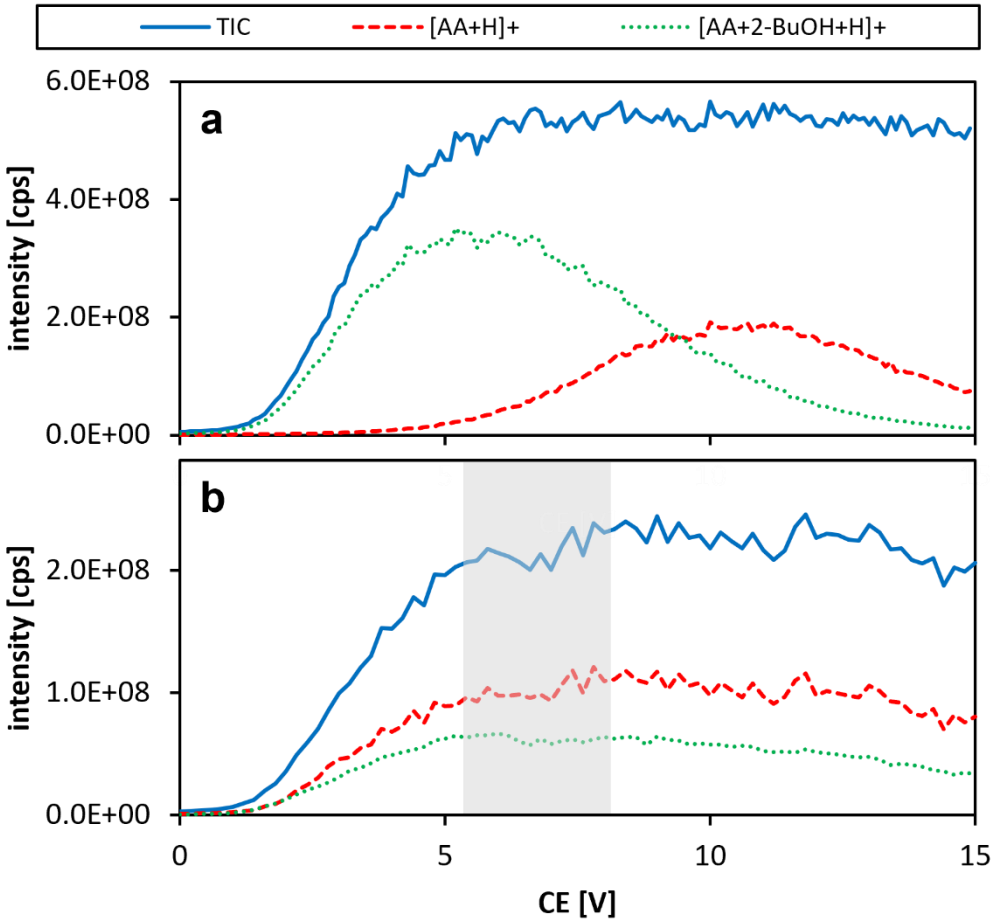

Figure 6.2: Declustering process of the first protonated analyte-2-BuOH cluster $[AA+2\text{-}BuOH+H]^{+}$ of L-tryptophan (**a**) and L-phenylalanine (**b**) depending on the collision energy *CE* in q2.

The result of the L-phenylalanine measurement deviates from this (see Figure 6.2**b**). In parallel with a comparable increase in TIC in a low *CE* range, the signal of the first cluster $[^{L}AA+2\text{-}BuOH+H]^{+}$ and of the bare ion $[^{L}AA+H]^{+}$ also increase relatively uniformly. Therefore, the maximum signal intensity of the bare ion $[^{L}AA+H]^{+}$ is higher. This indicates a weak binding energy, which leads to a declustering process even in a low *CE* range. In the range from about 5.5 to 8 V (see gray area in Figure 6.2**b**), the signal intensity of the $[^{L}AA+H]^{+}$ species increases in a small step at about 7 V, and the intensity of the cluster signal drops at a *CE* of about 6.5 V. This behavior is to be classified as an indication and not as reliable proof of stereoselective clustering. The steps in both mass traces are so weak that they are almost lost in noise. Due to the proximity of the two steps, a correlation seems possible; however, declustering would result in the identical *CE* value. Moreover, an exact

reproduction of the steps was not possible. Overall, there is much to suggest that these steps are not due to a physical effect and must be classified as artifacts. Thus, different binding energies could not be proven by declustering in MS^2 measurements but are also not refuted. The differences of the binding energies might be too low to be detected by this method, or the weaker clusters might be declustered in the ion optics before entering the q2. In accordance with the experimental results and the literature [79], phenylalanine is considered to have the greatest potential of success in enantiomeric separation, which is why the subsequent investigations are focused on this amino acid.

Optimization of DMS parameter

The addition of rac. 2-BuOH (0.15%) leads to the same cluster effect for both enantiomers of phenylalanine, as already mentioned (see left panel in Figure 6.3).

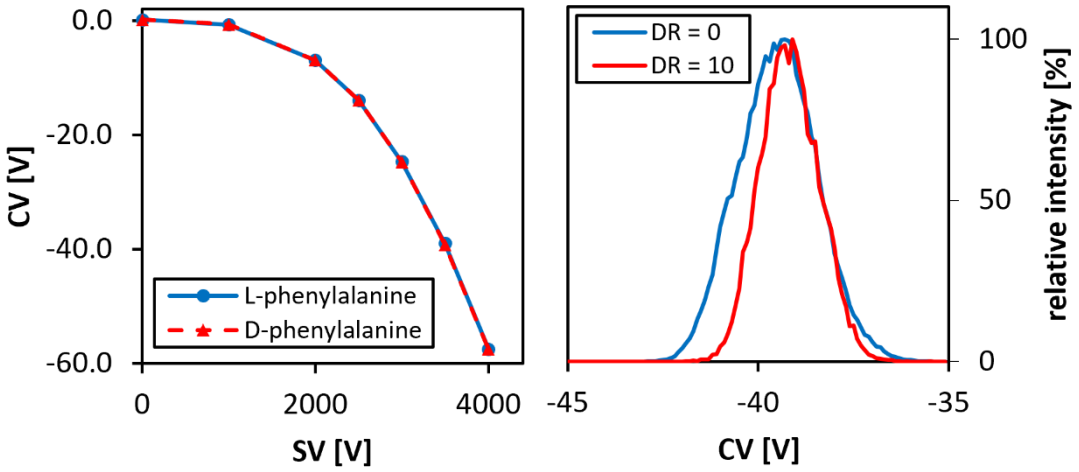

Figure 6.3: Dispersion plots of both protonated enantiomers of phenylalanine $[^{L/D}AA+H]^+$ (left panel) and ionograms of the protonated L-phenylalanine $[^{L}AA+H]^+$ at selected DMS resolutions *DR* (*SV* = 3500 V; right panel) recorded with rac. 2-BuOH (0.15%) added as gas-phase modifier in nitrogen (*DT* = 423.15 K).

Furthermore, at a *DT* of 423.15 K, the *CV* values are sufficiently large to detect even small absolute deviations due to stereoselective clustering. The peak wide should be minimized to detect even a weak ion separation, which is expected for an enantiomeric separation. The right panel of Figure 6.3 shows the effect of different *DR* settings on the peak width, which is decreasing by increasing *DR*. In parallel, the absolute intensity decreases sharply (compare Figure 6.7). For the selected parameters, a *DR* of 10 (system-intern parameter, no unit given) leads to a good compromise between peak width and signal intensity over the entire *SV* range. At an *SV* of 3500 V, the *DR* can also be increased significantly without the intensity dropping to a value that can no longer be evaluated.

6.1.2 Maruoka catalyst

The Maruoka catalyst ($C_{42}H_{36}BrF_6N$) differs from amino acids in several structural characteristics as shown in Figure 6.4 for the ion $[M\text{-}Br]^+$. The catalyst is characterized by a chirality axis through the charged nitrogen atom, which should be the center of modifier clusters. This could maximize the expected enantioselective interactions with a chiral modifier. In addition, the steric complexity of the uncharged part of the molecule is significantly higher than for all previous analytes. This structure results in the high quality as stereoselective catalyst with a product *enantiomeric excess ee* of up to 99% (depending on the reaction and the reaction conditions) [126]. Accordingly, the enantiomeric information, which is transported to the reactants, is strong, and the same qualitative features are necessary for an enantioselective cluster formation in the gas phase.

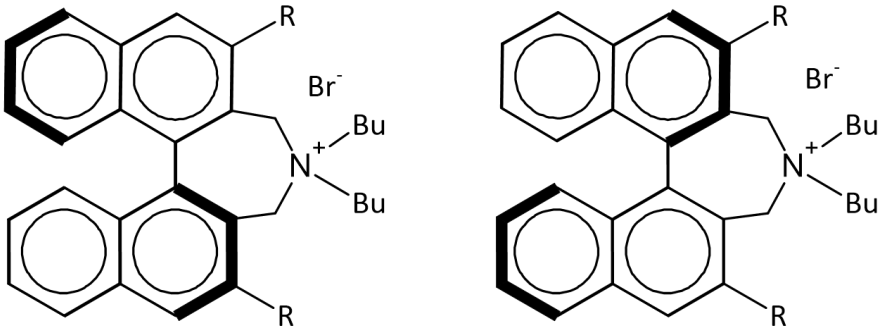

R = *3,4,5*-$F_3C_6H_2$

Figure 6.4: Structure of the Maruoka catalyst ion (left: *S*-enantiomer; right: *R*-enantiomer).

On the other hand, however, weak binding energies between analyte and modifier are expected due to the strong shielding of the charge. The resulting bond length between both could be so long that the chiral information of the catalyst is too weak to lead to observable differences in the cluster structures. As a result, the absolute cluster effects, and the difference between the two enantiomers might be very weak, which complicates stereoselective separation.
It should be noted that some of the preliminary measurements for the Maruoka catalyst were carried out in parallel by the Hopkins group of the University of Waterloo (Canada) with an identical instrument. This allows a comparison of results to exclude systematic errors and hardware problems as much as possible.

Cluster effect on the Maruoka catalyst

Due to the complex structure of the Maruoka catalyst ion (see Figure 6.4), the addition of a modifier (1.5%) results in a cluster effect which is not strong enough to compensate for the hard-sphere effect (leading to type-C behavior at DT = 423.15 K, see Figure 6.5**a**). The

cluster effect can be further weakened by increasing *DT*, as shown in Figure 6.5**b** for several typical modifiers.

It should be noted that the DMS conditions used for the Maruoka catalyst measurements lead to *CV* values deviating from 0 V even at an *SV* of 0 V, which does not make sense. This effect shows a strong dependence on the DMS parameters, such as the modifier used or the *DT*, and has already been observed in previous measurements (see Figure 4.9). Since only very small differences in *CV* are expected for an enantiomeric separation and the cluster effect is also weak, these *CV* shifts become significant in these investigations and could overlay both effects. Therefore, all dispersion plots in this chapter are calibrated to a *CV* of 0 V at an *SV* of 0 V (parallel shift along the y-axis). This method of evaluation leads to reproducible and, according to all experience, trustworthy results. However, the ionograms presented are not calibrated in this way, which must be considered in the interpretation. Furthermore, some measurements were carried out in MRM mode (m/z_{Q1} 668; m/z_{Q3} 541; *CE* = 42 V). The decisive factor here is whether unknown mass spectra (Q1 mode) or a defined species (MRM mode) are to be examined and analyzed.

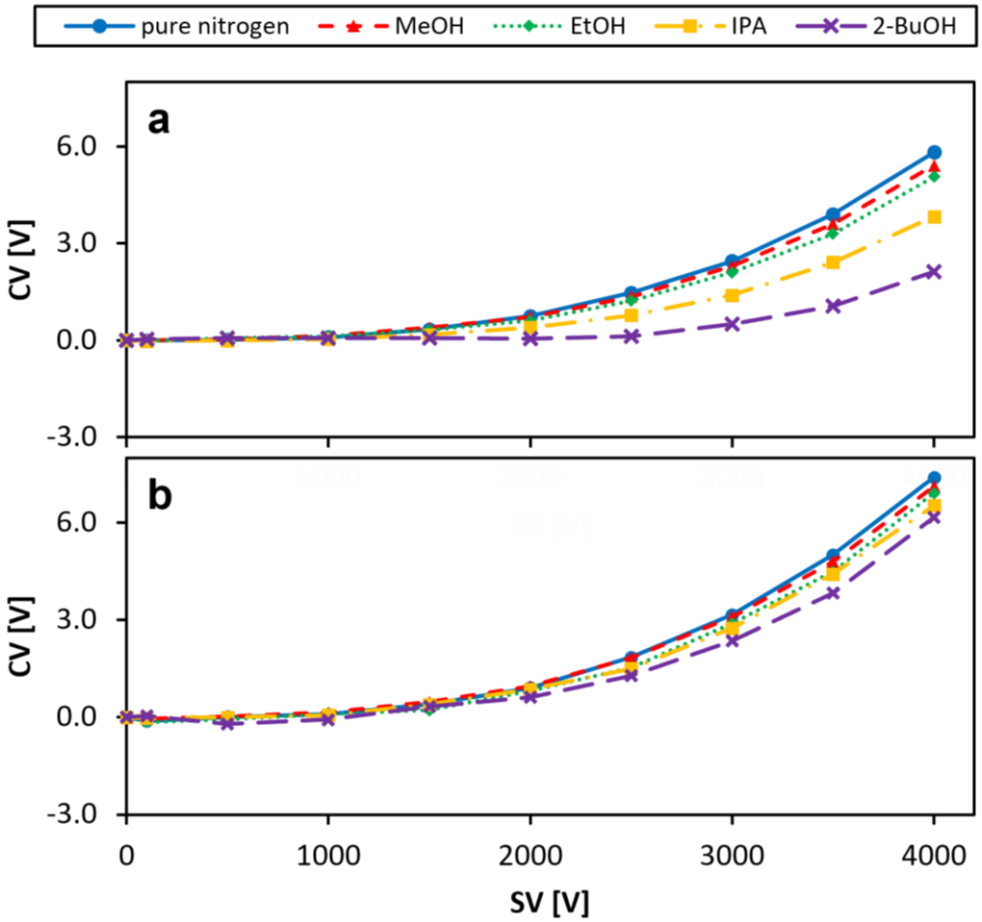

Figure 6.5: Calibrated dispersion plots of the (*S*)-Maruoka catalyst ion at selected DMS temperatures *DT* recorded with and without gas-phase modifier (1.5%) present in nitrogen: (**a**) 423.15 K; (**b**) 573.15 K.

The strength of the cluster effect decreases with the increasing size of the modifier at a *DT* of 423.15 K, as shown for a series of alcohols in Figure 6.5**a**, which is already known from previous work [23, 25]. However, as mentioned above, the absolute cluster effect is extremely weak, resulting in a dominant hard-sphere effect (type-C behavior). The cluster effect due to the modification with MeOH is so small that only minimal deviations occur compared to the modifier-free measurement. This indicates that the large MeOH cluster structures, which are known from the literature [13] and Chapter 4, cannot be formed in this case (see Figure 6.5**a**). An increase in the modifier size (EtOH) hardly strengthens the cluster effect. The addition of larger modifiers such as IPA or 2-BuOH leads to a more pronounced cluster effect, but it is still too weak to compensate for the hard-sphere effect. Thus, low mean cluster sizes in combination with a large ion led to a weak cluster effect. This observation is enhanced for each modifier by an increase in *DT* to 573.15 K (see Figure 6.5**b**). As a result, the addition of a modifier becomes increasingly insignificant and the behaviors with added modifier and in pure nitrogen converge. Accordingly, the low binding energy between modifier and analyte leads to low mean cluster sizes or even to bare ions already in low *SV* ranges. These qualitative observations were also confirmed by the Hopkins group; however, higher *CV* values were measured in Waterloo without a modifier. The quantitative difference can be explained by a lower background water mixing ratio compared to the measurements presented here, which causes a weak cluster effect. Since the quantitative differences are minimized by the addition of a modifier, this was not investigated further. Consequently, the chemical modification of the Maruoka catalyst ion to effect a significant change in behavior in DMS is more complicated than for other ions. The high steric hindrance at the charged position is preferred to maximize the stereoselectivity of cluster formation; however, simultaneously, it almost completely prevents cluster formation and thus the cluster effect. This would be a criterion for exclusion if the cluster effect cannot be enhanced.

Optimization of DMS temperature

Since the cluster effect on the Maruoka catalyst ion is negatively influenced by an increase in *DT*, the DMS cell is cooled down to achieve the opposite effect. By decreasing the *DT* to 398.15 K and adding rac. 2-BuOH (1.5%) as modifier, a type-B behavior occurs, even though the cluster effect is still relatively weak (see Figure 6.6). This trend continues with decreasing *DT* and is in line with previous experience (compare *Temperature effect in DMS*). The decrease in *DT* enables an increased mean cluster size in the low field and thus a stronger cluster effect. Accordingly, the strongest cluster effect occurs at lowest *DT* (348.15 K, see yellow curve in Figure 6.6). Further decrease in *DT* is difficult with the setup used, as there is no thermal shielding to hotter components and areas. Furthermore, undesirable side effects occur and are amplified with decreasing *DT*. At 348.15 K, the ionograms of the Maruoka catalyst ion show a shoulder at the negative side of the signal up to an *SV* of 3000 V, which must be taken into account during plotting. The two overlapping signals converge at an *SV* of 3000 V, causing a prominent bend in the dispersion plot (see yellow curve in Figure 6.6). Increasing the *DR* value causes the shoulder to disappear.

These measurements were performed in the MRM mode, whereby both signals can be assigned to the Maruoka catalyst ion with high probability. Accordingly, the double signal indicates an initial separation in the DMS cell, which seems to be physically illogical since in a low *SV* range the *CV* of each species should be 0 V. The precise source of this effect cannot be conclusively clarified at this point. Nevertheless, it can be avoided (*DR* > 0), and there is evidence of a type-A behavior, suggesting a significant cluster effect (see Figure 6.6).

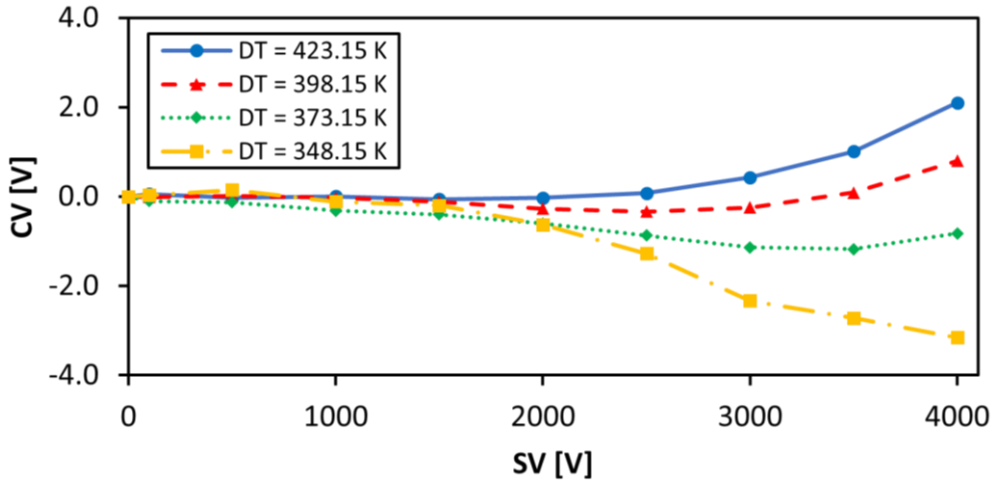

Figure 6.6: DMS temperature effect on the calibrated dispersion plots of the (*S*)-Maruoka catalyst ion recorded with rac. 2-BuOH (1.5%) added as gas-phase modifier in nitrogen (*DR* = 0; MRM mode: 668/541, *CE* = 42 V).

There are also large qualitive agreements in the *DT*-dependent results of the Hopkins group. One decisive difference is a type-B behavior that was detected at a *DT* of 333 K in Waterloo. However, this may be due to a different analyte concentration in the liquid phase and different *DR* values preventing the effect of a double signal. Thus, the type-A behavior at a *DT* of 348.15 K in Figure 6.6 could be an artifact, but the shift to negative *CV* values can be detected in both results and indicates a sufficient cluster effect at a *DT* of 348.15 K and an *SV* of 3500 V.

Optimization of DMS resolution

In addition to avoiding a second signal, the *DR* value is of great importance in increasing the resolving power of the DMS system. The effect of different *DR* settings on the signal of the Maruoka catalyst ion (MRM mode) with various modifier mixing ratios (rac. 2-BuOH) is shown in Figure 6.7. It becomes apparent that the basic *DR* dependence of the signal intensity and width presented in the right panel of Figure 6.3 for protonated phenylalanine can also be demonstrated for the Maruoka catalyst ion. Deviating from this, the double signal effect causes a variation of the peak shape. Thus, the combination of a modifier mixing ratio of 1.5% and a *DT* of 348.15 K leads to fronting as shown in the top panel

in Figure 6.7 (see green ionogram). An increase in *DR* results in an increasing Gaussian approximation (see bottom panels in Figure 6.7).

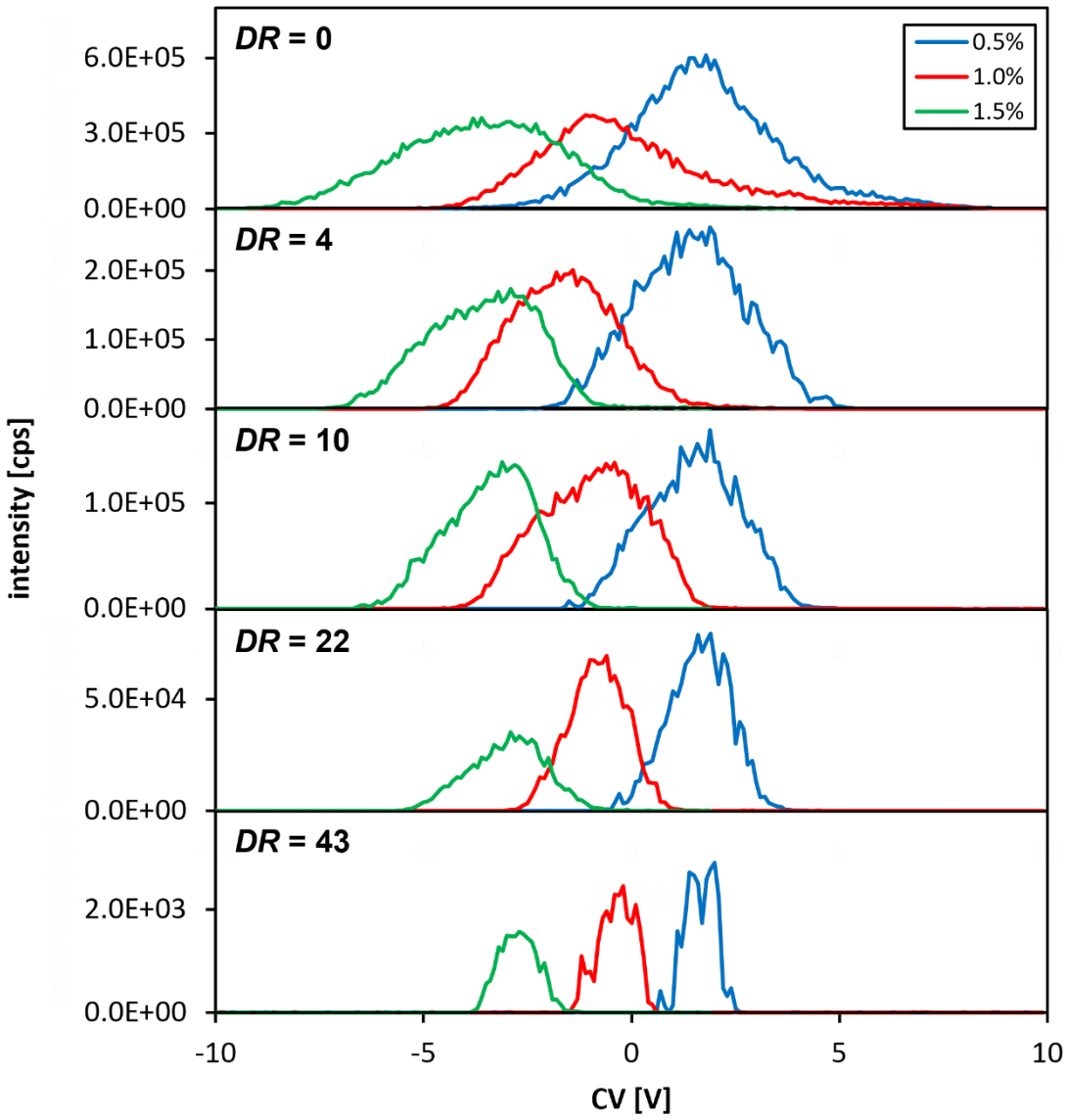

Figure 6.7: Ionograms of the (*S*)-Maruoka catalyst ion at selected DMS resolutions *DR* and with different mixing ratios of rac. 2-BuOH added as gas-phase modifier in nitrogen (*SV* = 4000 V; *DT* = 348.15 K; MRM mode: 668/541, *CE* = 42 V).

Accordingly, a compromise must be found among the signal intensity, peak width, and peak shape. A *DR* of 10 seems to fulfill the criteria as much as possible.

6.1.3 Optimized measurement parameters

An evaluation of all preliminary measurements shows that phenylalanine and the Maruoka catalyst have proven to be promising analytes, and they were therefore selected for further

investigations with enantiopure 2-BuOH. The measurement parameters adapted to each analyte are listed in Table 6.1. The analyte concentrations and the ion source parameters were individually optimized.

Table 6.1: Analytes and measurement parameter for studies with enantiopure 2-BuOH.

Analyte	Modifier	*MDC*	*SV*	*DT*	*DR*
(*R*/*S*)-Maruoka catalyst (0.2 µmol/L)	(*R*)-2-butanol	1.5%	0 to 4000 V	348.15 K	10
	(*R*/*S*)-2-butanol	0.5%; 1.0%; 1.5%	3500 V	348.15 K	10
L/D-phenylalanine (0.01 µmol/L)	(*R*/*S*)-2-butanol	0.15%	0 to 4000 V	423.15 K	10
			3500 V	423.15 K	10 (22; 26)

During the preliminary measurements and parallel studies, a potential systematic error due to the ionization with ESI became apparent. Thus, it is likely that charged nanodroplets exist in the DMS cell that could influence the cluster dynamics. The existence of this kind of nanodroplets is known from MS experiments and is described in the literature [59, 60].

6.2 Charged nanodroplets from ESI

As already mentioned in *Electrospray ionization*, there are many indications that the ideal ESI mechanism does not occur when using common ESI sources. There are increasing evidence that larger droplets than previously expected are formed in the ESI source and that highly charged nanodroplets occur in the high vacuum area [59, 60]. These highly charged nanodroplets are normally not directly observable by conventional analytical methods such as mass spectrometry. In this work, an adjustment of the Q1 of the QqQ system is necessary as mentioned in Section 3.1. When the product ion scan mode is used and the Q1 is switched to RF-only (droplet measurement), the Q1 filters out all species with a lower *m/z* ratio than the set cut-off value, while species with a higher *m/z* ratio should pass through. Thus, charged nanodroplets can pass through the Q1 and can be fragmented in the q2. In the following, the fragments are analyzed in the Q3. The cut-off value is set by the *m/z* ratio of the product ion ("product of"). The actual value, therefore, is slightly lower than the target value and can be determined at a sharp edge without fragmentation in q2 (*CE* = 0 V). Thus, the actual cut-off value for the product of 1100 is about 855.
The Maruoka catalyst and a series of thermometer ions are used as analytes for investigation of nanodroplets. Thermometer ions are characterized by a fixed fragmentation site with a highly reproducible fragmentation energy. The fragmentation ratio can be used to calculate the maximum effective temperature T_{eff} in a process such as an ion transfer [53]. In this work, five *para*-substituted benzylpyridine ions with different substituents R

(R = NO_2, Cl, CN, F, Me), which determine the fragmentation energy, are used. The cleavage of pyridine is the typical fragmentation reaction, as shown in Figure 6.8.

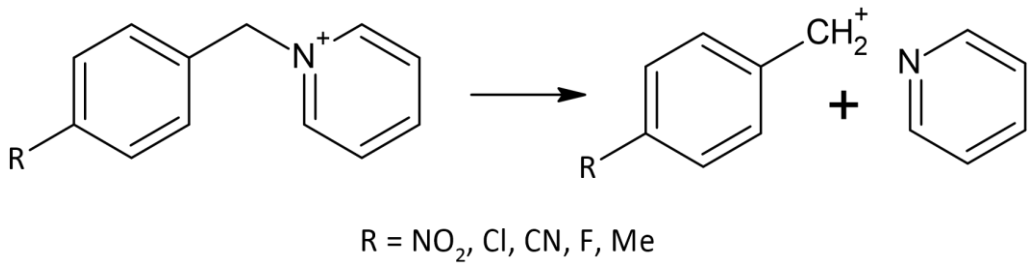

Figure 6.8: Structure of thermometer ions and the typical fragmentation reaction**.**

The droplet measurements are performed partly with and partly without a coupled DMS stage. The influence of the DMS parameters is of great interest, since the use of a DMS stage as a prefilter to prevent the MS system from contamination is known from the literature [59], and thus a dependence is likely. If complete evaporation occurs within the DMS cell, this could have a decisive impact on the chemical composition of the gas phase in this area and the ion separation. Otherwise, the effect of possible interactions between charged nanodroplets with gas-phase modifiers are also unpredictable at this point.

6.2.1 Charged nanodroplets

Even without the DMS cell installed, the curtain gas should defend the vacuum area against contaminations such as uncharged nanodroplets. However, this principle reaches its limits when the contaminations are charged like the highly charged nanodroplets in this theory. These can be electrically transported into the high vacuum area like bare ions or charged clusters. The preliminary droplet measurements of the thermometer ion series (dissolved in ACN/water, 1:1) with an added collision gas in q2 (*CAD* = 6; system-intern parameter, no unit given) leads to *CE*-dependent and qualitative reproducible mass spectra (see Figure 6.9). The source and MS parameters were set to common working ranges. It can therefore be assumed that the findings should be qualitatively transferable to standard measurements with the used MS system.
Since the thermometer ions are cut off by the Q1 in Rf-only mode, the bare ions should not be observable. However, already from a small *CE* of 10 V, the signals of the thermometer ions are detected (see blue area in Figure 6.9) as well as the typical fragment species (see red area in Figure 6.9). By increasing the *CE*, the intensities of the analyte signals are also increased, until the fragmentation reaction (see Figure 6.8) proceeds sufficiently quickly and the fragments become the main species of the thermometer ion series. This behavior cannot be explained with the textbook ESI mechanism and indicates the existence of larger species with a *m/z* ratio over the cut-off containing the thermometer ions (charged nanodroplets). Accordingly, by increasing the *CE*, the thermometer ions are first released from the nanodroplet and then fragmented.

Apart from the thermometer ion and fragment signals, an increased baseline can also be detected in the *m/z* range above the actual cut-off value (see top panel in Figure 6.9), but even under the cut-off, the intensity of the baseline differs from 0. Increasing the *CE* to 60 V shifts a kind of baseline wave into the *m/z* range from 300 to 800 (see middle panel in Figure 6.9), and no distinct signals are detected in it. Further increase of the *CE* to 150 V leads to a flattening of the baseline over the entire *m/z* range (see bottom panel in Figure 6.9). This observations also indicates a fragmented initial species such as nanodroplets. In the first step, smaller nanodroplets are split off with a preferred *m/z* ratio in the range from 300 to 800. However, this is not a defined number of fragment species, but a distribution due to the large number of variables such as the number and type of solvent species or the charge number. At a sufficiently high *CE* value (150 V), the nanodroplets are almost completely fragmentated and the wave disappears. It should be noted that for all three *CE* settings, a weak but distinct signal could be detected at an *m/z* ratio of about 337. A possible explanation for this is a contamination in the analyte solution. However, since this species does not appear to belong to either the baseline or the basic thermometer-ion system, it was not investigated further.

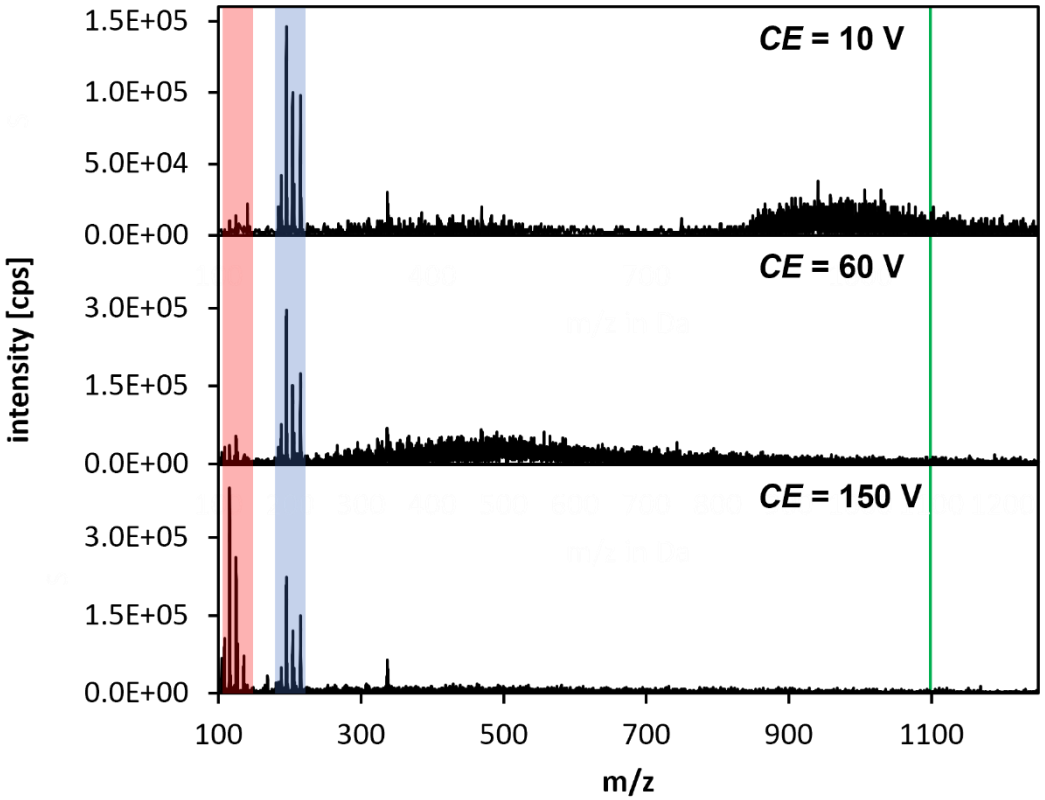

Figure 6.9: Droplet mass spectra of thermometer ions at selected collision energies *CE* recorded in pure nitrogen (T_{source} = 303.15 K; *IS* = 5500 V). Green line: Product of: 1100. Blue area: thermometer ion signals. Red area: fragment signals.

The release and subsequent fragmentation of the thermometer ions is a continuous process, as shown in Figure 6.10. At a *CE* of 0 V, only the primary nanodroplets are present, and

since the measured *m/z* range is set to a maximum of 1250 (low-mass mode of the mass spectrometer), the TIC is close to 0 (left scale in Figure 6.10). By increasing the *CE*, the fragmentation results a steep increase of the TIC and the signal of the CN-derivate (right scale in Figure 6.10). The TIC reaches its maximum at a *CE* of about 60 V and decreases with further increasing *CE* (see blue curve in Figure 6.10). This can be attributed to the nearly complete fragmentation of the initial nanodroplets. The signal of the CN-derivate reaches a sloping intensity plateau at a *CE* range from about 20 V to about 110 V with only a slight increase, which is also followed by a decrease in intensity (see red curve in Figure 6.10). The fragment signal increases weakly before increasing sharply with decreasing CN-derivate (see green curve in Figure 6.10).

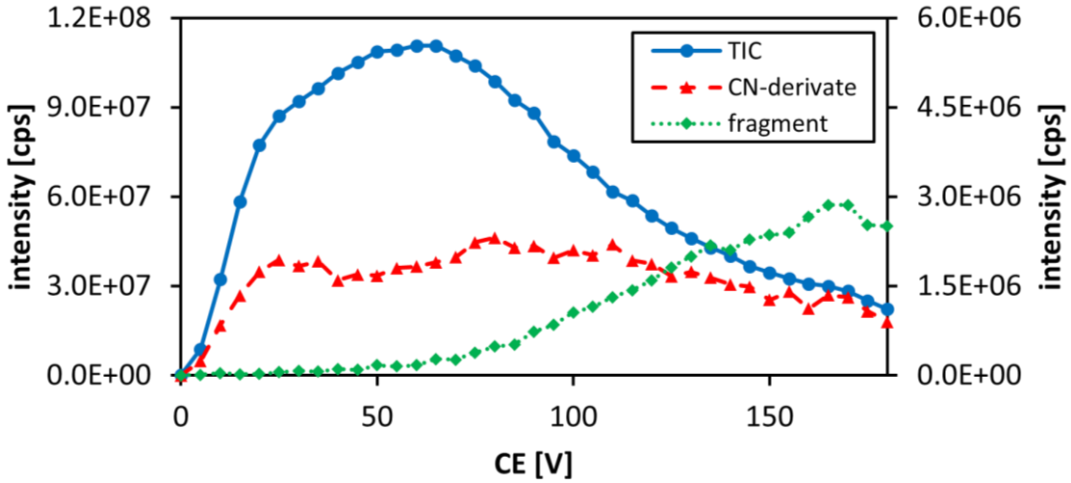

Figure 6.10: TIC (left scale) and chromatograms of the CN-derivate and fragment of the thermometer ions (right scale) depending on the collision energy *CE* recorded in pure nitrogen (droplet experiment; T_{source} = 303.15 K; *IS* = 5500 V; product of: 1100).

Overall, a behavior known from classic kinetics can be recognized. The increasing intensity of the signal of the CN-derivate and the following drop by fragmentation suggest the textbook behavior of consecutive reactions from the type shown in reaction 6.1 [127].

$$A \rightarrow B \rightarrow C \qquad \text{(R 6.1)}$$

In this case, a charged nanodroplet species is the A species, the CN-derivate is the B species, and the fragment is the C species. It should be noted that the TIC does not correspond to the A species in this case, but to the sum of several of B-like and C-like species arising from the charged nanodroplet (A species). The fragmentation of each species of the complex nanodroplet distribution represents a separate consecutive reaction system, which combines to form an extremely complex reaction system. The thermometer ions are only a small part of this system, but they can be used as a very simplified model of the whole system. The other thermometer ion derivates exhibit similar behaviors. The determination of kinetic values such as the reaction rate constants is only possible to a limited extent due

to the high signal fluctuations. Furthermore, these values are not of great interest at this point, which is why they were not determined.
The nanodroplet distribution can potentially be influenced by varying parameters such as the source temperature T_{source} or the *CAD*. To illustrate this phenomenon, Figure 6.11 shows the influence of T_{source} on the TIC as an example. An increase from 303.15 K to 473.15 K leads to a quantitative increase in TIC, while the qualitative behavior remains almost unchanged. Accordingly, this variation supports the detection of nanodroplets, but does not qualitatively change the spray behavior.

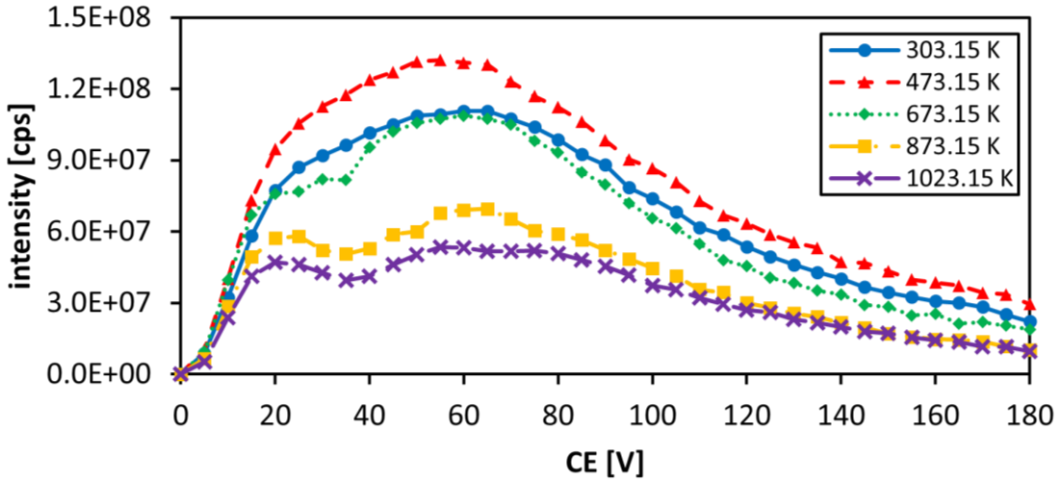

Figure 6.11: Effect of a variation of the source temperature T_{source} on the TIC (analyte: thermometer-ion series) depending on the collision energy *CE* recorded in pure nitrogen (droplet experiment; *IS* = 5500 V; product of: 1100).

Further increase in T_{source} leads to a decrease in maximum intensity (see Figure 6.11). In addition, a qualitative deviation occurs, since two maxima of the TIC are formed at different *CE* values. Both the qualitative and quantitative observations are amplified by a further increase in T_{source}. One possible explanation involves the overlay of different nanodroplet species, which react differently to a variation of T_{source}. This means that each species should be a kind of subdistribution. An increase in T_{source} could suppress or strongly influence one nanodroplet species, while another is hardly influenced. As a result, a second maximum is formed as the formation of individual nanodroplets species is significantly suppressed. The critical nanodroplet parameters should be a combination of the charge level, the composition, and the absolute size. Accordingly, this results in a multiple dimensional distribution that could include more than just two distinguishable species. The increase in T_{source} to 1023.15 K supports this assumption, as the second maximum appears to split further (see purple curve in the *CE* range from 40 to 100 V in Figure 6.11).
The nanodroplets are not an instrument-specific effect, as similar effects are also observable in MS systems with other inlets and from other manufacturers with common ESI sources. Thus, observations indicative of charged nanodroplet distributions have been documented for a quadrupole ion trap (Bruker amaZon QIT) and a time-of-flight instrument

(Agilent Q-ToF), both characterized by different designs of the ion optic [60]. Consequently, the formation of nanodroplets seems to be inevitable when using common ESI sources. However, Kang et al. demonstrated that the MS system can be protected from nanodroplet contaminations by using a DMS stage [59]. Therefore, the influence of the DMS stage and the DMS parameters on the nanodroplet distribution is investigated in what follows.

6.2.2 Differential mobility of nanodroplets

First, a DMS measurement was performed in the Q1 mode for the thermometer-ion series to obtain comparative values. In pure nitrogen, no strong cluster effect was observed, and a type-C behavior was obtained for each thermometer ion. Although the ion structures are similar (see Figure 6.8), a clear splitting of the different analytes is observable at a *DT* of 423.15 K and an *SV* of 4000 V, even though no baseline separation is achieved (see Figure 6.12). The ionograms of the thermometer ions can be recognized as Gaussian distributions with a typical *half width at half maximum* (HWHM) in the range from 1.08 ± 0.01 V to 1.12 ± 0.01 V.

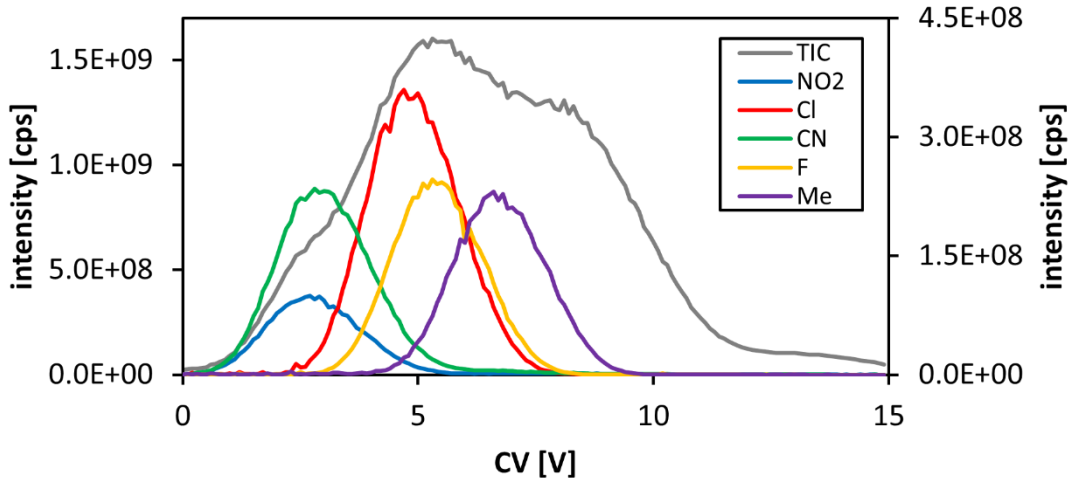

Figure 6.12: Ionograms of the TIC (left scale) and the thermometer ions (right scale) recorded in pure nitrogen (*SV* = 4000 V; *DT* = 423.15 K; *DR* = 0).

The TIC indicates at least one other species with a *CV* of about 8.5 V (see Figure 6.12) and the corresponding mass spectrum shows a signal at a *m/z* of 279. This appears to be a by-product from the synthesis or some other type of contamination that behaves differently compared to the thermometer ions. Moreover, a formation in the gas phase cannot be excluded. The different ions have various differential mobilities, which leads to a non-Gaussian distribution of the TIC. This observation is well known and was to be expected for the bare ions or at least small clusters, which are detected in Q1 mode.
A droplet measurement with a *CE* of 30 V with the same analyte solution and the same source parameters leads to a completely different result, as shown in Figure 6.13. The TIC

indicates a Gaussian distribution with a HWHM of 3.10 ± 0.09 V. Moreover, the thermometer ions behave qualitatively similar (see Figure 6.13): Gaussian-like distributions are detected with HWHM (determined from Gaussian distributions) in the range from 2.13 ± 0.17 V to 2.82 ± 0.10 V. In addition, only a weak ion splitting can be detected (ΔCV_{max} = 1.23 ± 0.37 V), implying that the nanodroplets as source of all thermometer ions are identical or at least similar. Nevertheless, the combination of the deviation from a perfect Gaussian distribution and the comparatively high HWHMs of the TIC and the thermometer ions suggest similar but slightly different nanodroplet species, which would also explain the small but present ΔCV_{max}. These observations indicate a complex nanodroplet distribution with possibly multiple subdistributions, which is consistent with the results of the droplet experiments without of the DMS stage (see Figure 6.11). Consequently, the thermometer-ion distribution in a nanodroplet seems to influence the behavior of the complete nanodroplet and is thus a parameter for the subdistributions.

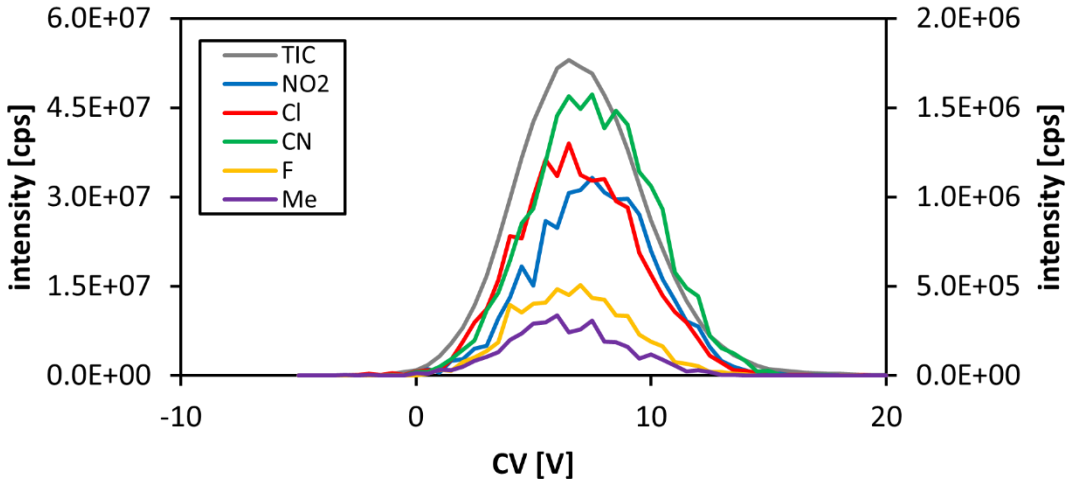

Figure 6.13: Ionograms of the TIC (left scale) and the thermometer ions (right scale) recorded in pure nitrogen (droplet experiment; *SV* = 4000 V; *DT* = 423.15 K; *DR* = 0; product of: 1100; *CE* = 30 V).

Furthermore, these results demonstrate a high stability of the nanodroplets, which not only passed through the ion optic of MS systems, but also through the DMS stage at an *SV* of 4000 V. A differential mobility of the nanodroplets could be proven, which could not be assumed in advance. Due to a complex and presumably dynamic structure as well as a comparably high inertia of the nanodroplets, a straight flight through the DMS cell would also have been possible and explainable. However, the high charge density, which can be assumed since a state close to the Rayleigh stability limit is expected, leads to a sufficiently large impact of the *SV* on the trajectory of the nanodroplet in the DMS cell. Consequently, the nanodroplets can be described as an almost classic ionic species. Accordingly, the filter effect of the DMS stage described by Kang et al. [59] is based on a different differential mobility and not on destruction of the nanodroplets. The quantitative comparation of Figures 6.12 and 6.13 indicates that such a filtering effect would not be expected in this case, since a superposition of both TICs can be observed. Thus, the differences in *CV* between

the nanodroplet distribution and the pure ions are too small to filter out only one of them, which is why the presence of nanodroplets must be considered by interpreting the DMS results. The influence of nanodroplets on the chemical environment in the DMS cell (e.g., through evaporation of solvent molecules) cannot be estimated. The intensity differences between both measurements are significant; but since the whole setup is not optimized for droplet experiments, which is evident from the strong noise in Figure 6.13, no conclusions can be drawn about the possible ratio of nanodroplets and bare ions. However, it is noticeable that the intensity ratios of the thermometer ions are different in the droplet measurement than in Q1 mode (compare Figures 6.12 and 6.13). This also indicates a different source of the ions in both measurements. The undefined species (*m/z* 279) could not be detected in the droplet measurements, which suggest that it is formed in the gas phase or the DMS cell after the ion spray. As a result, it is not part of a nanodroplet passing through the high-pass filter. Alternatively, all nanodroplets including this ion could be unstable, what seems to be rather unlikely.

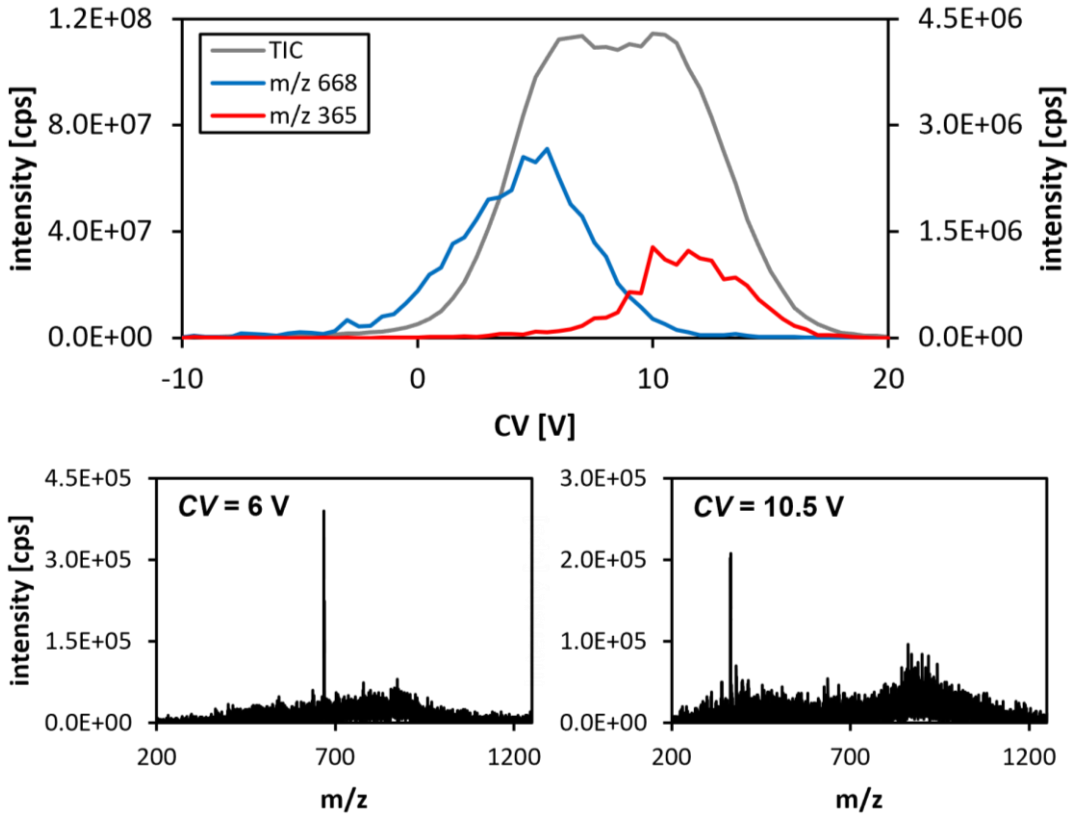

Figure 6.14: Ionograms (top panel) of the TIC (left scale), the Maruoka catalyst ion (*m/z* 668; right scale) and the second main signal (*m/z* 365; right scale) and the mass spectra at maximum compensation voltages CV (bottom panels) recorded in pure nitrogen (droplet experiment; *SV* = 4000 V; *DT* = 423.15 K; *DR* = 0; product of: 1100; *CE* = 30 V).

Replacing the thermometer-ion solution to the Maruoka catalyst in MeOH/water does not prevent the formation of nanodroplets. However, in this case, more clearly distinguishable

subdistributions appear to be formed, so that a double peak can be detected for the TIC, as shown in Figure 6.14 (top panel). The mass spectra at the maximum of the TIC (*CV* ≈ 6.0 V and 10.5 V) are shown in the bottom panels and reveal significant differences. At a *CV* of 6 V (see bottom, left panel in Figure 6.14), the signal of the Maruoka catalyst ion (*m/z* 668) stands out as the distinct signal from the baseline, while at 10.5 V (see bottom, right panel in Figure 6.14) the only distinct signal is found at *m/z* 365. This *m/z* ratio cannot be assigned to any typical fragment of the Maruoka catalyst and was not detected at any primary measurement. Thus, this should not indicate a classic contamination of the analyte solution. Instead, it seems to be either the product of a side reaction in the nanodroplet, which does not run in the gas phase, or it is a kind of contamination, which is discharged. In this case, it could not be detected in Q1 mode, but in droplet measurements, since the nanodroplets could prevent charge depletion. The ionograms of the distinct signals also indicate Gaussian distributions; however, the noise is so large that a plotting would no longer be justifiable. Comparison with the ionograms shows that the double peak of the TIC can effectively be explained by subdistributions of the nanodroplets (see top panel in Figure 6.14), which is likely due to the different main analytes. The mass spectra also show significant differences in the baseline structures. It cannot be definitively clarified whether more separatable subdistributions are the result of the varied analyte ions or the varied solvent compared to Figure 6.13. A combination of both is also possible. The absolute *CV* values of nanodroplets with the Maruoka catalyst ion are in a similar range as the *CV* values without modifier in Q1 mode (see Figure 6.5), which makes a separation of bare ions and nanodroplets impossible.
A similar differential mobility for all charged nanodroplets from an ESI process could be demonstrated, but these nanodroplets can only be completely separated from the bare ions in special cases. However, this would be necessary for a properly defined chemical environment in the DMS cell. Whether this can be achieved by the variation of the DMS parameters or by the addition of a gas-phase modifier would be decisive for the further procedure of enantiomeric separation.

Impact of DMS parameters

Increase in *DT* or *DR*, and thus in the residence time of the nanodroplets in the DMS cell, could potentially support the fragmentation into smaller nanodroplets or, ideally, into bare ions. In this manner, the filtering effect would become independent from different differential mobilities of the bare ions and the charged nanodroplets. Since it has already been demonstrated that a large proportion of the nanodroplet distribution is not completely fragmentated at high *E/N* (e.g., in the DMS process or ion optics), this is also not expected to be the case by increasing the DMS parameters. The effects of both DMS parameters on droplet measurements of the thermometer-ion series are shown in Figure 6.15.
Even with the maximum *DT* and *DR* values set (see right, bottom panel in Figure 6.15), the nanodroplets still pass through the DMS cell in observable numbers. An increase in *DT* from 423.15 K (see left panels in Figure 6.15) to 573.15 K (see right panels in Figure 6.15) does not ensure a significant drop in intensity, as would be expected in case of a strong fragmentation effect. Only a small loss of intensity can be observed for all signals of the

thermometer-ion series; however, the strong noises make an accurate intensity comparison inaccurate.

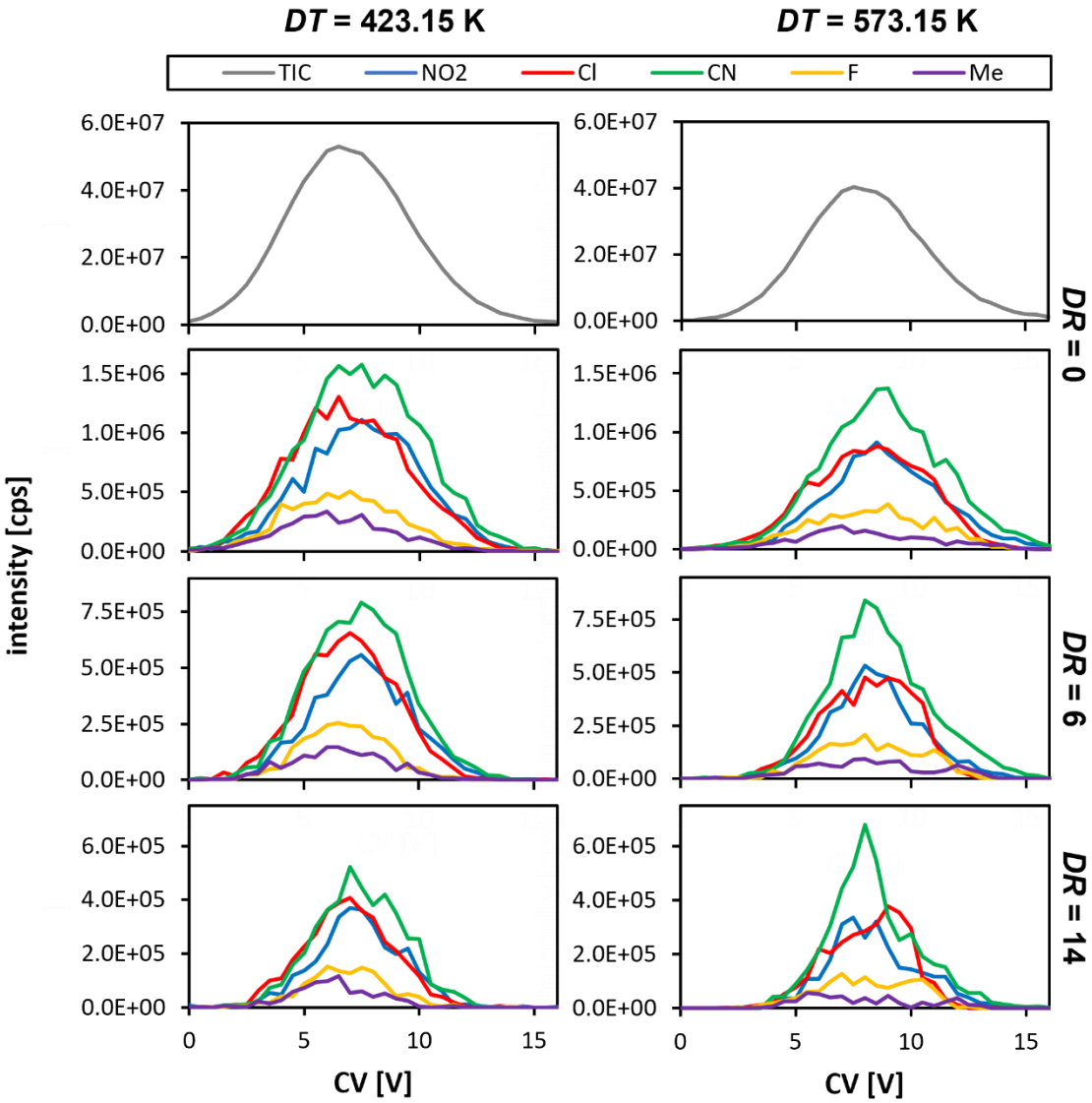

Figure 6.15: Ionograms of the TIC and the thermometer ions at selected DMS resolutions *DR* and DMS temperatures *DT* recorded in pure nitrogen (droplet experiment; *SV* = 4000 V; product of: 1100; *CE* = 30 V).

The situation is different with the TICs (see top panels in Figure 6.15), which are characterized by lower noise. The maximum of the TIC at a *DT* of 423.15 K is observable higher than at 573.15 K, and the total area under the curves also drops from about $3.51 \cdot 10^8$ counts to $2.60 \cdot 10^8$ counts. Since the source parameters were identical for both measurements, the same number of nanodroplets should have reached the DMS cell, provided that the impact of *DT* on T_{source} can be neglected in these ranges. Accordingly, an effect on the droplet distribution can be proven as well as an effect on the differential mobility, which can be seen in a *CV* shift (see top panels in Figure 6.15). This could be the effect of an unequal destruction of different nanodroplet species due to an increase in *DT*. However, a similar

shift of the thermometer-ion signals to higher *CV* values can also be detected (see bottom panels in Figure 6.15). This suggests that it is an actual *CV* shift—as known from bare ions—rather than a partial fragmentation of the nanodroplet distribution. An increase in *DR* leads to a narrowing of all signals as well as a loss of intensity, which is the typical effect. Thus, DMS parameters have typical effects on the differential mobility of nanodroplets, as it is also known from bare ions. Accordingly, the nanodroplets can still pass through the DMS cell due to a high stability, and they have an ion-like behavior in this process.
As shown in Figure 6.14, the nanodroplet subdistributions in droplet measurements of the Maruoka catalyst solution can be visualized through a double peak of the TIC. This effect is influenced by an increase in *DT*, as shown in Figure 6.16. A *DT* of 373.15 K leads to a significantly higher intensity of the analyte signal than higher *DT* settings. In parallel, the maximum of the TIC increases, and the second peak (located in the right flank of the main signal) decreases in maximum intensity with increasing *DT*, with only slight variation of the total peak area (373.15 K: $3.26 \cdot 10^8$ counts; 423.15 K: $3.23 \cdot 10^8$ counts; 573.15 K: $3.51 \cdot 10^8$ counts). This could be due to a shift of the nanodroplet distribution to smaller sizes, comparable to the shift of the cluster distribution in HiKE-IMS by increasing *E/N* (see Chapter 5). The smaller nanodroplets seem to be almost pure solvent nanodroplets, which is why the distinct signals disappear. Consequently, a chemical interaction of the different nanodroplet species, as well as a kind of fragmentation to smaller nanodroplets, could be observed. However, the appearance of nanodroplets in the MS system could not be prevented here either. The differential mobility is also influenced by the *DT*. Both the TIC and the analyte signal are shifted to a higher *CV* (see Figure 6.16) as known from the thermometer-ion series and bare ions. Thus, under constant DMS conditions and without a modifier, this nanodroplet distribution also behaves in a simplified manner like bare ions in DMS, whereby a fragmentation seems to appear.

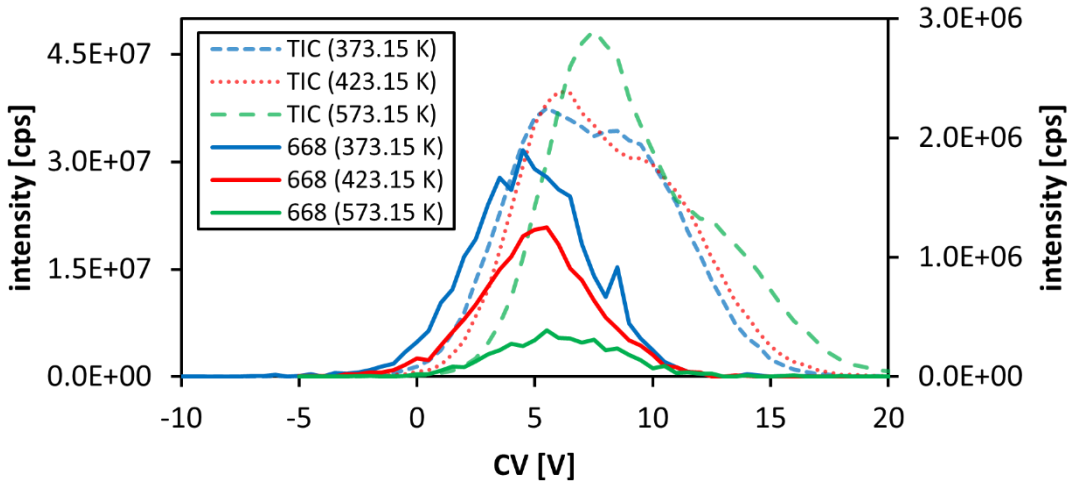

Figure 6.16: Ionograms of the TIC (left scale) and the (*S*)-Maruoka catalyst ion (*m/z* 668; right scale) at selected DMS temperatures *DT* recorded in pure nitrogen (droplet experiment; *SV* = 4000 V; product of: 1100; *CE* = 30 V).

In summary, the DMS parameter influences the charged nanodroplets, but the effect is quite similar to the effect on bare ions. Complete destruction of the nanodroplets cannot be realized in the ranges of the system used, although fragmentation to smaller nanodroplets seems to be possible under certain circumstances. Accordingly, the filtering effect reported by Kang et al. [59] must be the result of separation of the bare ions and the nanodroplets. The complete destruction of all nanodroplets by extreme increase in the DMS parameters seems possible, but not applicable, in the system used. Moreover, this would also lead to a fragmentation of the bare ions, which should make a useful application as a nanodroplet filter impossible. Therefore, the charged nanodroplets exhibit an almost ion-like behavior in all experiments presented so far. However, the addition of a gas-phase modifier could have an enormous influence on the nanodroplet compositions and thus on the chemistry and the behavior in DMS, which could be different from the behavior of bare ions.

Effect of modification on nanodroplets

The addition of a chemical modifier such as ACN or 2-BuOH to the curtain gas causes a cluster formation at bare ions. In nanodroplet analysis, clustering should be equivalent to a droplet growth, and a shift of the nanodroplet distribution to higher nanodroplet sizes would be imaginable. The crucial issue is whether the modifier becomes part of the nanodroplet and is directly equal to the solvent molecules or whether an independent layer is formed, which should lead to a cluster effect that is comparable to the effect known from bare ions. In order to clarify this question experimentally, the effect of the addition of 1.5% ACN to the curtain gas on the nanodroplet distribution formed when spraying the thermometer-ion solution is shown in Figure 6.17.

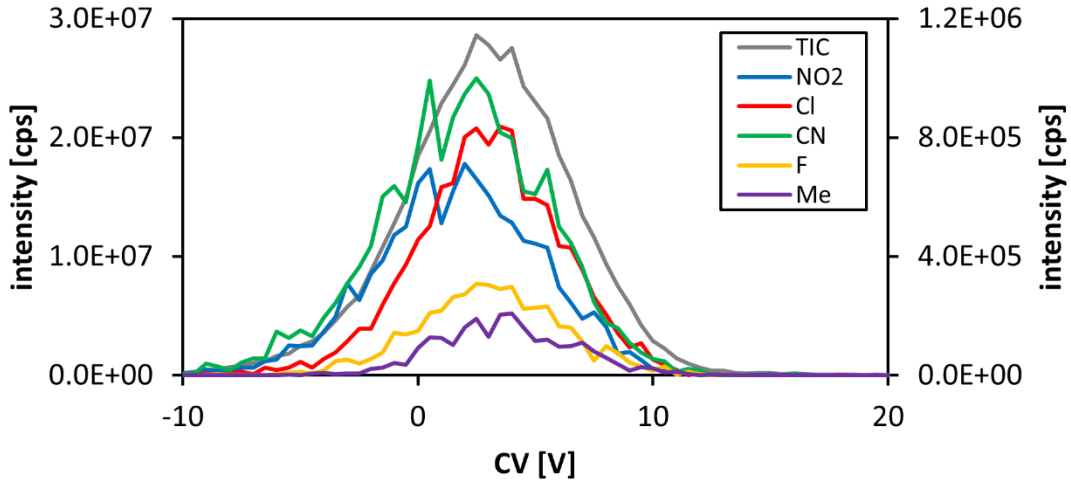

Figure 6.17: Cluster-like effect on ionograms of the TIC and the thermometer ions recorded with ACN (1.5%) added as gas-phase modifier in nitrogen (droplet experiment; *SV* = 4000 V; *DT* = 423.15 K; *DR* = 0; product of: 1100; *CE* = 30 V).

It must be noted that an effect is present, which is qualitatively similar to the cluster effect on bare ions (*CV* shift in a negative direction). Since it cannot be verified that the underlying mechanism is identical to the effect on a bare ion (cluster effect), this is declared as cluster-like effect in the discussion that follows. With otherwise unchanged measurement conditions, the addition of ACN leads to a decrease in the intensity of all distinct signals as well as the TIC (see Figure 6.17), compared to the droplet measurement without modifier (see Figure 6.13). However, since the intensity ratios of the thermometer-ion signals remain almost unchanged, the modifier seems to have no significant impact on the relative nanodroplet distribution. This observation could indicate modifier layers that are separated from the central nanodroplet and do not change the composition of the nanodroplets. The peak widths are increased by the addition of ACN, indicating a further splitting of the nanodroplet distribution (see Figure 6.17). Accordingly, the cluster-like effect is not identical on each nanodroplet. Based in the findings of Chapter 4, this indicates either a different absolute CCS variation associated with a different modifier layer thickness in this case, or a different relative CCS variation due to a different size of the central nanodroplet. The fact that only a splitting and not a complete separation of different nanodroplet species could be detected indicates a similar absolute growth of the nanodroplets. This could indicate incomplete layers, which have similar weak effects on different nanodroplets.

Table 6.2: Cluster-like effect on the TIC and the thermometer ions recorded with ACN (1.5%) added as gas-phase modifier in nitrogen at an *SV* of 4000 V (droplet experiment).

Species	***CV* [V] without modifier**	***CV* [V] + 1.5% ACN**	**Δ*CV* [V] cluster effect**
TIC	7.03 ± 0.11	2.96 ± 0.13	- 4.07 ± 0.17
R = NO_2	7.69 ± 0.24	1.78 ± 0.23	- 5.91 ± 0.33
R = Cl	6.96 ± 0.15	2.65 ± 0.31	- 4.31 ± 0.35
R = CN	7.65 ± 0.27	1.73 ± 0.33	- 5.92 ± 0.43
R = F	7.02 ± 0.33	3.00 ± 0.25	- 4.02 ± 0.41
R = Me	6.46 ± 0.28	3.52 ± 0.27	- 2.94 ± 0.39

The absolute *CV*s with and without modifier and the *CV* shifts (Δ*CV*) as a result of the cluster-like effect are listed in Table 6.2. While the dispersion of the thermometer-ion signals without modifier is 1.23 ± 0.37 V, it is 1.79 ± 0.43 V with the addition of ACN. Accordingly, the dispersions are identical within the error limits. The lack of an increase in dispersion can be explained by the *CV* steps of 0.5 V, which prevent smaller errors. Therefore, the increase which should be detected is in the range of the expected errors of this method. The Δ*CV*s of the individual thermometer ions show significant differences (see Figures 6.17 and 6.13 and Table 6.2). Although, the cluster-like effect on the nanodroplet subdistributions, which behave similarly without a modifier, is also very similar (identical

Δ*CV*s within the error limits, see Table 6.2). Thus, the nanodroplets of the NO_2 and the CN derivate show similar behavior and similar is observed for the nanodroplets of the Cl and the F derivate. The identical qualitative analyte pairing is also evident for the bare thermometer ions in pure nitrogen (see Figure 6.12). Accordingly, the included ion influences the behavior of a charged nanodroplet in DMS, which could suggest a size effect (CCS) but also a chemical effect (interactions with nitrogen and/or the modifier).
The addition of 1.5% rac. 2-BuOH as gas-phase modifier to the nanodroplet distribution of the Maruoka catalyst measurement leads to a significantly different cluster-like effect. The TIC undergoes a qualitative and quantitative change as shown in Figure 6.18. In addition to a strong *CV* shift in negative direction and a further broadening of the signal, the qualitative signal is switched from a double peak (see Figure 6.16) to a tailing peak (see Figure 6.18). The investigation of the Maruoka catalyst ion (*m/z* 668) shows that the shoulder includes the nanodroplets, which primarily include this species. Thus, the strength of the cluster-like effect on the nanodroplet species, which includes the Maruoka catalyst ion, is below average in this case. Overall, an enormous intensity loss of all species is observable due to the addition of rac. 2-BuOH. This could be the result of a charge depletion as it is known from supercharging [13, 37].

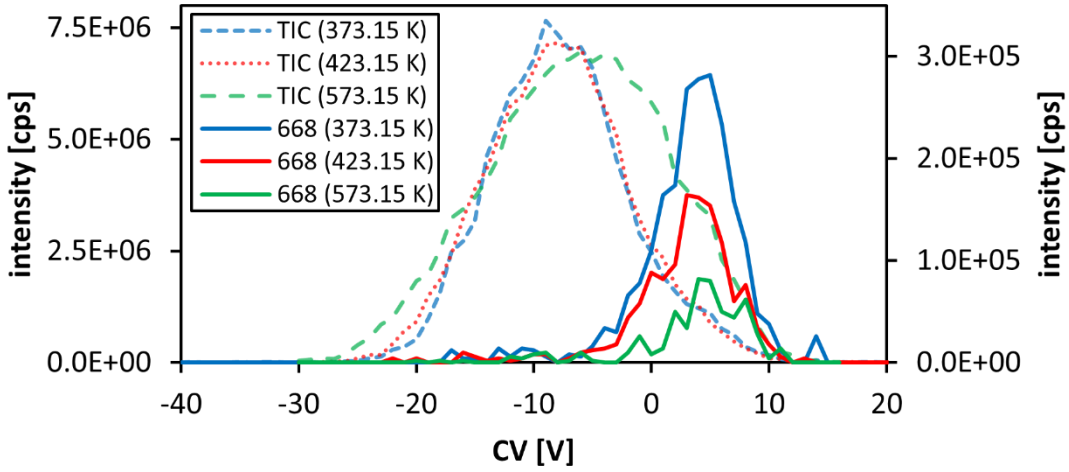

Figure 6.18: Cluster-like effect on ionograms of the TIC and the (S)-Maruoka catalyst ion recorded with rac. 2-BuOH (1.5%) added as gas-phase modifier in nitrogen (droplet experiment; *SV* = 4000 V; *DT* = 423.15 K; *DR* = 0; product of: 1100; *CE* = 30 V).

Furthermore, a *DT* dependence is also observable. As in pure nitrogen (see Figure 6.16), a decrease in intensity of the Maruoka catalyst signal can be observed in Figure 6.18. In addition, a *DT* of 573.15 K strongly supports the splitting of the droplet distribution, as shown by a broadened TIC. The *CV* of the TIC is also shifted in positive direction at 573.15 K (see green curve in Figure 6.18). This attenuation of the cluster-like effect is consistent with the experiences of bare ions.

The cluster-like effect leads to a *DT*-independent decrease in *CV* for the Maruoka catalyst ion of slightly more than 1 V, as shown in Table 6.3.

Table 6.3: Cluster-like effect on the Maruoka catalyst ion depending on the DMS temperature *DT* recorded with rac. 2-BuOH (1.5%) added as gas-phase modifier in nitrogen at an *SV* of 4000 V (droplet experiment).

DT	***CV* [V] without modifier**	***CV* [V] with modifier**	**Δ*CV* [V] Cluster effect**
373.15 K	4.75 ± 0.11	3.68 ± 0.43	- 1.07 ± 0.45
423.15 K	5.08 ± 0.12	3.38 ± 0.52	- 1.70 ± 0.53
573.15 K	6.26 ± 0.28	4.78 ± 0.56	- 1.48 ± 0.62

This argues against modifier layers, since otherwise an influence of the *DT* would be expected. It is possible that 2-BuOH as modifier and MeOH as solvent lead to different interactions than ACN. The different cluster structures of MeOH compared to ACN, as described by Haack et al. [13], could support diffusion into the droplet instead of the formation of a modifier layer. In this case, a transfer to other alcohols as modifiers would be conceivable. An influence of the compositions of the nanodroplet could also explain the qualitative variation of the TIC by adding 2-BuOH (see Figure 6.18). Nevertheless, this model cannot be conclusively confirmed or refuted with the present data. A weak influence of the *DT* is also possible, which is lost in the noise.
In summary, the nanodroplet distributions and subdistributions depend mainly on the sprayed solution and both the solvent and the ion seem to be the critical parameters. The nanodroplets from spraying the Maruoka catalyst solution showing a higher dependence on changes in the DMS parameters, which indicates a deviating chemical behavior. The cluster-like effect occurs with different basic mechanisms, depending on the chemical system. These could be modifier layer formations or a diffusion of the modifier into the nanodroplets. However, whether the modifier mixing ratio was high enough to lead to observable modifier layers could be questioned and should be investigated further. For this work, the only significant point is that all nanodroplets in DMS appear to behave like bare ions within certain limits and are therefore unlikely to be completely removed.

Droplet discrimination above of the actual cut-off value

As a side effect, the influence on the cut-off value was observed. Therefore, a hardware profile in high-mass mode was used and the target value was varied by a stepwise increasing of the “product of” value from 1000 to 2000. The resulting actual values were determined visually and are listed in Table 6.4.

Table 6.4: Actual value of the cut-off depending on the target value ("product of") for droplet experiments in high-mass mode.

target value	actual value
1000	777
1250	970
1500	1177
1750	1360
2000	1555

This method leads to a different influence of the *CE* on the TIC compared to the previous measurement (see Figure 6.11), as shown in Figure 6.19. In addition to the known qualitative curves at higher *CE* (> 20 V), the TIC increases to a first maximum at a *CE* of 5 V. The reason for this rash is not immediately clear. It could be a real chemical effect or even an electric artifact, which seems more likely since a chemical effect should be observable even in low-mass mode.

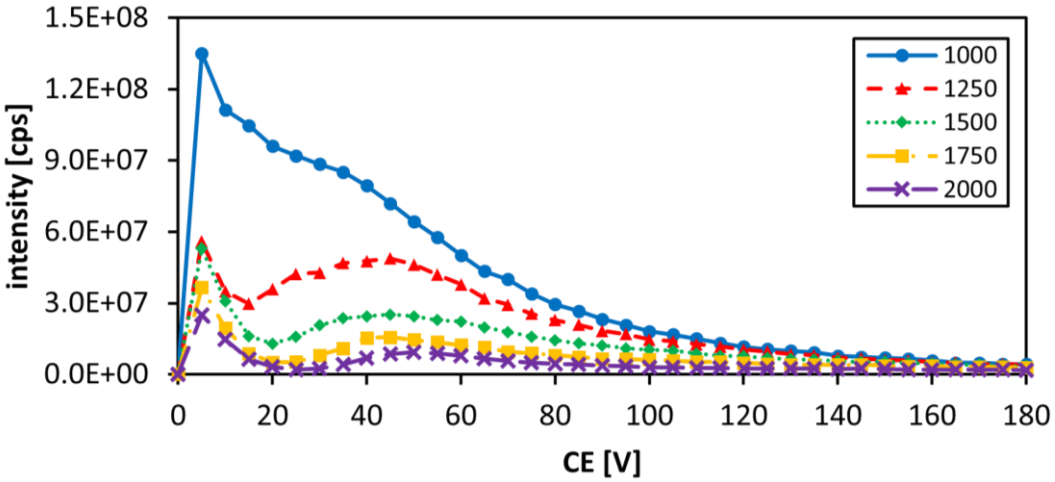

Figure 6.19: Effect of the target cut-off value ("product of") on the TIC (analyte: (*S*)-Maruoka catalyst) recorded in pure nitrogen (droplet experiment; *SV* = 0 V, *DT* = 423.15 K; *DR* = 0; *IS* = 5000 V; *CAD* = 6).

An increase of the target value leads to a great intensity loss (see Figure 6.19). In parallel, the maximum of the broad peak, which is known from Figure 6.11, is shifted to higher *CE*s. Consequently, a selective nanodroplet discrimination of less stabile nanodroplets, which would be fragmentated at lower *CE*s, is detected here. There are different explanations for this effect. On the one hand, it is possible that less stable nanodroplets are discriminated by the shift of the cut-off value. Therefore, the stability of the nanodroplets would be coupled to the *m/z* ratio, and the main nanodroplet distribution would have to start in the *m/z* range from about 777 (see Table 6.4), since even the first step leads to a significant *CE* shift and

intensity loss (see Figure 6.19). In this case, the nanodroplet distribution would be observable in Q1 mode, which does not happen. On the other hand, the increased cut-off value has an impact on the conditions in the Q1, which could lead to a fragmentation of less stable nanodroplets even with a higher *m/z* ratio. In this way, the lighter fragments would be filtered out by the high-pass filter function of the adjusted Q1. Thus, the Q1 would not represent a pure *m/z*-based filter as previously assumed but would additionally filter according to the stability of the nanodroplets. Accordingly, additional undetected nanodroplets could be part of the chemical system in the DMS cell, which are fragmented in the ion transfer before they can reach the q2 necessary for a detection.
Instead of the assumed nanodroplet discrimination, the *CE* shift of the second maximum of the TIC (see Figure 6.19) could also be explainable by an increased stability of the identical nanodroplets. Accordingly, the fragmentation would occur at higher *CE*s; however, no chemical explanations are known for these. Additionally, this theory is excluded by the findings in Figure 6.20.

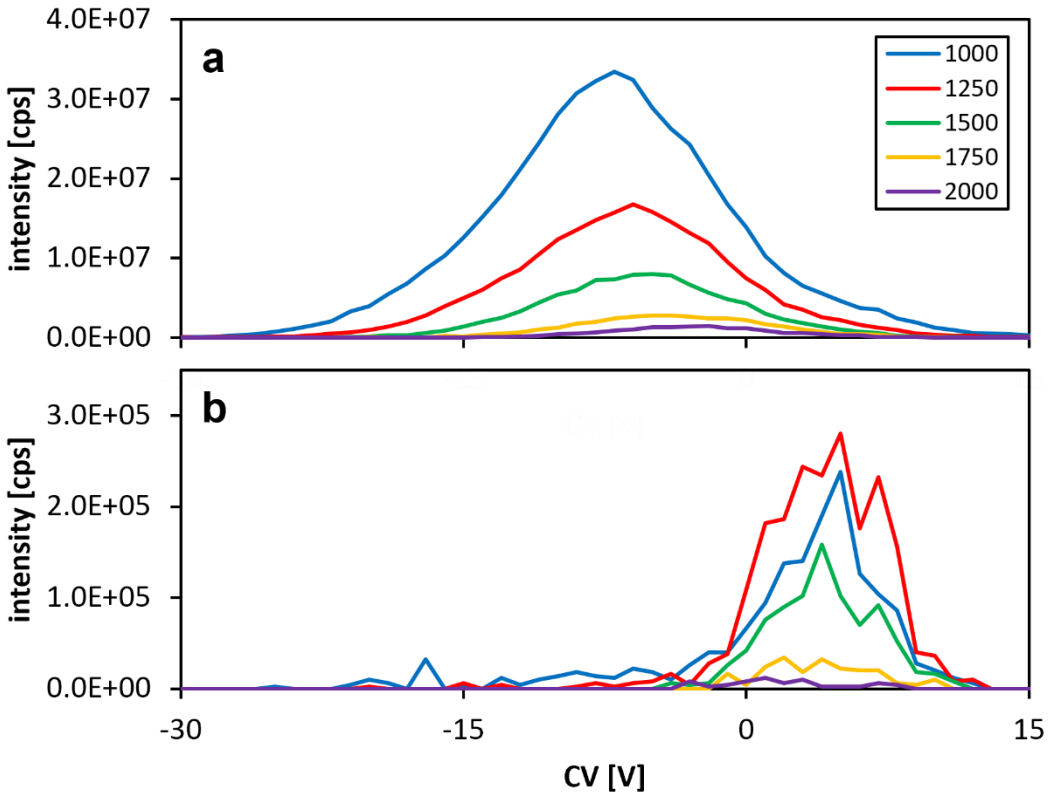

Figure 6.20: Effect of the target cut-off value ("product of") on the ionograms of the TIC (**a**) and the (*S*)-Maruoka catalyst ion (**b**) recorded with rac. 2-BuOH (1.5%) added as gas-phase modifier in nitrogen (droplet experiment, *SV* = 4000 V; *DT* = 423.15 K; *DR* = 0; *IS* = 5000 V; *CAD* = 6).

At an *SV* of 4000 V, the TIC (see Figure 6.20**a**) is shifted to higher *CV*s with increasing target value of the cut-off in combination with a significant intensity loss. The Maruoka catalyst ion (see Figure 6.20**b**, *m/z* 668) only reflects the intensity loss. Therefore, the nanodroplets, which mainly include the Maruoka catalyst ion, are partially destroyed but

not changed in their chemical behavior, which is why the *CV* shift of the maximum of the TIC should be the result of a different nanodroplet distribution. Thus, selective fragmentation in Q1 seems to be likely.
In conclusion, all results of the nanodroplet investigations indicate that it is impossible to avoid charged nanodroplets or to separate them completely from the bare ions when using a common ESI source, although not even all nanodroplet species appear to be observable. Therefore, it is useful to determine if another ionization method could solve the nanodroplet problem before testing an enantiomeric separation with an enantiopure modifier.

6.3 Alternative ionization methods

The usually distributed ESI sources are designed for a reproducible and reliable ionization. The textbook spray behavior is often lost in the process, which can lead, for example, to a mixed ionization mechanism (e.g., additional corona discharge at the tip of the ESI needle) or in a non-optimal Taylor cone. Both effects were detected at common ESI needles running under standard conditions. As a result, effects like the previously proven nanodroplets distribution can be formed, which should not happen by a textbook spray. Since the source design often prevents an ionization with a textbook spray, another ionization method might be more suitable.

6.3.1 Common APCI source

The used ion source makes it possible to switch the ionization method from ESI to APCI by changing the probe and using the integrated corona discharge needle (compare *Turbo V™ Ion Source*). For the formation of highly charged nanodroplets, ionization in the liquid phase and subsequent spraying should be necessary. Thus, the transfer of the uncharged analyte into the gas phase and the following ionization as in APCI should prevent the formation of highly charged nanodroplets.
The initial measurements of the Maruoka catalyst with the APCI probe indicate a different problem. The structure (compare Figure 6.4) and the molecular mass of the Maruoka catalyst (748.64 g/mol) suggest a rather low vapor pressure under standard conditions. Thus, the mixing ratio in the gas phase is negligible. Evaporation can be supported by increasing the source temperature T_{source} and a T_{source} of about 573.15 K was necessary to achieve a sufficiently high gas-phase mixing ratio for an observable mass signal. At 723.15 K the intensity was highest, but even under these conditions no comparable high intensity was achieved as with the ESI probe. The addition of rac. 2-BuOH as a gas-phase modifier leads to a further loss of intensity, as shown in Figure 6.21. Already, a comparatively low modifier mixing ratio of 0.5% (see Figure 6.21**b2**) reduces the signal intensity of the Maruoka catalyst ion (*m/z* 668) to less than half of what it is without a modifier (see yellow curve in Figure 6.21). Simultaneously, the TIC increases can be attributed to protonated 2-BuOH clusters $[(2\text{-BuOH})_x+H]^+$ (see green and red curves in Figure 6.21). An additional increase in the modifier mixing ratio to 1.0% (see Figure 6.21**c**) or 1.5% (see Figure 6.21**d**) has a

slightly opposite effect on the TIC and the intensities of the protonated 2-BuOH clusters $[(2\text{-BuOH})_x+H]^+$ (*m/z* 129 and *m/z* 223), while the analyte signal (*m/z* 668) decreases only slightly in intensity. Because of the low intensity, even small absolute deviations cause strong relative noise, as shown by the signal of the Maruoka catalyst ion (see yellow curve in Figure 6.21).

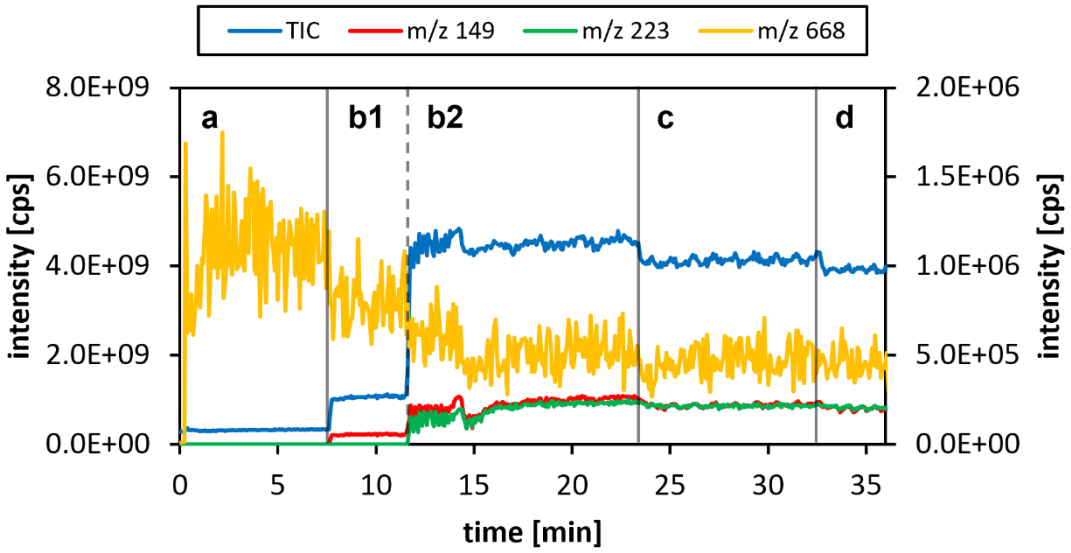

Figure 6.21: TIC (*m/z* 10 – 900, left scale) and chromatograms of protonated 2-BuOH clusters $[(2\text{-BuOH})_x+H]^+$ (x = 2: *m/z* 149; x = 3: *m/z* 223, left scale) and the (*S*)-Maruoka catalyst ion (*m/z* 668; right scale) recorded with different mixing ratios of rac. 2-BuOH as gas-phase modifier added in nitrogen (APCI, T_{source} = 723.15 K; Q1 mode): (**a**) pure nitrogen; (**b1**) 0.5% (modifier line not filled); (**b2**) 0.5%; (**c**) 1.0%; (**d**) 1.5%.

Nevertheless, the signal stability in MRM mode at 723.15 K is high enough to perform evaluable DMS measurements as compared to the ESI results (see Figure 6.22). The results of these measurements demonstrate a thermal connection between the ion source and the DMS cell, which was expected due to the missing thermodynamic separation of the two areas. While the source temperature for the ESI experiments T_{ESI} was set to 273.15 K (since no cooling unit is part of the ion source, the real temperature was about 300 K) and thus below the set *DT*, the source temperature for the APCI experiments T_{APCI} was significantly higher with a value of 723.15 K. As a result, the actual temperature in the DMS cell is increased due to T_{APCI}, and the strength of cluster effect is further reduced, as shown in Figure 6.22. Even at the lowest *DT* of 373.15 K, the cluster effect is reduced due to T_{APCI} to such an extent that the Maruoka catalyst ion almost exhibits a type-C behavior.
The increase in *DT* and the resulting decrease in the strength of the cluster effect would reduce the small chance of enantiomeric separation with enantiopure 2-BuOH. If a thermodynamic separation of the ion source and the DMS cell is not possible, APCI is unsuitable for the planed investigations of the Maruoka catalyst. Such an adjustment would only be

possible with a complex structural adjustment of the hardware, which could not be realized in this work.

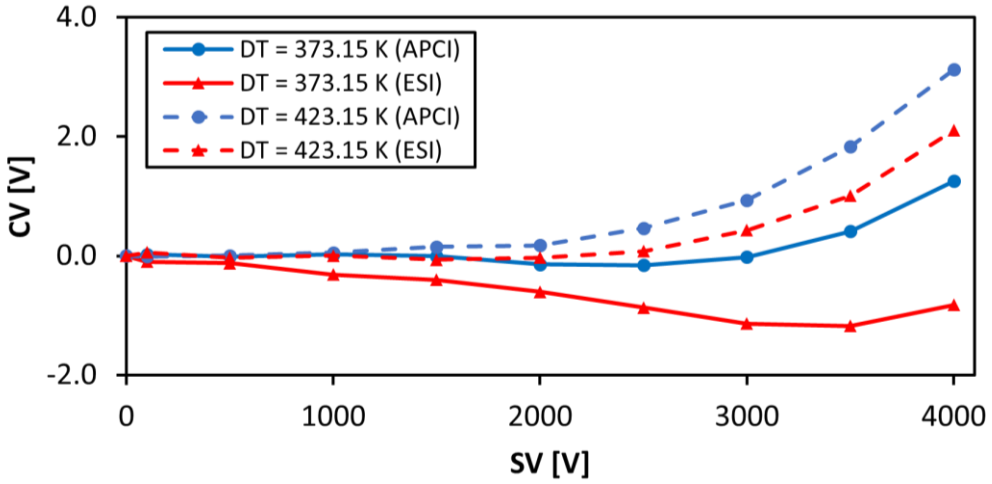

Figure 6.22: Calibrated dispersion plots of the (*S*)-Maruoka catalyst ion at selected DMS temperatures *DT*, ionization methods (ESI or APCI) and source temperatures (T_{ESI} = 273.15 K, T_{APCI} = 723.15 K) recorded with rac. 2-BuOH (1.5%) added as gas-phase modifier in nitrogen (*DR* = 0; MRM mode: 668/541, *CE* = 42 V).

6.3.2 Custom APLI source

The APLI enables a spatially punctual and chemical selective ionization through targeted focusing on a position. By strongly focusing the laser beam, scanning an ion source becomes possible, as shown by Lorenz [46]. Furthermore, a substance-specific ionization can be targeted by the used wavelength λ, whereby the absorption range of the analyte is crucial. A common laser system for APLI is a pulsed KrF^* exciplex laser emitting a λ of 248 nm (about 5.00 eV), because aromatic species such as pyrene typically adsorb well in this area. Pyrene is also a standard analyte for APLI and is therefore frequently used to characterize APLI sources [46, 128]. The structure of the Maruoka catalyst also exhibits an aromatic system (compare Figure 6.4), which is why an ionization with APLI might be possible. In addition, no nanodroplet formation is to be expected in APLI.
The custom APLI source (see *APLI source*) can be operated theoretically with any laser system. For the first results presented in the following, the NT340 UV/VIS/IR OPO (EKSPLA) was applied. This laser system is based on an *optical parametric oscillator* (OPO) and can be tuned to λ from 192 to 4400 nm [101]. For these experiments, it was set to 266 nm (about 4.66 eV) and pulsed with 10 Hz. The pulse energy for these settings is reported with over 10 mJ [101]. In the absence of experience concerning the behavior of the Maruoka catalyst as an analyte in APLI, the operation of the custom APLI source was initially tested and verified using pyrene. A pyrene solution of 10 µmol/L in MeOH/water (1:1) was sprayed using the standard probes (ESI and APCI) of the Turbo V™ Ion Source,

with the spray positioned centrally in front of the DMS entrance. The laser beam was repositioned for each measurement to optimize the number of ions detected. The ESI probe protruding into the source area makes it possible to direct the laser beam through the spray cone. In addition, the *IS* can be set to support the spray conditions and to increase the signal intensity, as shown in Figure 6.23. By increasing the *IS*, the TIC also increases; however, since the ion source is still an adapted ESI source, increasing the *IS* over a critical level leads to a second ionization mechanism, which is running parallel to the laser ionization. In the *IS* range from 0 to 2000 V, the TIC is almost completely dominated by the pyrene cation $[M]^+$ (*m/z* 202), which is generated by APLI, which is why a deactivation of the laser (see white areas in Figure 6.23) leads to an intensity drop to almost zero. At an *IS* of 2500 V, the protonated pyrene cation $[M+H]^+$ (*m/z* 203) is significantly observable both with an activated and deactivated laser. The proportion of the $[M+H]^+$ signal increases with increasing *IS* regardless of whether the laser is activated or not (compare green curve in Figure 6.23). This indicates a parallel ionization with APLI (main ion species: $[M]^+$) and ESI (main ion species: $[M+H]^+$). Moreover, the intensity of the $[M]^+$ signal increases, but it does so less than the intensity of the $[M+H]^+$ signal. Furthermore, the laser induced ionization leads to a significantly lower signal stability than the ESI mechanism (see Figure 6.23). The first DMS tests with the APLI source also indicate problems with the laser positioning. Thus, an increased baseline could be detected, which was independent of the *CV*, when the laser beam is directed straight through the laser window and the spray cone into the ion source (see Figure 3.1). With this laser position, the laser beam passes through the DMS cell, so that laser-induced reactions occur even after the ionization area. The position of the laser window and the structure of the ion source prevents an orthogonal laser beam, such that an axis-shifted positioning is the best solution in this case.

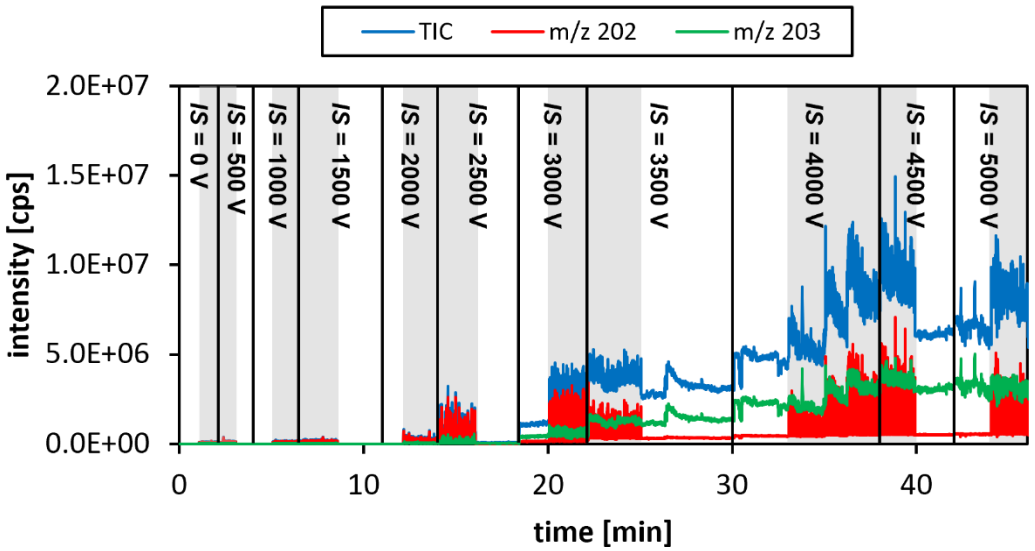

Figure 6.23: Effect of ion spray voltage *IS* on the TIC (*m/z* 201-204), the pyrene cation $[M]^+$ (*m/z* 202), and the protonated pyrene cation $[M+H]^+$ (*m/z* 203) recorded in pure nitrogen (APLI). Gray area: laser activated; laser system: NT340 UV/VIS/IR OPO, 10 Hz, 266 nm; ESI probe.

Switching to the APCI probe allows ionization of pyrene with APLI and provides evaluable DMS results, since a sufficiently high mixing ratio of uncharged analyte can be achieved in the gas phase. However, the vapor pressure of the Maruoka catalyst is too low to achieve a mixing ratio high enough for an effective ionization in the gas phase at room temperature. The still existing thermal connection between the ion source and the DMS cell again prevents the use of an APCI probe for the enantiomeric separation (compare Section 6.3.1).
Instead, the optimized setup with the ESI probe allows laser-induced ionization of the Maruoka catalyst (10 µmol/L in MeOH/water) and DMS measurements in MRM mode. Based on the experience from the pyrene experiments, the *IS* was set to zero to avoid the ESI mechanism (compare white areas in Figure 6.23), which could lead to charged nanodroplets. The resulting ionograms with and without a modifier (1.5% of rac. 2-BuOH) at different *SV* values and a *DT* of 423.15 K are shown in Figure 6.24. These ionograms are characterized by a great peak width, low intensity, and strong noise. The experience related in Section 6.1.2 suggests that the necessary reduction in *DT* would further broaden the signals, which can be prevented by increasing *DR*, but this would lead to a decrease in intensity. If the peak shape results from already known effects—such as laser-induced reactions in the DMS cell or whether it is, for example, an artifact due to the very low intensity—cannot be conclusively determined.

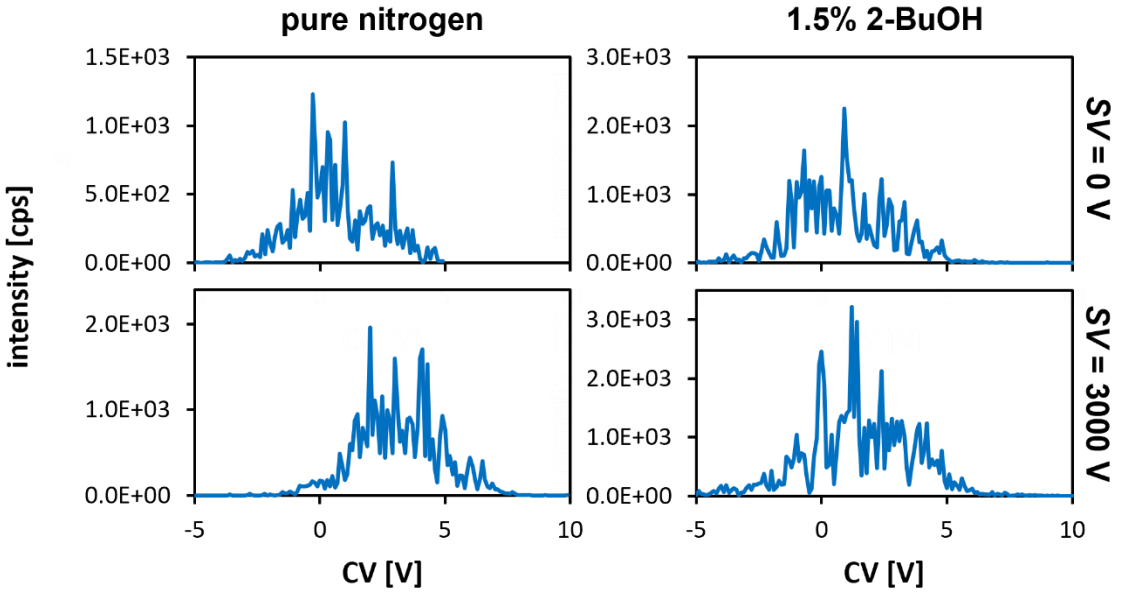

Figure 6.24: Ionograms of the (*S*)-Maruoka catalyst ion depending on the separation voltage *SV* recorded without and with rac. 2-BuOH (1.5 %) added as gas-phase modifier in nitrogen (APLI: *DT* = 423.15 K; *DR* = 0; MRM mode: 668/541, *CE* = 42 V). Laser system: NT340 UV/VIS/IR OPO, 10 Hz, 266 nm; ESI probe.

The instability of the signal coincides with the observations to the pyrene cation $[M]^+$ (*m/z* 202) with an activated laser system (see gray area in Figure 6.23). Thus, this observation seems to be based on the laser system and not only on the low signal intensity. The NT340 UV/VIS/IR OPO is a pulsed laser and so the ionization is also pulsed, which should

be averaged out by a sufficiently high number of summed mass spectra. In fact, a pulsed intensity fluctuation shown in Figure 6.25 could be observed, and a similar observation was also found for the pyrene experiments. It becomes clear that the TIC does not only follow one pulsed function; the sequence of the peak forms and intensities (compare the signals at about 1.2 and 3.7 min in Figure 6.25) indicates at least two overlaying functions, which might be the result of the uncoordinated interaction of the laser system and the MS system. It should be noted that the signal of the Maruoka catalyst ion occurs simultaneously with the increase of the TIC. That demonstrates the laser-induced ionization of the analyte.

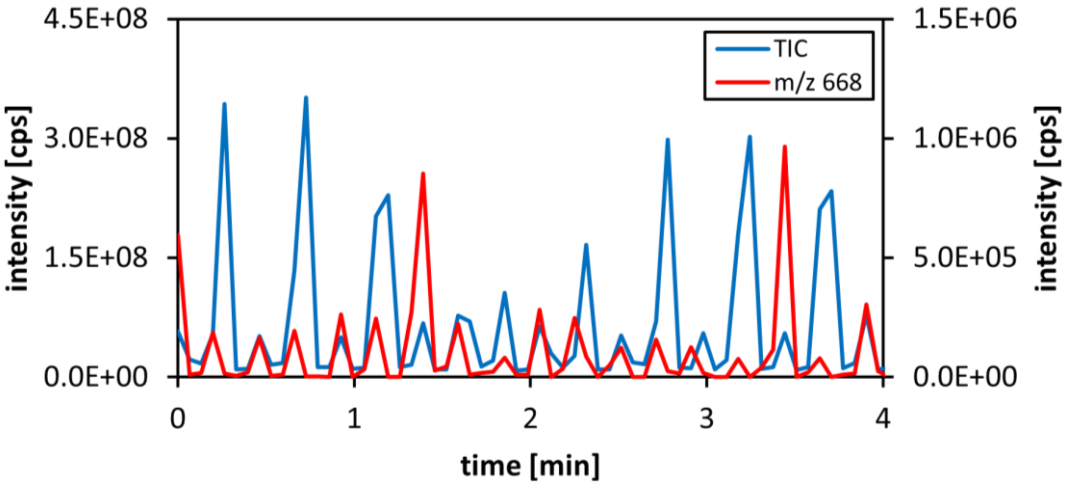

Figure 6.25: Signal stability of the TIC (*m/z* 10–800, left scale) and the (*S*)-Maruoka catalyst ion (*m/z* 668, right scale) using the custom APLI source. Laser system: NT340 UV/VIS/IR OPO, 10 Hz, 266 nm; ESI probe.

A significantly increased laser frequency could counteract the inconsistency of the ionization. Since this is not possible with the OPO laser, it was replaced by the FQSS 266-200 laser system (CryLas). This system is a solid-state laser, also has a λ of 266 nm, and allows a frequency of up to 60 Hz [102]. The pulse energy was set to 200 µJ, however, a strong noise leads to actual values of about 160 to 200 µJ. The axis-shifted positioning of the laser beam and simultaneous focusing on the spray cone for an optimal ionization was not possible due to poor focusing. Nevertheless, ionization of pyrene was detected, but the laser-induced ionization of the Maruoka catalyst was not possible by using this laser system due to the lack of focusing, which is increased by an increase in temperature during operation. The pulse energy also showed a strong dependency on the working temperature and dropped significantly after a relatively short operation time of the laser system. Therefore, this laser system seems to be unsuitable for a long-term measurement.
In summary, the simple APLI setup does not allow a reproducible and stable ionization, because both laser systems, the position of the laser window, and the source design make continuous or quasi-continuous ionization limited to the source area impossible. For this work, APLI could only become an alternative to ESI with a completely redesigned ion

source and an alternative laser system. The necessary effort, in terms of time and experimentation, would be far beyond the scope of this work. In addition, compared to pyridine, the Maruoka catalyst does not prove itself to be an optimal analyte for APLI.

6.3.3 Common nanoESI source

In contrast to an ESI source, which commonly operates at high *IS* and solvent flow, a nanoESI source operates at lower values. This should lead to more of a textbook ESI mechanism and could prevent the formation of charged nanodroplets. This theory was tested by spraying and ionizing the Maruoka catalyst with the NanoSpray® III Ion Source (Sciex), which is installed directly in front of the DMS cell (see *nanoESI source*). In this way, the *IS* and the solvent flow were set as low as possible to achieve the greatest possible contrast to the common ESI source. Since the nanoESI emitter has a tapered and significantly smaller inner diameter than the emitters of the ESI or APCI probe, clogging occurs more frequently than with the other emitters. This occurred often between two measurement sessions, which is why the emitter was switched at the beginning of almost every measurement day; as a result, the position of the emitter, the solvent flow rate, and the source parameters had to be reoptimized. Therefore, only a qualitative comparison of the results from different days could be made in terms of intensity. After confirming general functionality of the source, droplet experiments were performed. These clearly demonstrate the presence of charged nanodroplets, as shown in Figure 6.26. The TIC qualitatively corresponds to the observations of the droplet measurements with an ESI source in high-mass mode (see Figure 6.19). An increase in CE causes a release of the Maruoka catalyst ion (*m/z* 668; see red curve in Figure 6.26), which is subsequently fragmented into the first typical fragment (*m/z* 541; see green curve in Figure 6.26). An undefined species (*m/z* 365; see yellow curve in Figure 6.26) can be observed, which also appears in Figure 6.14.

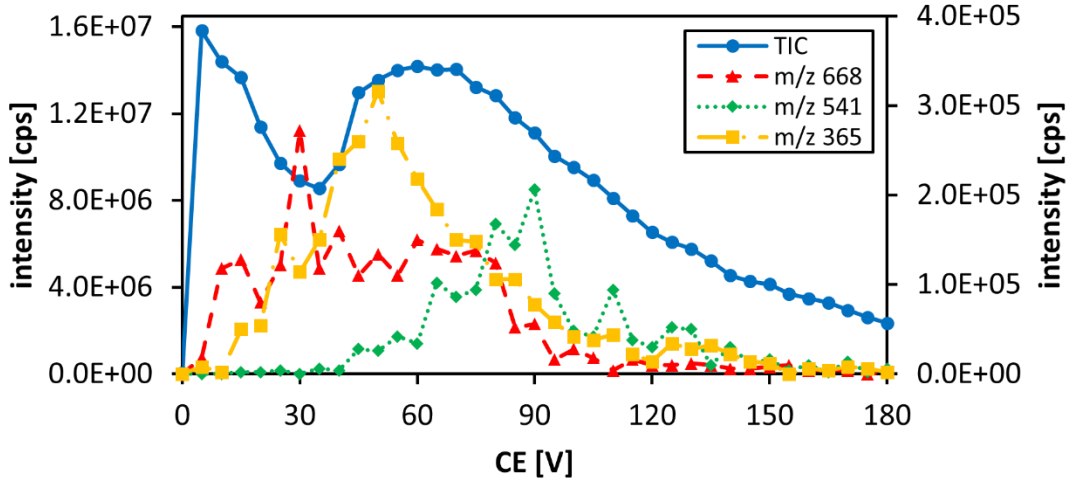

Figure 6.26: TIC (left scale) and chromatograms (right sale) of the (*S*)-Maruoka catalyst ion (*m/z* 668), the first main fragment (*m/z* 541) and an undefined signal (*m/z* 365) depending on the collision energy *CE* (nanoESI; droplet experiment; product of: 1100; *IS* = 2500 V).

Further characteristics of the charged nanodroplet distributions could also be reproduced with the nanoESI source, such that the wave of the baseline (compare Figure 6.9) also appears qualitative. The charged nanodroplets cannot be prevented due to increasing the *DT*, a variation in the *IS*, or any other source parameter such as the nebulizer gas (*GS1*). These results suggest that even with nanoESI, a nanodroplet distribution comparable to the ESI results cannot be avoided. Thus, there is no advantage to switching to the nanoESI source. Moreover, the signal reproducibility and stability of the ESI source is significantly higher, which is mainly due to an open design of the nanoESI source. As a result of the open design, the nanoESI source is susceptible to external influences, as shown in Figure 6.27. At irregular times (red arrows in Figure 6.27), an air vortex was actively created outside the ion source. For this purpose, a simple sheet of paper was waved in front of the MS system to simulate unavoidable air turbulences from normal laboratory work. Even slight air turbulences in front of or beside the ion source led to massive drops in performance. This effect, which was actively generated here, could also be detected as a result of open doors or even through air conditioners.

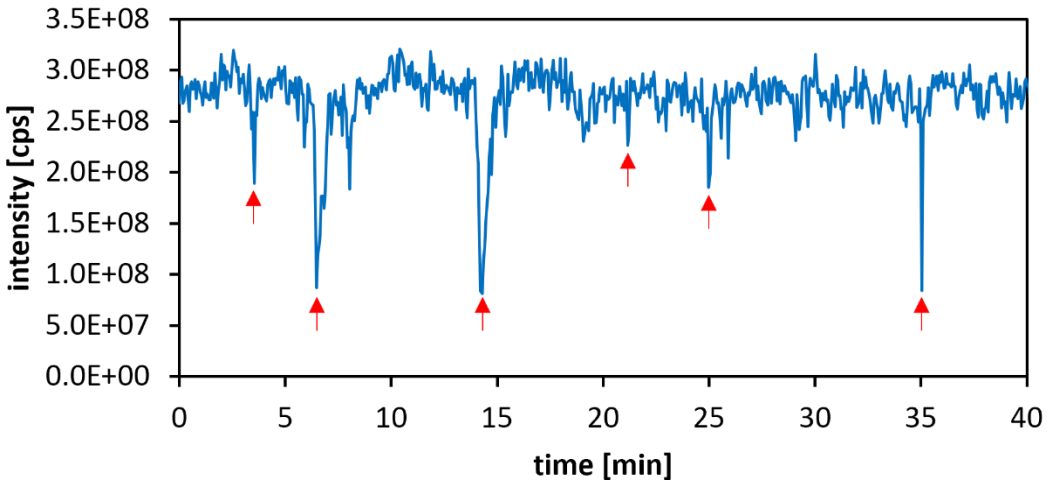

Figure 6.27: Signal dropouts of the TIC due to active air turbulences generated outside the nanoESI source (red arrows, analyte: Maruoka catalyst).

It is likely that extra shielding of the nanoESI source could lead to a less vulnerable source. Nevertheless, the emitters susceptible to clogging prevent high reproducibility over several measurement days. The presence of a nanodroplet distribution could possibly be preventable by further optimizations of the source parameter, but all data indicate that the source design does not allow a nanodroplet-free ionization.

6.3.4 Comparison and conclusion

In summary, the ionization with any ion source leads to several positive as well as negative properties for the enantiomeric separation, which are summarized in Table 6.5. The perfect ionization method cannot be determined, and a compromise must be found. In this context,

a distinction must be established between undesirable effects that can be balanced and exclusion criteria that preclude the use of the ion source in the form presented here or even the entire method.
The APCI mode of the Turbo V^{TM} Ion Source can be clearly excluded for the ionization of the Maruoka catalyst since evaporation is not realizable with this source design in combination with a sufficiently low source temperature (see Figure 6.22). The custom APLI source fulfills the identical exclusion criteria when it is operated with the APCI probe. On the other hand, the ESI probe also does not result in a stable signal (see Figure 6.25). Additionally, the laser beam is parallel to the ion stream, which easily leads to an uncontrolled ionization in the DMS cell and thus distorts the results. In sum, these points preclude the APLI source in the presented design. The results of the ESI source and the nanoESI source differ only slightly in the relevant areas, as a charged nanodroplet distribution was proven for both methods (see Figures 6.19 and 6.26). A quantitative difference of the distribution is likely and expected, but with the available data it is not possible to make a meaningful comparison. Therefore, the lack of signal stability and reproducibility of the nanoESI source are the decisive criteria.

Table 6.5: Main pros/expectations and cons/problems of the different ion sources respectively ionization methods investigated (ESI, APCI, APLI and nanoESI) in terms of potential application for enantiomeric separation in DMS.

Ion source/ ionization method	Pros/ expectations	Cons/ problems
ESI	Good reproducibility and great constancy	Unavoidable charged nanodroplets in the DMS and MS stages
APCI	Good reproducibility and great constancy No nanodroplets are expected	High T_{source} needed for evaporation of the analyte → weakening of the cluster effect
APLI	Selective ionization No nanodroplets are expected	No stable signal realizable Ionization in the DMS cell
nanoESI	**In theory**: textbook ESI mechanism → No nanodroplets are expected	Similar problems with charged nanodroplets High susceptibility to external influences

In conclusion, the ESI source is the most promising ion source for the enantiomeric separation despite the nanodroplets distribution. The interpretation of results must always consider the undefinable chemical environment in the DMS cell and possible interactions of

the bare ions with the nanodroplets. It must be mentioned that this choice of ionization method is based on the Maruoka catalyst as analyte. Thus, the exclusion criteria of the APCI probe are not valid for every analyte, as demonstrated with pyrene in the APLI source. Through an adapted source design, the excluded ionization methods could also become realistic alternatives for analytes with a low vapor pressure at room temperature. For this purpose, a large technical and temporal development effort would be.

6.4 Modification with enantiopure modifier

The interactions of a particular enantiomer of a chiral ion with a chiral modifier molecule lead, in a highly simplified manner, to one of two possible stereoselective cluster structures, depending on the stereoselectivity of the modifier: a matching combination leading in an optimal assembly, or a non-matching combination leading in a less fitting assembling. The structural difference between the two formations, and thus the difference in CCS, should be reinforced by increasing the steric hindrance of the modifier or analyte. As a result, the addition of a rac. modifier to a rac. mixture of ions leads to four combinations of one ion with one modifier molecule, which can be divided into two pairs of clusters structures (the matching and the non-matching combinations). Accordingly, each pair should have the same CCS, since they are mirrored structures. If in a DMS measurement the proportions of matching and non-matching combinations are different for both enantiomers of an analyte, enantiomeric separation is theoretically possible. This assumption is critical for enantiomeric separation and is investigated in the following way. The charged enantiopure Maruoka catalyst and phenylalanine are modified with enantiopure 2-BuOH. Based on the experience of the previous experiments, the common ESI source and the settings shown in Table 6.1 were used. Additionally, the MRM method was used for both analytes (Maruoka catalyst: 668/541 and *CE* = 43 V; phenylalanine: 166/120 and *CE* = 20 V). The *CV* was increased in 0.1 V steps for the dispersion plots and in 0.05 V steps for the ionograms. It should be noted that only a limited amount of enantiopure 2-BuOH was available and therefore, not every measurement was repeated with both enantiomers of the modifier, but with both enantiomers of the ion. To avoid performance fluctuations as much as possible, all measurements with the enantiopure modifier were performed on the same day and with as few parameter changes as possible (e.g., with as few *DT* conversions as possible). Both analytes are first considered independently and then the results are combined and evaluated.

6.4.1 Maruoka catalyst

First, an enantiomeric separation of the Maruoka catalyst was experimentally investigated with the resulting calibrated dispersion plots shown in Figure 6.28. As gas-phase modifiers, rac. 2-BuOH (see Figure 6.28**a**) and enantiopure (*R*)-2-BuOH (see Figure 6.28**b**) in a mixing ratio of 1.5% were used. The rac. 2-BuOH does not lead to enantiomeric separation within the error limits up to an *SV* of 3000 V. This observation was expected, since the stereoselective cluster structures occur in equal proportions for both enantiomers. Only

with an enantiomeric excess can the cluster structure distribution become unbalanced, and an enantiomeric separation can be possible. A slight deviation at higher *SV* can be explained by signal noise and non-perfect Gaussian curves as the consequence of a low *DT* and the presence of a modifier (compare Figures 6.7 and 6.29). The absolute deviation at an *SV* of 4000 V is extremely small ($|\Delta CV| < 0.3$ V) and just visible in Figure 6.28**a** due to low *CV* range plotted (-4 to 1 V). Similar deviations must also be expected for the addition of enantiopure modifiers, which is why an actual separation must significantly exceed this to be recognized. The addition of an enantiopure modifier (see Figure 6.28**b**) also does not lead to an enantiomeric separation at an *SV* in the range from 0 to 3500 V. At an *SV* of 4000 V, a ΔCV of 0.251 ± 0.121 V can be observed, which is in the range of the deviation with rac. 2-BuOH and therefore cannot be reliably attributed to a stereoselective cluster formation. Accordingly, there are either no different matching and non-matching combinations with different cluster structures or the possible effect of stereoselective cluster formation is too weak to be detected by the system used. Therefore, the resolution would be too low.

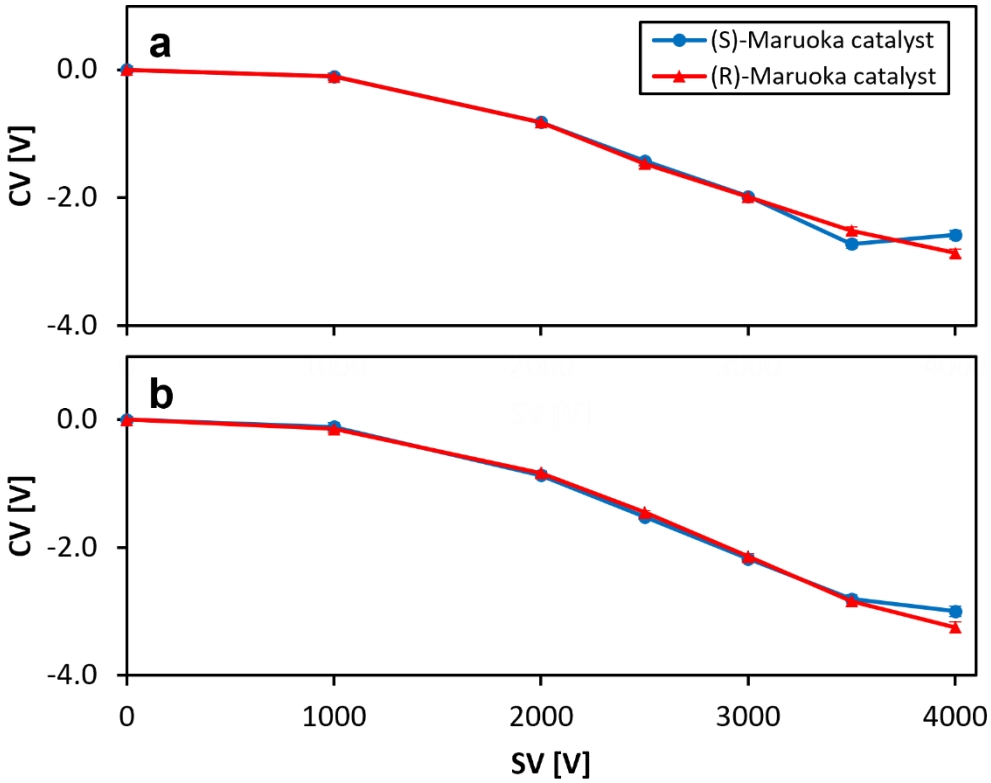

Figure 6.28: Calibrated dispersion plots of the (*R*/*S*)-Maruoka catalyst ion recorded with gas-phase modifier (1.5%) present in nitrogen: (**a**) rac. 2-BuOH, (**b**) (*R*)-2-BuOH.

Another explanation would be that the chiral information is lost by a too high mean cluster size because of a high modifier mixing ratio. In this case, the cluster structure would become independent of the central ion to some extent when there is a sufficiently high number of clustered modifier molecules. Such behavior could be supported by delocalized charge,

as shown by Haack et al. for the protonated MeOH cluster systems [13]. Thus, in Figure 6.29, the ionograms of the Maruoka catalyst ion at an *SV* of 3500 V with added enantiopure 2-BuOH in different mixing ratios are shown and the *CV* values are summarized in Table 6.6. The reduced step size when increasing the *CV* should also increase the resolution. The ionograms show more Gaussian shapes with decreasing modifier mixing ratio, which is consistent with the observations from Figure 6.7. This visual effect is confirmed by the mathematical errors, which decrease with decreasing modifier mixing ratio (see Table 6.6). The actual measurement errors are likely to be significantly higher but can only be determined to a limited extent since no reliable conclusions can be made about the performance of the DMS system under the non-typical conditions used for these experiments.

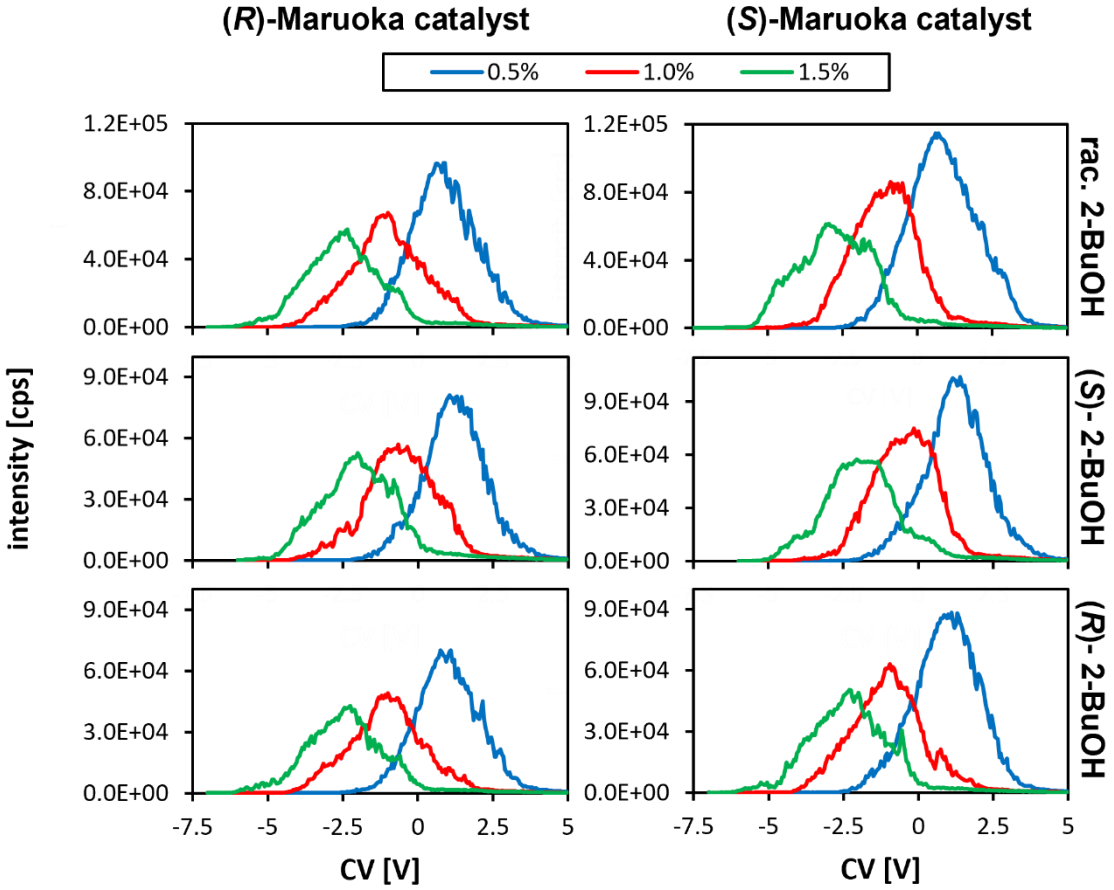

Figure 6.29: Ionograms of the (*R*/*S*)-Maruoka catalyst ion recorded with rac./(*R*/*S*)-2-BuOH (different mixing ratios) added as gas-phase modifier in nitrogen (*SV* = 3500 V).

As shown in Figure 6.28 and Table 6.6, a slightly different *CV* can be detected for both enantiomers of the Maruoka catalyst ion with 1.5% rac. 2-BuOH, which is slightly higher than the calculated error range. Again, this should not be the result of a different cluster structure and can therefore be attributed to inaccuracies based on the signal shape, which decrease with decreasing modifier mixing ratio. The difference in *CV* is small enough that no real ion separation can be mentioned. In contrast, the addition of enantiopure 2-BuOH could lead to a different cluster effect on the enantiomers of the Maruoka catalyst ion and

thus to a different *CV*, but these are almost identical within the error limits in every measurement (compare the results in each row in Table 6.6). Thus, enantiomeric separation cannot be observed for a particular enantiomer of the modifier. However, it is notable that the addition of (*S*)-2-BuOH leads to a slightly weaker cluster effect than the addition of (*R*)-2-BuOH. The addition of 1.5% (*R*)-2-BuOH leads to a *CV* increased by 0.447 ± 0.063 V compared to the modification with (*S*)-2-BuOH for the (*R*)-Maruoka catalyst ion (see bold values in Table 6.6). The (*S*)-Maruoka catalyst ion behaves in a comparable way, both qualitatively and quantitatively. Consequently, there is much to suggest that this is not the result of a stereoselective cluster formation, as this would lead to a reversed sequence with the (*S*)-Maruoka catalyst ion. Instead, this could be the result of a different actual purity of the modifier.

Table 6.6: Compensation voltages of the (*R*/*S*)-Maruoka catalyst ion recorded with rac./(*R*/*S*)-2-BuOH (different mixing ratios) added as gas-phase modifier in nitrogen at an *SV* of 3500 V.

Modifier	**Modifier mixing ratio**	***CV* [V] (*R*)-Maruoka catalyst**	***CV* [V] (*S*)-Maruoka catalyst**
racemic 2-butanol	0.5%	0.889 ± 0.026	0.850 ± 0.019
	1.0%	-0.980 ± 0.038	-1.097 ± 0.027
	1.5%	**-2.478 ± 0.039**	**-2.690 ± 0.047**
(*S*)-2-butanol	0.5%	1.200 ± 0.024	1.249 ± 0.024
	1.0%	-0.537 ± 0.037	-0.465 ± 0.032
	1.5%	**-1.984 ± 0.046**	**-1.894 ± 0.046**
(*R*)-2-butanol	0.5%	0.996 ± 0.019	0.934 ± 0.021
	1.0%	-0.998 ± 0.039	-1.036 ± 0.041
	1.5%	**-2.431 ± 0.043**	**-2.326 ± 0.045**

In summary, no signs of an enantiomeric separation could be established. The few *CV* shifts are weak, independent of the stereoselectivities of modifier and ion, and can be adequately explained independently of stereoselective cluster formation.

6.4.2 Phenylalanine

The experiences of the previous section suggest that a possible enantiomeric influence on the cluster effect through chemical modification with enantiopure 2-BuOH is likely to be rather weak. Therefore, phenylalanine with a stronger absolute cluster effect could lead to an observable absolute effect even with a small relative stereoselective impact. However, the dispersion plots do not show an enantiomeric separation for any stereoselective combination of protonated phenylalanine and 2-BuOH (0.15%), as shown in Figure 6.30. It

should be noted that the deviations in *CV* as known from Figure 6.28, also partly occurs, but due to the greater *CV* range plotted (-70 to 10 V) they are not observed in Figure 6.30.

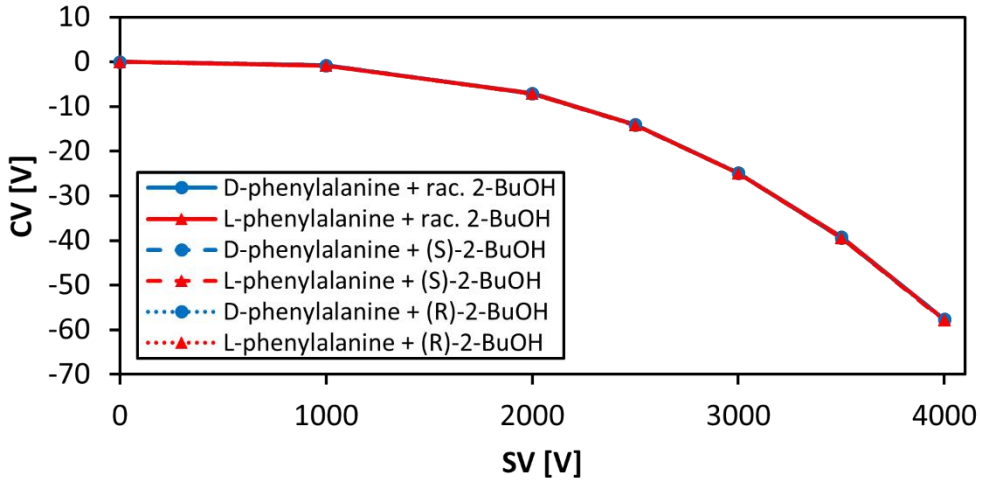

Figure 6.30: Calibrated dispersion plots of the protonated D/L-phenylalanine recorded with rac./(*R*/*S*)-2-BuOH (0.15%) added as gas-phase modifier in nitrogen.

Thus, the *CV* range of the dispersion plots in Figure 6.30 could lead to a distorted conclusion, suggesting a lack of stereoselective clustering. To avoid this, the cluster effect at an *SV* of 3500 V is examined in more detail. In addition, the limit of narrowing due to increasing the *DR* should also be tested for enantiopure modifier (compare Table 6.1). Therefore, the ionograms of phenylalanine with (*R*)-2-BuOH added as gas-phase modifier and different *DR* settings are shown in Figure 6.31 (**a**: L-enantiomer; **b**: D-enantiomer).

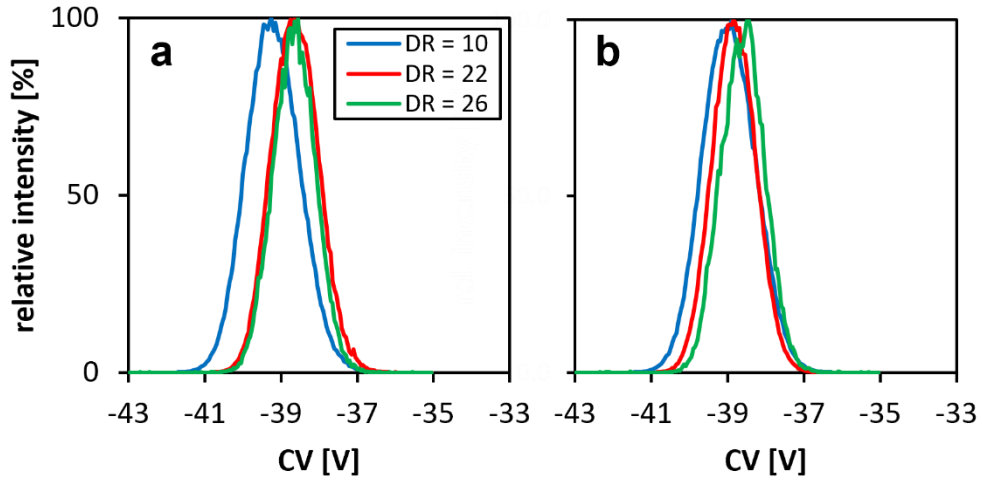

Figure 6.31: Ionograms of the protonated phenylalanine (**a**: L-enantiomer; **b**: D-enantiomer) at selected DMS resolutions *DR* recorded with (*R*)-2-BuOH (0.15%) added as gas-phase modifier in nitrogen (*SV* = 3500 V).

The common DMS settings lead to almost Gaussian distribution with a low level of noise (see Figure 6.31), which is confirmed by small mathematical errors, as shown in Table 6.7. One consequence of this is a high reproducibility, which is also clearly shown in Figure 6.30. The increase of the residence time in the DMS cell provides the expected sink of the HWHM: For L-phenylalanine (see Figure 6.31**a**), the HWHM decreases from 0.804 ± 0.003 V at a *DR* of 10, over 0.706 ± 0.006 V (*DR* = 22) to 0.643 ± 0.005 V (*DR* = 26). Simultaneously, by increasing the *DR* from 10 to 26, a drop in intensity—of about 99.51% in maximum height and 99.61% in area—takes place. In addition to these expected effects, the increase in *DR* leads to an increase in *CV*. Similar effects are observable for D-phenylalanine (see Figure 6.31**b**) and by modifying with (*S*)-2-BuOH. Thus, the qualitative effects of the *DR* variation on the *CV* are not based on stereoselective interactions in the gas phase.

Table 6.7: Compensation voltages of the protonated L/D-phenylalanine at selected DMS resolutions *DR* recorded with rac./(*R*/*S*)-2-BuOH (0.15%) added as gas-phase modifier in nitrogen at an *SV* of 3500 V.

Modifier	***DR***	***CV* [V] L-phenylalanine**	***CV* [V] D-phenylalanine**
rac. 2-butanol	**10**	**-39.137 ± 0.008**	**-39.196 ± 0.008**
(*S*)-2-butanol	**10**	**-39.372 ± 0.007**	**-39.158 ± 0.004**
	26	-38.717 ± 0.008	-38.750 ± 0.010
(*R*)-2-butanol	**10**	**-39.197 ± 0.008**	**-38.954 ± 0.007**
	22	-38.623 ± 0.008	-38.829 ± 0.004
	26	-38.650 ± 0.006	-38.600 ± 0.009

Stereoselective interactions should be detected in a different strength of the cluster effect and thus in the *CV* values. In this context, the increasing resolution by increasing *DR* is not rated higher than the intensity loss and the shifting in *CV*, which is why a *DR* of 10 was used for the following experiments. The ionograms of both phenylalanine enantiomers modified with rac. 2-BuOH, (*R*)-2-BuOH, and (*S*)-2-BuOH are shown in Figure 6.32, and the corresponding *CV*s are marked bold in Table 6.7. Similar to the results shown in Figure 6.30, the cluster effect and thus the *CV* is visually independent of the stereoselective information. Only two ionograms deviate marginally from the others in Figure 6.32. The combination of L-phenylalanine with (*S*)-2-BuOH indicates a slight *CV* shift in negative direction, while the ionogram of D-phenylalanine with (*R*)-2-BuOH is slightly shifted in the opposite direction, which is confirmed by the *CV* values (see Table 6.7). However, the stereoselective combinations with deviated ionograms should lead to mirrored cluster structures from each other and thus the identical behavior in DMS is expected. Therefore, the difference in *CV* cannot be attributed to stereoselective interactions.

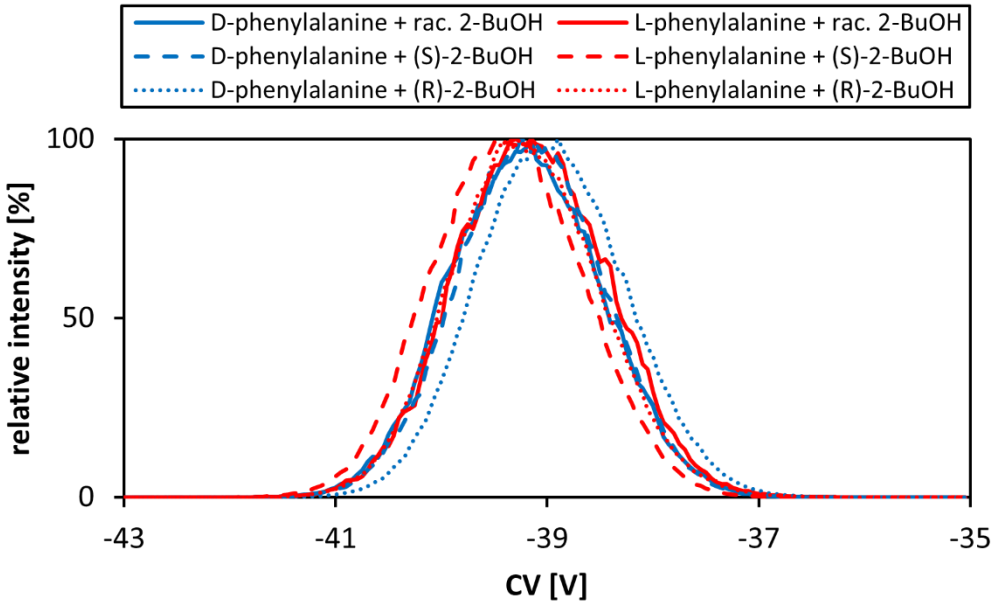

Figure 6.32: Ionograms of the protonated D/L-phenylalanine recorded with rac./(*R*/*S*)-2-BuOH (0.15%) added as gas-phase modifier in nitrogen (*SV* = 3500 V).

It should be noted that the low error limits due to the low noise led to different *CV* within the error limits in several cases. Once again, however, no stereoselective effect can be detected here.

6.4.3 Interpretation

All in all, no experimental enantiomeric separation can be proven. Although the investigations of both the Maruoka catalyst and phenylalanine indicates small deviations in individual stereoselective ion-modifier combinations, but no underlying systematic is recognizable. Instead, these artifacts can be explained with measurement inaccuracies, since most of the deviating measurement points show displacements in the order of magnitude of the measurement steps by increasing the *CV*. Nevertheless, these results do not disprove beyond doubt the enantiomeric separation due to the gas phase modification with a chiral modifier in DMS. There are different explanations for the absence of observable stereoselective interactions. First, the charged nanodroplet distribution discussed in Section 6.2 could cause the expected effect and create an undefined chemical environment in the DMS cell. Thus, for example, achiral solvent species can reach the DMS cell and become a second modifier, which forms clusters with the bare ions. This would shield the chiral information. Moreover, the interactions with nitrogen or with contaminations such as water could lead to similar effects. Another explanation is that the resolution of the DMS system is too low. According to this explanation, the stereoselective effect would be so weak that it might lead to a minimal enantiomeric separation. Both possibilities could potentially be verified by elaborate hardware adaptions.

Another possibility that could prevent an enantiomeric separation would be if the steric hindrances of both analyte enantiomers and the modifier are too low to result in different cluster structures with different CCS. In this case, no basis for an enantiomeric separation exists.
Finally, the model of matching and non-matching interactions might be too simple to represent the complex and dynamic reaction system. Through a large number of possible clustering positions, there is a broad cluster distribution with different CCSs. The dynamic clustering-declustering process leads to a statistically medium differential mobility over the entire DMS process. Consequently, two different stereoselective combinations of an ion and a modifier can lead to cluster distributions, which are significantly different but almost identical in the medium CCS and the bonding energies in the cluster structures. Accordingly, the differential mobility and the behavior in DMS is almost identical.

6.5 Numerical studies on stereoselective clustering

Because of the lack of an experimental enantiomeric separation in DMS, numerical studies are used to determine stereoselective clustering. The complex structure of the Maruoka catalyst with many degrees of freedom (compare Figure 6.4) makes a numerical study costly and time consuming. Therefore, only protonated chiral amino acids (alanine and phenylalanine) are simulated as ions for simplicity, which are clustered with 2-BuOH in the next step. These chemical systems allow a more detailed examination with significantly less computational effort. Nevertheless, the cluster structures are still complex; therefore, approximations and further simplifications are necessary.
In the first step, the geometries of bare reactants (protonated amino acids and 2-BuOH) were optimized on the B3LYP/6-31++G(d,p) level of theory (compare Section 3.5). The stability was determined by the sums of the electronic energy E_0 and the Gibbs free energy corrections G_{corr}, which is calculated for each conformer n (in the following: G_n). The minimum value G_{min} for each species defines the most stable conformer, which was used as input for the geometry optimizations of the first cluster $[^{L/D}AA+(R/S)\text{-2-BuOH+H}]^+$. Only the L-enantiomer of the amino acid ^{L}AA was clustered with a 2-BuOH molecule. This method was carried out with both enantiomers of 2-BuOH. Already at this point, it should lead to different stable clusters and different main cluster species, if stereoselective clustering proceeds. In the next step, the CCSs of the main reactants and cluster species were calculated using the MobCal-MPI code (compare Section 3.5) [111]. Based on the calculated CCS, it can be estimated whether different cluster structures also lead to differences in the differential mobility. However, it should be noted that this method examines only a fragmentary part of reality. Thus, only the first cluster $[^{L}AA+(R/S)\text{-2-BuOH+H}]^+$ is investigated while larger clusters are ignored. Moreover, the dynamic of the cluster system is ignored, which cannot be ignored in reality even under constant conditions (compare Chapter 5). Accordingly, the following calculations should be understood as numerically proof-of-concept and not as definitive proof. Nevertheless, it can be assumed that if stereoselective clustering is not evident, then the theoretical basis for enantiomeric separation is lacking.

6.5.1 Reactant optimization

The geometrical optimization and the following CCS calculation for 2-BuOH (both enantiomers) leads to the results shown in Figure 6.33.

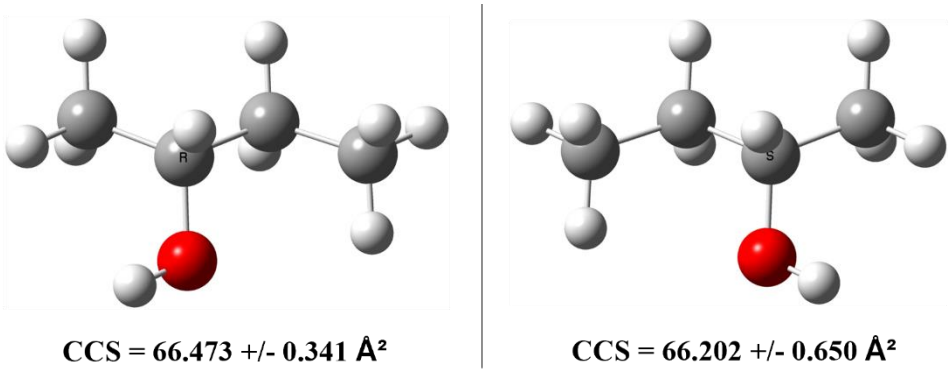

Figure 6.33: Optimized geometries of 2-BuOH (*R*-enantiomer: left; *S*-enantiomer: right) calculated at the B3LYP/6-31++G(d,p) level of theory and the CCSs calculated with the MobCal-MPI code.

The optimized structures are mirror images within the error limits, which is not surprising, since the behavior of both enantiomers should be identical in an achiral environment. Energetically, both enantiomers differ by only $2.72 \cdot 10^{-5}$ eV, which corresponds to about $4.28 \cdot 10^{-7}$% and can be considered almost identical. The CCSs are also identical within the error limits. Although other conformers are possible in addition to the geometries shown in Figure 6.33 due to marginal differences in G_n. The mirror image pair formation can be verified for the entire geometrical distributions. In a further simplification and to keep the number of calculated cluster structures within feasible limits, only the three most stable geometries of each 2-BuOH enantiomer were used, which differ mainly by a rotation of the hydroxy group around the C-O bond.
In Figure 6.34, the optimized geometries of the protonated L-amino acids $[^{L}AA+H]^{+}$ are presented. In addition to protonated L-phenylalanine (^{L}Phe), which was experimentally investigated in the previous sections, protonated L-alanine (^{L}Ala) was also calculated as ionic species. As the structurally least complex chiral amino acid, alanine is the ideal choice for targeted pretesting. Only one clear main species emerges for the protonated L-alanine (see left structure in Figure 6.34), while the protonated L-phenylalanine has several similar stable conformers (see right structures in Figure 6.34). These can differ noticeably in geometry and CCS.

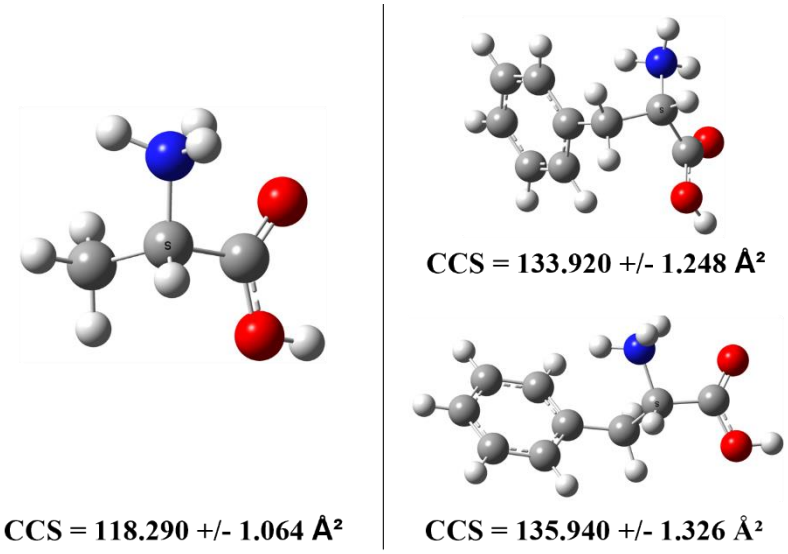

Figure 6.34: Optimized geometries of protonated L-alanine (left) and L-phenylalanine (right) calculated at the B3LYP/6-31++G(d,p) level of theory and the CCSs calculated with the MobCal-MPI code.

In this case, the relative probability of a conformer *n*, which is defined as p_n, becomes important. For a distribution of *x* conformers, it can be calculated with Equation 6.1 based on the Boltzmann distribution [110, 127]:

$$p_n = \frac{1}{Z} \cdot e^{\frac{G_n - G_{min}}{k_b T}} \tag{6.1}$$

Here, the Boltzmann constant is defined as k_b and the sum of the probabilities of all conformers *x* is defined as *Z* (see Equation 6.2).

$$Z = \sum_n^x e^{\frac{G_n - G_{min}}{k_b T}} \tag{6.2}$$

Based on p_n, a statement can be made about the importance of a conformer for the entire distribution. For the protonated L-phenylalanine, two main species can be detected, which together account more than 99% of the distribution (see right structures in Figure 6.34).

6.5.2 Numeric investigations of cluster structures

The Gibbs free energy of a clustering reaction $\Delta_R G$ can be calculated using the energetic information of the thermodynamic calculation (compare Equation 3.1), from which the stability of a cluster can be derived. However, a simplification is conducted since it is not the exact cluster stability that is of interest in this study but rather the question of a relatively different cluster structure and stability in dependence of the stereoselectivity of the modifier. If $\Delta_R G$ were significantly different for the formation of the main cluster species with each enantiomer of the modifier, a different cluster strength would be evident. However,

only 2-BuOH and one amino acid were used as reactants, and these are energetically identical within the limits of simplifications for all cluster reactions of the same distribution considered. This should make it possible to formulate qualitative statements about the relative cluster stability based on the thermodynamic information of the optimized cluster structures. This approach can be applied under the condition that only the first cluster of a single cluster distribution $[^{L}AA+(R/S)\text{-2-BuOH+H}]^{+}$ is studied. The cluster structures were optimized using the main conformers of the reactants for the input files (see Figures 6.33 and 6.34).

Alanine

In this way, the optimized cluster structures of the protonated ^{L}Ala and 2-BuOH $[^{L}Ala+(R/S)\text{-2-BuOH+H}]^{+}$ were determined, which are shown in Figure 6.35.

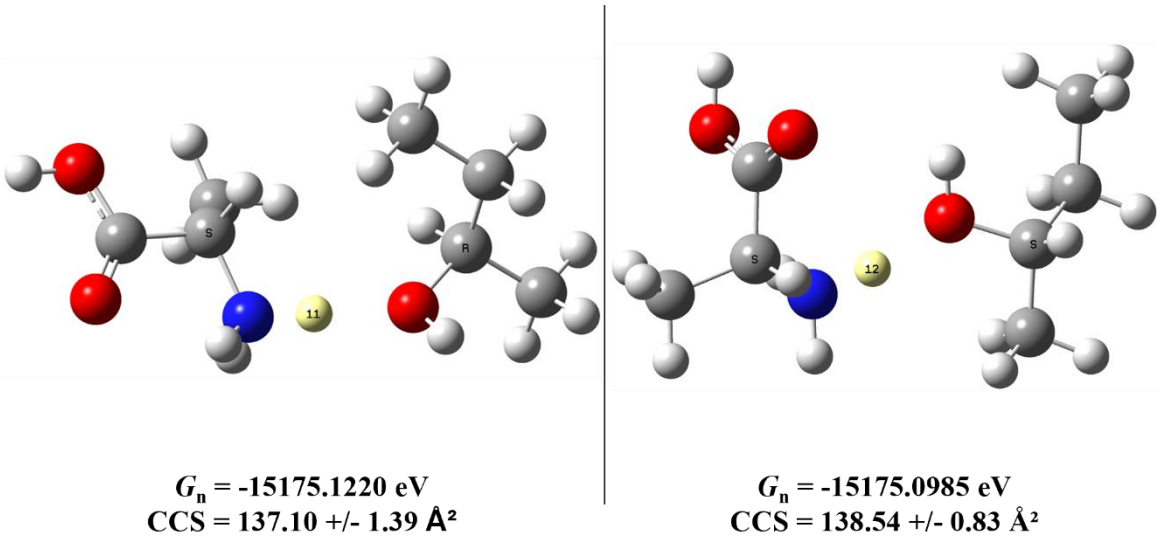

Figure 6.35: Optimized geometries of L-alanine clustered with (*R*)-2-BuOH (left) and (*S*)-2-BuOH (right) calculated at the B3LYP/6-31++G(d,p) level of theory and the CCSs calculated with the MobCal-MPI code.

Both cluster structures share some visual similarities in geometry, such as the intermolecular orientation of the hydroxy group of the modifier to a hydrogen atom of the NH_3^+ group. However, the hydrogen atom to which the hydroxy group is orientated depends on the stereoselectivity of the modifier ((*R*)-2-BuOH: H11; (*S*)-2-BuOH: H12; see Figure 6.35). Despite this noticeable structural difference and a small difference in the calculated G_n values (ΔG_n = 0.0234 eV), the calculated CCS of both clusters are identical within the error limits. In addition, it should be noted that the cluster distribution for each modifier is flat, and so a high number of different conformers is possible. In Table 6.8, the four most stable of each distribution are listed.

Table 6.8: Relative stability of the four main $[^{L}Ala+(R/S)\text{-}2\text{-}BuOH+H]^+$ species of each stereoselective cluster distribution calculated at the B3LYP/6-31++G(d,p) level of theory and the CCSs calculated with the MobCal-MPI code.

Cluster species	G_n [eV]	G_n - G_{min} [eV]	CCS [Å²]
$[^{L}Ala+(R)\text{-}2\text{-}BuOH+H]^+$ ((*R*)-cluster)	**-15175.1220**	**0.0000**	**137.10 ± 1.39**
	-15175.1150	**0.0071**	**140.83 ± 1.01**
	-15175.0999	0.0222	138.91 ± 0.97
	-15175.0939	0.0281	137.70 ± 1.20
$[^{L}Ala+(S)\text{-}2\text{-}BuOH+H]^+$ ((*S*)-cluster)	-15175.0985	0.0000	138.54 ± 0.83
	-15175.0946	0.0039	135.32 ± 1.25
	-15175.0941	0.0044	137.11 ± 1.19
	-15175.0900	0.0085	137.71 ± 1.38

These parts of the cluster distributions show for the $[^{L}Ala+(S)\text{-}2\text{-}BuOH+H]^+$ clusters (in the following (*S*)-cluster) a flat distribution, while the $[^{L}Ala+(R)\text{-}2\text{-}BuOH+H]^+$ (in the following (*R*)-cluster) distribution has two main conformers (see bold values in Table 6.8), which differs from the rest of the distribution. However, the main conformers cover only about a quarter of the invested cluster distribution (according to Equation 6.1) due to a still relatively small G_n gap, which is why the entire cluster distribution must be considered. The further distribution also shows a flat trend in a similar G_n range such as the (*S*)-cluster distribution (see Table 6.8). The CCSs does not show a direct connection to thermodynamic values and both distributions do not show a clear trend.
The different cluster structures and distributions suggest that enantiomeric separation could be theoretically possible, although the numeric results suggest a weak effect. One explanation is that the steric hindrances of the carbon structures of the modifier and the ion are too small to cause more intense stereoselective clustering. Accordingly, alanine does not appear to be optimal for this kind of enantiomeric separation. However, there are also no experimental results to the contrary. Therefore, another numeric study is performed with phenylalanine. The more sterically demanding carbon structure should increase the previously indicated effects. Furthermore, enantiomeric separation in IMS was experimentally shown by Dwivedi et al. [79], although this could not be confirmed by DMS experiments in the present work (see Section 6.4).

Phenylalanine

As shown in Figure 6.34, the protonated ^{L}Phe has two main conformers, but all main cluster conformers $[^{L}Phe+(R/S)\text{-}2\text{-}BuOH+H]^+$ are based on the more stable ^{L}Phe conformer (see right bottom in Figure 6.34), which was checked by using Equation 6.1. In Figure 6.36 the

most stable cluster conformers [^{L}Phe+(*R*/*S*)-2-BuOH+H]$^{+}$ and the calculated G_n and CCS values are presented.

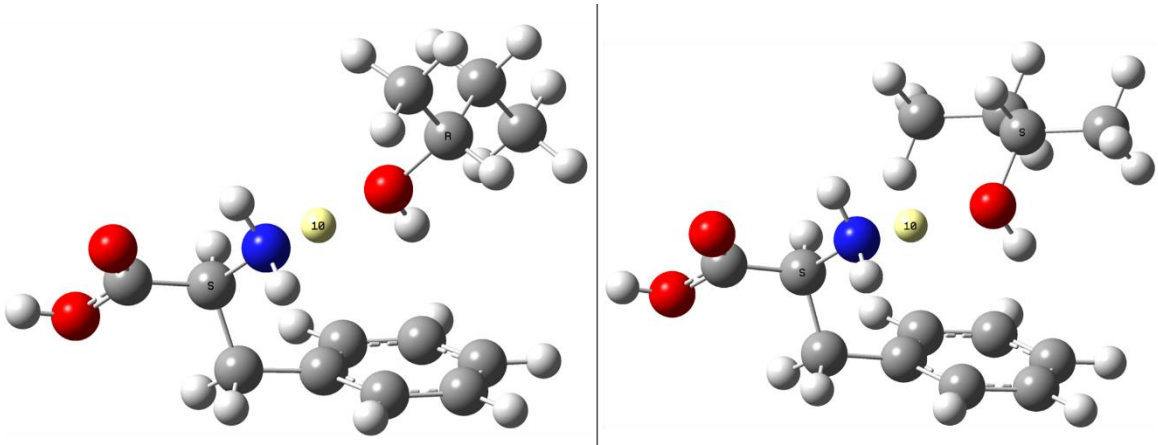

G_n = -21461.1901 eV
CCS = 157.25 +/- 1.54 Å²

G_n = -21461.1795 eV
CCS = 155.88 +/- 1.00 Å²

Figure 6.36: Optimized geometries of L-phenylalanine clustered with (*R*)-2-BuOH (left) and (*S*)-2-BuOH (right) calculated at the B3LYP/6-31++G(d,p) level of theory and the CCSs calculated with the MobCal-MPI code.

Equivalent to the results of clustered ^{L}Ala, the ^{L}Phe clusters [^{L}Phe+(*R*/*S*)-2-BuOH+H]$^{+}$ exhibit different main conformers depending on the enantiomer of the modifier (see Figure 6.36). However, the energetic difference is significantly smaller (ΔG_n = 0.0106 eV) and the CCSs are also identical in the error limits. Once again, however, cluster distributions must be considered. For a better overview of the cluster distributions, the four main species of both distributions are listed in Table 6.9.

As in the previous section, the (*R*)-clusters [^{L}Phe+(*R*)-2-BuOH+H]$^{+}$ are more stable compared to the (*S*)-clusters [^{L}Phe+(*S*)-2-BuOH+H]$^{+}$ (compare G_n in Tables 6.8 and 6.9). One difference is that this effect can be detected for ^{L}Phe not only for the main cluster structures but also for the next stable conformers. Accordingly, the stronger steric hindrance of ^{L}Phe does not cause a stronger absolute effect on the cluster stability, but the effect seems to be observable over a larger range of the cluster distributions. It should be noted that the difference in the cluster stability is extremely small. Once again, the CCSs show no clear modifier-dependent trend. Whether a mean difference can be observed in the average of the entire cluster distribution is estimated using the mean CCS. Therefore, the weighted average of the CCS was calculated for the most stable about 80% of each distribution. In this way, a difference of only 0.30 Å^2 could be identified ($CCS_{(S)\text{-cluster}}$= 157.03 Å^2; $CCS_{(R)\text{-cluster}}$= 157.33 Å^2), which is clearly smaller than the typical error limits of the method used. Accordingly, both the cluster stability and the CCS do not exhibit a strong stereoselective effect, which would be necessary for an enantiomeric separation in DMS.

Table 6.9: Relative stability of the four main [^{L}Phe+(*R*/*S*)-2-BuOH+H]$^{+}$ species of each stereoselective cluster distribution calculated at the B3LYP/6-31++G(d,p) level of theory and the CCSs calculated with the MobCal-MPI code.

Cluster species	G_n [eV]	G_n - G_{min} [eV]	CCS [Å^2]
[^{L}Phe+(*R*)-2-BuOH+H]$^{+}$ ((*R*)-cluster)	-21461.1901	0.0000	157.25 ± 1.54
	-21461.1727	0.0174	156.03 ± 1.33
	-21461.1725	0.0175	159.19 ± 1.77
	-21461.1709	0.0192	155.63 ± 1.47
[^{L}Phe +(*S*)-2-BuOH+H]$^{+}$ ((*S*)-cluster)	-21461.1795	0.0000	155.88 ± 1.00
	-21461.1667	0.0128	159.87 ± 1.35
	-21461.1653	0.0142	153.87 ± 1.04
	-21461.1634	0.0161	160.36 ± 1.63

In summary, it can be stated that both amino acids create different stereoselective cluster distributions. Accordingly, it comes down to low but observable differences in G_n, while the calculated CCSs show hardly any stereoselective dependence in the averages of the entire cluster distributions. It should be noted that the differences in G_n are in the order of 10^{-2} eV at most. To classify this value, the geometry distribution of $[Me_4N+(ACN)_2]^+$ calculated by Haack [110] at the B3LYP-GD3/6-31++G(d-p) level of theory is used. Depending on the position of the modifier molecules in the cluster structure, energetic differences in the order 10^{-1} eV could be shown (determined via the differences of the zero-point corrected binding energies) [110]. Therefore, the stereoselective differences in G_n are in a range that appears to be quantitatively negligible. Nevertheless, the systematically higher cluster stability of the (*R*)-clusters indicates stereoselective clustering in the gas phase, but the steric hindrance of the modifier is too small to lead to significantly different cluster distributions in CCS. Thus, increasing the steric hindrance of the modifier is necessary. This is a rather theoretical approach since a higher steric hindrance of the modifier would be associated with lower vapor pressure. For this reason, the use of such sterically more demanding modifier as gas-phase modifier becomes increasingly unrealistic.

Again, it should be noted that the calculations are only a rough approximation of reality. For simplicity, parts of the cluster distribution were neglected (i.e., only the most stable conformers were investigated) and larger cluster sizes were not calculated at all. Furthermore, the cluster process in DMS is characterized by large dynamics, which is not recreated by these calculations. Moreover, the inconstant conditions in the DMS cell, such as the *SV* or the temperature gradient, are not represented. Therefore, the numerical results should be understood as an indication of a maximally weak stereoselective effect and not as a definite result that can be directly applied to reality.

6.6 Summary and conclusion

The theory of an enantiomeric separation in DMS using a chiral, enantiopure gas-phase modifier is based on the work of Dwivedi et al. [79], which reported such a separation in IMS. Therefore, an enantiomeric separation in DMS could be possible, and the experience from the previous chapters on clustering in the gas phase also does not argue against this idea. Since this approach has not yet been established, the ideal experimental conditions were determined first (see Table 6.1) and, in a series of preliminary measurements, the Maruoka catalyst and phenylalanine were selected as promising analytes. While phenylalanine was already enantiomerically separated in IMS [79], the Maruoka catalyst is a rather unknown analyte for this kind of application. It is characterized by a more complex structure at the chiral position compared to phenylalanine (see Figure 6.4), and a stereoselective clustering could be amplified. At the same time, the absolute cluster effect is relatively weak, making a low *DT* necessary, while the absolute effect on phenylalanine is significantly stronger (compare Figures 6.3 and 6.5). The study of both chiral analytes—which differ significantly in the behavior in DMS, the type of chirality, and the stereoselective structure—should cover a wide range of chiral ions to maximize the chances of successful enantiomeric separation.

In addition to the investigated ions and DMS conditions, the impact of the ionization method is of great importance. The common ionization with an ESI source indicates a crucial problem in the formation of highly charged nanodroplets. Unlike the textbook ESI mechanism, these charged nanodroplets can pass the ion inlet of common MS systems as demonstrated by Markert et al. [60], which was also demonstrated in this work (see Figure 6.9). The behavior of charged nanodroplets in DMS was experimentally studied. A nanodroplet behavior similar to bare ions is established at an *SV* of 4000 V (see Figures 6.13 and 6.14), and the addition of a gas-phase modifier also led to a cluster-like effect. Furthermore, the wide nanodroplet distributions are composed of many undefined subdistributions. Depending on the sprayed solution and the DMS conditions, the subdistributions of one main distribution behave similarly (see Figure 6.17) or show noticeable differences (see Figure 6.18). It could be demonstrated that the main share of charged nanodroplets also pass the DMS cell. A total separation of bare ions and nanodroplets is not possible with the given system, which is problematic for enantiomeric separation since interactions of nanodroplets and bare ions, which could disturb stereoselective clustering, cannot be excluded. In addition, other modifiers can enter the DMS cell as part of a nanodroplet, resulting in an undefined gas-phase composition. Consequently, a variation of the ionization method offers itself to prevent the formation of a nanodroplet distribution. However, it became apparent that the low vapor pressure of the Maruoka catalyst excludes a sufficiently high ion yield by ionization in the gas phase, which includes both APCI and APLI. The commercial nanoESI source also does not lead to a textbook ESI mechanism, and the formation of highly charged nanodroplets could not be prevented (see Figure 6.26). Therefore, a change of the ion source was not carried out due to the lack of promising alternatives (see Table 6.5).

Even with the optimized measurement conditions, an enantiomeric separation was not observable experimentally for both analytes. The smallest differences in the *CV* due to the addition of stereoselective modifiers under otherwise identical conditions can be attributed to measurement inaccuracies. Furthermore, these can usually only be determined mathematically (see Figure 6.29 and Table 6.6), and the slight fluctuations cannot be identified as stereoselective effect (see Figure 6.32). A numerical study of alanine and phenylalanine reaches a quantitatively similar result. The CCS of the first protonated clusters of the L amino acids with both enantiomers of 2-BuOH $[^{L}AA+(R/S)\text{-2-BuOH+H}]^{+}$ were identical within the error limits and only minimal differences in the cluster stability were observed (see Figures 6.35 and 6.36). However, it could be demonstrated that for both amino acids many similar stable cluster structures must be considered (see Tables 6.8 and 6.9). On average, no quantitively different CCS could be demonstrated for the distributions either, but a systematically smaller cluster stability by using (*S*)-2-BuOH could be demonstrated. This systematics indicates stereoselective clustering.

In summary, the stereoselective clustering of a chiral ion with enantiopure 2-BuOH did not lead to an enantiomeric separation either in experimental or in numerical studies. In particular, the numerical results indicate a steric hindrance of both the ions and the modifier that is too low to lead to a significantly different cluster structure. A theoretical solution would be the addition of a sterically more complex modifier; however, the increasing vapor pressure could become a problem since mixing ratios in percentage range are necessary in DMS. Furthermore, the experimental approach also led to problems, such as the nanodroplet distribution or the thermodynamic connection of the ion source and the DMS cell. These have effects on ion-modifier interactions that cannot yet be estimated. The chemical composition of the gas phase in the DMS cell also cannot be prevented from contaminations such as water. Accordingly, the results of the underlying work of Dwivedi et al. [79] could not be reproduced and confirmed. The experimental and especially the numerical findings rather point away from the enantiomeric separation by adding enantiopure 2-BuOH to the gas phase. Nevertheless, the experimental results are not absolutely comparable because the instrument design and analytical methods differ greatly.

7 Overall summary, conclusion, and outlook

The interaction of ions and neutral species in the gas phase and, in particular, the cluster chemistry is of great importance for several analytical methods such as mass spectrometry, ion mobility spectrometry, and differential mobility spectrometry (see Chapter 1). For this reason, the aim of this work was the mainly experimental investigation of such interactions. Since this is an extremely broad topic, the focus was on individual subtopics, and the results should be combined to fundamental findings, which can be transferred to different analytical methods and chemical systems. These provide a reliable interpretation of the resulting spectra. Based on previous and parallel experimental and numerical studies, the following subtopics were examined:

- The effect of the ion structure on cluster formation (Chapter 4).
- Actual clustering and declustering process under constant conditions, depending on the reduced field strength (Chapter 5).
- Enantiomeric separation as a result of stereoselective cluster formation, using an enantiopure gas-phase modifier (Chapter 6).

Since the experimental approaches used to investigate the individual subtopics have already been summarized in the corresponding chapters, these will not be repeated in detail. Instead, the general findings, the thematic connection of the individual subtopics, and the resulting conclusions will be highlighted. Furthermore, the outlook for further studies will be given.

First, the cluster effect as a function of the ion structure was investigated at amines and diamines using a commercial DMS-MS coupling and a common ESI source for ionization. The relative CCS ratio between ion and modifier strongly influences the differential mobility, whereby an increase in CCS of the ion leads to a decreasing cluster effect. Even in pure nitrogen, the equivalent dependence of the interaction with polarized nitrogen on the ion structure could be shown. A quantitative comparison of different ions is only legitimate if the increasing ion structure does not lead to other effects such as shielding of the charged

position. However, structural variations at or close to the charged position influence the structure of the cluster due to a steric and chemical adaption of the ion. The modifier also influences the impact of the ion structure. In an MeOH cluster, the charge is delocalized, while it is centered in an ACN cluster. As a result, for individual combinations of ions and modifiers, the expected CCS-dependent decreasing of the cluster effect can be reversed or completely changed. In the event of multiple charging, a further effect could be shown. If there is a large distance between charged positions, largely independent cluster systems occur, while a short distance leads to a combined cluster system. This results in either nearly doubling the cluster effect or a reduction of the increasing.

The actual clustering process was investigated using HiKE-IMS. Ionization in the gas phase using a corona discharge prevents the investigation of analytes with a low vapor pressure and consequently mainly solvent clusters were investigated. The permanent presence of water in non-ignorable mixing ratios provided the opportunity to investigate mixed clusters, which should also have been present in the previous DMS-MS measurements. The permanent accumulation of water to nearly all ionic species is shown by a steady increase of the reduced ion mobility with increased reduced field strength. Such individual species did not exhibit this behavior. An increase in the humidity and a decrease in temperature both support higher mean cluster sizes and a decreased ion mobility. In this context, it is not relevant if a mixed cluster or a pure water cluster was observed. Only at high reduced field strengths, a constant reduced ion mobility hinted at nearly bare ions. Similar effects by the addition of modifier into the gas phase were expected but could hardly or not at all be detected due to an insufficient mixing ratio of the modifier. In addition, the actual declustering process can be investigated with HiKE-IMS. Species which are connected in a chemical system, could be identified through a shift in intensity by increasing the reduced field strength. These chemical systems are very likely to be cluster systems. Furthermore, a dynamic switch between connected species was demonstrated due to a plateau between the signals in a HiKE-IM spectrum. Accordingly, a dynamic clustering-declustering process even under constant energetic conditions was established. The combination of these dynamic clustering processes and other reactions lead to a complex chemical systems which produces more than just one defined ionic species.

The findings of the two subtopics were used to investigate stereoselective clustering in the gas phase. The addition of enantiopure 2-BuOH as modifier in the common DMS by investigating the Maruoka catalyst or phenylalanine should lead to an enantiomeric separation. This work neither experimentally nor numerically enabled an observable enantiomeric separation. The numerical results indicate a qualitative effect in the cluster stability of the first cluster, which is unlikely to be quantitatively measurable. According to the findings from Chapter 4, increasing the relative CCS of the modifier could increase these effects; however, the vapor pressure of an increasing modifier seems to make this impossible.

In addition, a modification of the mass spectrometer makes it possible to perform droplet experiments, and the presence of highly charged nanodroplets in the high vacuum area was demonstrated. These nanodroplets are formed in the ESI process, which must therefore differ from the textbook mechanism. A nanodroplet distribution is formed, which can be further divided into subdistributions. The chemical composition (solvents as well as ionic

species) defines the subdistributions and within the DMS process, a behavior known from bare ions was demonstrated. These nanodroplets have a differential mobility and a cluster-like effect by adding a modifier, as shown in the research. A separation of bare ions and highly charged nanodroplets was not possible. Consequently, contaminations in the DMS cell cannot be prevented, and these can interact with the bare ions. A change of the ionization method to prevent the generation of highly charged nanodroplets was excluded due to the lack of a suitable alternative.

Overall, the findings of the three subtopics can be combined to form generally valid results on cluster chemistry in the gas phase. A dynamic clustering-declustering process also occurs under constant chemical conditions and at reduced pressure and leads to a complex chemical system. As a result, the assignment of individual signals (e.g., in IMS) to one ionic species must be questioned as this would imply a nearly constant species in the entire analytical process. Instead, each signal represents a part of a dynamic chemical system. Furthermore, the effect of the ion structure on cluster formation is attributed to steric and chemical effects, and further charges can lead to single or multiple cluster centers depending on the ion structure and the added modifier. Moreover, a deviation of the textbook mechanism for the ionization with ESI was shown and further investigated. The stability of the charged nanodroplets is high enough to pass the DMS process and the ion inlet of common mass spectrometers. Accordingly, the presence of these species must be considered in any gas-phase process after ionization with an ESI source. A precise classification as liquid phase or as cluster is complicated and not finally feasible.
All data indicate that these are universally valid findings, which can be transferred to comparable systems. Nevertheless, only small ions were used in this work. In the case of larger ionic species such as oligopeptides or even peptides, further effects are expected.

This work clearly shows the complexity of the gas-phase chemistry of ions. The findings fit into the whole picture but also represent only a fragment. For a more accurate and resilient interpretation of analytical spectra, a deeper understanding of such effects is necessary, which is why further investigations must follow. In particular, the processes in HiKE-IMS and the highly charged nanodroplets require a more in-depth numerical and experimental investigation.

List of abbreviations

$\Delta CV_{\mathbf{X}\rightarrow\mathbf{Y}}$	difference in the compensation voltage between **X** and **Y**
$\Delta_R G$	Gibbs free energy of reaction
λ	wavelength
μ_D	electrical dipole moment
2-BuOH	2-butanol
ACE	acetone
ACN	acetonitrile
APCI	atmospheric pressure chemical ionization
AP	atmospheric pressure
API	atmospheric pressure ionization
APLI	atmospheric pressure laser ionization
CCS	collision cross section
CI	chemical ionization
CID	collision-induced dissociation
CRM	charge residue model
CV/ *CoV*	compensation voltage
DC	direct current
DeP	dew point
DFT	density functional theory
DMMP	dimethyl-phosphonate
DMO	DMS offset
DMS	differential mobility spectrometry
DP	declustering potential
DR	DMS resolution
DT	DMS temperature
DTIMS	drift tube IMS
E	electric field strength
E/N	reduced field strength
E_0	electronic energy
ee	enantiomeric excess
E_{high}	electric field strength of high field
EI	electron ionization
E_{low}	electric field strength of low-field
ESI	electrospray ionization

FAIMS	field asymmetric waveform ion mobility spectrometry
G_{corr}	Gibbs free energy correction
G_{min}	minimum sum of electonic energy and Gibbs free energy
G_n	sum of electonic energy and Gibbs free energy of species *n*
GS1	nebulizer gas
GS2	heater gas
HiKE-IMS	high kinetic energy - ion mobility spectrometry
HiKE-IMS-MS	high kinetic energy - ion mobility - mass spectrometry coupling
HWHM	half width at half maximum
IMS	ion mobility spectrometry
IMS-MS	ion mobility - mass spectrometry coupling
IP	impact partner (inert)
IPA	2-propanol
IS	ion spray voltage
K	absolute ion mobility
K_0	reduced ion mobility
KED	kinetic energy distribution
$^{L/D}$AA	L/D-enantiomer of an amino acid
$^{L/D}$Ala	L/D-enantiomer of alanine
$^{L/D}$Phe	L/D-enantiomer of phenylalanine
LC	liquid chromatography
l_d	length of the drift tube
LMCO	low mass cut-off
m	mass
m/z	mass-to-charge ratio
M	neutral analyte species
M^+	analyte cation
MDC	modifier compositions
MeOH	methanol
M^{II}	metal with oxidation state +II
MRM	multiple reaction monitoring
MS	mass spectrometry
N	gas number density
N_0	gas number density under standard conditions
nanoESI/ nESI	nano electrospray ionization
OPO	optical parametric oscillator
p	pressure
p_0	standard pressure
pre-RIP	pre-reactant ion peak
PTR	proton transfer reaction
Q1	first quadrupole of a QqQ
q2	second quadrupole (collision cell) of a QqQ
Q3	third quadrupole of a QqQ
QIT	quadrupole ion trap
QqQ	triple quadrupole system
rac.	racemic
ref	reference amino acid

REMPI	resonance enhanced multi photon ionization
RF	radio frequency
RIP	reactant ion peak
R_P	resolution power
SEM	secondary electron multiplier
SRM	selective reaction monitoring
SV	separation voltage
T	(background) temperature
T_0	standard temperature
tandem MS/ MS^n	tandem mass spectrometry
T_{APCI}	source temperature (APCI)
t_d	drift time
T_{eff}	effective temperature
T_{ESI}	source temperature (ESI)
T_h	temperature by electric heating
t_{high}	high-field time
TIC	total ion chromatogram
t_{low}	low-field time
Tof-MS	time-of-flight mass spectrometry
T_{source}	source temperature
v_d	drift velocity

List of Figures

List of Tables

References

[1] S. A. McLuckey and M. Mentinova: Ion/neutral, ion/electron, ion/photon, and ion/ion interactions in tandem mass spectrometry: Do we need them all? Are they enough?, *Journal of the American Society of Mass Spectrometry*, **2011**, 22(1), 3-12, DOI: 10.1007/s13361-010-0004-9.

[2] A. P. Bruins: Mass spectrometry with ion sources operating at atmospheric pressure, *Mass Spectrometry Reviews*, **1991**, 10(1), 53-77, DOI: 10.1002/mas.1280100104.

[3] P. Kebarle, S. K. Searler, A. Zolla, J. Scarborough, and M. Arshadi: The Solvation of the Hydrogen Ion by Water Molecules in the Gas Phase. Heats and Entropies of Solvation of Individual Reactions: $H^+(H_2O)_{n-1} + H_2O \rightarrow H^+(H_2O)_n$, *Journal of the American Chemical Society*, **1967**, 89(25), 6393-6399, DOI: 10.1021/ja01001a001.

[4] B. B. Schneider, E. G. Nazarov, F. Londry, P. Vouros, and T. R. Covey: Differential mobility spectrometry/mass spectrometry history, theory, design optimization, simulations, and applications, *Mass Spectrometry Reviews*, **2016**, 35(6), 687-737, DOI: 10.1002/mas.21453.

[5] W. S. Hopkins: Determining the properties of gas-phase clusters, *Molecular Physics*, **2015**, 113(21), 3151-3158, DOI: 10.1080/00268976.2015.1053545.

[6] J. L. Campbell, M. Zhu, and W. S. Hopkins: Ion-Molecule Clustering in Differential Mobility Spectrometry: Lessons Learned from Tetraalkylammonium Cations and their Isomers, *Journal of the American Society for Mass Spectrometry*, **2014**, 25(9), 1583-1591, DOI: 10.1007/s13361-014-0939-3.

[7] A. Good, D. A. Durden, and P. Kebarle: Ion–Molecule Reactions in Pure Nitrogen and Nitrogen Containing Traces of Water at Total Pressures 0.5–4 torr. Kinetics of Clustering Reactions Forming $H^+(H_2O)_n$, *The Journal of Chemical Physics*, **1970**, 52(1), 212-221, DOI: 10.1063/1.1672667.

[8] V. G. Anicich: An index of the literature for bimolecular gas phase cation-molecule reaction kinetics, *JPL Publication 03-19*, **2003**, Pasadena, CA, USA.

[9] M. L. Gross and R. M. Caprioli: The Encyclopedia of mass spectrometry Volume 6 Ionization Methods, 1st. ed., *Elsevier*, **2007**, Oxford, Oxon, UK.

[10] H. Kambara and I. Kanomata: Determination of Impurities in Gases by Atmospheric Pressure Ionization Mass Spectrometry, *Analytical Chemistry*, **1977**, 49(2), 270-275, DOI: 10.1021/ac50010a023.

[11] L. Sleno and D. A. Volmer: Ion activation methods for tandem mass spectrometry, *Journal of Mass Spectrometry*, **2004**, 39(10), 1091-1112, DOI: 10.1002/jms.703.

[12] A. K. Shukla and J. H. Futrell: Tandem mass spectrometry: dissociation of ions by collisional activation, *Journal of Mass Spectrometry*, **2000**, 35(9), 1069-1090, DOI: 10.1002/1096-9888(200009)35:9<1069::AID-JMS54>3.0.CO;2-C.

[13] A. Haack, C. Polaczek, M. Tsolakis, M. Thinius, H. Kersten, and T. Benter: Charge Retention/Charge Depletion in ESI-MS: Theoretical Rationale, *Journal of the American Society of Mass Spectrometry*, **2020**, 31(4), 785-795, DOI: 10.1021/jasms.9b00045.

[14] Y. Brachthäuser: Aufbau, Inbetriebnahme und Charakterisierung eines AP-IMS, Master-Thesis, *Bergische Universität Wuppertal*, **2013**, Wuppertal, NRW, Germany.

[15] J. A. de Gouw, M. Krishnamurthy, and S. R. Leone: The mobilities of ions and cluster ions drifting in polar gases, *Journal of Chemical Physics*, **1997**, 106(14), 5937-5942, DOI: 10.1063/1.473609.

[16] T. R. Covey, B. A. Thomson, and B. B. Schneider: Atmospheric pressure ion sources, *Mass Spectrometry Reviews*, **2009**, 28(6), 870-897, DOI: 10.1002/mas.20246.

[17] D. E. Clemmer and M. F. Jarrod: Ion Mobility Measurements and their Applications to Clusters and Biomolecules, *Journal of Mass Spectrometry*, **1997**, 32(6), 577-592, DOI: 10.1002/(SICI)1096-9888(199706)32:6<577::AID-JMS530>3.0.CO;2-4.

[18] D. Erdogdu, W. Wißdorf, M. Allers, A. T. Kirk, H. Kersten, S. Zimmermann, and T. Benter: Simulation of Cluster Dynamics of Proton-Bound Water Clusters in a High Kinetic Energy Ion-Mobility Spectrometer, *Journal of the American Society for Mass Spectrometry*, **2021**, 32(9), 2436-2450, DOI: 10.1021/jasms.1c00140.

[19] B. B. Schneider, T. R. Covey, S. L. Coy, E. V. Krylov, and E. G. Nazarov: Chemical Effects in the Separation Process of a Differential Mobility/Mass Spectrometer System, *Analytical Chemistry*, **2010**, 82(5), 1867-1880, DOI: 10.1021/ac902571u.

[20] D. Auerbach, J. Aspenleiter, and D. A. Volmer: Description of Gas-Phase Ion/Neutral Interactions in Differential Ion Mobility Spectrometry: CV Prediction Using Calibration Runs, *Journal of the American Society for Mass Spectrometry*, **2014**, 25(9), 1610-1621, DOI: 10.1007/s13361-014-0934-8.

[21] B. B. Schneider, T. R. Covey, and E. G. Nazarov: DMS-MS separations with different transport gas modifiers, *International Journal for Ion Mobility Spectrometry*, **2013**, 16(3), 207-216, DOI: 10.1007/s12127-013-0130-8.

[22] A. Kafle, S. L. Coy, B. M. Wong, A. J. Fornace Jr., J. J. Glick, and P. Vouros: Understanding Gas Phase Modifier Interactions in Rapid Analysis by Differential Mobility-Tandem Mass Spectrometry, *Journal of the American Society for Mass Spectrometry*, **2014**, 25(7), 1098-1113, DOI: 10.1007/s13361-013-0808-5.

[23] F. Stappert, B. Schneider, M. Thinius, W. Wissdorf, H. Kersten, T. Covey, J. Hager, and T. Benter: Effects of chemical dynamics and clustering reactions of chemical modifiers with analyte ions in differential mobility spectrometry (DMS), *Proceedings of the 65th ASMS Conference on Mass Spectrometry and Allied Topics*, **2017**, Indianapolis, IN, USA.

[24] D. Erdogdu, W. Wissdorf, F. Stappert, H. Kersten, and T. Benter: Chemical Kinetics and Ion Transport Simulations: Cluster Dynamics in Differential Ion Mobility Spectrometry, *Proceedings of the 67th ASMS Conference on Mass Spectrometry and Allied Topics*, **2019**, Atlanta, GA, USA.

[25] F. Stappert: Untersuchungen zur chemischen Dynamik und Clusterbildung bei der Ionentrennung in der differentiellen Mobilitätsspektrometrie (DMS), Master-Thesis, *Bergische Universität Wuppertal*, **2017**, Wuppertal, NRW, Germany.

[26] R. Fernández-Maestre, C. Wu, and H. H. Hill Jr.: Using a buffer gas modifier to change separation selectivity in ion mobility spectrometry, *International Journal of Mass Spectrometry*, **2010**, 298(1-3), 2-9, DOI: 10.1016/j.ijms.2010.08.009.

[27] Z. Izadi, M. Tabrizchi, H. Borsdorf, and H. Farrokhpour: Humidity Effect on the Drift Times of the Reactant Ions in Ion Mobility Spectrometry, *Analytical Chemistry*, **2019**, 91(24), 15932-15940, DOI: 10.1021/acs.analchem.9b04450.

[28] K. M. Roscioli, M. R. Lamabadusuriya, C. S. Harden, A. J. Midey, C. Wu, W. F. Siems, and H. H. Hill Jr.: Structure selective ion molecule interactions (SSIMI) in ion mobility spectrometry, *International Journal for Ion Mobility Spectrometry*, **2014**, 17(1), 43-53, DOI: 10.1007/s12127-013-0143-3.

[29] E. Waraksa, U. Perycz, J. Namieśnik, M. Sillanpää, T. Dymerski, M. Wójtowicz, and J. Puton: Dopants and gas modifiers in ion mobility spectrometry, *Trends in Analytical Chemistry*, **2016**, 82, 237-249, DOI: 10.1016/j.trac.2016.06.009.

[30] A. A. Shvartsburg: Differential Ion Mobility Spectrometry – Nonlinear Ion Transport and Fundamentals of FAIMS, *CRC Press*, **2009**, Boca Raton, FL, USA, DOI: 10.1201/9781420051070.

[31] J. Sunner, G. Nicol, and P. Kebarle: Factors Determining Relative Sensitivity of Analytes in Positive Mode Atmospheric Pressure Ionization Mass Spectrometry, *Analytical Chemistry*, **1988**, 60(13), 1300-1307, DOI: 10.1021/ac00164a012.

[32] W. Wißdorf, B. Schneider, T. Covey, J. Hager, and T. Benter: Is differential mobility chemically driven? Evidence and simulations for chemical effects as a primary separation factor in DMS, *Proceedings of the 64th ASMS Conference on Mass Spectrometry and Allied Topics*, **2016**, San Antonio, TX, USA.

[33] D. Erdogdu, W. Wissdorf, C. Polaczek, F. Stappert, H. Kersten, T. Benter, M. Allers, A. T. Kirk, and S. Zimmermann: Simulation of Cluster Dynamics in High Kinetic Energy IMS (HiKE-IMS), *Proceedings of the 67th ASMS Conference on Mass Spectrometry and Allied Topics*, **2019**, Atlanta, GA, USA.

[34] I. Dzidic, D. I. Carroll, R. N. Stillwell, and E. C. Horning: Comparison of Positive Ions Formed in Nickel-63 and Corona Discharge Ion Sources Using Nitrogen, Argon, Isobutane, Ammonia and Nitric Oxideas Reagents in Atmospheric Pressure Ionization Mass Spectrometry, *Analytical Chemistry*, **1976**, 48(12), 1763-1768, DOI: 10.1021/ac50006a035.

[35] D. I. Carroll, I. Dzidic, E. C. Horning, and R. N. Stillwell: Atmospheric Pressure Ionization Mass Spectrometry, *Applied Spectroscopy Reviews*, **1981**, 17(3), 337-406, DOI: 10.1080/05704928108060409.

[36] D. Müller: Development of a kinetically controlled plasma induced chemical ionization source, Dissertation, *Bergische Universität Wuppertal*, **2019**, Wuppertal, NRW, Germany, DOI: 10.25926/qtrc-ka79.

[37] M. Thinius, C. Polaczek, M. Langner, S. Bräkling, A. Haack, H. Kersten, and T. Benter: Charge Retention/Charge Depletion in ESI-MS: Experimental Evidence, *Journal of the American Society of Mass Spectrometry*, **2020**, 31(4), 773-784, DOI: 10.1021/jasms.9b00044.

[38] J. B. Fenn, M. Mann, C. K. Meng, S. F. Wong, and C. M. Whitehouse: Electrospray Ionization for Mass Spectrometry of Large Biomolecules, *Science*, **1989**, 246(4926), 64-71, DOI: 10.1126/science.2675315.

[39] M. Thinius, H. Kersten, and T. Benter: Characterization of an API-MS Ion Transfer Stage, *GDCh Wissenschaftsforum Chemie*, **2017**, Berlin, Berlin, Germany.

[40] A. R. Johnson and E. E. Carlson: Collision-Induced Dissociation Mass Spectrometry: A Powerful Tool for Natural Product Structure Elucidation, *Analytical Chemistry*, **2015**, 87(21), 10668-10678, DOI: 10.1021/acs.analchem.5b01543.

[41] X. Li, Y. Huang, P. B. O'Connor, and C. Li: Structural Heterogeneity of Doubly-Charged Peptide b-Ions, *Journal of the American Society for Mass Spectrometry*, **2011**, 22(2), 245-254, DOI: 10.1007/s13361-010-0036-1.

[42] J. R. Enders and J. A. Mclean: Chiral and Structural Analysis of Biomolecules Using Mass Spectrometry and Ion Mobility-Mass Spectrometry, *Chirality*, **2009**, 21(1E), E253-E264, DOI: 10.1002/chir.20806.

[43] G. A. Harris, D. M. Hostetler, C. Y. Hampton, and F. M. Fernández: Comparison of the Internal Energy Deposition of Direct Analysis in Real Time and Electrospray Ionization Time-of-Flight Mass Spectrometry, *Journal of the American Society for Mass Spectrometry*, **2010**, 21(5), 855-863, DOI: 10.1016/j.jasms.2010.01.019.

[44] C. Ieritano, J. Featherstone, A. Haack, M. Guna, J. L. Campbell, and W. S. Hopkins: How Hot Are Your Ions in Differential Mobility Spectrometry?, *Journal of the American Society for Mass Spectrometry*, **2020**, 31(3), 582-593, DOI: 10.1021/jasms.9b00043.

[45] B. Liu, S. Brøsted Nielsen, P. Hvelplund, H. Zettergren, H. Cederquist, B. Manil, and B. A. Huber: Collision-Induced Dissociation of Hydrated Adenosine Monophosphate Nucleotide Ions: Protection of the Ion in Water Nanoclusters, *Physical Review Letters*, **2006**, 97(13), 1-4, DOI: 10.1103/PhysRevLett.97.133401.

[46] M. Lorenz: Räumlich und zeitlich aufgelöste Photoionisierung als Werkzeug zur Charakterisierung von Atmosphärendruckionenquellen in der Massenspektrometrie, Dissertation, *Bergische Universität Wuppertal*, **2014**, Wuppertal, NRW, Germany, URN: urn:nbn:de:hbz:468-20111014-145040-5.

[47] W. Wißdorf: Simulation of Ion Dynamics in Atmospheric Pressure Ionization Sources, Dissertation, *Bergische Universität Wuppertal*, **2011**, Wuppertal, NRW, Germany, URN: urn:nbn:de:hbz:468-20141009-103409-0.

[48] V. A. Derpmann: Development and Characterization of capillary Atmospheric Pressure Electron Capture Ionization (cAPECI), Dissertation, *Bergische Universität Wuppertal*, **2014**, Wuppertal, NRW, Germany, URN: urn:nbn:de:hbz:468-20150410-102234-8.

[49] K. Kroll, D. Erdogdu, T. Kutsch, W. Wißdorf, H. Kersten, and T. Benter: Progress in the development of a kinetically controlled chemical ionization setup, *Proceedings of the 66th ASMS Conference on Mass Spectrometry and Allied Topics*, **2018**, San Diego, CA, USA.

[50] D. Erdogdu, M. Allers, W. Wissdorf, C. Markert, H. Kersten, S. Zimmermann, and T. Benter: Chemical Reaction and Transport Simulations of Positive Reactant Ions in High Kinetic Energy Ion Mobility Spectrometry (HiKE-IMS); *Proceedings of the 68th ASMS Conference on Mass Spectrometry and Allied Topics 'Reboot'*, **2020**, virtual.

[51] J. H. Gross: Mass Spectrometry – A Textbook, *Springer-Verlag*, **2004**, Berlin Heidelberg, Germany.

[52] J.J. Thomson; Bakerian Lecture: Rays of positive electricity, *Proceedings of the Royal Society. Series A, - Mathematical and Physical Science*, **1913**, 89(607), 1-20, DOI: 10.1098/rspa.1913.0057.

[53] M. Thinius, N. Rutenbach, W. Wißdorf, H. Kersten, and T. Benter: Evaluation of kinetic energy distributions in API-MS ion transfer stages, *Proceedings of the 66th ASMS Conference on Mass Spectrometry and Allied Topics*, **2018**, San Diego, CA, USA.

[54] P. Kebarle and U. H. Verkerk: Electrospray: From ions in solution to ions in the gas phase, what we know now, *Mass Spectrometry Reviews*, **2009**, 28(6), 898-917, DOI: 10.1002/mas.20247.

[55] A. Gomez and K. Tang: Charge and fission of droplets in electrostatic sprays, *Physics of Fluids*, **1994**, 6(1), 404-414, DOI: 10.1063/1.868037.

[56] J. N. Smith, R. C. Flagan, and J. L. Beauchamp: Droplet Evaporation and Discharge Dynamics in Electrospray Ionization, *Journal of Physical Chemistry A*, **2002**, 106(42), 9957-9967, DOI: 10.1021/jp025723e.

[57] A. Venter, P. E. Sojka, and R. G. Cooks: Droplet Dynamics and Ionization Mechanisms in Desorption Electrospray Ionization Mass Spectrometry, *Analytical Chemistry*, **2006**, 78(24), 8549-8555, DOI: 10.1021/ac0615807.

[58] R. L. Grimm and J. L. Beauchamp: Evaporation and Discharge Dynamics of Highly Charged Droplets of Heptane, Octane, and *p*-Xylene Generated by Electrospray Ionization, *Analytical Chemistry*, **2002**, 74(24), 6291-6297, DOI: 10.1021/ac025889b.

[59] Y. Kang, B. B. Schneider, and T. R. Covey: On the Nature of Mass Spectrometer Analyzer Contamination, *Journal of the American Society of Mass Spectrometry*, **2017**, 28(11), 2384-2392, DOI: 10.1007/s13361-017-1747-3.

[60] C. Markert, M. Thinius, L. Lehmann, C. Heintz, F. Stappert, W. Wissdorf, H. Kersten, T. Benter, B. B. Schneider, and T. R. Covey: Observation of charged droplets from electrospray ionization (ESI) plumes in API mass spectrometers, *Analytical and Bioanalytical Chemistry*, **2021**, 413(22), 5587-5600, DOI: 10.1007/s00216-021-03452-y.

[61] J. Chang, P. A. Lawless, and T. Yamamoto: Corona Discharge Processes, *IEEE Transaction on Plasma Science*, **1991**, 19(6), 1152-1166, DOI: 10.1109/27.125038.

[62] A. A. Viggiano, F. Dale, and J. F. Paulson: Proton transfer reactions of $H^+(H_2O)_{n=2-11}$ with methanol, ammonia, pyridine, acetonitrile, and acetone, *The Journal of Chemical Physics*, **1988**, 88(4), 2469-2477, DOI: 10.1063/1.454027.

[63] R. S. Blake, P. S. Monks, and A. M. Ellis: Proton-Transfer Reaction Mass Spectrometry, *Chemical Reviews*, **2009**, 109(3), 861-896, DOI: 10.1021/cr800364q.

[64] A. Raffaelli and A. Saba: Atmospheric pressure photoionization mass spectrometry, *Mass Spectrometry Reviews*, **2003**, 22(5), 318-331, DOI: 10.1002/mas.10060.

[65] M. Constapel, M. Schellenträger, O. J. Schmitz, S. Gäb, K. J. Brockmann, R. Giese, and T. Benter: Atmospheric-pressure laser ionization: a novel ionization method for liquid chromatography/mass spectrometry, *Rapid Communications in Mass Spectrometry*, **2005**, 19(3), 326-336, DOI: 10.1002/rcm.1789.

[66] AB Sciex: 6500 and 6500+ Series of Instruments – System User Guide, **2015**, RUO-IDV-05-2095-A.

[67] D. J. Douglas: Linear quadrupoles in mass spectrometry, *Mass Spectrometry Reviews*, **2009**, 28(6), 937-960, DOI: 10.1002/mas.20249.

[68] J. W. Hager and J. C. Y. Le Blanc: Product ion scanning using a Q-q-$Q_{linear\ ion\ trap}$ (Q TRAP™) mass spectrometer, *Rapid Communications in Mass Spectrometry*, **2003**, 17(10), 1056-1064, DOI: 10.1002/rcm.1020.

[69] B. Domon and R. Aebersold: Mass Spectrometry and Protein Analysis, *Science*, **2006**, 312(5771), 212-217, DOI: 10.1126/science.1124619.

[70] S. Gallien, E. Duriez, and B. Domon: Selected reaction monitoring applied to proteomics, *Journal of Mass Spectrometry*, **2011**, 46(3), 298-312, DOI: 10.1002/jms.1895.

[71] G. A. Eiceman and Z. Karpas: Ion Mobility Spectrometry, 2nd ed., *CRC Press*, **2005**, Boca Raton, FL, USA.

[72] M. J. Manard and P. R. Kemper: Ion Mobility Mass Spectrometry: The design of a new high-resolution ion mobility instrument with applications toward electronic-state characterization of first-row transition metal cations, *International Journal of Mass Spectrometry*, **2016**, 402, 1-11, DOI: 10.1016/j.ijms.2016.02.014.

[73] J. Langejuergen, M. Allers, J. Oermann, A. Kirk, and S. Zimmermann: High Kinetic Energy Ion Mobility Spectrometer: Quantitative Analysis of Gas Mixtures with Ion Mobility Spectrometry, *Analytical Chemistry*, **2014**, 86(14), 7023-7032, DOI: 10.1021/ac5011662.

[74] A. B. Kanu, P. Dwivedi, M. Tam, L. Matz, and H. H. Hill Jr.: Ion mobility-mass spectrometry, *Journal of Mass Spectrometry*, **2008**, 43(1), 1-22, DOI: 10.1002/jms.1383.

[75] C. Lapthorn, F. Pullen, and B. Z. Chowdhry: Ion mobility spectrometry-mass spectrometry (IMS-MS) of small molecules: Separating and assigning structures to ions, *Mass Spectrometry Reviews*, **2013**, 32(1), 43-71, DOI: 10.1002/mas.21349.

[76] A. T. Kirk and S. Zimmermann: Bradbury-Nielsen vs. Field switching shutters for high resolution drift tube ion mobility spectrometers, *International Journal for Ion Mobility Spectrometry*, **2014**, 17(3-4), 131-137, DOI: 10.1007/s12127-014-0153-9.

[77] Z. Berant, Z. Karpas, and O. Shahal: Effects of Temperature and Clustering on Mobility of Ions in CO_2, *Journal of Physical Chemistry*, **1989**, 93(21), 7529-7532, DOI: 10.1021/j100358a052.

[78] Smiths Detection: Chemical Agent Detector LCD 3.3 – Operational Instruction/User Manual, **2008**, Issue 1.

[79] P. Dwivedi, C. Wu, L. M. Matz, B. H. Clowers, W. F. Siems, and H. H. Hill Jr.: Gas-Phase Chiral Separations by Ion Mobility Spectrometry, *Analytical Chemistry*, **2006**, 78(24), 8200-8206, DOI: 10.1021/ac0608772.

[80] B. B. Schneider, T. R. Covey, S. L. Coy, E. V. Krylov, and E. G. Nazarov: Planar differential mobility spectrometer as a pre-filter for atmospheric pressure ionization mass spectrometry, *International Journal of Mass Spectrometry*, **2010**, 298(1-3), 45-54, DOI: 10.1016/j.ijms.2010.01.006.

[81] J. Lozeille, E. Winata, P. Soldán, E. P. F. Lee, L. A. Viehland, and T. G. Wright: Spectroscopy of $Li^+ \cdot Rg$ and Li^+-Rg transport coefficients (Rg = He-Rn), *Physical Chemistry Chemical Physics*, **2002**, 4(15), 3601-3610, DOI: 10.1039/b111675d.

[82] A. Wilks, M. Hart, A. Koehl, J. Somerville, B. Boyle, and D. Ruiz-Alonso: Characterization of a miniature, ultra-high-field, ion mobility spectrometer, *International Journal for Ion Mobility Spectrometry*, **2012**, 15(3), 199-222, DOI: 10.1007/s12127-012-0109-x.

[83] M. Allers, A. T. Kirk, N. von Roßbitzky, D. Erdogdu, R. Hillen, W. Wissdorf, T. Benter, and S. Zimmermann: Analyzing Positive Reactant Ions in High Kinetic Energy Ion Mobility Spectrometry (HiKE-IMS) by HiKE-IMS-MS, *Journal of the American Society of Mass Spectrometry*, **2020**, 31(4), 812-821, DOI: 10.1021/jasms.9b00087.

[84] E. G. Nazarov, S. L. Coy, E. V. Krylov, R. A. Miller, and G. A. Eiceman: Pressure Effects in Differential Mobility Spectrometry, *Analytical Chemistry*, **2006**, 78(22), 7697-7706, DOI: 10.1021/ac061092z.

[85] I. A. Buryakov, E. V. Krylov, A. L. Makas, E. G. Nazarov, V. V. Pervukhin, and U. K. Rasulev: Separation of ions according to mobility in a strong AC electric field, *Soviet technical physics letters*, **1991**, 17, 446-447.

[86] AB Sciex: Analyst® 1.6.3 Software - SelexION® Technology for 5500 and 6500 Series Systems and SelexION®+ Technology for 6500+ Series Systems – User Guide, **2015**, RUO-IDV-05-0275-C.

[87] E. V. Krylov: Pulses of Special Shapes Formed on a Capacitive Load, *Instruments and Experimental Techniques*, **1997**, 40(5), 628-631.

[88] R. W. Purves and R. Guevremont: Electrospray Ionization High-Field Asymmetric Waveform Ion Mobility Spectrometry − Mass Spectrometry, *Analytical Chemistry*, **1999**, 71(13), 2346-2357, DOI: 10.1021/ac981380y.

[89] B. B. Schneider, T. R. Covey, S. L. Coy, E. V. Krylov, and E. G. Nazarov: Control of chemical effects in the separation process of a differential mobility mass spectrometer system, *European Journal of Mass Spectrometry*, **2010**, 16(1), 57-71, DOI: 10.1255/ejms.1025.

[90] A. Berthod: Chiral Recognition in Separation Methods – Mechanisms and Applications, *Springer-Verlag*, **2010**, Berlin Heidelberg, Germany, DOI: 10.1007/978-3-642-12445-7.

[91] W. H. Pirkle and T. C. Pochapsky: Considerations of Chiral Recognition Relevant to the Liquid Chromatographic Separation of Enantiomers, *Chemical Reviews*, **1989**, 89(2), 347-362, DOI: 10.1021/cr00092a006.

[92] S. Allenmark and V. Schurig: Chromatography on chiral stationary phases, *Journal of Materials Chemistry*, **1997**, 7(10), 1955-1963, DOI: 10.1039/a702403g.

[93] V. Domalain, M. Hubert-Roux, V. Tognetti, L. Joubert, C. M. Lange, J. Rouden, and C. Afonso: Enantiomeric differentiation of aromatic amino acids using traveling wave ion mobility-mass spectrometry, *Chemical Science*, **2014**, 5(8), 3234-3239, DOI: 10.1039/c4sc00443d.

[94] A. Mie, M. Jörntén-Karlsson, B. Axelsson, A. Ray, and C. T. Reimann: Enantiomer Separation of Amino Acids by Complexation with Chiral Reference Compounds and High-Field Asymmetric Waveform Ion Mobility Spectrometry: Preliminary Results and Possible Limitations, *Analytical Chemistry*, **2007**, 79(7), 2850-2858, DOI: 10.1021/ac0618627.

[95] W. A. Tao, D. Zhang, E. N. Nikolaev, and R. G. Cooks: Copper(II)-Assisted Enantiomeric Analysis of D,L-Amino Acids Using the Kinetic Method: Chiral Recognition and Quantification in the Gas Phase, *Journal of the American Chemical Society*, **2000**, 122(43), 10598-10609, DOI: 10.1021/ja000127o.

[96] S. Lee, S. Park, Y. Hong, J. Lee, J. Kim, D. Yoon, X. Kong, S. Lee, and H. B. Oh: Chiral differentiation of D- and L-alanine by permethylated β-cyclodextrin: IRMPD spectroscopy and DFT methods, *Physical Chemistry Chemical Physics*, **2017**, 19(22), 14729-14737, DOI: 10.1039/c7cp01085k.

[97] AB Sciex: Analyst® 1.6 Software - Software Reference Guide, **2011**.

[98] M. Wojdyr: Fityk: a general-purpose peak fitting program, *Journal of Applied Crystallography*, **2010**, 43(5), 1126-1128, DOI: 10.1107/S0021889810030499.

[99] AB Sciex: Turbo V™ Ion Source – Operator Guide, **2014**, RUO-IDV-05-0940-D.

[100] AB Sciex: NanoSpray® Ionenquelle - Bedienerhandbuch, **2019**, RUO-IDV-05-0811-DE-G.

[101] Ekspla: NT340 SERIES – High Energy Broadly Tunable, Datasheet, rev.: 20210423.

[102] CryLaS GmbH: FQSS 266-200 – Diode pumped passively Q-switched solid state laser, Datasheet, 2018, rev.: 1.5.

[103] AB Sciex: SelexION® Technology: The Solution to Selectivity Challenges in Quantitative Analysis - Differential Mobility Separations Enhanced with Chemical Modifiers: A Higher Dimension in Selectivity, **2019**, RUO-MKT-02-3251-C.

[104] D. Erdogdu: Chemische Kinetik- und Ionentransportsimulationen des protongebundenen Wasserclustersystems in der Ionenmobilitätsspektrometrie, Master-Thesis, *Bergische Universität Wuppertal*, **2018**, Wuppertal, NRW, Germany.

[105] A. T. Kirk, D. Grube, T. Kobelt, C. Wendt, and S. Zimmermann: High-Resolution High Kinetic Energy Ion Mobility Spectrometer Based on a Low-Discrimination Tristate Ion Shutter, *Analytical Chemistry*, **2018**, 90(9), 5603-5611, DOI: 10.1021/acs.analchem.7b04586.

[106] A. R. Katritzky, C. H. Watson, Z. Dega-Szafran, and J. R. Eyler: Collisionally Activated Dissociation of *N*-Alkylpyridinium Cations to Pyridine and Alkyl Cations in the Gas Phase, *Journal of the American Chemical Society*, **1990**, 112(7), 2471-2478, DOI: 10.1021/ja00163a001.

[107] M. J. Frisch, G. W. Trucks, H. B. Schlegel, G. E. Scuseria, M. A. Robb, J. R. Cheeseman, G. Scalmani, V. Barone, G. A. Petersson, H. Nakatsuji, X. Li, M. Caricato, A. V. Marenich, J. Bloino, B. G. Janesko, R. Gomperts, B. Mennucci, H. P. Hratchian, J. V. Ortiz, A. F. Izmaylov, J. L. Sonnenberg, D. Williams-Young, F. Ding, F. Lipparini, F. Egidi, J. Goings, B. Peng, A. Petrone, T. Henderson, D. Ranasinghe, V. G. Zakrzewski, J. Gao, N. Rega, G. Zheng, W. Liang, M. Hada, M. Ehara, K. Toyota, R. Fukuda, J. Hasegawa, M. Ishida, T. Nakajima, Y. Honda, O. Kitao, H. Nakai, T. Vreven, K. Throssell, J. A. Montgomery, Jr., J. E. Peralta, F. Ogliaro, M. J. Bearpark, J. J. Heyd, E. N. Brothers, K. N. Kudin, V. N. Staroverov, T. A. Keith, R. Kobayashi, J. Normand, K. Raghavachari, A. P. Rendell, J. C. Burant, S. S. Iyengar, J. Tomasi, M. Cossi, J. M. Millam, M. Klene, C. Adamo, R. Cammi, J. W. Ochterski, R. L. Martin, K. Morokuma, O. Farkas, J. B. Foresman, and D. J. Fox: Gaussian 16, Revision A.03, *Gaussian, Inc.*, **2016**, Wallingford, CT, USA.

[108] R. D. Dennington II, T. A. Keith, and J. M. Millam: GaussView 6.0.16: *Semichem, Inc.*, **2016**, Shawnee Mission, KS, USA.

[109] J. W. Ochterski: Thermochemistry in Gaussian, **2000**, http://gaussian.com/thermo/ (visited on January 8, 2022).

[110] A. Haack: Theoretical Investigations on Cluster Formation in Mass Spectrometry, Dissertation, *Bergische Universität Wuppertal*, **2020**, Wuppertal, NRW, Germany, DOI: 10.25926/x68p-cx61.

[111] C. Ieritano, J. Course, J. L. Campbell, and W. S. Hopkins: A parallelized molecular collision cross section package with optimized accuracy and efficiency, *Analyst*, **2019**, 144(5), 1660-1670, DOI: 10.1039/c8an02150c.

[112] H. Wincel: Gas-phase clustering of protonated amino acids with acetonitrile, *Chemical Physics Letters*, **2010**, 488(4-6), 219-222, DOI: 10.1016/j.cplett.2010.02.030.

[113] C. Polaczek, A. Haack, M. Thinius, W. Wißdorf, H. Kersten, and T. Benter: Ion-solvent interactions in nanoESI-MS: Characterization of charge depletion and charge conservation (supercharging) processes, *Proceedings of the 66th ASMS Conference on Mass Spectrometry and Allied Topics*, **2018**, San Diego, CA, USA.

[114] C. Polaczek, C. Thoben, M. Allers, A. Haack, S. Zimmermann, and T. Benter: Chemical modification of the matrix gas: Comparison experiments with ESI-MS and ESI-IMS-MS, *Proceedings of the 68th ASMS Conference on Mass Spectrometry and Allied Topics 'Reboot'*, **2020**, virtual.

[115] C. Polaczek, M. Thinius, H. Kersten, and T. Benter: Ion-solvent interactions in nanoESI-MS: Comparison of different ion transfer settings and analyzer systems, *52. DGMS-Jahrestagung/ 52nd DGMS annual meeting*, **2019**, Rostock, MV, Germany.

[116] C. Polaczek: Investigation of Ion-Solvent Interactions in Electrospray Ionization Mass Spectrometry, Dissertation, *Bergische Universität Wuppertal*, **2021**, Wuppertal, NRW, Germany, DOI: 10.25926/xntq-c882.

[117] B. B. Schneider, E. G. Nazarov, and T. R. Covey: Peak capacity in differential mobility spectrometry: effects of transport gas and gas modifiers, *International Journal for Ion Mobility Spectrometry*, **2012**, 15(3), 141-150, DOI: 10.1007/s12127-012-0098-9.

[118] J. A. Silveira, K. L. Fort, D. Kim, K. A. Servage, N. A. Pierson, D. E. Clemmer, and D. H. Russell: From Solution to the Gas Phase: Stepwise Dehydration and Kinetic Trapping of Substance P Reveals the Origin of Peptide Conformations, *Journal of the American Chemical Society*, **2013**, 135(51), 19147-19153, DOI: 10.1021/ja4114193.

[119] D. R. Linde (editor): CRC Handbook of Chemistry and Physics, 84th Edition, *CRC Press*, **2003**, Boca Raton, FL, USA.

[120] Z. Karpas, Z. Bernat, and R.M. Stimac: An Ion Mobility Spectrometry/Mass Spectrometry (IMS/MS) Study of the Site of Protonation in Anilines, *Structural Chemistry*, **1990**, 1(2-3), 201-204, DOI: 10.1007/BF00674262.

[121] Z. Karpas: Ion Mobility Spectrometry of Aliphatic and Aromatic Amines, *Analytical Chemistry*, **1989**, 61(7), 684-689, DOI: 10.1021/ac00182a009.

[122] C. Kune, C. Delvaux, J. R. N. Haler, L. Quinton, G. Eppe, E. De Pauw, and J. Far: A Mechanistic Study of Protonated Aniline to Protonated Phenol Substitution Considering Tautomerization by Ion Mobility Mass Spectrometry and Tandem Mass Spectrometry, *Journal of the American Society for Mass Spectrometry*, **2019**, 30(11), 2238-2249, DOI: 10.1007/s13361-019-02321-4.

[123] Wolfram|Alpha: Knowledgebase, **2020**, https://www.wolframalpha.com/input/?i=+vapor+pressure++1%2C2-Diaminoethane+19%C2%B0C (visited on December 17, 2021).

[124] E. P. L. Hunter and S. G. Lias: Evaluated Gas Phase Basicities and Proton Affinities of Molecules: An Update, *Journal of Physical and Chemical Reference Data*, **1998**, 27(3), 413-656, DOI: 10.1063/1.556018.

[125] A. Wakisaka, H. Abdoul-Carime, Y. Yamamoto and Y. Kiyozumi: Non-ideality of binary mixtures Water–methanol and water–acetonitrile from the viewpoint of clustering structure, *Journal of the Chemical Society - Faraday Transactions*, **1998**, 94(3), 369-374, DOI: 10.1039/a705777f.

[126] M. Kitamura, S. Shirakawa, and K. Maruoka: Powerful Chiral Phase-Transfer Catalysts for the Asymmetric Synthesis of α-Alkyl- and α,α-Dialkyl-α-amino Acids, *Angewandte Chemie – International Edition*, **2005**, 44(10), 1549-1551, DOI: 10.1002/anie.200462257.

[127] P. L. Houston: Chemical Kinetics and Reaction Dynamics, *Dover Publication, inc.*, **2006**, Mineola, New York, USA.

[128] H. Kersten: Development of an Atmospheric Pressure Ionization source for *in situ* monitoring of degradation products of atmospherically relevant volatile organic compounds, Dissertation, *Bergische Universität Wuppertal*, **2011**, Wuppertal, NRW, Germany, URN: urn:nbn:de:hbz:468-20110418-092806-6.